UNIVERSIDADE CATÓLICA PORTUGUESA

Hybrid-Trefftz Finite Elements for Elastostatic and Elastodynamic Problems in Porous Media

Tese apresentada à Universidade Católica Portuguesa para obtenção do grau de doutor em Engenharia Civil

Por: **CAO DUC TOAN**

Sob orientação de:

Professor Doutor Ionut Dragos Moldovan
Professor Doutor João António Teixeira de Freitas

FACULDADE DE ENGENHARIA
UNIVERSIDADE CATÓLICA PORTUGUESA

Agosto, 2013

Abstract

The displacement and stress models of the hybrid-Trefftz finite element formulation are applied to the elastostatic and elastodynamic analysis of two-dimensional saturated and unsaturated porous media problems.

The formulation develops from the classical separation of variables in time and space, but it leads to two time integration strategies. The first is applied to periodic problems, which are discretized in time using Fourier analysis. A mixed finite element approach is used in the second strategy for discretization in time of non-periodic/transient problems. These strategies lead to a series of uncoupled problems in the space dimension, which is subsequently discretized using either the displacement or the stress model of the hybrid-Trefftz finite element formulation. The main distinction between the two models is in the way that the interelement continuity is enforced. The displacement model enforces the interelement compatibility, while the stress model enforces the interelement equilibrium.

As is typical of Trefftz methods, for both models, the approximation bases are constrained to satisfy locally the homogeneous form of the domain (Navier) equations. The free-field solutions of these equations are derived in cylindrical coordinates and used to construct the domain approximations of the hybrid-Trefftz displacement and stress elements. If the original equations are non-homogeneous, the influence of the source terms is modelled using Trefftz-compliant solutions of the corresponding static problem.

For saturated porous media, the finite element models are based on the Biot's theory. It assumes an elastic solid phase fully permeated by a compressible liquid phase obeying the Darcy's law. For the modelling of unsaturated porous media, the finite elements are formulated using the theory of mixtures with interfaces. The model is thermodynamically consistent and considers the full coupling between the solid, fluid and gas phases, including the effects of relative (seepage) accelerations. Small displacements and linear-elastic material behaviour are assumed for all models.

Keywords

Biphasic medium

Triphasic medium

Hybrid finite elements

Hybrid-Trefftz finite elements

Acknowledgments

This thesis has been completed during the fifth year that I have spent full time as a PhD student at Engineering Faculty, the Catholic University of Portugal and as a member researcher at Trefftz research groups at IST, Technical University of Lisbon.

First and foremost, I wish to thank my supervisors, Professor I.D. Moldovan and J.A.T Freitas, who gave me the great opportunity to come to Lisbon and guided my research. Many thanks to them for the fruitful discussions and for inspiring many of the ideas and results are presented in this thesis. Above all, I thank them for their trust and their guidance during my PhD period in Lisbon. I have also learned from them many great scientific skills which will be helpful for my future career.

I would like to thank other colleagues and friends who gave me very much enjoyable moments both in private and scientific life. It is also an occasion to thank my Vietnamese friends and the Vietnamese community who have encouraged and helped me during my period in Portugal.

I would like to thank my family, especially my mother and father for always believing in me, for their continuous love and their supports in my decisions.

Finally, I want to stress that the thesis would not be completed without the support of Fundação para a Ciência a Tecnologia through research contracts PTDC/ECM/70781/2006 and the Ph.D grant.

Lisbon, Portugal, August 05, 2013

CAO DUC TOAN

Contents

List of Figures

List of Tables

List of Symbols and Notations

General symbols, vector, matrices and tensors

$\boldsymbol{\mathcal{D}}$: Gradient matrix

$\boldsymbol{\mathcal{D}}^*$: Divergence matrix

$\boldsymbol{\nabla}$: Gradient vector

$\boldsymbol{\nabla}^2$: Laplacian operator

$\boldsymbol{\nabla}^T$: Divergence vector

$\hat{\imath}$: Imaginary unit $\sqrt{-1}$

t : Time

Δt : Time increment

ω : Frequency

V: Domain of multi-phasic medium

Γ: Boundary of the medium

Γ_σ: Neumann boundary of the medium

Γ_u: Dirichlet boundary of the medium

$\boldsymbol{d}_0$: Local structural damping matrix

$\boldsymbol{c}_0$: Local material damping matrix

$\boldsymbol{k}_0$: Local elastic stiffness matrix

$\boldsymbol{u}^0$: Initial displacement;

$\boldsymbol{v}^0$: Initial velocity;

$\boldsymbol{a}^0$: Initial acceleration;

N: Number of spectral problems in space;

$\boldsymbol{M}$: Finite element mass matrix;

$\boldsymbol{C}$: Finite element damping matrix;

$\boldsymbol{K}$: Finite element stiffness matrix;

$\boldsymbol{F}$: Loading vector;

$\boldsymbol{N}$: Unit outward normal matrix

$\boldsymbol{k}$: Generalized stiffness matrix

$\boldsymbol{\rho}$: Generalized density matrix

$\boldsymbol{t}_{\Gamma}$: Prescribed Cauchy stresses

$\boldsymbol{u}_{\Gamma}$: Prescribed displacements

$\boldsymbol{\sigma}$: Generalized stress

$\boldsymbol{\varepsilon}$: Generalized strain

$\boldsymbol{u}$: Generalized displacement

$\boldsymbol{t}$: Generalized traction

$\boldsymbol{U}_d$: Trefftz dynamic displacement approximations

$\boldsymbol{U}_s$: Trefftz static displacement approximations

$\boldsymbol{U}_r$: Rigid body modes

$\boldsymbol{S}_d$: Trefftz dynamic stress approximations

$\boldsymbol{S}_s$: Trefftz static stress approximations

Material characteristics

ω_0 : Biot's characteristic frequency

ξ : Dissipation

ζ : Fluid content

g : Gravitational acceleration

ν_k : Kinematic viscosity

k : Hydraulic conductivity

$\mathbb{k}_I$: Intrinsic permeability of the solid matrix

$\mathbb{k}$: Permeability of the solid matrix

a : Tortuosity factor

λ : Lamé's first coefficient of the drained rock

ν : Poisson's coefficient of the drained rock

α : Biot's first coefficient

e : Void ratio

n^W : Liquid volume fraction

Q : Biot's modulus (Biot's second coefficient)

E : Young's modulus of the drained rock

μ : Lamé's second coefficient (shear modulus of the drained rock)

K_d : Bulk modulus of the drained rock

K_S : Bulk modulus of the solid matrix

K_W : Bulk modulus of the fluid

K_N : Bulk modulus of the air

K : Bulk modulus of the mixture

ρ_d : Drained rock density

ρ_S : Solid matrix density

ρ_W : Fluid density

ρ_N : Air density

ρ : Mixture density

μ^S and λ^S : Lamé's coefficients for triphasic problems

$\lambda_{\rho e}^S$, Θ^W and Θ^N : Elastic constants

S_r: Saturation

υ^W : Dynamic viscosity of the water

υ^N : Dynamic viscosity of the air

k_r^W and k_r^N Relative permeability of the water and of the air

Chapter 1
Introduction

1.1 Object and objectives

In the context of solid mechanics, the Rayleigh-Ritz method is the theoretical foundation of the conforming displacement (conventional) finite elements. Their behaviour is thoroughly studied and well understood. Currently, they form the vast majority of the finite elements implemented in general purpose software. Various reasons justified, however, the introduction of alternative finite element approximations, aiming at eliminating some of the limitations of the conventional elements. The first reason is the relative "importance" of the physical quantities modelled by the elements for the engineering practice. Conventional elements produce compatible solutions, which tend to underestimate both displacements and stresses. From an engineering perspective, however, the stress field is typically more relevant, and therefore a method producing equilibrated solutions may be more appealing. The second reason is related to the constraint that stands at the core of the Rayleigh-Ritz method, requiring that the domain approximation functions should satisfy locally the boundary compatibility equations. This condition drastically restricts the choice of the approximation functions and practically eliminates the option of using elements with different shape functions in the same mesh. Finally, for some problems (e.g. fourth-order boundary value problems), higher order of continuity is required for the approximation functions, which is particularly difficult to ensure.

Identifying the Rayleigh-Ritz conformity constraint as the single most important cause of the above limitations, non-conventional elements essentially replace the strong (local) compatibility compliance with a weak one, which is explicitly enforced in the formulation. Distinct approximations must then be used for domain and boundary fields, which caused these approaches to be coined "hybrid" or "multidomain" methods [1]. While the solution is no longer locally compatible, this strategy does succeed in avoiding all the above limitations of the conventional elements.

Adopting the perspective presented in [2], the hybrid formulations include the three classes of elements, namely hybrid-mixed, (pure) hybrid and hybrid-Trefftz elements. In the hybrid-

mixed formulation, no constraints are placed on the domain approximation bases and all field conditions are enforced on average. The strength of this formulation is its ability to accommodate any approximation basis, as, for instance, computer-friendly digital functions, as reported in [3]. The downside of tailoring the approximation functions to the computer is the need to use a high number of degrees of freedom to reach good accuracy, as the functions bear little physical information on the modelled problem. Conversely, the hybrid-Trefftz formulation requires the domain approximation functions to satisfy locally all domain equations. The major feature of the hybrid-Trefftz elements is the richness of information contained in the approximation basis. This trait allows these elements to yield highly accurate solutions with a relatively small number of degrees of freedom and considerably enhances their robustness to issues hindering the behaviour of conventional elements. Moreover, all coefficients of the solving system are defined by boundary integrals, thus eliminating the geometrical constraints the conventional elements must typically observe. The price paid, however, is the lack of flexibility in choosing the approximation functions, which may be numerically heavy to implement and not allow analytic integration. As the domain approximation functions only satisfy the homogeneous form of the domain equations, they are unable to account for eventual non-homogeneous terms induced, for instance, by the presence of body forces, temperature gradients, non-linear terms and initial conditions. Particular solution functions must then be added to the domain basis to restore its key properties, but they may not be easy to obtain analytically. Finally, hybrid elements are a compromise between hybrid-mixed and hybrid-Trefftz elements. The domain approximation functions of hybrid elements are constrained to satisfy locally either the equilibrium or the compatibility conditions. In all three formulations, the boundary approximation basis is unrestricted and inter-element continuity conditions are enforced in weak form.

The objective of this work is to report on the formulation, implementation and validation of hybrid-Trefftz finite elements for modelling the response of saturated and unsaturated porous media with linear-elastic behaviour under static and dynamic (harmonic and transient) excitations.

The mechanical response of such materials is highly relevant in Soil Mechanics, but fields like Materials Science, Ecology and Biomechanics also deal frequently with saturated and unsaturated media (e.g. noise barriers, pollutant transport, cartilage and bone mechanics). A

considerable breadth of mathematical models is available for multi-phase materials. They range from single-phase continuous models with modified mechanical characteristics to account for the presence of various phases to fully coupled multi-phase models, taking into account the micro- and macro-scale interaction of the constituents.

Single-phase models are typically sufficient for modelling the short-term dynamic behaviour of low-permeability porous media (e.g. clays), where the relative motion of the fluid phases in respect to the solid phase is limited and thus marginally influences the response of the mixture (frozen medium behaviour). A single compressional wave (with large wavelength) and a shear wave propagate through single-phase materials, as the fluid seepage is too limited to accommodate the propagation of compressional waves through fluid motion. Under such conditions, conventional elements are generally sufficient for a sound representation of the material response, except for the case where the medium is nearly incompressible.

Conversely, the fluid seepage plays an essential role in the dynamic response of semi-pervious and pervious materials. Less constrained relative motion accounts for the presence of secondary, short wavelength, compressional waves, propagating through fluid phases. Because of their reduced wavelength, secondary compressional waves are very difficult (and indeed at times practically impossible) to model using conventional elements, as the well-known restriction of using at least six finite elements per wavelength excessively limits their leading dimension.

The practical importance of such situations motivates the investment in the formulation, implementation and validation of hybrid-Trefftz finite elements and justifies the focus of this work on the response of semi-pervious and pervious porous media. Indeed, the research reported here shows that hybrid-Trefftz finite elements are essentially wavelength-independent, mainly due to the physical significance of their approximation functions, which satisfy locally all domain equations. For the same reason, infinite domains, incompressible media, awkward topologies and gross mesh distortions are also efficiently modelled by these elements.

The formulation of the hybrid-Trefftz elements is based on their perception as a particular case of hybrid elements where the domain basis collects functions that satisfy locally the homogeneous Navier (or Beltrami) equation governing the problem. If the problem is non-homogeneous, other approximation functions must be added to the basis to account for the

source terms. As in the case of all hybrid elements, hybrid-Trefftz elements are encoded into two dual models, namely the displacement model and the stress model, depending on whether the inter-element continuity is enforced in terms of boundary displacement or the boundary traction. The hybrid-Trefftz displacement (stress) model approximates the solid displacement and fluid seepage (stress and pore pressure) fields in the domain of the element, using bases that satisfy locally the domain compatibility (equilibrium) equation. The equilibrium (compatibility) equations are enforced on average using the functions in the displacement (stress) approximation basis as weighting functions. Independently of the basis adopted in the domain, the boundary tractions (displacements) are also approximated on the Dirichlet (Neumann) boundary of the element and used to enforce in a weak form the displacement (traction) continuity, thus generating weak kinematically (statically) admissible solutions, while the boundary traction (displacement) continuity is enforced explicitly. The option of building hierarchically both domain and boundary bases endorses the use of solvers with p-adaptive refinement capabilities, as the coefficients of the finite element systems corresponding to previous (weaker) levels of refinement must not be calculated anew. The option of not condensing the finite element systems on the boundary variables generates highly sparse and strongly localized coefficient matrices, supporting the use of parallel-processing routines for the construction of the system.

After presenting their formulations, the displacement and stress models of the hybrid-Trefftz finite elements are thoroughly tested in order to assess their performance in terms of accuracy, convergence and robustness. A considerable number of tests is performed on problems with known analytic solution, in order to evaluate the ability of the models to accurately recover the exact solution under different loading conditions. The tests focus the stability of the finite element solution under wide wavelength variations, near-incompressibility conditions and gross mesh distortion, as such situations commonly occur in geo and biomechanical applications involving porous materials. More complex problems are solved to assess the quality of the solutions in terms of continuity, smoothness and enforcement of the boundary conditions. The results are validated using results for similar testing setups, performed using the finite element package ABAQUS™ [4].

1.2 State-of-the-art

The work reported here is rooted in previous research efforts developed in two main directions: the development of hybrid-Trefftz finite elements (including their supporting mathematical theory), and the derivation of mathematical models to characterize the static and dynamic behaviours of biphasic and triphasic media. Some of the most relevant contributions to these topics are synthesized next.

1.2.1 Hybrid –Trefftz finite element formulation

The roots of the Trefftz method for solving boundary-value problems can be traced back to 1926, when Erich Trefftz challenged the Ritz method suggesting the use of trial functions taken from the free-field solution of the governing differential equation and weighting them in a way that approximately satisfies the boundary conditions [5]. Originality and relevance of his contribution were questioned at the time, as it recovered a popular method to solve one-dimensional boundary-value problems.

Present recognition is very much due to the work of J. Jirousek on the use of the concept in finite element modelling [6], to the contribution of I. Herrera on selection of basis functions [7], and to the popularity of the boundary element method.

The seminal work of J. Jirousek enjoyed significant popularity and inspired various other contributions throughout the 1980s, both from his co-workers [8-10] and other authors e.g. [11, 12]. The contributions of I. Herrera were instrumental for providing a sound mathematical basis to the method, including the formulation of a completeness criterion (TH-completeness), convergence conditions and variational principles [7, 13, 14]. In 1993, this theory was extended to non-symmetric differential operators [15], endorsing the use of discontinuous Trefftz functions

During the 1990s, two distinct approaches to the Trefftz method were suggested by Y.K Cheung and J.A.T. Freitas. The former author adopted the classical boundary element method strategy to solve the boundary integral equation obtained through the weak enforcement of the governing equations, using Trefftz functions for weighting, e.g. [16, 17]. Conversely, the second approach is rooted in the finite element theory. Hybrid-Trefftz elements are regarded as a

particular case of hybrid elements, where the domain approximation functions satisfy *a priori* all the domain equations [2]. This perspective is used in this work.

The major strength of the hybrid-Trefftz formulation is that the trial functions embody the physical features of the modelled phenomenon. A direct consequence of this trait is that all coefficients present in the solving system are reduced to boundary integral expressions, thus eliminating the restrictions posed on the topology of the conventional elements. This property, typical of the boundary element method, strengthens the finite element method at no additional cost, as the bases remain regular and the solving system sparse and Hermitian. Moreover, the physical meaningfulness of the trial functions enhances the convergence and stability of the hybrid-Trefftz elements as compared to the conventional elements.

The favourable traits of the hybrid-Trefftz finite elements motivated, mainly in the last three decades, a steady increase of their range of application.

The first application of the Trefftz concept to potential problems dates back to 1964 [18], followed, more than 20 years later, by the systematic work of Zielinski and Zienkiewicz [11], already including Herrera's HT-completeness criterion for constructing the approximation bases. More recent applications of Trefftz elements to potential problems are due to Shaw [19], Leitão [20] and, in the context of heat conduction, Balakrishnan [21], Jirousek [22] and Qin [23].

A significant number of applications of the hybrid-Trefftz elements were reported for linear elasticity problems defined on homogeneous and isotropic media. One of the earliest applications to plane elasticity is due to Jirousek [6], in the context of the so called (at the time) Large Element Method. As the name indicates, the method presented excellent stability and convergence properties, and was therefore affordable to use supersized finite elements. A considerable research effort was dedicated by J.A.T. Freitas and his co-workers to the solution of elastostatic problems using hybrid-Trefftz elements. The formulation of the hybrid-Trefftz displacement model for elastostatics was reported in [24], while the theoretical frame for deriving the stress model in [25]. A comparative study of the alternative models, including their (complementary) formulation, implementation and numerical performance is presented in [26]. The displacement and stress models, which are conceptually similar to the so called 'traction frame' and 'displacement frame' Trefftz elements of J. Jirousek, were found to perform well numerically and offer similar convergence and robustness properties. Application of the same

elements to shape optimization and crack analysis problems were subsequently reported in [27]. Trefftz elements for plane poroelasticity problems were also reported by Jin [28]. Extensions of the hybrid-Trefftz formulations for plane elastostatics to three dimensions were reported by Freitas [29] and Piltner [30-32].

The application of hybrid-Trefftz elements to elastodynamic problems is dependent on the choice of a time integration method that preserves the hyperbolicity of the original problem in time, namely by transforming it into a series of elliptic problems involving space variables only. Because of this restriction, the integration in time has been typically performed using the Discrete Fourier Transform. Applications along these lines have been reported by Cismasiu and Freitas, in [33, 34]. A detailed study of the development and implementation of hybrid-Trefftz elements for plane elastodynamics can be found in [35]. The applications of the Trefftz concept to the elastodynamic response of fluids are still quite limited [36, 37]. Also limited are the reports on the development of hybrid-Trefftz elements for the modelling of piezoelectric materials [38, 39].

In the field of structural mechanics, a wide breadth of hybrid-Trefftz elements was reported for the modelling of plates. For Kirchhoff plates, the first authors to report such elements, in the late 1980s, were Jirousek and his co-authors [10, 40, 41]. Throughout the 1990s, they gradually extended their formulations to thick plates [42, 43]. Parallel contributions to the analysis of thick plates were reported by Piltner [32, 44, 45]. Still in the 1990s, hybrid-Trefftz elements for the buckling and post-buckling analysis of thin plates [46] and for thin [47] and thick [48] plates on elastic foundations were reported by Q.H. Qin.

In the last five years, a series of articles reported on the extension of the hybrid-Trefftz formulations to elastostatic and elastodynamic problems defined on multi-phase porous media. The Trefftz elements for biphasic elastostatics reported in [49] follow the perspective of regarding hybrid-Trefftz models as special cases of the corresponding hybrid models, with the essential difference that the domain trial functions are free-field solutions of the homogeneous form of the governing equation. Hybrid-Trefftz elements for the elastodynamic analysis of Biot theory-compliant saturated soils were reported by Freitas and Moldovan in [50-53]. The first cited article reports on the solution of harmonic (spectral) problems. The other three articles address mainly non-periodic and transient problems. A novel time integration technique, first

reported in [54], was used instead of the conventional Discrete Fourier Transform for the time integration of the governing equations. It has the merit of generating time-discretized problems defined by spectral-like equations (the generalized frequency results complex), independently on the functions that are used in the time basis, thus endorsing the use of the same finite element formulation in space for harmonic, periodic and transient problems. The energy statements associated with the formulations were recovered and sufficient conditions for the uniqueness of the finite element solutions were stated.

The extension of the hybrid-Trefftz displacement and stress models to unsaturated media with elastic behaviour was reported in [55] and [56], respectively. Both papers focus on higher-permeability (semi-pervious and pervious) soils, due to the difficulties they pose to conventional elements. It is shown that the compressional waves travelling through the fluid phases are very difficult to model using conventional elements, due to their limiting-low wavelengths, especially for higher frequency excitations. Conversely, hybrid-Trefftz elements are virtually frequency-independent and thus capable of correctly recover all travelling waves.

The extension of the Trefftz concept to non-linear problems must be approached with caution. Indeed, its straightforward application would require the recomputation of the trial basis at every iteration, which is unfeasible for most applications. It is, however, possible to use hybrid elements built up with Trefftz-compliant trial functions. The formulation does not reduce, in general, to boundary integrals only, but the advantage of having physically meaningful trial functions is, nevertheless, preserved. Some examples of non-linear problems addressed using hybrid(-Trefftz) elements are reported in [12, 22, 57, 58], for heat transfer, plane and tri-dimensional elastoplasticity, respectively.

Unlike boundary elements, hybrid-Trefftz elements typically use the regular (rather than fundamental) solutions of the governing equations to construct the trial basis in the domain of the element. However, the Trefftz basis can be enriched with fundamental and other singular stress solutions to enhance its ability to handle local effects without mesh refinement. Indeed, stress concentrations around crack tips, holes or concentrated loads can be dealt with by enriching the approximation basis with optional functions that accurately represent the local solution in the vicinity of the singularity. Research on this topic is actually older than the formal establishment of the Trefftz finite element method itself, and pioneered by Tong [59] and Lin [60]. In their

work, 'super elements' were used only in the vicinity of the stress concentration, the rest of the domain being covered by conventional elements. Local effects due to discontinuous and localized loads were modelled using hybrid-Trefftz elements by Venkatesh [61-63], while stress concentrations at crack tips and corners were analysed by Jirousek [9].

From the computational implementation perspective, efficient error estimators for hybrid-Trefftz elements were proposed by Jirousek [8]. Also, special attention was paid to p-adaptivity, exploiting the hierarchical nature of the approximation bases [64] and to parallel processing, which is particularly effective when the finite element is implemented in explicit (un-condensed) form [65].

Reviews on the hybrid-Trefftz element formulations and their application can be found in [66-69].

1.2.2 Applications to biphasic problems

A biphasic medium consists of a solid phase (the solid skeleton) fully permeated by a compressible liquid phase, generally obeying Darcy's law. The early research on porous media was due to the work of P. Fillunger and published a century ago [70]. Ten years later, in 1923, Terzaghi [71] developed a more intuitive theory for the mechanical behaviour of porous media, proposing a new way to model the interaction between the solid skeleton and the pore fluid. However, only the one-dimensional case was covered. These two contributions form the basis of all porous media theories used today.

The work of P. Fillunger led to the Theory of Porous Media. It is based on the concept of immiscible superimposed continua and on the theory of mixtures [72, 73] and was later extended using the concept of volume fractions [74-77].

In 1941, M.A. Biot published the first of a series of articles extending Terzaghi's theory to account for the interaction between the solid skeleton and the viscous fluid [78] in the three-dimensional case. Initially covering only the isotropic elastostatic case, the theory was later extended to anisotropic media [79] and elastodynamics [80, 81]. The elastodynamic theory proved mathematically the existence of a secondary compressional wave propagating through the fluid phase. Quite elusive in laboratory measurements, this wave was confirmed experimentally

by Plona [82], more than two decades later. The Rayleigh waves predicted by the Biot's theory were determined, on a half-space medium, by Jones [83] and Deresiewicz [84].

The similarity between the two alternative theories was proven by Bowen [74], who found that the Biot's theory is a special case of the Theory of Porous Media, with constant volume fractions. Two decades later, Schanz and Diebels [85] demonstrated that the wave forms are the same in the two theories. Moreover, they have proved numerically the perfect equivalence between the theories in the case of incompressible constituents. If the phases are compressible, however, the results are significantly different.

Significant research effort has been dedicated in the last 30 years to the formulation and numerical solution of problems defined by the Biot's theory. Some initial studies (e.g. Bowen, 1982) used the displacements in the solid matrix, the fluid seepage and the pore pressure as primary unknowns ($u-w-p$ formulation). Irreducible forms with only two primary unknowns were later obtained by Simon et al. [86] by either eliminating the seepage from the governing equations ($u-p$ formulation), or the pore pressure ($u-w$ formulation). From the $u-w$ formulation, a solid displacement-fluid displacement ($u-U$) formulation can be derived. Using the $u-w$ approach, Kim et al. [87] derived an analytical closed-form solution for the propagation velocities of both compressional waves for a one-dimensional saturated porous medium subjected to harmonic excitations, thus allowing for the computation of the damping coefficients of various geologic materials. Still employing the $u-w$ formulation, Halpern and Christiano [88] assessed the response of axisymmetric porous media subjected to harmonic point loads. For plane strain problems, Degrande [61] used spectral finite elements to evaluate the influence of the hydraulic conductivity and the excitation frequency on the response of biphasic media. For infinite media, Akiyoshi et al. [89] derived a set of absorbing boundary conditions, valid for both $u-w$ and $u-p$ formulations, and used it to solve plane-strain problems involving transient loads. An infinite element was later derived by Khalili et al. [90] and applied to the modelling of wave propagation through a saturated porous medium semi-infinite column.

Finite element models based on Biot's formulation are also discussed in the review of Zienkiewicz and Shiomi [91].

1.2.3 Applications to triphasic problems

The analysis of elastic wave propagation through triphasic media is an important issue in fields like Geomechanics (e.g. unsaturated soils), Biomechanics (e.g. the bone tissue) and Ecology (e.g. pollutant transport). Triphasic media are assemblages of solid particles that form a porous solid skeleton, with the pores filled with two immiscible fluids, namely a liquid (typically water) and a gas (or non-wetting fluid, typically air). The dynamic response of triphasic media may be significantly influenced by the microscopic interaction at the interfaces between the solid, liquid and gas phases. In such cases, traditional theories, treating the medium as a single-phase material, are insufficiently accurate, and models that rigorously take into account the effects of these inter-actions must be adopted.

As shown in the previous section, the Biot's theory [80] is frequently used as a mathematical model for the wave propagation in biphasic (saturated) media. Biot's theory is relatively simple, well understood and thoroughly confirmed by experiments. Due to these merits, various attempts were made to reduce the triphasic problem to a biphasic problem, under certain sets of conditions. For nearly saturated media, an equivalent biphasic model was proposed, with the compressibility of the fluid phase increased to account for the presence of air bubbles by Smeulders [92]. A heuristic relation between the equivalent compressibility of the liquid and the saturation was established. An equivalent biphasic theory valid for a wider saturation range was derived by Berryman [93], and by extending a model initially suggested by Brutsaert [94]. The theory assumes that pore pressure variations are equal in both fluids, so that the capillary pressure may be considered constant.

Biot's theory, however, does not rigorously take into account the microscopic interactions between the various phases of the unsaturated medium, which may play an important role in its macroscopic behaviour. To overcome this limitation, two classes of approaches were suggested, namely the theory of mixtures and the averaging theory. The theory of mixtures applies the classical equations of continuum mechanics at the macroscopic level and uses the concept of volume fractions to account for the motion of individual phases. Volume fractions are treated as internal variables and additional equations (closure equations) are formulated to account for their variation in [95]. The models based on the theory of mixtures were improved to include the effects of the drag and capillary forces on the interfaces between the various phases in [96] and

[97]. The alternative averaging theory applies the classical equations of continuum mechanics at the microscopic level and uses averaging operators to model the macroscopic behaviour. This approach is rooted in the work of Hassanizadeh and Gray [98-100]. Averaged quantities include the densities of the three phases, the stress tensor and the seepage velocities of the fluid phases [101]. Under dynamic loading, all triphasic models predict the existence of three compressional waves and a single shear wave.

Comprehensive reviews of the literature available on the mathematical models for unsaturated soils are due to de Boer [102, 103] and Sheng [104, 105] .

Approximate solutions of problems defined by the mathematical models presented above are typically found using the finite element method and indeed many finite elements have been reported in the recent years for the analysis of unsaturated media. However, the physical complexity of the dynamic response of such media leads to modeling difficulties, which are typically avoided by adopting various simplifying assumptions. Some of the most widely used simplifying hypotheses involve assuming that the solid skeleton is totally rigid [106] (only models adequately free flow problems), neglecting the motion of the gas phase [107] (is only capable of recovering two compressional waves) or neglecting the velocities and accelerations of all phases [101] (fails to model the propagation of waves). Arguably the most common simplifying assumption present in finite element models involves neglecting the seepage acceleration [108]. This option endorses the use of fluid pressures, rather than fluid displacements, as primary variables, leading to the so-called $u^S - p^W - p^N$ formulation. The finite element models based on this approach yield correct solutions for low permeability media, where the compressional waves travelling through the fluid phases are highly attenuated, but may significantly diverge from the correct solution in the case of pervious materials.

1.3 Overview

This work is organized in five chapters, following a general-to-specific logic.

Following this introductory chapter, the general description of elastostatic and elastodynamic problems defined on multi-phase porous media is presented in Chapter 2. The basic hypotheses of the mathematical model and the differential equations governing the response of a multi-phase medium subjected to static or dynamic excitations are recalled. The definition of the problem is

complemented with the static and kinematic boundary conditions and with the definition of the initial conditions. The solution techniques used to solve these problems are presented. To perform the time integration of time-dependent problems, two methods are used, namely the Discrete Fourier Transform (used for periodic problems) and a Galerkin weighted residual approach (used for non-periodic and transient problems). For the integration in space of static and time-discretized problems, hybrid-Trefftz finite elements are formulated. As mentioned above, they are encoded in two dual models, labelled displacement and stress models. For both models, however, the domain basis is constructed using functions that satisfy locally the homogeneous form of the governing equation. If the problem is non-homogeneous, a particular solution must be added to the Trefftz basis to account for the presence of the source terms. A general method for the construction of approximate particular solutions when no analytic particular solution is available is also presented in Chapter 2.

Chapter 3 reports on the application of the general framework given in Chapter 2 to the modelling of static and dynamic problems defined on biphasic (saturated) media. This study is extended in Chapter 4 to triphasic (unsaturated) media. The free-field general solutions of the governing equations are obtained and their main physical properties thoroughly discussed for each application. Special attention is given to the implementation of the hybrid-Trefftz elements. The kinematic and static indeterminacies of the displacement and stress models are discussed and a post-processing procedure to obtain the rigid-body displacements (which cannot be recovered by the stress model since they do not induce stresses to the medium) is presented. One of the central objectives of this work is the assessment of the convergence and robustness properties of the hybrid-Trefftz elements when dealing with problems that hinder the behaviour of conventional finite elements. For all elements, the convergence under p- and h-refinement is assessed and quantified using average convergence rates. The sensitivity of the elements to gross mesh distortions, near-incompressibility of the constituents and the wavelength of the propagating wave is evaluated. Finally, the results obtained using hybrid-Trefftz elements on rather complex physical problems are validated against the solutions predicted by the commercial finite element software ABAQUS^{TM}.

Chapter 5 presents the general conclusions of this work and identifies valid research lines to be pursued in the future.

Chapter 2

Hybrid-Trefftz elements for elastostatic and elastodynamic problems

The main objective of this chapter is to present the general description of the physical problems addressed in this work and their numerical solution using hybrid-Trefftz finite elements. The presentation is kept as general as possible, in order to set a coherent framework for all subsequent developments

The general description of static and dynamic problems defined on biphasic and triphasic media is given in Section 2.1. The governing equations are presented and the involved quantities defined. The boundary and, in the case of dynamic problems, the initial conditions complete the definition of the problem.

The remaining sections of this chapter introduce the solution method for the problems defined in Section 2.1. The approach used here follows the methodology previously reported by Freitas and his co-workers [50, 55, 56, 109-111]. It consists in regarding the hybrid-Trefftz finite element as a particular case of the hybrid finite elements, where the domain approximation basis is restricted to functions that satisfy locally the homogeneous differential equation governing the problem. These functions are typically derived by constructing either Navier or Beltrami equations and by subsequently solving them using the displacement and stress potential functions, respectively.

The Navier approach is used in this work. The hybrid-Trefftz solution of static problems is presented in Section 2.2. The alternative hybrid-Trefftz displacement and stress models are built on the approximations of the displacement and stress fields, respectively, in the domain of the elements, and of the traction and displacement fields, respectively, on the essential boundary of the elements. In the case of the displacement element, the domain approximation is complemented by stress-free displacement modes, which recover the rigid body displacement of the solid phase and the free flow of the fluid phase. Such displacements can only be recovered in the post-processing phase when the stress model is used.

The solution strategy adopted for dynamic problems defined on multi-phase media is presented in Sections 2.3 and 2.4. The time integration of the governing equations is performed first (Section 2.3), using the well-known Discrete Fourier Transform for periodic problems and the weighted-residual approach presented in [54] for non-periodic and transient problems. The hyperbolic problem in time is reduced to a series of elliptic problems in space, which are subsequently solved using hybrid-Trefftz finite elements (Section 2.4). For non-periodic problems, the time-discretized equations are non-homogeneous, due to the presence of initial condition dependent terms. In this case, the Trefftz- basis fails to recover the influence of the non-homogeneous terms and particular solution functions must be added to the basis to account for their effect.

A method for generating approximate particular solutions for the non-homogeneous problems obtained after the time discretization of transient problems is presented in Section 2.5. The method constructs the particular solution using functions that satisfy locally the homogeneous form of the corresponding static problem (i.e. the problem obtained after discarding both non-homogeneous and time derivative terms from the governing equation). The approach can be used with both displacement and stress models, generating solutions that satisfy locally the domain compatibility and equilibrium equations, respectively. The general and the particular solution functions are treated as two parts of the same basis and combined to satisfy weakly domain equilibrium (displacement model) or compatibility (stress model) and the essential boundary conditions.

2.1 Definition of elastostatic and elastodynamic problems

A geometrically and physically linear formulation of elastostatic and elastodynamic problems is presented here. The equations defined below are general in the sense that they are valid (with distinct definitions of the terms involved) for single-phase, biphasic and triphasic media, under both static and dynamic loading conditions. Periodic, non-periodic and transient excitations are also accommodated by the model.

2.1.1 Domain and boundaries

Consider the medium V represented in Figure 2.1, consisting, in the most general case, of a matrix of solid particles in contact with each other (the solid skeleton), with the pores filled with

a wetting fluid (e.g. water) and a non-wetting fluid (e.g. air). If the non-wetting fluid is absent, the medium is saturated (biphasic). The problem description given next is adaptable to solid (single-phase) media removing the equations and variables related to the fluid phase. For such situation, hybrid-Trefftz elements are reported in [49].

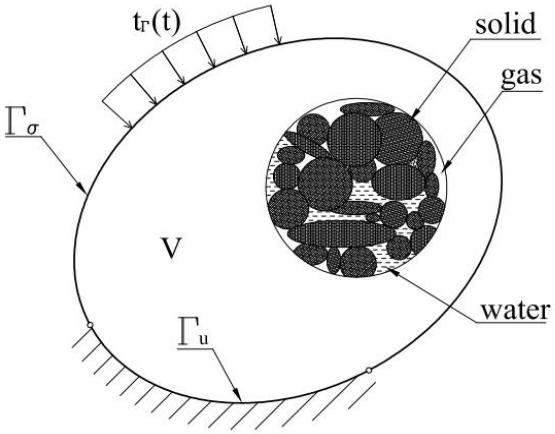

Figure 2.1: Domain, Neumann, and Dirichlet boundaries

The boundary Γ of the medium is formed by the complementary Dirichlet (Γ_u) and Neumann (Γ_σ) parts ($\Gamma = \Gamma_\delta \cup \Gamma_u$ and $\phi = \Gamma_\delta \cap \Gamma_u$), where the displacements of each phase, the tractions in the solid phase and the pore pressures in the fluid phases are prescribed.

2.1.2 Governing equations

Assuming an infinitesimal cut of the domain V, the domain equilibrium and compatibility equations are written as,

$$\boldsymbol{\mathcal{D}}\boldsymbol{\sigma}(x,y,t) + \boldsymbol{b}(x,y,t) = \boldsymbol{r}(x,y,t) \quad \text{in } V \tag{2.1}$$

$$\boldsymbol{\varepsilon}(x,y,t) = \boldsymbol{\mathcal{D}}^{*}\boldsymbol{u}(x,y,t) \quad \text{in } V \tag{2.2}$$

The divergence and gradient operators $\boldsymbol{\mathcal{D}}$ and $\boldsymbol{\mathcal{D}}^{*}$ are adjoint in geometrically linear problems. The independent components of the total stress and pore pressure fields, and of the strain and fluid content fields are collected in vectors $\boldsymbol{\sigma}(x,y,t)$ and $\boldsymbol{\varepsilon}(x,y,t)$. Vector $\boldsymbol{u}(x,y,t)$ collects the displacements in all phases and $\boldsymbol{b}(x,y,t)$ is the body force vector. Symbol $\boldsymbol{r}(x,y,t)$ denotes a generic right hand side term. It is null in elastostatic problems and combines velocity and acceleration effects in elastodynamic problems. As its explicit expression depends on the

specific problem to be solved, its definition is presented for each situation in the respective section.

The constitutive relations are written in the alternative stiffness and flexibility forms,

$$\boldsymbol{\sigma}(x,y,t) = \boldsymbol{k}\boldsymbol{\varepsilon}(x,y,t) \quad \text{in } V \tag{2.3}$$

$$\boldsymbol{\varepsilon}(x,y,t) = \boldsymbol{f}\boldsymbol{\sigma}(x,y,t) \quad \text{in } V \tag{2.4}$$

where matrices $\boldsymbol{k}$ and $\boldsymbol{f}$ define the material properties.

In the Neumann boundary conditions,

$$\boldsymbol{N}\boldsymbol{\sigma}(x,y,t) = \boldsymbol{t}_{\Gamma}(x,y,t) \quad \text{on } \Gamma_{\sigma} \tag{2.5}$$

vector $\boldsymbol{t}_{\Gamma}$ collects the applied tractions and pore pressures and the components of the unit outward normal to the boundary are organized in matrix $\boldsymbol{N}$.

On the Dirichlet boundary, the domain displacements $\boldsymbol{u}$ must be compatible with the imposed displacements collected in vector $\boldsymbol{u}_{\Gamma}$:

$$\boldsymbol{u}(x,y,t) = \boldsymbol{u}_{\Gamma}(x,y,t) \quad \text{on } \Gamma_{u} \tag{2.6}$$

The initial displacements and velocities of the dynamic system are known a priori and their components collected in vectors $\boldsymbol{u}^0(x,y)$ and $\boldsymbol{v}^0(x,y)$, respectively:

$$\boldsymbol{u}(x,y,0) = \boldsymbol{u}^0(x,y) \tag{2.7}$$

$$\boldsymbol{v}(x,y,0) = \boldsymbol{v}^0(x,y) \tag{2.8}$$

The references in equations (2.1) to (2.5) are detailed in the appendices.

2.1.3 Interior boundary conditions

Assume that the domain V represented in Figure 2.1 is discretized into finite elements and let the domain of a generic element be denoted by V^e and its boundary by Γ^e. Boundary Γ^e is formed, in general, by the complementary Neumann (Γ_{σ}^e) and Dirichlet (Γ_{u}^e) parts, where equations (2.5) and (2.6) are prescribed, respectively, and the interior (Γ_{i}^e) part, where the boundary equilibrium and compatibility conditions (2.9) and (2.10) must be satisfied,

$$\boldsymbol{t}^i(x,y,t) + \boldsymbol{t}^k(x,y,t) = \boldsymbol{0} \quad \text{on } \Gamma_{i}^e \tag{2.9}$$

$$\boldsymbol{u}^i(x,y,t) = \boldsymbol{u}^k(x,y,t) \quad \text{on } \Gamma_{i}^e \tag{2.10}$$

where i and k denote the two finite elements that share the interior boundary Γ_i^e (Figure 2.2).

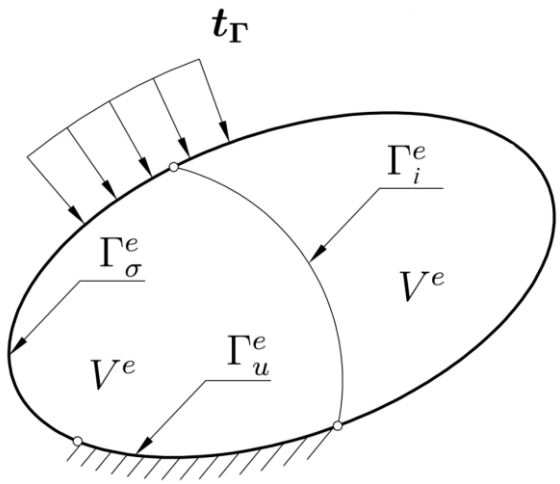

Figure 2.2: Finite elements, Neumann, and Dirichlet boundaries

In what regards geometry and shape, hybrid-Trefftz elements bear no restrictions on the number of edges and nodes because the domain approximations are strictly hierarchical. Also, due to their high robustness to gross mesh distortion [112], they are not bounded by the regularity restrictions typical of conventional elements.

2.2 Hybrid-Trefftz elements for elastostatic problems

The elastostatic problem is obtained by setting to zero the right hand side term of equation (2.1), to yield,

$$\boldsymbol{\mathcal{D}\sigma} + \boldsymbol{b} = \boldsymbol{0} \quad \text{in } V \tag{2.11}$$

Domain equations (2.2) and (2.3) and boundary equations (2.5) and (2.6) are valid for elastostatic problems, but the respective fields are time-independent.

The formulations of the displacement and stress models of hybrid-Trefftz finite elements are presented next. The displacement model is constructed on the direct approximation of the domain displacement fields in all phases, using functions that satisfy locally the Navier equation,

$$\boldsymbol{\mathcal{D}k\mathcal{D}^*u} + \boldsymbol{b} = \boldsymbol{0} \quad \text{in } V \tag{2.12}$$

obtained by merging the domain equations (2.2), (2.3) and (2.12). Consequently, the solutions of the hybrid-Trefftz displacement model locally satisfy the equilibrium, compatibility and elasticity conditions in the domain of the element.

The same applies to the stress model, the difference being that it is the stress field that is directly approximated, as shown below.

Beside the domain approximations, independent approximations of the traction/pore pressure and displacement fields are constructed on the essential boundaries of the displacement and stress elements, respectively. Unlike domain bases, boundary bases are not constrained to satisfy other conditions, except for completeness and linear independence.

2.2.1 Hybrid-Trefftz displacement element

❖ **Approximation bases**

The homogeneous form of the Navier equation (2.12) admits two types of free-field solutions: strain-generating solutions and rigid-body modes. Let subsets of these classes of solutions be collected in bases $\boldsymbol{U}_s$ and $\boldsymbol{U}_r$, respectively. The bases are constructed hierarchically, may contain arbitrary numbers of functions, and are used to approximate the displacement field in the domain of the element as:

$$\boldsymbol{u} = \boldsymbol{U}_s\boldsymbol{X}_s + \boldsymbol{U}_r\boldsymbol{X}_r + \boldsymbol{u}_0 \quad \text{in } V^e \tag{2.13}$$

In equation (2.13), vectors $\boldsymbol{X}_s$ and $\boldsymbol{X}_r$ collect the generalized displacements corresponding to the functions listed in the displacement bases $\boldsymbol{U}_s$ and $\boldsymbol{U}_r$, while vector $\boldsymbol{u}_0$ contains particular solution terms satisfying the non-homogeneous form of equation (2.12). Their main purpose is to model the effect of the body force $\boldsymbol{b}$. If local effects (e.g. stress concentrations) are expected, however, vector $\boldsymbol{u}_0$ may include as well enrichment functions to enhance the ability of the element to model singular fields, as reported in [112].

The approximation of the strain/fluid content fields in the domain of the element is now obtained from definition (2.13) by locally enforcing the domain compatibility equation (2.2),

$$\boldsymbol{\varepsilon} = \boldsymbol{E}_s\boldsymbol{X}_s + \boldsymbol{\varepsilon}_0 \quad \text{in } V^e \tag{2.14}$$

The rigid body modes, causing no strain, do not contribute to approximation (2.14).

The stress/pore pressure approximation (2.15) is obtained from definition (2.14) by enforcing locally the elasticity equation (2.3),

$$\boldsymbol{\sigma} = \boldsymbol{S}_s\boldsymbol{X}_s + \boldsymbol{\sigma}_0 \quad \text{in } V^e \tag{2.15}$$

The approximation functions present in equations (2.13), (2.14) and (2.15) must satisfy the Trefftz constraints listed in Table 1.

Equilibrium equations	Compatibility equations	Elasticity equations
$\mathcal{D}\boldsymbol{S}_s = \boldsymbol{0}$	$\boldsymbol{E}_s = \mathcal{D}^* \boldsymbol{U}_s$	$\boldsymbol{S}_s = \boldsymbol{k}\boldsymbol{E}_s$
	$\boldsymbol{0} = \mathcal{D}^* \boldsymbol{U}_r$	
$\mathcal{D}\boldsymbol{\sigma}_0 + \boldsymbol{b} = \boldsymbol{0}$	$\boldsymbol{\varepsilon}_0 = \mathcal{D}^* \boldsymbol{u}_0$	$\boldsymbol{\sigma}_0 = \boldsymbol{k}\boldsymbol{\varepsilon}_0$

Table 1: Trefftz constraints for static problems

The traction (Cauchy stress) field is independently approximated on the Dirichlet and interior boundaries of the element (extended Dirichlet boundary, $\overline{\Gamma}_u^e = \Gamma_u^e \cup \Gamma_i^e$) as:

$$\boldsymbol{t} = \boldsymbol{Z}\boldsymbol{P} \quad \text{on } \overline{\Gamma}_u^e \tag{2.16}$$

The boundary traction approximation basis $\boldsymbol{Z}$ is constructed hierarchically. It must observe no other constraints apart from linear independence and completeness.

❖ **Domain statement**

The domain equation of the hybrid-Trefftz displacement element is derived enforcing on average the equilibrium equation (2.11), using the approximation functions collected in basis (2.13), for weighting,

$$\int \boldsymbol{U}_j^* (\mathcal{D}\boldsymbol{\sigma} + \boldsymbol{b}) dV^e = \boldsymbol{0} \tag{2.17}$$

where $\boldsymbol{U}_j^*$ denotes the transpose conjugate of matrix $\boldsymbol{U}_j$ and $j = \{ s,\ r\}$.

Integrating by parts the first term in the left hand side of equation (2.17) and explicitly enforcing the natural boundary condition (2.5) on the Neumann boundary of the element yields:

$$\int \boldsymbol{U}_j^* (\mathcal{D}\boldsymbol{\sigma} + \boldsymbol{b})\, dV^e = \int \boldsymbol{U}_j^* \boldsymbol{t}_\Gamma d\Gamma_\sigma^e + \int \boldsymbol{U}_j^* \boldsymbol{Z} d\overline{\Gamma}_u^e \boldsymbol{P} - \int \left(\mathcal{D}^* \boldsymbol{U}_j\right)^* \boldsymbol{\sigma}\, dV^e + \int \boldsymbol{U}_j^* \boldsymbol{b}\, dV^e \tag{2.18}$$

Enforcing approximations (2.13) and (2.15) into equations (2.18), and using properties given in Table 1 yields the following equations:

$$\boldsymbol{K}_{ss}\boldsymbol{X}_s - \boldsymbol{B}_s\boldsymbol{P} = \boldsymbol{t}_{\Gamma_s}^u - \boldsymbol{t}_{0_s}^u \tag{2.19}$$

$$-\boldsymbol{B}_r\boldsymbol{P} = \boldsymbol{t}_{\Gamma_r}^u - \boldsymbol{t}_{0_r}^u \tag{2.20}$$

In equations (2.19) and (2.20), the following definitions hold:

$$\boldsymbol{K}_{ss} = \int \boldsymbol{U}_s^* (\boldsymbol{N}\boldsymbol{S}_s) d\Gamma^e \tag{2.21}$$

$$\boldsymbol{B}_j = \int \boldsymbol{U}_j^* \boldsymbol{Z} d\bar{\Gamma}_u^e \tag{2.22}$$

$$\boldsymbol{t}_{\Gamma_j}^u = \int \boldsymbol{U}_j^* \, \boldsymbol{t}_\Gamma d\Gamma_\sigma^e \tag{2.23}$$

$$\boldsymbol{t}_{0_j}^u = \boldsymbol{K}_j^0 - \boldsymbol{b}_j^u = \int \boldsymbol{U}_j^* \, (\boldsymbol{N}\boldsymbol{\sigma}_0) d\Gamma^e \tag{2.24}$$

$$\boldsymbol{b}_j^u = \int \boldsymbol{U}_j^* \, \boldsymbol{b} \, dV^e \tag{2.25}$$

$$\boldsymbol{K}_j^0 = \int \left(\boldsymbol{\mathcal{D}}^* \boldsymbol{U}_j\right)^* \boldsymbol{\sigma}_0 \, dV^e \tag{2.26}$$

❖ **Boundary statement**

The boundary statement of the hybrid-Trefftz displacement element is obtained enforcing on average essential conditions (2.6) and (2.10) on the extended Dirichlet boundary of the element, using the functions collected in basis $\boldsymbol{Z}$ for weighting.

On the exterior Dirichlet boundary of the element, this procedure yields,

$$\int \boldsymbol{Z}^* (\boldsymbol{u} - \boldsymbol{u}_\Gamma) d\Gamma_u^e = \boldsymbol{0} \tag{2.27}$$

Inserting approximation (2.13) into the above expression and using definition (2.22), the following boundary equation is obtained,

$$-\sum_j \left(\boldsymbol{B}_j^* \boldsymbol{X}_j\right) = \boldsymbol{u}_0^u - \boldsymbol{u}_\Gamma^u \tag{2.28}$$

where:

$$\boldsymbol{u}_\Gamma^u = \int \boldsymbol{Z}^* \boldsymbol{u}_\Gamma \, d\Gamma_u^e \tag{2.29}$$

$$\boldsymbol{u}_0^u = \int \boldsymbol{Z}^* \boldsymbol{u}_0 \, d\Gamma_u^e \tag{2.30}$$

On the interior boundary shared by elements i and k, compatibility condition (2.10) is enforced weakly as,

$$\int \boldsymbol{Z}^* \left(\boldsymbol{u}^i - \boldsymbol{u}^k\right) d\Gamma_i^e = \boldsymbol{0} \tag{2.31}$$

Insertion of definitions (2.22) and (2.30) into the above equation leads to the inter-element compatibility equation:

$$-\sum_j \left[\left(\boldsymbol{B}_j^i\right)^* \boldsymbol{X}_j^i\right] + \sum_j \left[\left(\boldsymbol{B}_j^k\right)^* \boldsymbol{X}_j^k\right] = (\boldsymbol{u}_0^u)^k - (\boldsymbol{u}_0^u)^i \tag{2.32}$$

❖ **Solving system**

The governing system of the displacement element is constructed merging together the domain and boundary statements (2.19) and (2.28) (or (2.32) for interior boundaries), to yield:

$$\begin{bmatrix} \boldsymbol{K}_{ss} & \boldsymbol{0} & -\boldsymbol{B}_s \\ \boldsymbol{0} & \boldsymbol{0} & -\boldsymbol{B}_r \\ -\boldsymbol{B}_s^* & -\boldsymbol{B}_r^* & \boldsymbol{0} \end{bmatrix} \begin{bmatrix} \boldsymbol{X}_s \\ \boldsymbol{X}_r \\ \boldsymbol{P} \end{bmatrix} = \begin{bmatrix} \boldsymbol{t}_{\Gamma_s}^u - \boldsymbol{t}_{0_s}^u \\ \boldsymbol{t}_{\Gamma_r}^u - \boldsymbol{t}_{0_r}^u \\ \boldsymbol{u}_0^u - \boldsymbol{u}_\Gamma^u \end{bmatrix} \tag{2.33}$$

System (2.33) is Hermitian, as the stiffness matrix $\boldsymbol{K}_{ss}$ is Hermitian, and sparse, if not condensed on the boundary variables $\boldsymbol{P}$ (which is the option used here). Under the same assumption, system (2.33) is also strongly localized, and thus well suited to parallel processing. Indeed, the generalized displacement vector $\boldsymbol{X}_j$ is strictly element dependent, while the generalized traction vector $\boldsymbol{P}$ can be shared by at most two connecting elements. Moreover, as the domain and boundary bases are strictly hierarchical and no summation of coefficients is required in the assemblage process, system (2.33) is also well suited to adaptive refinement.

2.2.2 Hybrid-Trefftz stress element

❖ **Approximation bases**

The stress model is derived by directly approximating the stress/pore pressure field in the domain of the element as:

$$\boldsymbol{\sigma} = \boldsymbol{S}_s \boldsymbol{Y}_s + \boldsymbol{\sigma}_0 \quad \text{in } V^e \tag{2.34}$$

In the above definition, basis $\boldsymbol{S}_s$ is a subset of the general solutions of the equilibrium equation (2.11), vector $\boldsymbol{Y}_s$ collects the respective weights, and vector $\boldsymbol{\sigma}_0$ collects particular solutions to equilibrate the body forces. However, enrichment functions may also be added to the basis, as for the displacement element, provided they are self-equilibrated.

The domain strain/fluid content and displacement bases are obtained from the stress basis (2.34) enforcing the elasticity and compatibility conditions (2.4) and (2.2):

$$\boldsymbol{\varepsilon} = \boldsymbol{E}_s \boldsymbol{Y}_s + \boldsymbol{\varepsilon}_0 \quad \text{in } V^e \tag{2.35}$$

$$\boldsymbol{u} = \boldsymbol{U}_d \boldsymbol{Y}_d + \boldsymbol{u}_0 \quad \text{in } V^e \tag{2.36}$$

As they are constrained to satisfy the same domain equations, the functions collected in the domain bases are the same for both models. Therefore, they must satisfy the Trefftz constraints

listed in Table 1. However, stress model does not include rigid body modes, as they generate no stresses.

The displacement field is independently approximated on the Neumann and interior boundaries of the element (extended Neumann boundary, $\overline{\Gamma}_\sigma^e = \Gamma_\sigma^e \cup \Gamma_i^e$) as:

$$\boldsymbol{u} = \boldsymbol{Z}\boldsymbol{Q} \qquad \text{on } \overline{\Gamma}_\sigma^e \tag{2.37}$$

Except for completeness and linear independence, no restrictions are enforced on the functions collected in the (hierarchical) boundary basis $\boldsymbol{Z}$.

❖ **Domain statement**

The domain equation of the hybrid-Trefftz stress element is derived by enforcing on average the compatibility (2.2) and elasticity (2.4) conditions, using the functions collected in basis (2.34) for weighting:

$$\int \boldsymbol{S}_s^* (\boldsymbol{f}\boldsymbol{\sigma} - \boldsymbol{\mathcal{D}}^* \boldsymbol{u})\, dV^e = \boldsymbol{0} \tag{2.38}$$

Integrating by parts the second term of equation (2.38) allows the explicit enforcement of the Dirichlet boundary condition (2.6) and the insertion of the displacement approximation (2.37) on the extended Neumann boundary:

$$\int \boldsymbol{S}_s^* \boldsymbol{f}\boldsymbol{\sigma}\, dV^e = \int \boldsymbol{S}_s^* (\boldsymbol{\mathcal{D}}^* \boldsymbol{u})\, dV^e = \int (\boldsymbol{N}\boldsymbol{S}_s)^* \boldsymbol{u}_\Gamma d\Gamma_u^e + \int (\boldsymbol{N}\boldsymbol{S}_s)^* \boldsymbol{Z} d\overline{\Gamma}_\sigma^e \boldsymbol{Q} - \int (\boldsymbol{\mathcal{D}}\boldsymbol{S}_s)^* \boldsymbol{u}\, dV^e \tag{2.39}$$

Inserting approximations (2.34) and (2.36) into equation (2.39), and using properties given in Table 1, equation (2.39) is written as,

$$\boldsymbol{\mathcal{F}}_{ss} \boldsymbol{Y}_s - \boldsymbol{A}_s \boldsymbol{Q} = \boldsymbol{u}_\Gamma^\sigma - \boldsymbol{u}_0^\sigma \tag{2.40}$$

where:

$$\boldsymbol{\mathcal{F}}_{ss} = \int (\boldsymbol{N}\boldsymbol{S}_s)^* \boldsymbol{U}_s d\Gamma^e \tag{2.41}$$

$$\boldsymbol{A}_s = \int (\boldsymbol{N}\boldsymbol{S}_s)^* \boldsymbol{Z} d\overline{\Gamma}_\sigma^e \tag{2.42}$$

$$\boldsymbol{u}_\Gamma^\sigma = \int (\boldsymbol{N}\boldsymbol{S}_s)^* \boldsymbol{u}_\Gamma d\Gamma_u^e \tag{2.43}$$

$$\boldsymbol{u}_0^\sigma = \int \boldsymbol{S}_s^* \boldsymbol{f}\boldsymbol{\sigma}_0\, dV^e + \int (\boldsymbol{\mathcal{D}}\boldsymbol{S}_s)^* \boldsymbol{u}_0\, dV^e = \int (\boldsymbol{N}\boldsymbol{S}_s)^* \boldsymbol{u}_0 d\Gamma^e \tag{2.44}$$

❖ **Boundary statement**

To obtain the boundary statement of the hybrid-Trefftz stress element, essential conditions (2.5) and (2.9) are enforced on the extended Neumann boundary, using the functions collected in basis $\boldsymbol{Z}$ for weighting. On the exterior Neumann boundary this yields:

$$\int \boldsymbol{Z}^*(\boldsymbol{N\sigma} - \boldsymbol{t}_\Gamma) d\Gamma_\sigma^e = \boldsymbol{0} \tag{2.45}$$

Using definitions (2.34) and (2.42), equation (2.45) becomes,

$$-\boldsymbol{A}_s^* \boldsymbol{Y}_s = \boldsymbol{t}_0^\sigma - \boldsymbol{t}_\Gamma^\sigma \tag{2.46}$$

where:

$$\boldsymbol{t}_\Gamma^\sigma = \int \boldsymbol{Z}^* \boldsymbol{t}_\Gamma \, d\Gamma_\sigma^e \tag{2.47}$$

$$\boldsymbol{t}_0^\sigma = \int \boldsymbol{Z}^* \boldsymbol{N\sigma}_0 \, d\Gamma_\sigma^e \tag{2.48}$$

On the interior boundary shared by elements i and k, equilibrium condition (2.9) is enforced weakly as:

$$\int \boldsymbol{Z}^* \left(\boldsymbol{t}^i + \boldsymbol{t}^k\right) d\Gamma_i^e = \boldsymbol{0} \tag{2.49}$$

Using definitions (2.42) and (2.48) leads to the inter-element equilibrium equation:

$$-\left(\boldsymbol{A}_s^i\right)^* \boldsymbol{X}_s^i - (\boldsymbol{A}_s^k)^* \boldsymbol{X}_s^k = (\boldsymbol{t}_0^\sigma)^k + (\boldsymbol{t}_0^\sigma)^i \tag{2.50}$$

❖ **Solving system**

The governing system of the hybrid-Trefftz stress element is obtained by combining the domain and boundary statements (2.40) and (2.46) (or (2.50) for interior boundaries), to yield:

$$\begin{bmatrix} \boldsymbol{\mathcal{F}}_s & -\boldsymbol{A}_s \\ -\boldsymbol{A}_s^* & \boldsymbol{0} \end{bmatrix} \begin{bmatrix} \boldsymbol{Y}_s \\ \boldsymbol{Q} \end{bmatrix} = \begin{bmatrix} \boldsymbol{u}_\Gamma^\sigma - \boldsymbol{u}_0^\sigma \\ \boldsymbol{t}_0^\sigma - \boldsymbol{t}_\Gamma^\sigma \end{bmatrix} \tag{2.51}$$

System (2.51) shares the same algebraic properties as system (2.33) of the hybrid-Trefftz displacement element.

It should be noted that the stress model in unable to estimate the rigid-body and free-flow displacements, as they do not cause stress in the domain of the element. The rigid-body/free-flow displacements are recovered in the post-processing phase, as discussed in Section 3.1.8 for biphasic media and Section 4.1.7 for triphasic media.

2.3 Integration in time of elastodynamic problems

The equilibrium equation of the elastodynamic problem is recovered by setting the right hand side term of equation (2.1) to,

$$\boldsymbol{r} = \boldsymbol{d}_0\dot{\boldsymbol{u}} + \boldsymbol{\rho}_0\ddot{\boldsymbol{u}} \tag{2.52}$$

where $\boldsymbol{\rho}_0$ and $\boldsymbol{d}_0$ are the (local, symmetric) density and structural damping matrices. They are defined in Appendix A for triphasic media and Appendix D for biphasic media.

Under definition (2.52), the equilibrium equation is:

$$\boldsymbol{\mathcal{D}\sigma} + \boldsymbol{b} = \boldsymbol{d}_0\dot{\boldsymbol{u}} + \boldsymbol{\rho}_0\ddot{\boldsymbol{u}} \quad \text{in } V \tag{2.53}$$

Domain equations (2.2) to (2.4), boundary and initial conditions (2.5) to (2.8) complete the description of the dynamic problem. As shown for static problems, the domain equations can be merged into the Navier equation, which now takes the following form:

$$\boldsymbol{\mathcal{D}k\mathcal{D}^*u} + \boldsymbol{b} = \boldsymbol{d}_0\dot{\boldsymbol{u}} + \boldsymbol{\rho}_0\ddot{\boldsymbol{u}} \quad \text{in } V \tag{2.54}$$

In order to support the application of hybrid-Trefftz elements, the integration in time of the governing equations is performed first. Regardless of the time-integration method, the hyperbolic problem (2.54) is reduced to a series of elliptic equations in space, which are subsequently solved using hybrid-Trefftz finite elements.

A wide range of techniques are available for the time discretization of the dynamic problem. Essentially, these include finite difference based direct techniques (e.g. the Euler, Runge-Kutta and Newmark classes of methods), transform-based techniques (e.g. Fourier and Laplace transforms), weighted-residual approaches (e.g. [54]) and finite element approximations simultaneously in space and time. For an integrated perspective over a significant number of time integration techniques, the reader is referred to the work of Tamma (e.g. [113, 114]).

In this work, the Discrete Fourier Transform (DFT) [115, 116] is used for the time discretization of periodic problems. For non-periodic and transient problems , where the initial condition are relevant, the weighted-residual approach presented in [54] is used. The method has the merit of generating time-discretized problems defined by spectral-like (elliptic) equations, independently of the functions that are used in the time basis, thus endorsing the use of the same finite element formulation for periodic and transient problems. The method is unconditionally stable and, depending on the adopted time basis, can be applied with large time steps [51].

Both DFT and weighted-residual methods are based on separation of variables in time and space. Letting $\boldsymbol{\alpha}(x,y,t)$ represent a generic field, this is written as,

$$\boldsymbol{\alpha}(x,y,t) = \sum_{n=1}^{N} W_n(t)\, \boldsymbol{\alpha}_n(x,y) \quad \text{in } V \tag{2.55}$$

The difference between the DFT and weighted residual methods is in the functions selected for the time basis and in the way that the governing equations are enforced over the time of the analysis.

2.3.1 Time integration of periodic problems

Periodic problems are typically solved using DFT, especially when the applied excitation is smooth enough to be well approximated by trigonometric functions. The DFT is equivalent to defining the time basis present in equation (2.55) as $W_n(t) = \frac{1}{T} e^{\hat{\imath}\omega_n t}$, where T is the period of the problem, $\omega_n = n\Delta\omega$ is the n^{th} spectral frequency and $\Delta\omega = \frac{2\pi}{T}$. With this, the approximations of the domain displacement, strain and stress fields are expressed as:

$$\boldsymbol{u}(x,y,t) = \tfrac{1}{T}\textstyle\sum_{n=1}^{N} \boldsymbol{u}_n(x,y)\, e^{\hat{\imath}\omega_n t} \tag{2.56}$$

$$\boldsymbol{\varepsilon}(x,y,t) = \tfrac{1}{T}\textstyle\sum_{n=1}^{N} \boldsymbol{\varepsilon}_n(x,y)\, e^{\hat{\imath}\omega_n t} \tag{2.57}$$

$$\boldsymbol{\sigma}(x,y,t) = \tfrac{1}{T}\textstyle\sum_{n=1}^{N} \boldsymbol{\sigma}_n(x,y)\, e^{\hat{\imath}\omega_n t} \tag{2.58}$$

Substitution of the above definitions into the equilibrium equation (2.53) yields a series of N equations of type,

$$\boldsymbol{\mathcal{D}}\boldsymbol{\sigma}_n + \boldsymbol{b}_n + \omega_n^2 \boldsymbol{\rho}_n \boldsymbol{u}_n = \boldsymbol{0} \quad \text{in } V \tag{2.59}$$

where $\boldsymbol{\rho}_n = \boldsymbol{\rho_0} + \frac{\hat{\imath}}{\omega_n}\boldsymbol{d}_0$, $\hat{\imath}$ is imaginary unit, and $\boldsymbol{b}_n$ is the n^{th} spectral component of the body force:

$$\boldsymbol{b}_n = \int_{-T/2}^{T/2} \boldsymbol{b}\, e^{-\hat{\imath}\omega_n t} dt \tag{2.60}$$

$$\boldsymbol{b}(x,y,t) = \tfrac{1}{T}\textstyle\sum_{n=1}^{N} \boldsymbol{b}_n(x,y)\, e^{\hat{\imath}\omega_n t} \tag{2.61}$$

Substitution of approximations (2.56) to (2.58) into the compatibility and elasticity equations (2.2), (2.3) and (2.4) yields:

$$\boldsymbol{\varepsilon}_n = \boldsymbol{\mathcal{D}}^* \boldsymbol{u}_n \quad \text{in } V \tag{2.62}$$

$$\boldsymbol{\sigma}_n = \boldsymbol{k}\boldsymbol{\varepsilon}_n \quad \text{in } V \tag{2.63}$$

$$\boldsymbol{\varepsilon}_n = \boldsymbol{f}\boldsymbol{\sigma}_n \quad \text{in } V \tag{2.64}$$

On the boundary of the medium, the applied forces and displacements are expanded using the DFT,

$$\boldsymbol{t}_{\Gamma_n} = \int_{-T/2}^{T/2} \boldsymbol{t}_\Gamma \, e^{-\hat{\imath}\omega_n t} dt \tag{2.65}$$

$$\boldsymbol{t}_\Gamma(x,y,t) = \frac{1}{T}\sum_{n=1}^{N} \boldsymbol{t}_{\Gamma_n}(x,y)\, e^{\hat{\imath}\omega_n t} \quad \text{on } \Gamma_\sigma \tag{2.66}$$

$$\boldsymbol{u}_{\Gamma_n} = \int_{-T/2}^{T/2} \boldsymbol{u}_\Gamma \, e^{-\hat{\imath}\omega_n t} dt \tag{2.67}$$

$$\boldsymbol{u}_\Gamma(x,y,t) = \frac{1}{T}\sum_{n=1}^{N} \boldsymbol{u}_{\Gamma_n}(x,y)\, e^{\hat{\imath}\omega_n t} \quad \text{on } \Gamma_u \tag{2.68}$$

and the boundary conditions (2.5), (2.6), (2.9) and (2.10) acquire their spectral forms (2.69) to (2.72),

$$\boldsymbol{N}\boldsymbol{\sigma}_n = \boldsymbol{t}_{\Gamma_n} \quad \text{on } \Gamma_\sigma \tag{2.69}$$

$$\boldsymbol{u}_n = \boldsymbol{u}_{\Gamma_n} \quad \text{on } \Gamma_u \tag{2.70}$$

$$\boldsymbol{t}_n^i + \boldsymbol{t}_n^k = \boldsymbol{0} \quad \text{on } \Gamma_i^e \tag{2.71}$$

$$\boldsymbol{u}_n^i = \boldsymbol{u}_n^k \quad \text{on } \Gamma_i^e \tag{2.72}$$

2.3.2 Time integration of transient problems

The procedure given in [54] is applied here for time integration of transient problems. Any complete, linear independent and differentiable basis of functions can be used as time basis in equation (2.55). The total duration of the problem is split into time steps of size Δt. The governing equations are enforced using a weighted residual approach in each time step.

According to the Galerkin method, the functions contained in the time basis are used as test functions in the weak enforcement of the governing equations. This procedure is applied first to the velocity and acceleration definitions, on the current time interval Δt,

$$\int_0^{\Delta t} \widehat{W}_m(\boldsymbol{v} - \dot{\boldsymbol{u}}) dt = \boldsymbol{0} \tag{2.73}$$

$$\int_0^{\Delta t} \widehat{W}_m(\boldsymbol{a} - \dot{\boldsymbol{v}})dt = \boldsymbol{0} \tag{2.74}$$

where $\widehat{W}_m$ represents the complex conjugate of generic function $\widehat{W}_m(t)$.

It is convenient to define the square matrices $\boldsymbol{H}$ and $\boldsymbol{G}$, with the generic terms given by:

$$H_{mn} = \frac{1}{\Delta t}\int_0^{\Delta t} \widehat{W}_m W_n dt \tag{2.75}$$

$$G_{mn} = \widehat{W}_m(\Delta t)W_n(\Delta t) - \int_0^{\Delta t} \dot{\widehat{W}}_m W_n dt \tag{2.76}$$

Equations (2.73) and (2.74) can be uncoupled if the time basis is constructed such that matrices $\boldsymbol{H}$ and $\boldsymbol{G}$ are related through a diagonal matrix of constants [54],

$$\boldsymbol{H\Psi} = \boldsymbol{G} \tag{2.77}$$

to yield the following velocity and acceleration estimates,

$$\Delta t\, \boldsymbol{v}_n = \Psi_n \boldsymbol{u}_n - \psi_n \boldsymbol{u}^0, \quad \text{for } n = \{1, N\} \tag{2.78}$$

$$\Delta t\, \boldsymbol{a}_n = \Psi_n \boldsymbol{v}_n - \psi_n \boldsymbol{v}^0 \tag{2.79}$$

where Ψ_n is the n^{th} diagonal term of matrix $\boldsymbol{\Psi}$ and:

$$\psi_n = \sum_{m=1}^{N} \bar{H}_{nm}\widehat{W}_m(0) \tag{2.80}$$

In equation (2.80) $\bar{H}_{nm}$ denotes the general term of the inverse of matrix $\boldsymbol{H}$. Note that condition (2.77) should not be seen as a limitation of the method. Following the procedure detailed in [54], this condition can be secured for any type of functions collected in the time basis (e.g. polynomial, trigonometric or wavelet functions).

Following the same strategy, the weak enforcement of equations (2.53), (2.2) to (2.6), (2.9) and (2.10) using the time basis $W_m(t)$ for testing, and the enforcement of results (2.78) and (2.79) in the resulting expressions, yield a series of N uncoupled problems in space variables only,

$$\boldsymbol{\mathcal{D}\sigma}_n + \omega_n^2 \boldsymbol{\rho}_n \boldsymbol{u}_n = \boldsymbol{F}_n^0 \quad \text{in } V \tag{2.81}$$

$$\boldsymbol{\varepsilon}_n = \boldsymbol{\mathcal{D}}^* \boldsymbol{u}_n \quad \text{in } V \tag{2.82}$$

$$\boldsymbol{\sigma}_n = \boldsymbol{k\varepsilon}_n \quad \text{in } V \tag{2.83}$$

$$\boldsymbol{\varepsilon}_n = \boldsymbol{f\sigma}_n \quad \text{in } V \tag{2.84}$$

$$\boldsymbol{N}\boldsymbol{\sigma}_n = \boldsymbol{t}_{\Gamma_n} \quad \text{on } \Gamma_\sigma \tag{2.85}$$

$$\boldsymbol{u}_n = \boldsymbol{u}_{\Gamma_n} \quad \text{on } \Gamma_u \tag{2.86}$$

$$\boldsymbol{t}_n^i + \boldsymbol{t}_n^k = \boldsymbol{0} \quad \text{on } \Gamma_i^e \tag{2.87}$$

$$\boldsymbol{u}_n^i = \boldsymbol{u}_n^k \quad \text{on } \Gamma_i^e \tag{2.88}$$

where the generalized frequency ω_n is defined as,

$$\omega_n = -\hat{\imath}\frac{\psi_n}{\Delta t} \tag{2.89}$$

and is generally complex.

The non-homogeneous term present in the equilibrium equation (2.81) is defined as,

$$\boldsymbol{F}_n^0 = -\frac{\psi_n}{\Delta t}(\hat{\imath}\omega_n\boldsymbol{\rho}_n\boldsymbol{u}^0 + \boldsymbol{\rho}_0\boldsymbol{v}^0) - \boldsymbol{b}_n \tag{2.90}$$

and includes the influence of initial conditions and the body force:

$$\boldsymbol{b}_n = \frac{1}{\Delta t}\sum_{m=1}^{N}\bar{H}_{nm}\int_0^{\Delta t}\widehat{W}_m\boldsymbol{b}dt \tag{2.91}$$

Finally, the kinematic and static boundary conditions are given by:

$$\boldsymbol{u}_{\Gamma_n} = \frac{1}{\Delta t}\sum_{m=1}^{N}\bar{H}_{nm}\int_0^{\Delta t}\widehat{W}_m\boldsymbol{u}_\Gamma dt \tag{2.92}$$

$$\boldsymbol{t}_{\Gamma_n} = \frac{1}{\Delta t}\sum_{m=1}^{N}\bar{H}_{nm}\int_0^{\Delta t}\widehat{W}_m\boldsymbol{t}_\Gamma dt \tag{2.93}$$

Note that the index n associated to each of the spectral problem will be dropped from this point forward, for simplicity.

2.4 Integration in space of elastodynamic problems

Both Fourier and weighted-residual time integration methods yield the same type of elliptic time discretized equations. This justifies the use of the same hybrid-Trefftz elements for the integration in space, regardless of the periodicity of the problem and of the time integration method adopted for its solution. The only difference between the time-discretized equations yielded by the two approaches is the source (non-homogeneous) term of the equilibrium equation, which includes, in general, the influence of the initial conditions in the weighted-residual approach, as opposed to the DFT.

When body forces, thermal gradients or initial conditions are present in the governing equations, Trefftz-compliant bases may fail to recover the solution of the resulting non-homogeneous problem. This is certainly the case of problems with non-trivial initial solutions. Moreover, particular solutions of the non-homogeneous problem are not available, domain integral terms emerge in the solving system. In such situations, weak particular solution functions can be added to the Trefftz basis to model the effect of the source terms.

The best approach is to choose strong particular solutions, that is, local solutions of the non-homogeneous form of the governing equation. When this is possible, the problem is reduced to the boundary of the domain and all advantages of the Trefftz method are preserved. Such particular solutions were reported, for instance, in [23] for elastostatic beams subjected to own weight and for hollow cylinders subjected to axisymmetric temperature field with logarithmic variation. When more complex source functions are considered, however, it is generally not possible to find strong particular solutions, and approximate (weak) solutions must be used instead.

The displacement and stress model of the hybrid-Trefftz element are described below, assuming that the particular solution is known. The issue of numerically evaluating the particular solution of the time-discretized problem is addressed in Section 2.5.

2.4.1 Hybrid-Trefftz displacement element

❖ **Approximation bases**

Let the displacement of the various constituents of the medium be approximated in the domain of the element using functions that satisfy locally the homogeneous form of the governing equations (2.81) to (2.84), collected in basis $\boldsymbol{U}_d$:

$$\boldsymbol{u} = \boldsymbol{U}_d \boldsymbol{X}_d + \boldsymbol{u}_0 \quad \text{in } V^e \tag{2.94}$$

In equation (2.94), vector $\boldsymbol{X}_d$ collects the generalized displacements corresponding to the functions listed in the displacement basis, while the particular solution vector $\boldsymbol{u}_0$ models the effect of the non-homogeneous term $\boldsymbol{F}^0$.

The approximation of the generalized strain field in the domain of the element is obtained from definition (2.94) by locally enforcing the domain compatibility equation (2.82):

$$\boldsymbol{\varepsilon} = \boldsymbol{E}_d \boldsymbol{X}_d + \boldsymbol{\varepsilon}_0 \quad \text{in } V^e \tag{2.95}$$

The dependent stress approximation (2.96) is obtained from definition (2.95) by enforcing locally the elasticity equations (2.83):

$$\boldsymbol{\sigma} = \boldsymbol{S}_d \boldsymbol{X}_d + \boldsymbol{\sigma}_0 \quad \text{in } V^e \tag{2.96}$$

The approximation functions present in expressions (2.94), (2.95) and (2.96) must satisfy the Trefftz constraints listed in Table 2. It should be noted that approximations in equations (2.94) and (2.96) do not satisfy, in general, the equilibrium equation (2.81), which is enforced below, in a weak form.

Equilibrium equations	**Compatibility equations**	**Elasticity equations**
$\boldsymbol{\mathcal{D}} \boldsymbol{S}_d + \omega^2 \boldsymbol{\rho} \boldsymbol{U}_d = \boldsymbol{0}$	$\boldsymbol{E}_d = \boldsymbol{\mathcal{D}}^* \boldsymbol{U}_d$	$\boldsymbol{S}_d = \boldsymbol{k} \boldsymbol{E}_d$
	$\boldsymbol{\varepsilon}_0 = \boldsymbol{\mathcal{D}}^* \boldsymbol{u}_0$	$\boldsymbol{\sigma}_0 = \boldsymbol{k} \boldsymbol{\varepsilon}_0$

Table 2: Trefftz constraints of displacement model for dynamic problems

The traction field is independently approximated on the Dirichlet and interior boundaries of the element ($\overline{\Gamma}_u^e = \Gamma_u^e \cup \Gamma_i^e$) as:

$$\boldsymbol{t} = \boldsymbol{Z} \boldsymbol{P} \quad \text{on } \overline{\Gamma}_u^e \tag{2.97}$$

Except for completeness and linear independence, no restrictions are enforced on the functions collected in the (hierarchical) boundary basis $\boldsymbol{Z}$. In particular, the traction approximation (2.97) is not derived from the traction field produced by approximation (2.96), although the two should be consistent upon convergence. Generalized traction vector $\boldsymbol{P}$ collects the weights associated to each of the shape functions present in basis $\boldsymbol{Z}$ and have no particular physical significance.

❖ **Domain statement**

The domain statement of the hybrid-Trefftz displacement element is obtained by enforcing weakly the equilibrium equation (2.81), using the displacement basis (2.94) for weighting:

$$\int \boldsymbol{U}_d^* (\boldsymbol{\mathcal{D}} \boldsymbol{\sigma} + \omega^2 \boldsymbol{\rho} \boldsymbol{u} - \boldsymbol{F}^0) \, dV^e = \boldsymbol{0} \tag{2.98}$$

The integration by parts of the first term of equation (2.98) forces the emergence of the boundary terms, in which the boundary equilibrium equation (2.85) and the Dirichlet boundary approximation (2.97) are enforced:

$$\int \boldsymbol{U}_d^* \boldsymbol{\mathcal{D}\sigma}\, dV^e = \int \boldsymbol{U}_d^*\, \boldsymbol{t}_\Gamma d\Gamma_\sigma^e + \int \boldsymbol{U}_d^*\, \boldsymbol{Z} d\bar{\Gamma}_u^e \boldsymbol{P} - \int (\boldsymbol{\mathcal{D}}^* \boldsymbol{U}_d)^* \boldsymbol{\sigma}\, dV^e \tag{2.99}$$

Enforcing approximations (2.94) and (2.96) in equations (2.98) and (2.99), respectively, and using properties given in Table 2, the equation (2.98) is be written as,

$$\boldsymbol{D}_{dd}\boldsymbol{X}_d - \boldsymbol{B}_d \boldsymbol{P} = \boldsymbol{t}_\Gamma^u - \boldsymbol{t}_0^u \tag{2.100}$$

where:

$$\boldsymbol{D}_{dd} = \int \boldsymbol{U}_d^* (\boldsymbol{N}\boldsymbol{S}_d) d\Gamma^e \tag{2.101}$$

$$\boldsymbol{B}_d = \int \boldsymbol{U}_d^* \boldsymbol{Z} d\bar{\Gamma}_u^e \tag{2.102}$$

$$\boldsymbol{t}_\Gamma^u = \int \boldsymbol{U}_d^*\, \boldsymbol{t}_\Gamma d\Gamma_\sigma^e \tag{2.103}$$

$$\boldsymbol{t}_0^u = \boldsymbol{K}_0 - \omega^2 \boldsymbol{M}_0 + \boldsymbol{F}^u \tag{2.104}$$

$$\boldsymbol{F}^u = \int \boldsymbol{U}_d^*\, \boldsymbol{F}^0 dV^e \tag{2.105}$$

$$\boldsymbol{K}_0 = \int (\boldsymbol{\mathcal{D}}^* \boldsymbol{U}_d)^* \boldsymbol{\sigma}_0\, dV^e \tag{2.106}$$

$$\boldsymbol{M}_0 = \int \boldsymbol{U}_d^* \boldsymbol{\rho}\boldsymbol{u}_0\, dV^e \tag{2.107}$$

The non-homogeneous term $\boldsymbol{F}^0$ present in the equilibrium equation (2.81) causes the emergence of domain integrals in the right hand side of equation (2.100). If analytic solutions of the non-homogeneous problems exist,

$$\boldsymbol{\mathcal{D}\sigma}_0 + \omega^2 \boldsymbol{\rho}\boldsymbol{u}_0 = \boldsymbol{F}^0 \tag{2.108}$$

definition (2.104) is reduced to the boundary integral:

$$\boldsymbol{t}_0^u = \int \boldsymbol{U}_d^*\, (\boldsymbol{N}\boldsymbol{\sigma}_0) d\Gamma^e \tag{2.109}$$

❖ **Boundary statement**

The boundary statement of the hybrid-Trefftz displacement element is obtained enforcing on average essential conditions (2.86) and (2.88) on the extended Dirichlet boundary of the element, using the functions collected in basis $\boldsymbol{Z}$ for weighting.

On the exterior Dirichlet boundary of the element, this procedure yields:

$$\int \boldsymbol{Z}^*(\boldsymbol{u}-\boldsymbol{u}_\Gamma)d\Gamma_u^e = \boldsymbol{0} \tag{2.110}$$

Inserting approximation (2.94) into the above expression and using definition (2.102), the following boundary equation is recovered,

$$-\boldsymbol{B}_d^*\boldsymbol{X}_d = -\boldsymbol{u}_\Gamma^u + \boldsymbol{u}_0^u \tag{2.111}$$

where:

$$\boldsymbol{u}_\Gamma^u = \int \boldsymbol{Z}^*\boldsymbol{u}_\Gamma\, d\Gamma_u^e \tag{2.112}$$

$$\boldsymbol{u}_0^u = \int \boldsymbol{Z}^*\boldsymbol{u}_0\, d\Gamma_u^e \tag{2.113}$$

On the interior boundary shared by elements i and k, compatibility condition (2.88) is enforced weakly as:

$$\int \boldsymbol{Z}^*\left(\boldsymbol{u}^i-\boldsymbol{u}^k\right) d\Gamma_i^e = \boldsymbol{0} \tag{2.114}$$

Insertion of definition (2.102) into the above equation leads to the inter-element compatibility equation:

$$-\left(\boldsymbol{B}_d^i\right)^*\boldsymbol{X}_d^i + \left(\boldsymbol{B}_d^k\right)^*\boldsymbol{X}_d^k = (\boldsymbol{u}_\Gamma^0)^k - (\boldsymbol{u}_\Gamma^0)^i \tag{2.115}$$

❖ **Solving system**

The solving system (2.116) of the hybrid-Trefftz displacement element is obtained by collecting the domain equation (2.100) and boundary statement (2.111), for exterior Dirichlet boundaries, or (2.115), for interior boundaries:

$$\begin{bmatrix}\boldsymbol{D}_{dd} & -\boldsymbol{B}_d\\ -\boldsymbol{B}_d^* & \boldsymbol{0}\end{bmatrix}\begin{bmatrix}\boldsymbol{X}_d\\ \boldsymbol{P}\end{bmatrix} = \begin{bmatrix}\boldsymbol{t}_\Gamma^u - \boldsymbol{t}_0^u\\ -\boldsymbol{u}_\Gamma^u + \boldsymbol{u}_0^u\end{bmatrix} \tag{2.116}$$

System (2.116) is highly sparse (typically, more than 90% of its coefficients are null) and strongly localized, if not condensed on the boundary variables. Consequently, the system can be handled using efficient procedures especially designed for sparse systems. As shown in Section 2.2.1, the hybrid-Trefftz displacement element is well suited to adaptive p-refinement and parallel processing procedures.

2.4.2 Hybrid-Trefftz stress element

❖ **Approximation bases**

The stress model is constructed on the direct approximation of the stress/pore pressure fields in the domain of the element using the general and particular solutions of the equilibrium equation (2.81) as shape function:

$$\boldsymbol{\sigma} = \boldsymbol{S}_d \boldsymbol{Y}_d + \boldsymbol{\sigma}_0 \quad \text{in } V^e \tag{2.117}$$

In the above definition, vector $\boldsymbol{Y}_d$ collects the generalized stresses associated with the functions listed in the stress basis. Vector $\boldsymbol{\sigma}_0$ collects particular solutions to equilibrate the non-homogeneous term $\boldsymbol{F}^0$.

A dependent domain displacement basis is constructed such as to satisfy locally equilibrium equation (2.81):

$$\boldsymbol{u} = \boldsymbol{U}_d \boldsymbol{Y}_d + \bar{\boldsymbol{u}}_0 \quad \text{in } V^e \tag{2.118}$$

The domain strain basis is obtained from the stress basis (2.117) enforcing the elasticity condition (2.84).

$$\boldsymbol{\varepsilon} = \boldsymbol{E}_d \boldsymbol{Y}_d + \boldsymbol{\varepsilon}_0 \quad \text{in } V^e \tag{2.119}$$

The functions collected in (2.117) to (2.119) satisfy the constraints listed in Table 3. The equilibrium equation (2.81) is satisfied locally, On the other hand, the displacement and strain approximations do not satisfy, in general, the compatibility condition (2.82) , which is enforced in a weak form.

Equilibrium equations	**Compatibility equations**	**Elasticity equations**
$\boldsymbol{\mathcal{D}S}_d + \omega^2 \boldsymbol{\rho U}_d = \boldsymbol{0}$	$\boldsymbol{E}_d = \boldsymbol{\mathcal{D}}^* \boldsymbol{U}_d$	$\boldsymbol{S}_d = \boldsymbol{kE}_d$
$\boldsymbol{\mathcal{D}\sigma}_0 + \omega^2 \boldsymbol{\rho}\bar{\boldsymbol{u}}_0 = \boldsymbol{0}$		$\boldsymbol{\varepsilon}_0 = \boldsymbol{f\sigma}_0$

Table 3: Trefftz constraints of stress model for dynamic problems

The displacement field is independently approximated on the Neumann and interior boundaries of the element (extended Neumann boundary, $\overline{\Gamma}_\sigma^e = \Gamma_\sigma^e \cup \Gamma_i^e$) as:

$$\boldsymbol{u} = \boldsymbol{ZQ} \quad \text{on } \overline{\Gamma}_\sigma^e \tag{2.120}$$

Except for completeness and linear independence, no restrictions are enforced on the functions collected in the (hierarchical) boundary basis $\boldsymbol{Z}$.

❖ **Domain statement**

The domain equation of the hybrid-Trefftz stress element is derived by enforcing on average the compatibility (2.82) and elasticity (2.84) conditions, using the functions collected in basis (2.117) for weighting:

$$\int \boldsymbol{S}_d^*(\boldsymbol{f}\boldsymbol{\sigma} - \boldsymbol{\mathcal{D}}^*\boldsymbol{u})\, dV^e = \boldsymbol{0} \tag{2.121}$$

Integrating by parts the second term of equation (2.121) allows the explicit enforcement of the Dirichlet boundary condition (2.86) and the insertion of the displacement approximation (2.120) on the extended Neumann boundary:

$$\int \boldsymbol{S}_d^*(\boldsymbol{\mathcal{D}}^*\boldsymbol{u})\, dV^e = \int (\boldsymbol{N}\boldsymbol{S}_d)^*\, \boldsymbol{u}_\Gamma d\Gamma_u^e + \int (\boldsymbol{N}\boldsymbol{S}_d)^*\, \boldsymbol{Z} d\bar{\Gamma}_\sigma^e \boldsymbol{Q} - \int (\boldsymbol{\mathcal{D}}\boldsymbol{S}_d)^* \boldsymbol{u}\, dV^e \tag{2.122}$$

Enforcing approximations (2.117) and (2.118) into equation (2.121) and space (2.122), and using properties given in Table 3, equation (2.121) yields,

$$\boldsymbol{\mathcal{F}}_{dd}\boldsymbol{Y}_d - \boldsymbol{A}_d\boldsymbol{Q} = \boldsymbol{u}_\Gamma^\sigma - \boldsymbol{u}_0^\sigma \tag{2.123}$$

where:

$$\boldsymbol{\mathcal{F}}_{dd} = \int (\boldsymbol{N}\boldsymbol{S}_d)^*\, \boldsymbol{U}_d d\Gamma^e \tag{2.124}$$

$$\boldsymbol{A}_d = \int (\boldsymbol{N}\boldsymbol{S}_d)^*\, \boldsymbol{Z} d\bar{\Gamma}_\sigma^e \tag{2.125}$$

$$\boldsymbol{u}_\Gamma^\sigma = \int (\boldsymbol{N}\boldsymbol{S}_d)^*\, \boldsymbol{u}_\Gamma d\Gamma_u^e \tag{2.126}$$

$$\boldsymbol{u}_0^\sigma = \boldsymbol{\mathcal{F}}_0 - \omega^{-2}\bar{\boldsymbol{M}}_0 + \omega^{-2}\boldsymbol{F}^\sigma \tag{2.127}$$

$$\boldsymbol{F}^\sigma = \int (\boldsymbol{\mathcal{D}}\boldsymbol{S}_d)^*\, \boldsymbol{\rho}^{-1}\boldsymbol{F}^0 dV^e \tag{2.128}$$

$$\boldsymbol{\mathcal{F}}_0 = \int \boldsymbol{S}_d^* \boldsymbol{f}\boldsymbol{\sigma}_0\, dV^e \tag{2.129}$$

$$\bar{\boldsymbol{M}}_0 = \int (\boldsymbol{\mathcal{D}}\boldsymbol{S}_d)^*\, \boldsymbol{\rho}^{-1}\boldsymbol{\mathcal{D}}\boldsymbol{\sigma}_0 dV^e \tag{2.130}$$

As shown for the displacement element, the domain integral term present in the right hand side of equation (2.127) is reduced to the boundary integral (2.131) if analytic solutions exist for the non-homogeneous domain equations:

$$\boldsymbol{u}_0^\sigma = \int (\boldsymbol{N}\boldsymbol{S}_d)^*\, \bar{\boldsymbol{u}}_0 d\Gamma_u^e \tag{2.131}$$

❖ **Boundary statement**

Essential conditions (2.85) and (2.87) are enforced on the Neumann and interior boundaries of the element, respectively, using the functions collected in basis $\boldsymbol{Z}$ for testing.

On the Neumann boundary, this yields:

$$\int \boldsymbol{Z}^*(\boldsymbol{N\sigma} - \boldsymbol{t}_\Gamma) d\Gamma_\sigma^e = \boldsymbol{0} \tag{2.132}$$

Using definitions (2.117) and (2.125), equation (2.132) becomes:

$$-\boldsymbol{A}_d^* \boldsymbol{Y}_d = \boldsymbol{t}_0^\sigma - \boldsymbol{t}_\Gamma^\sigma \tag{2.133}$$

where:

$$\boldsymbol{t}_\Gamma^\sigma = \int \boldsymbol{Z}^* \boldsymbol{t}_\Gamma \, d\Gamma_\sigma^e \tag{2.134}$$

$$\boldsymbol{t}_0^\sigma = \int \boldsymbol{Z}^* \boldsymbol{N\sigma}_0 \, d\Gamma_\sigma^e \tag{2.135}$$

On the interior boundary shared by elements i and k, equilibrium condition (2.87) is enforced weakly as,

$$\int \boldsymbol{Z}^* \left(\boldsymbol{t}^i + \boldsymbol{t}^k\right) d\Gamma_i^e = \boldsymbol{0} \tag{2.136}$$

Using definitions (2.125) and (2.135) leads to the inter-element equilibrium equation:

$$-\left(\boldsymbol{A}_d^i\right)^* \boldsymbol{X}_d^i - \left(\boldsymbol{A}_d^k\right)^* \boldsymbol{X}_d^k = (\boldsymbol{t}_0^\sigma)^k + (\boldsymbol{t}_0^\sigma)^i \tag{2.137}$$

❖ **Solving system**

The hybrid-Trefftz stress element governing system is obtained by combining the domain and boundary statements (2.123) and (2.133) (or (2.137) for interior boundaries), to yield:

$$\begin{bmatrix} \boldsymbol{\mathcal{F}}_{dd} & -\boldsymbol{A}_d \\ -\boldsymbol{A}_d^* & \boldsymbol{0} \end{bmatrix} \begin{bmatrix} \boldsymbol{Y}_d \\ \boldsymbol{Q} \end{bmatrix} = \begin{bmatrix} \boldsymbol{u}_\Gamma^\sigma - \boldsymbol{u}_0^\sigma \\ \boldsymbol{t}_0^\sigma - \boldsymbol{t}_\Gamma^\sigma \end{bmatrix} \tag{2.138}$$

System (2.138) shares the same algebraic properties as system (2.116) of the hybrid-Trefftz displacement element.

2.5 Particular solutions

For simple source functions (e.g. constant body forces), analytic particular solutions may be available for equations (2.81) to (2.83). When this is the case, all terms present in the hybrid-Trefftz finite element equations derived in Section 2.4 are reduced to boundary integral expressions [23].

Unfortunately, in most dynamic problems, no analytic particular solutions are available because of the presence of the initial condition terms, and approximate expressions of the

particular solution must be found instead. The objective of this section is to show that important simplifications of the formulations derived in Section 2.4 are obtained if the particular solution is constructed using functions that satisfy the homogeneous form of the static problem presented in Section 2.2. These functions are labelled here static (or particular solution) functions.

Along with the Trefftz-compliant (i.e. dynamic) functions, the static functions are used to enforce weakly the domain equations and their weights are obtained from the solution of the finite element solving system, written for the whole mesh.

❖ **Particular solution bases**

The option followed here is to define the particular solution vectors $\boldsymbol{u}_0$, $\boldsymbol{\varepsilon}_0$ and $\boldsymbol{\sigma}_0$ as,

$$\boldsymbol{u}_0 = \boldsymbol{U}_s \boldsymbol{X}_s + \boldsymbol{U}_r \boldsymbol{X}_r \tag{2.139}$$

$$\boldsymbol{\varepsilon}_0 = \boldsymbol{E}_s \boldsymbol{X}_s \tag{2.140}$$

$$\boldsymbol{\sigma}_0 = \boldsymbol{S}_s \boldsymbol{X}_s \tag{2.141}$$

The above definitions hold for both displacement and stress models, with the distinction that the generalized displacements $\boldsymbol{X}_s$ and $\boldsymbol{X}_r$ are replaced by the general stresses $\boldsymbol{Y}_s$ in the case of the stress model.

The approximation functions presented in equations (2.139) to (2.141) satisfy the domain equations:

$$\mathcal{D}\boldsymbol{S}_s = \boldsymbol{0} \tag{2.142}$$

$$\boldsymbol{E}_s = \mathcal{D}^* \boldsymbol{U}_s \tag{2.143}$$

$$\mathcal{D}^* \boldsymbol{U}_r = \boldsymbol{0} \tag{2.144}$$

$$\boldsymbol{S}_s = \boldsymbol{k}\boldsymbol{E}_s \tag{2.145}$$

The functions collected in the particular solution bases are generally well known and numerically simpler than their dynamic counterparts. They satisfy locally compatibility and elasticity equations (2.82) and (2.83), but do not satisfy locally the equilibrium equation (2.81).

It should be noted that since the stress model of the hybrid-Trefftz elements requires the local enforcement of the equilibrium equation, definition (2.139) does not hold for the particular solution $\overline{\boldsymbol{u}}_0$ present in definition (2.118). However, using property (2.142), equation (2.108) provides a simple definition for $\overline{\boldsymbol{u}}_0$ as,

$$\bar{\boldsymbol{u}}_0 = \omega^{-2}\boldsymbol{\rho}^{-1}\boldsymbol{F}^0 \tag{2.146}$$

The weights of the static functions can be determined, along with the weights of the dynamic functions, by enforcing the same domain and boundary equations as described in Section 2.4 for the coupled approach.

❖ **Displacement model**

Despite the different physical grounds they are established on, the static bases defined by equations (2.139) to (2.141) and the dynamic bases defined in Section 2.4 satisfy locally the same domain equations (compatibility and elasticity), and fail to satisfy the dynamic equilibrium equation.

This observation justifies the strategy of enforcing the same domain and boundary equations on both parts of the trial basis in order to determine their weights. No algorithmic distinction is thus made between the dynamic and static trial functions. They are integrated in the same domain basis and left to combine in the best possible way in order to satisfy the domain and boundary conditions that are enforced on them.

The finite element equations derived in Section 2.4 are rewritten next, to explicitly account for the presence of both parts of the domain basis.

The enforcement of the equilibrium equation (2.81) using the functions collected in bases $\boldsymbol{U}_d, \boldsymbol{U}_s$ and $\boldsymbol{U}_r$ for weighting (see Section 2.4.1) causes the domain statement (2.100) to assume the following form,

$$\boldsymbol{D}_{jd}\boldsymbol{X}_d + \boldsymbol{D}_{js}\boldsymbol{X}_s + \boldsymbol{D}_{jr}\boldsymbol{X}_r - \boldsymbol{B}_j\boldsymbol{P} = \boldsymbol{t}^u_{\Gamma_j} - \boldsymbol{t}^u_{0_j} \tag{2.147}$$

where $j = \{d,\ s,\ r\}$ and:

$$\boldsymbol{D}_{dd} = \int \boldsymbol{U}^*_d(\boldsymbol{N}\boldsymbol{S}_d)d\Gamma^e \tag{2.148}$$

$$\boldsymbol{D}_{js} = \int \boldsymbol{U}^*_j(\boldsymbol{N}\boldsymbol{S}_s)d\Gamma^e - \omega^2 \int \boldsymbol{U}^*_j\boldsymbol{\rho}\boldsymbol{U}_s dV^e \tag{2.149}$$

$$\boldsymbol{D}_{jr} = -\omega^2 \int \boldsymbol{U}^*_j\boldsymbol{\rho}\boldsymbol{U}_r dV^e \tag{2.150}$$

$$\boldsymbol{B}_j = \int \boldsymbol{U}^*_j\boldsymbol{Z}d\bar{\Gamma}^e_u \tag{2.151}$$

$$\boldsymbol{t}^u_{\Gamma_j} = \int \boldsymbol{U}^*_j\,\boldsymbol{t}_\Gamma d\Gamma^e_\sigma \tag{2.152}$$

$$\boldsymbol{t}^u_{0_j} = \int \boldsymbol{U}^*_j\,\boldsymbol{F}^0 dV^e \tag{2.153}$$

If ω^2 is real and the material stiffness ($\boldsymbol{k}$) and generalized mass ($\boldsymbol{\rho}$) matrices are Hermitian, matrices $\boldsymbol{D}_{ds}$ and $\boldsymbol{D}_{dr}$ are the transpose conjugates of matrices $\boldsymbol{D}_{sd}$ and $\boldsymbol{D}_{rd}$, and thus assume boundary integral expressions,.

The generalized frequency is real when direct time-integration methods are used. Conversely, the weighted-residual method suggested by Freitas [54] generally leads to complex values of the algorithmic frequencies. The generalized mass matrix $\boldsymbol{\rho}$ is Hermitian when the velocity-induced terms are absent from the governing equation (2.53). The material stiffness matrix $\boldsymbol{k}$ is Hermitian in all practical linear applications known to the author.

If the conditions stated above are not observed, the volume integrals present in expression (2.149) and (2.150) do not have, in general, analytic expression and may be difficult to compute numerically because of the oscillatory nature of the dynamic trial functions collected in basis $\boldsymbol{U}_d$.

The boundary equation (2.111) takes the form,

$$-\sum_j\left(\boldsymbol{B}_j^*\boldsymbol{X}_j\right)=-\boldsymbol{u}_\Gamma^u \tag{2.154}$$

where $\boldsymbol{u}_\Gamma^u$ is defined by equation (2.112).

Under these definitions, the hybrid-Trefftz displacement element solving system collects the domain and boundary statements (2.147) and (2.154), to yield,

$$\begin{bmatrix}\boldsymbol{D}_{dd} & \boldsymbol{D}_{ds} & \boldsymbol{D}_{dr} & -\boldsymbol{B}_d\\ \boldsymbol{D}_{sd} & \boldsymbol{D}_{ss} & \boldsymbol{D}_{sr} & -\boldsymbol{B}_s\\ \boldsymbol{D}_{rd} & \boldsymbol{D}_{rs} & \boldsymbol{D}_{rr} & -\boldsymbol{B}_r\\ -\boldsymbol{B}_d^* & -\boldsymbol{B}_s^* & -\boldsymbol{B}_r^* & \boldsymbol{0}\end{bmatrix}\begin{bmatrix}\boldsymbol{X}_d\\ \boldsymbol{X}_s\\ \boldsymbol{X}_r\\ \boldsymbol{P}\end{bmatrix}=\begin{bmatrix}\boldsymbol{t}_{\Gamma_d}^u-\boldsymbol{t}_{0_d}^u\\ \boldsymbol{t}_{\Gamma_s}^u-\boldsymbol{t}_{0_s}^u\\ \boldsymbol{t}_{\Gamma_r}^u-\boldsymbol{t}_{0_r}^u\\ -\boldsymbol{u}_\Gamma^u\end{bmatrix} \tag{2.155}$$

System (2.155) shares the same algebraic properties as system (2.116) of the hybrid-Trefftz displacement element. Consequently, the addition of new trial functions to the finite element bases does not require all solving system coefficients to be calculated a new. Instead, only the lines and columns corresponding to the new additions to the bases need to be determined.

The solution of system (2.155) yields unique estimates for all domain fields. They are recovered using expressions (2.94), (2.95) and (2.96), with the particular solution terms given by expressions (2.139) to (2.141). It should, however, be noted that, besides the compatible estimate,

$$\boldsymbol{u}=\boldsymbol{U}_d\boldsymbol{X}_d+\boldsymbol{U}_s\boldsymbol{X}_s+\boldsymbol{U}_r\boldsymbol{X}_r \tag{2.156}$$

an equilibrated solution can be obtained, in the post-processing phase, using definition (2.146) for the particular solution,

$$\boldsymbol{u} = \boldsymbol{U}_d \boldsymbol{X}_d + \omega^{-2} \boldsymbol{\rho}^{-1} \boldsymbol{F}^0 \tag{2.157}$$

As both estimates should be equal upon convergence, their comparison provides a useful error measure at marginal computational cost.

Independent estimates are obtained for the traction fields on the Dirichlet and interior boundaries of the elements either by projecting on the boundary the domain stress field given by equation (2.96), or by using the boundary approximation (2.97). The difference between the boundary traction solutions can also be used as an error measure.

❖ **Stress model**

Following the procedure adopted in Section 2.4.2, the weak enforcement of the compatibility equation (2.82) using the functions collected in bases $\boldsymbol{S}_d$ and $\boldsymbol{S}_s$ for weighting, yields the following domain equations:

$$\boldsymbol{\mathcal{F}}_{jd} \boldsymbol{Y}_d + \boldsymbol{\mathcal{F}}_{js} \boldsymbol{Y}_s - \boldsymbol{A}_j \boldsymbol{Q} = \boldsymbol{u}_{\Gamma_j}^{\sigma} - \boldsymbol{u}_{0_j}^{\sigma} \tag{2.158}$$

where $j = \{d,\ s\}$ and,

$$\boldsymbol{\mathcal{F}}_{jd} = \int \left(\boldsymbol{N}\boldsymbol{S}_j\right)^* \boldsymbol{U}_d d\Gamma^e \tag{2.159}$$

$$\boldsymbol{\mathcal{F}}_{ss} = \int (\boldsymbol{N}\boldsymbol{S}_s)^* \boldsymbol{U}_s d\Gamma^e \tag{2.160}$$

$$\boldsymbol{\mathcal{F}}_{ds} = \int (\boldsymbol{N}\boldsymbol{S}_d)^* \boldsymbol{U}_s d\Gamma^e - \int (\boldsymbol{\mathcal{D}}\boldsymbol{S}_d)^* \boldsymbol{U}_s \, dV^e \tag{2.161}$$

$$\boldsymbol{A}_j = \int \left(\boldsymbol{N}\boldsymbol{S}_j\right)^* \boldsymbol{Z} d\bar{\Gamma}_{\sigma}^e \tag{2.162}$$

$$\boldsymbol{u}_{\Gamma_j}^{\sigma} = \int \left(\boldsymbol{N}\boldsymbol{S}_j\right)^* \boldsymbol{u}_{\Gamma} d\Gamma_u^e \tag{2.163}$$

$$\boldsymbol{u}_{0_d}^{\sigma} = \int (\boldsymbol{\mathcal{D}}\boldsymbol{S}_d)^* \, \bar{\boldsymbol{u}}_0 dV^e \tag{2.164}$$

$$\boldsymbol{u}_{0_s}^{\sigma} = \boldsymbol{0} \tag{2.165}$$

If the material flexibility matrix $\boldsymbol{f}$ is Hermitian, which is the case in virtually all linear applications, matrix $\boldsymbol{\mathcal{F}}_{\mathrm{ds}}$ can be reduced to a boundary integral expression and matrices $\boldsymbol{\mathcal{F}}_{\mathrm{ds}}$ and $\boldsymbol{\mathcal{F}}_{\mathrm{sd}}$ are conjugate transpose of each other. Conversely, matrix $\boldsymbol{\mathcal{F}}_{\mathrm{ds}}$ cannot be reduced to a boundary integral if the flexibility matrix $\boldsymbol{f}$ is non Hermitian.

Substitution of definition (2.141) into the boundary statement (2.133) yields,

$$-\sum_j \left(\boldsymbol{A}_j^* \boldsymbol{Y}_j\right) = -\boldsymbol{t}_\Gamma^\sigma \tag{2.166}$$

where $\boldsymbol{t}_\Gamma^\sigma$ is given by expression (2.134).

The solving system of the stress model is obtained combining the domain and boundary statements (2.158) and (2.166),

$$\begin{bmatrix} \boldsymbol{\mathcal{F}}_{dd} & \boldsymbol{\mathcal{F}}_{ds} & -\boldsymbol{A}_d \\ \boldsymbol{\mathcal{F}}_{sd} & \boldsymbol{\mathcal{F}}_{ss} & -\boldsymbol{A}_s \\ -\boldsymbol{A}_d^* & -\boldsymbol{A}_s^* & \boldsymbol{0} \end{bmatrix} \begin{bmatrix} \boldsymbol{Y}_d \\ \boldsymbol{Y}_s \\ \boldsymbol{Q} \end{bmatrix} = \begin{bmatrix} \boldsymbol{u}_{\Gamma_d}^\sigma - \boldsymbol{u}_{0_d}^\sigma \\ \boldsymbol{u}_{\Gamma_s}^\sigma \\ -\boldsymbol{t}_\Gamma^\sigma \end{bmatrix} \tag{2.167}$$

System (2.167) shares the algebraic properties of the system (2.155) of the displacement element. However, unlike the displacement element, all terms present in the matrix of coefficients are defined by boundary integrals when the local flexibility matrix $\boldsymbol{f}$ is Hermitian.

Equilibrated and compatible domain displacement solutions can be obtained, in the post-processing phase, using expressions (2.157).

Also, two independent estimates can be recovered for the displacement fields on the Neumann and interior boundaries of the stress element, by either projecting the domain displacement field on the boundary or using the independent approximation (2.120).

Chapter 3

Hybrid-Trefftz elements for biphasic media

Chapter 3 addresses the modelling of the static (steady-state) and dynamic response of biphasic media and is based on the contributions and results reported in [49, 109, 111, 112, 117]. The alternative stress and displacement models of the hybrid-Trefftz finite element formulation are formulated for the static and dynamic problems and their performance is assessed through a comprehensive set of numerical tests.

The central objective of Section 3.1 is to present the formulation and implementation of the hybrid-Trefftz displacement (HTD) and stress (HTS) models for static poroelasticity problems defined on biphasic media (e.g. water-saturated soils). The models are obtained from the corresponding hybrid models by restricting the domain trial functions to a solution subset of the governing Navier equation. This reduces the problem to the boundaries of the elements, a trademark feature of both Trefftz and boundary element methods, with the added advantage that the solving system results sparse and Hermitian, as typical of hybrid finite elements.

The performance assessment of the HTD and HTS models for the analysis of static biphasic problems is presented in Section 3.2. The numerical tests are designed to investigate the effects of both p- and h-refinement on the convergence of the finite element predictions to known analytic solutions, and to assess the stability of the elements when confronted with issues that typically hinder the application of conventional finite elements, such as near-incompressibility of the medium and gross mesh distortion. The results of a more complex simulation are also presented and compared with those obtained using commercial finite element software ABAQUS^{TM} [4].

The second part of Chapter 3 extends the study summarized above to the analysis of the dynamic response of biphasic media. Section 3.3 opens with a detailed description of the elastodynamic problems for saturated porous media, stated in a general form in Chapter 2. After deriving the governing Navier equation, the Helmholtz decomposition is applied to define domain approximation functions satisfying all field equations. They are used to set up the approximation bases of the alternative HTD and HTS finite element models. The influence of

non-null initial conditions is modelled using the free-field solutions of the associated static problem.

The dynamic response of biphasic media is modelled for both periodic and non-periodic excitations in Section 3.4. The technique of time discretization for periodic problems described in Section 2.3.1 is used to test for a complex problem with harmonic load. This problem is solved using both HTD and HTS models for a wide range of frequencies, in order to evaluate the recovery and stability of the solutions in terms of inter-element continuity and the enforced boundary conditions.

Section 3.4 also includes a comprehensive set of tests on non-periodic (consolidation) problems, which are designed to investigate convergence increasing the degree of the approximation in time (p-refinement) and subdividing the period of the analysis (h-refinement through multi-stepping). The performance of the HTD and HTS models are assessed using the coupled approach for implementing the particular solution presented in Section 2.5. The results are compared with those obtained using commercial finite element software ABAQUS^{TM} [4].

3.1 Formulation of static problems

The mathematical model presented in Sections 2.1 is specialized here to simulate the static (steady-state) response of biphasic media. After establishing the notation, the Trefftz approximation basis is defined and used to define the solving systems for the displacement and stress models of the hybrid-Trefftz finite element formulation. Particular attention is given to avoiding spurious modes caused by over-constraining the pore pressure fields. Also, a post-processing algorithm for the recovery of the rigid-body components of the displacement field is devised for the stress element.

3.1.1 Mathematical model

The mathematical model considered for the analysis is the solid displacement-fluid seepage ($u-w$) variant of the Biot theory of porous media [80], assuming an elastic solid phase fully permeated by a liquid phase with a flow governed by Darcy's law. Both phases are considered compressible. The schematic representation given in Figure 2.1 for the domain, V, and the

decomposition of the boundary, Γ,defined in Section 2.1 can still be used removing the non-wetting fluid (air) phase.

Equations (2.2), (2.3) and (2.11) can be used to model the response of the body under static conditions, where the independent components of the (total) stress and strain tensors in the solid phase and the pore fluid pressure (π) and fluid content (ζ) are organized in two vectors, $\boldsymbol{\sigma}(x,y) = \{\sigma_{xx} \quad \sigma_{yy} \quad \sigma_{xy} \quad \pi\}^T$ and $\boldsymbol{\varepsilon}(x,y) = \{\varepsilon_{xx} \quad \varepsilon_{yy} \quad 2\varepsilon_{xy} \quad \zeta\}^T$, respectively. Vector $\boldsymbol{u}(x,y) = \{u_x \quad u_y \quad w_x \quad w_y\}^T$ collects the solid skeleton displacement and the fluid seepage is expressed as $\boldsymbol{w}(x,y) = \{w_x \quad w_y\}^T = n^w(\boldsymbol{u}^w - \boldsymbol{u}^s)$, where n^w is the volume fraction and $\boldsymbol{u}^w(x,y) = \{u_x^w \quad u_y^w\}^T$ the absolute displacement vector in the fluid phase. The mass densities of the mixture and of the liquid phase are denoted by ρ and ρ_w, respectively.

Vectors $\boldsymbol{t}_\Gamma(x,y) = \{t_{\Gamma x} \quad t_{\Gamma y} \quad \pi_\Gamma\}^T$ and $\boldsymbol{u}_\Gamma(x,y) = \{u_{\Gamma x} \quad u_{\Gamma y} \quad w_{\Gamma_n}\}^T$, presented in boundary equilibrium (2.5) and compatibility (2.6) equations, collect the components of the applied tractions (applied pore pressure, for the fluid phase) and of the imposed displacements (imposed normal seepage), respectively.

Neglecting the body force b, the Navier equation (2.12) simplifies to,

$$\boldsymbol{\mathcal{D}k\mathcal{D}}^*\boldsymbol{u} = \boldsymbol{0} \quad \text{in } V \tag{3.1}$$

Using the definitions given in Appendix D and letting $\boldsymbol{\nabla}$ and $\boldsymbol{\nabla}^T$ define the gradient and divergence operators and $\boldsymbol{\nabla}^2$ the Laplacian, the above equation yields a system of two differential equations on the solid phase displacements $\boldsymbol{u}$ and the fluid seepage $\boldsymbol{w}$:

$$\begin{cases} \boldsymbol{\nabla}[(k_{12}+k_{33})\boldsymbol{\nabla}^T\boldsymbol{u} + k_{14}\boldsymbol{\nabla}^T\boldsymbol{w}] + k_{33}\boldsymbol{\nabla}^2\boldsymbol{u} = \boldsymbol{0} \\ \boldsymbol{\nabla}[k_{14}\boldsymbol{\nabla}^T\boldsymbol{u} + k_{44}\boldsymbol{\nabla}^T\boldsymbol{w}] = \boldsymbol{0} \end{cases} \tag{3.2}$$

The solution of the homogeneous system (3.2) can be obtained defining biharmonic and harmonic displacement potentials, which generate coupled and uncoupled displacement modes used below to setup approximation bases $\boldsymbol{U}_b$ and $\boldsymbol{U}_h$. The corresponding stress modes $\boldsymbol{S}_b$ and $\boldsymbol{S}_h$, are pressure-free. One constant pore pressure mode is found and the solution is included in bases $\boldsymbol{S}_\pi$ and $\boldsymbol{U}_\pi$. The rigid-body displacements and free flow modes that solve system (3.2) define bases $\boldsymbol{U}_r$ and $\boldsymbol{U}_f$. Their corresponding stress and pore pressure fields are null. It is noted that singular solutions of system (3.2) can also be found. They can be used to

enrich the regular basis when problems with expected singularities are modelled, e.g. stress concentration problems, like those involving wedges, notches and cracks [118].

3.1.2 Trefftz approximation functions

The solution sets mentioned above, namely biharmonic and harmonic solutions and the constant pore pressure and null-stress modes are defined next.

❖ **Biharmonic solutions**

When biharmonic displacement potentials are used to construct the solution set $\boldsymbol{U}_b$ of the Navier equation (3.1), they generate one single constant stress mode, plus a family of complex conjugate stress modes of higher degree. In the meantime, $\boldsymbol{U}_b$ and $\boldsymbol{S}_b$ collect the radial and tangential components of the respective fields.

The linear displacement mode and the associated constant stress field are:

$$\boldsymbol{U}_{b_0} = \begin{bmatrix} 1 \\ 0 \\ -\alpha \\ 0 \end{bmatrix} r \tag{3.3}$$

$$\boldsymbol{S}_{b_0} = \begin{bmatrix} 2(\lambda+\mu) \\ 2(\lambda+\mu) \\ 0 \\ 0 \end{bmatrix} \tag{3.4}$$

The higher-degree displacement and stress modes have the following expressions, for degrees $n \geq 1$:

$$\boldsymbol{U}_{b_n} = \frac{1}{2(n+1)\mu} \begin{bmatrix} [(\lambda+3\mu)-(n+1)(\lambda+\mu)] \\ \pm\hat{\imath}\,[(\lambda+3\mu)+(n+1)(\lambda+\mu)] \\ -2\alpha\mu \\ \pm 2\alpha\mu\,\hat{\imath} \end{bmatrix} r^{n+1}\, exp[\pm\hat{\imath}\, n\theta] \tag{3.5}$$

$$\boldsymbol{S}_{b_n} = \begin{bmatrix} -(n-2)(\lambda+\mu) \\ (n+2)(\lambda+\mu) \\ \pm\hat{\imath}\, n(\lambda+\mu) \\ 0 \end{bmatrix} r^n\, exp[\pm\hat{\imath}\, n\theta] \tag{3.6}$$

❖ **Harmonic solutions**

Harmonic displacement potentials generate deviatoric modes with frozen medium (null seepage) behaviour. For degrees $n \geq 0$, pairs of complex conjugate solutions of the Navier equation (3.1) are obtained and collected in the basis $\boldsymbol{U}_h$:

$$\boldsymbol{U}_h = \frac{1}{2(n+1)\mu}\begin{bmatrix} 1 \\ \pm\hat{\imath} \\ 0 \\ 0 \end{bmatrix} r^{n+1}\, exp[\pm\hat{\imath}\,(n+2)\theta] \tag{3.7}$$

The corresponding stress field $\boldsymbol{S}_h$ is:

$$\boldsymbol{S}_h = \begin{bmatrix} 1 \\ -1 \\ \pm\hat{\imath} \\ 0 \end{bmatrix} r^{n}\, exp[\pm\hat{\imath}\,(n+2)\theta] \tag{3.8}$$

❖ **Constant pore pressure solution**

If a constant pore pressure is applied to the fluid phase, it generates a hydrostatic state of stress $\boldsymbol{S}_w$ and a radial seepage field $\boldsymbol{U}_w$:

$$\boldsymbol{U}_w = \begin{bmatrix} 0 \\ 0 \\ \frac{1}{2Q} \\ 0 \end{bmatrix} r \tag{3.9}$$

$$\boldsymbol{S}_w = \begin{bmatrix} \alpha \\ \alpha \\ 0 \\ 1 \end{bmatrix} \tag{3.10}$$

❖ **Null stress solutions**

Besides the stress generating modes described above, the following rigid-body displacement modes defined on the solid phase also satisfy the Navier equation (3.1):

$$\boldsymbol{U}_{rs} = \begin{bmatrix} 0 & cos\,\theta & sin\,\theta \\ r & -sin\,\theta & cos\,\theta \\ 0 & 0 & 0 \\ 0 & 0 & 0 \end{bmatrix} \tag{3.11}$$

In the fluid phase, five linear free flow modes are identified,

$$\boldsymbol{U}_{rf} = \begin{bmatrix} 0 & 0 & 0 & 0 & 0 \\ 0 & 0 & 0 & 0 & 0 \\ cos\,\theta & sin\,\theta & 0 & r\,sin\,2\theta & r\,cos\,2\theta \\ -sin\,\theta & cos\,\theta & r & r\,cos\,2\theta & -r\,sin\,2\theta \end{bmatrix} \tag{3.12}$$

along with $n+2$ free flow modes of degree $n \geq 2$, with $0 \leq k \leq n-1$:

$$\boldsymbol{U}_f = \begin{bmatrix} 0 & 0 & 0 \\ 0 & 0 & 0 \\ sin^n\theta\,cos\,\theta & sin\,\theta\,cos^n\theta & (k + cos^2\theta - n\,sin^2\theta)\,sin^k\theta\,cos^{n-k-1}\theta \\ -sin^{n+1}\theta & -cos^{n+1}\theta & -(1+n)\,sin^{k+1}\theta\,cos^{n-k}\theta \end{bmatrix} r^n \tag{3.13}$$

3.1.3 Trefftz approximation bases

The Trefftz bases are constructed combining the solutions defined above, to yield the following expressions for the hybrid-Trefftz approximations (2.13) and (2.34),

$$\boldsymbol{u} = \boldsymbol{U}_s\boldsymbol{X}_s + \boldsymbol{U}_w X_w + \boldsymbol{U}_{rs}\boldsymbol{X}_{rs} + \boldsymbol{U}_{rw}\boldsymbol{X}_{rw} + \boldsymbol{u}_0 \tag{3.14}$$

$$\boldsymbol{\sigma} = \boldsymbol{S}_s\boldsymbol{Y}_s + \boldsymbol{S}_w Y_w + \boldsymbol{\sigma}_0 \tag{3.15}$$

The rigid-body and pure flow modes are absent in the stress approximation (3.15) because they produce neither stress nor pore pressure fields. In the expressions above, $\boldsymbol{U}_w$, $\boldsymbol{S}_w$ and $\boldsymbol{U}_{rs}$ are given by definitions (3.9), (3.10) and (3.11) and the remaining terms are grouped as follows:

$$\boldsymbol{U}_s = (\boldsymbol{U}_{b_0} \quad \boldsymbol{U}_{b_n} \quad \boldsymbol{U}_h) \tag{3.16}$$

$$\boldsymbol{S}_s = (\boldsymbol{S}_{b_0} \quad \boldsymbol{S}_{b_n} \quad \boldsymbol{S}_h) \tag{3.17}$$

$$\boldsymbol{U}_{rw} = (\boldsymbol{U}_{rf} \quad \boldsymbol{U}_f) \tag{3.18}$$

The stress and displacement bases defined above satisfy the equilibrium, compatibility and elasticity conditions (2.2), (2.3) and (2.11) and, consequently, the Trefftz constraints listed in Table 1. In general, the bases are implemented at element level and expressed in a local (polar) system of reference with origin at the barycenter of the element and axes parallel to the principal directions of the element. It is stressed that this form of implementation of Trefftz bases is used in all tests presented in this chapter.

The dimension of basis $\boldsymbol{S}_s$ with degree d_σ is, according to equations (3.3) to (3.8),

$$N_\sigma = 4d_\sigma + 3 \tag{3.19}$$

while equations (3.12) and (3.13) set the dimension of the seepage basis $\boldsymbol{U}_{rw}$ with degree d_f to:

$$N_f = \frac{1}{2}\left(d_f + 1\right)\left(d_f + 4\right) \tag{3.20}$$

3.1.4 Solving system for the displacement element

Apart from the domain approximation (3.14), independent approximations of the generalized tractions are assumed on the extended Dirichlet boundary of the displacement element:

$$\boldsymbol{t} = \boldsymbol{Z}_s \boldsymbol{P}_s + \boldsymbol{Z}_w \boldsymbol{P}_w \tag{3.21}$$

The hierarchical bases $\boldsymbol{Z}_s$ and $\boldsymbol{Z}_w$ define independent approximations of the boundary normal and tangential components of the traction in the solid phase and of the pore pressure, respectively.

The explicit form of the solving system (2.33) for the hybrid-Trefftz displacement (HTD) element is,

$$\left[\begin{array}{cccc|cc} \boldsymbol{K}_{ss} & \bullet & \bullet & \bullet & -\boldsymbol{B}_{ss} & \bullet \\ \bullet & K_{ww} & \bullet & \bullet & \bullet & -\boldsymbol{B}_{ww} \\ \bullet & \bullet & \bullet & \bullet & -\boldsymbol{B}_{rs} & \bullet \\ \bullet & \bullet & \bullet & \bullet & \bullet & -\boldsymbol{B}_{rw} \\ \hline -\boldsymbol{B}^*_{ss} & \bullet & -\boldsymbol{B}^*_{rs} & \bullet & \bullet & \bullet \\ \bullet & -\boldsymbol{B}^*_{ww} & \bullet & -\boldsymbol{B}^*_{rw} & \bullet & \bullet \end{array}\right] \cdot \left[\begin{array}{c} \boldsymbol{X}_s \\ X_w \\ \boldsymbol{X}_{rs} \\ \boldsymbol{X}_{rw} \\ \hline \boldsymbol{P}_s \\ \boldsymbol{P}_w \end{array}\right] = \left[\begin{array}{c} \boldsymbol{t}^u_{\Gamma_s} - \boldsymbol{t}^u_{0_s} \\ t^u_{\Gamma_w} - t^u_{0_w} \\ \boldsymbol{t}^u_{\Gamma_{rs}} - \boldsymbol{t}^u_{0_{rs}} \\ \boldsymbol{t}^u_{\Gamma_{rw}} - \boldsymbol{t}^u_{0_{rw}} \\ \hline \boldsymbol{u}^u_{0_s} - \boldsymbol{u}^u_{\Gamma_s} \\ \boldsymbol{u}^u_{0_w} - \boldsymbol{u}^u_{\Gamma_w} \end{array}\right] \tag{3.22}$$

where the following definitions apply, with $j = \{s, w\}$ identifying the solid and fluid phases:

$$\boldsymbol{K}_{jj} = \int \boldsymbol{U}^*_j (\boldsymbol{N}\boldsymbol{S}_j) d\Gamma^e \tag{3.23}$$

$$\boldsymbol{B}_{jj} = \int \boldsymbol{U}^*_j \boldsymbol{Z}_j d\bar{\Gamma}^e_u \tag{3.24}$$

$$\boldsymbol{B}_{rj} = \int \boldsymbol{U}^*_{rj} \boldsymbol{Z}_j d\bar{\Gamma}^e_u \tag{3.25}$$

$$\boldsymbol{t}^u_{\Gamma_{(r)j}} = \int \boldsymbol{U}^*_{(r)j} \boldsymbol{t}_\Gamma d\Gamma^e_\sigma \tag{3.26}$$

$$\boldsymbol{t}^u_{0_{(r)j}} = \int \boldsymbol{U}^*_{(r)j} (\boldsymbol{N}\boldsymbol{\sigma}_0) d\Gamma^e \tag{3.27}$$

$$\boldsymbol{u}^u_{\Gamma_j} = \int \boldsymbol{Z}^*_j \boldsymbol{u}_\Gamma d\Gamma^e_u \tag{3.28}$$

$$\boldsymbol{u}_{0_j}^{u} = \int \boldsymbol{Z}_j^{*} \boldsymbol{u}_0 d\Gamma_u^e \tag{3.29}$$

In the domain of the element, system (3.22) yields unique estimates for the displacement and seepage fields, which are computed using definition (3.14), and for the stress and pore pressure fields, computed from equation (3.15) (unknowns $\boldsymbol{Y}_j$ are substituted by $\boldsymbol{X}_j$).

Estimates for the two components of the tractions in the solid phase and for the normal component of tractions in the fluid phase are not unique, however, as the same fields can be alternatively computed from the domain stress field using equations (3.15) and from the boundary approximation (3.21). The difference can be used to assess the solution error, as the two approximations should produce the same results upon full convergence.

3.1.5 Solving system for the stress element

The generalized displacements on the extended Neumann boundary of the hybrid-Trefftz stress element are approximated as follows:

$$\boldsymbol{u} = \boldsymbol{Z}_s \boldsymbol{Q}_s + \boldsymbol{Z}_w Q_w \tag{3.30}$$

Basis $\boldsymbol{Z}_s$ collects functions associated to the approximation of the components of solid phase displacements normal and tangential to the boundary. This basis is hierarchical, independent from the domain displacement approximation (3.14) and only constrained to completeness and linear independence. Basis $\boldsymbol{Z}_w = (0 \quad 0 \quad 1)^T$ is used to approximate the fluid seepage in the boundary normal direction. It is assumed to be constant in order to avoid dependencies in the solving system, as explained in Section 3.1.7.

The explicit form of solving system (2.51) for the HTS element is,

$$\left[\begin{array}{cc:c:c} \mathcal{F}_{ss} & \bullet & -\boldsymbol{A}_{ss} & \circ \\ \bullet & \mathcal{F}_{ww} & -\boldsymbol{A}_{ws} & -A_{ww} \\ \hline -\boldsymbol{A}_{ss}^{*} & -\boldsymbol{A}_{ws}^{*} & \bullet & \circ \\ \hdashline \circ & -A_{ww}^{*} & \circ & \circ \end{array}\right] \cdot \left[\begin{array}{c} \boldsymbol{Y}_s \\ Y_w \\ \hline \boldsymbol{Q}_s \\ \hdashline Q_w \end{array}\right] = \left[\begin{array}{c} \boldsymbol{u}_{\Gamma_s}^{\sigma} - \boldsymbol{u}_{0_s}^{\sigma} \\ u_{\Gamma_w}^{\sigma} - u_{0_w}^{\sigma} \\ \hline \boldsymbol{t}_{0_s}^{\sigma} - \boldsymbol{t}_{\Gamma_s}^{\sigma} \\ \hdashline t_{0_w}^{\sigma} - t_{\Gamma_w}^{\sigma} \end{array}\right] \tag{3.31}$$

where the following definitions apply, with $i, j = \{s, w\}$:

$$\boldsymbol{\mathcal{F}}_{jj} = \int (\boldsymbol{N}\boldsymbol{S}_j)\boldsymbol{U}_j d\Gamma^e \tag{3.32}$$

$$\boldsymbol{A}_{ij} = \int (\boldsymbol{N}\boldsymbol{S}_i)^* \boldsymbol{Z}_j d\bar{\Gamma}_\sigma^e \tag{3.33}$$

$$\boldsymbol{u}_{\Gamma_j}^\sigma = \int \left(\boldsymbol{N}\boldsymbol{S}_j\right)^* \boldsymbol{u}_\Gamma d\Gamma_u^e \tag{3.34}$$

$$\boldsymbol{u}_{0_j}^\sigma = \int \left(\boldsymbol{N}\boldsymbol{S}_j\right)^* \boldsymbol{u}_0 d\Gamma^e \tag{3.35}$$

$$\boldsymbol{t}_{\Gamma_j}^\sigma = \int \boldsymbol{Z}_j{}^* \boldsymbol{t}_\Gamma \, d\Gamma_\sigma^e \tag{3.36}$$

$$\boldsymbol{t}_{0_j}^\sigma = \int \boldsymbol{Z}_j{}^* (\boldsymbol{N}\boldsymbol{\sigma}_0) d\Gamma_\sigma^e \tag{3.37}$$

In the domain of the element, system (3.31) yields unique estimates for the stress and pore pressure fields, which are computed using definition (3.15). However, the displacement and seepage fields are not uniquely defined, as the rigid-body modes (3.14) are stress-free and consequently absent from the stress model approximation (3.15). They can be recovered in the post-processing phase, as shown in Section 3.1.8.

On the extended Neumann boundary of the element, the normal and tangential components of the solid phase displacement and the normal component of the fluid seepage can be calculated using boundary approximation (3.30) or, alternatively, the domain displacement approximation (3.14). The two independent estimates should yield the same results upon full convergence.

3.1.6 Indeterminacy numbers of the HTD model

The solving system (3.22) may contain linearly-dependent equations. Their presence and number depend on the mesh, the boundary conditions and the relative dimensions of the domain and boundary bases. These dependencies can be handled using appropriate solvers, generally with satisfactory results. However, it is best to identify their causes and ensure that the solving systems are free from spurious modes [119].

In the context of elastostatic applications, a sufficient condition to ensure that the relative dimension of the bases do not induce spurious modes is to require that the displacement element is kinematically indeterminate, under the assumption that all equations are linearly independent. However, spurious modes in systems (3.22) may remain active even when this condition is respected. The cause of this phenomenon can be traced back to a physical feature of the poroelastostatic problem, namely the fact that the pore pressure can only be constant. This may cause system (3.22) to become over-determinate, thus causing spurious modes.

This problem can be solved in different ways. The option followed here is designed to preserve generality in terms of numerical implementation, in the sense that poroelastostatic hybrid-Trefftz elements can be programmed with the same logic independently of the model, stress or displacement, and of the boundary conditions, with or without prescribed boundary pressure fields.

Assume that system (3.22) is written for a single-element mesh, meaning that the inter-element boundary variables and the associated inter-element compatibility conditions are absent. According to equations (3.14), (3.19) and (3.20), the dimension of the domain basis is,

$$N_x = N_\sigma + N_f + 4 \tag{3.38}$$

Assuming that polynomial functions are used for the boundary approximation, the dimension of the boundary basis (3.21) is defined as follows,

$$N_p = N_{ps} + N_{pw} \tag{3.39}$$

$$N_{ps} = 2s\left(1+d_{ps}\right) \tag{3.40}$$

$$N_{pw} = s\left(1+d_{pw}\right) \tag{3.41}$$

where N_{ps} and N_{pw} are the dimensions of the traction and pore pressure bases $\boldsymbol{Z}_s$ and $\boldsymbol{Z}_w$, with degrees d_{ps} and d_{pw}, and s is the number of sides that form the Dirichlet boundary of the element. For the sake of simplicity, and without limiting the scope of the presentation, expressions (3.40) and (3.41) are obtained under the assumption that the same degree of approximation is used on all sides of the element.

The first two sets of equilibrium equations in system (3.22) show that the stress inducing modes are always statically indeterminate, with indeterminacy numbers:

$$\alpha_s = N_{ps} > 0 \tag{3.42}$$

$$\alpha_w = N_{pw} > 0 \tag{3.43}$$

It is important to clarify the role of the third and fourth sets of equilibrium conditions in system (3.22). As the stress and pressure fields are self-equilibrated, their role is to ensure that the approximations used for the boundary forces and the pore pressure are not arbitrary: their resultants must satisfy the global equilibrium conditions.

The three equations forming the third set of equilibrium equations in system (3.22) are always linearly independent and have the following static indeterminacy number,

$$\alpha_{rs} = N_{ps} - 3 \tag{3.44}$$

which is non-negative regardless of the degree d_{ps} of the boundary basis $\boldsymbol{Z}_s$ if the number of Dirichlet sides (s) of the element is larger than one. If $s = 1$, d_{ps} must be larger than zero for the set to be statically indeterminate. This is obviously a weak restriction, as the dimension of basis $\boldsymbol{Z}_s$ is mainly conditioned by the necessity of adequately enforcing the compatibility equation on the Dirichlet boundary of the element, i.e. the fifth set of equations in system (3.22).

On the other hand, to ensure a non-negative static indeterminacy number for the fourth set of equations in system (3.22), the following condition must be met,

$$\alpha_{rw} = N_{pw} - N_f \geq 0 \tag{3.45}$$

setting a rather strong restriction on the degree d_{pw} of the boundary basis $\boldsymbol{Z}_{\boldsymbol{w}}$, which must, in general, be larger than the degree d_f of the basis used for the free fluid flow:

$$d_{pw} \geq d_f \tag{3.46}$$

This reasoning can be dualized to state the kinematic admissibility conditions of the last two sets of equations in system (3.22).

The kinematic indeterminacy of the first set of compatibility equations, that is, the fifth set in system (3.22), implies that,

$$\beta_{ps} = N_\sigma + 3 - N_{ps} \geq 0 \tag{3.47}$$

which essentially ensures that the degree of the boundary approximation does not exceed the degree of the strain inducing domain modes:

$$d_\sigma \geq d_{ps} \tag{3.48}$$

The kinematic indeterminacy condition on the second set of compatibility equations is:

$$N_f + 1 - N_{pw} \geq 0 \tag{3.49}$$

Combined with equation (3.45), condition (3.49) eventually yields:

$$N_f \leq N_{pw} \leq N_f + 1 \tag{3.50}$$

Equation (3.50) is a strong restriction on the choice of the degree d_{pw} of the boundary basis $\boldsymbol{Z}_w$ and, depending on the number of Dirichlet sides and the degree d_f of the free flow basis $\boldsymbol{U}_{rw}$, may indeed be impossible to satisfy (e.g. when $d_f = 1$ and $s = 4$).

If more than one element is used to construct the mesh, the restriction can be removed (without loss of generality) redefining the support of the free fluid flow approximation $\boldsymbol{U}_{rw}$ as the whole domain in analysis rather than the domain of every element. The governing system preserves its form (3.22) and its algebraic properties, with the difference that the fourth equilibrium equation is now written on the exterior boundary of the domain, to yield,

$$-\sum_{j=1}^{N_{\Gamma_u}} \left(\boldsymbol{B}_{rw} \boldsymbol{P}_w \right)_j = \sum_{k=1}^{N_{\Gamma_\sigma}} \left(\boldsymbol{t}^u_{\Gamma_{rw}} \right)_k - \boldsymbol{t}^u_{0_{rw}} \tag{3.51}$$

where N_{Γ_u} and N_{Γ_σ} represent the numbers of exterior Dirichlet and Neumann sides of the domain, respectively. Also, term $\boldsymbol{t}^u_{0rw}$ is now defined as a boundary integral taken over the exterior boundary of the domain. The boundary seepage compatibility equations written on the interior boundaries also lose the boundary terms $\boldsymbol{B}^*_{rw}$. They only remain present on the exterior Dirichlet boundaries of the domain.

3.1.7 Indeterminacy numbers of the HTS model

In order to define the indeterminacy numbers for the hybrid-Trefftz stress element, consider system (3.31), written for a single element. The total number of static degrees of freedom is equal to the dimension of the domain basis,

$$N_y = N_\sigma + 1 \tag{3.52}$$

combining N_σ harmonic and biharmonic modes and the single pore pressure mode, see equation (3.19). The total number of kinematic degrees of freedom is,

$$N_q = N_{qs} + N_{qw} \tag{3.53}$$

$$N_{qs} = 2s\left(1 + d_{qs}\right) \tag{3.54}$$

$$N_{qw} = s\left(1 + d_{qw}\right) \tag{3.55}$$

where N_{qs} and N_{qw} are the dimensions of the boundary bases $\boldsymbol{Z}_s$ and $\boldsymbol{Z}_w$ present in definition (3.30), assuming degrees of approximation d_{qs} and d_{qw}. As for the displacement element, expressions (3.54) and (3.55) are obtained considering that the same degree is used on all sides.

The compatibility (i.e. first two) equations of system (3.31) are always indeterminate, with kinematic indeterminacy numbers equal to:

$$\beta_s = N_{qs} \tag{3.56}$$

$$\beta_w = N_{qs} + N_{qw} \tag{3.57}$$

The static indeterminacy condition of the first set of boundary equilibrium equations,

$$\alpha_{qs} = N_\sigma + 1 - N_{qs} \geq 0 \tag{3.58}$$

is observed, in general, if the degree of the boundary approximation does not exceed the degree of the stress approximation:

$$d_\sigma \geq d_{qs} \tag{3.59}$$

The static indeterminacy condition of the second (pressure) boundary condition,

$$\alpha_{qw} = 1 - N_{qw} = 1 - s\left(1 + d_{qw}\right) \geq 0 \tag{3.60}$$

deserves special attention in this context, as it clearly cannot be met unless $d_{qw} = 0$ and the element has one single Neumann (or interior) side.

To clarify the source of the problem, it should be noted that the second boundary equation is used to enforce the pressure equilibrium on each Neumann and interior boundary of the element. As the pore pressure can only be constant, it is allocated one single degree of freedom, $Y_w = 0$, in the domain approximation (3.15), whose value only requires one equation to be determined. This is the reason why basis $\boldsymbol{Z}_w$ is defined with a single mode.

However, as shown in Figure 3.1, even when the pressure equilibrium is enforced in the weakest possible way (constant approximation for the boundary seepage), all but one of the equations written for an element are redundant.

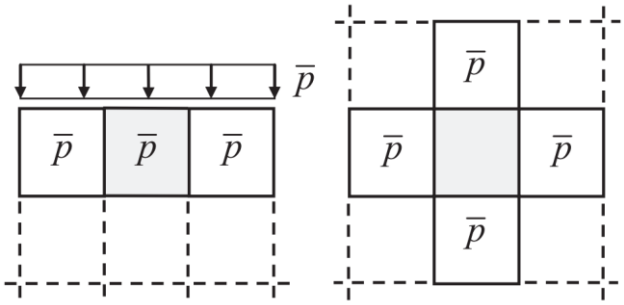

Figure 3.1: Over-constrained domain pressure fields

Instead of developing a logic that ensures that only one pressure continuity condition is transmitted to each element of the mesh, the option followed here is to redefine the support of pressure approximation present in definition (3.15) as the whole domain in analysis, instead of defining it at element level.

The governing system still preserves form (3.31), with the only difference that the second (domain compatibility) equation is now defined at structural level. This means that this equation now only collects boundary terms defined on the exterior (structural) Neumann boundary, the inter-element boundaries no longer being part of it,

$$\mathcal{F}_{ww} Y_w - \sum_{j=1}^{N_{\Gamma_\sigma}} \left(\boldsymbol{A}_{ws} \boldsymbol{Q}_s + A_{ww} Q_w \right)_j = \sum_{k=1}^{N_{\Gamma_u}} \left(u^{\sigma}_{\Gamma_w} \right)_k - u^{\sigma}_{0_w} \tag{3.61}$$

where N_{Γ_σ} and N_{Γ_u} are the numbers of exterior Neumann and Dirichlet sides, respectively. In equation (3.61), terms $\mathcal{F}_{ww}$ and $u^{\sigma}_{0_w}$ are now defined as boundary integrals taken on the whole domain. Terms $\boldsymbol{A}^*_{ws}$ and A^*_{ww} also vanish from the inter-element equilibrium equations, remaining present only on the exterior Neumann sides of the domain.

3.1.8 Recovery of the stress-free modes

This section addresses the a posteriori recovery of the rigid-body and free flow modes in the implementation of the hybrid-Trefftz stress model, absent from the approximation basis (3.15) and, consequently, from the solving system (3.31).

When the displacement field needs to be calculated in the domain of the elements, the rigid-body and free flow modes collected in bases $\boldsymbol{U}_{rs}$ and $\boldsymbol{U}_{rw}$ must be determined in the post-processing phase. This is done enforcing the displacement continuity conditions on the exterior Dirichlet boundary Γ_u as well as on all inter-element boundaries, Γ_i.

Various strategies to achieve this are discussed in [119]. The option used here is to express the continuity conditions in terms of boundary normal and tangential displacements in the solid phase and boundary normal fluid seepage and to enforce them weakly on all boundaries, in a single step.

After solving system (3.31), approximation (3.14) can be written in the following form,

$$\boldsymbol{u} = \boldsymbol{U}_r \boldsymbol{X}_r + \bar{\boldsymbol{u}} \tag{3.62}$$

where $\boldsymbol{U}_r = (\boldsymbol{U}_{rs} \quad \boldsymbol{U}_{rw})$, $\boldsymbol{X}_r^T = (\boldsymbol{X}_{rs} \quad \boldsymbol{X}_{rw})$ and vector $\bar{\boldsymbol{u}}$ is known from the processing phase:

$$\bar{\boldsymbol{u}} = \boldsymbol{U}_s \boldsymbol{Y}_s + \boldsymbol{U}_w Y_w + \boldsymbol{u}_0 \tag{3.63}$$

Considering a set of test functions $\boldsymbol{W}$ (whose degree should not exceed the degree of the domain approximation basis), the compatibility conditions on the Dirichlet and inter-element boundaries are written as, respectively,

$$\int \boldsymbol{W}^* \left(\boldsymbol{n}\boldsymbol{U}_r\right) d\Gamma_u \, \boldsymbol{X}_r = \int \boldsymbol{W}^* \left(\boldsymbol{u}_\Gamma - \boldsymbol{n}\bar{\boldsymbol{u}}\right) d\boldsymbol{\Gamma}_u \tag{3.64}$$

$$\int \boldsymbol{W}^* \left(n\,\boldsymbol{U}_r\right) d\Gamma_i \, \boldsymbol{X}_r^j - \int \boldsymbol{W}^* \left(n\,\boldsymbol{U}_r\right) d\Gamma_i \, \boldsymbol{X}_r^k = \int \boldsymbol{W}^* \left(n\,\bar{\boldsymbol{u}}^k - \boldsymbol{n}\bar{\boldsymbol{u}}^j\right) d\Gamma_i \tag{3.65}$$

where n is the direction cosine matrix used to obtain the boundary normal and tangential components of the displacements. Equation (3.65) should be written once for all adjacent elements j and k.

Equations (3.64) and (3.65) lead to a system of equations which is solved for the unknown weights $\boldsymbol{X}_r$ associated with the rigid body and free flow modes. As system (3.64)-(3.65) is, in general, over-determinate, it needs to be solved in its (Hermitian) least-square form.

3.2 Solution of static problems

Four sets of tests are presented in this section. Convergence of the HTD and HTS finite element solutions is analyzed under p- and h-refinement conditions. The tests on robustness address two issues in terms of numerical stability, namely sensitivity to mesh distortion and sensitivity to quasi-incompressibility. The last test is used to illustrate the performance of the HTD and HTS models, as compared with conventional (conform) finite elements.

3.2.1 Convergence under *p*- and *h*-refinement

The numerical applications presented in this section are performed on the biphasic body represented in Figure 3.2, with dimensions of $r_{min} = 10.0m$, $r_{max} = 20.0m$ and $\theta = 0.5\,rad$. A water-saturated Molsand soil with the properties defined in Appendix E is used in the test.

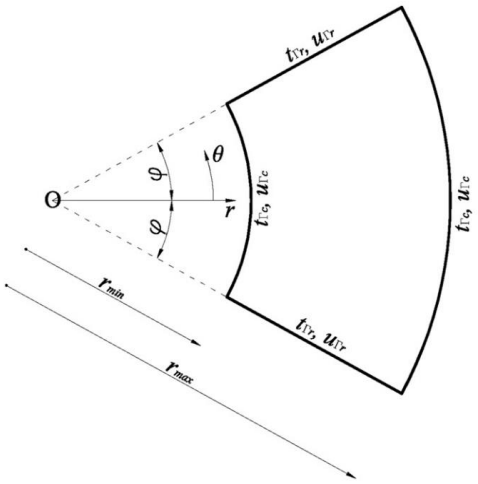

Figure 3.2: Model for convergence and robustness tests

As error measures are sensitive to reference values, an exact, analytical solution is used as reference. This solution is defined here using a singular solution of the Navier equation (3.1), obtained from the biharmonic displacement potential $\phi(r,\theta) = r^2\,log(r)$, which is not included in the regular displacement and stress bases (3.14) and (3.15) as it causes the stress field to be singular at the origin. This reference solution is used to setup the boundary conditions of the test, either the surface tractions (for the displacement model) or the displacements (for the stress model) applied on all exterior sides of the domain shown in Figure 3.2.

Under these conditions, the normal and tangential components of the solid phase tractions on the radial boundaries are given by expression (3.66), while equation (3.67) defines the same quantities on the circular sides of the medium (the boundary pore pressure is null):

$$\boldsymbol{t}_{\Gamma_r} = -\frac{\mu}{r}\begin{bmatrix} cos\,\theta + sin\,\theta \\ cos\,\theta - sin\,\theta \end{bmatrix} \tag{3.66}$$

$$\boldsymbol{t}_{\Gamma_c} = \frac{\mu}{r}\begin{bmatrix} \frac{2\lambda+3\mu}{\mu}(cos\,\theta + sin\,\theta) \\ cos\,\theta - sin\,\theta \end{bmatrix} \tag{3.67}$$

The normal and tangential components of the solid phase displacement field and the normal component of the fluid seepage on the radial boundaries of the domain are given by expression (3.68), while their counterparts on the circular boundaries are defined by relation (3.69):

$$\boldsymbol{u}_{\Gamma_r} = \frac{\pm 1}{4\mu}\begin{bmatrix} [3\lambda + 7\mu + 2(\lambda + 3\mu)\log r](\cos\theta - \sin\theta) \\ -[\lambda + 5\mu + 2(\lambda + 3\mu)\log r](\cos\theta + \sin\theta) \\ -4\mu\alpha(\log r + 1)(\cos\theta - \sin\theta) \end{bmatrix} \tag{3.68}$$

$$\boldsymbol{u}_{\Gamma_c} = \frac{\pm 1}{4\mu}\begin{bmatrix} [\lambda + 5\mu + 2(\lambda + 3\mu)\log r](\cos\theta + \sin\theta) \\ [3\lambda + 7\mu + 2(\lambda + 3\mu)\log r](\cos\theta - \sin\theta) \\ -4\mu\alpha(\log r + 1)(\cos\theta + \sin\theta) \end{bmatrix} \tag{3.69}$$

The choice of signs in these expressions follows from the orientation the boundary outward normal.

The normal and shear (total) stress fields corresponding to the tests described above are presented in Figure 3.3.

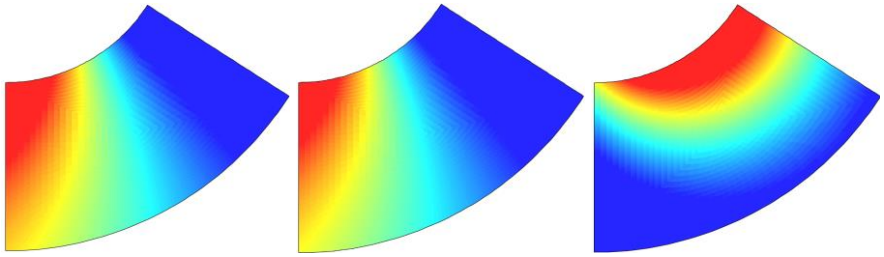

a) $\boldsymbol{\sigma}_{rr}$ field b) $\boldsymbol{\sigma}_{\theta\theta}$ field c) $\boldsymbol{\sigma}_{r\theta}$ field

Figure 3.3: Reference stress fields in biphasic static problems

The *p*- and *h*-convergence rates are assessed using the error in the finite element estimates of the deformation energy. For the domain represented in Figure 3.2, the analytic expression of the deformation energy is,

$$E = \varphi \int_{r_{min}}^{r_{max}} \boldsymbol{S}_{\phi}^{*} \boldsymbol{f} \boldsymbol{S}_{\phi} \cdot r dr \tag{3.70}$$

where $\boldsymbol{S}_{\phi}$ is the stress field (obtained from potential ϕ) equilibrating the applied tractions (3.66) and (3.67). The finite element deformation energy is computed as follows,

$$E_{FE} = \frac{1}{2}\sum_{j=1}^{N_e}(\boldsymbol{X}_s^{*}\boldsymbol{K}_{ss}\boldsymbol{X}_s + X_w^{*}K_{ww}X_w)_j \tag{3.71}$$

$$E_{FE} = \frac{1}{2}\sum_{j=1}^{N_e}(\boldsymbol{Y}_s^{*}\boldsymbol{\mathcal{F}}_{ss}\boldsymbol{Y}_s + Y_w^{*}\mathcal{F}_{ww}Y_w)_j \tag{3.72}$$

where N_e is the total number of (displacement or stress) elements in the mesh.

It should be noted that material and geometrical scaling is used in all tests presented here in order to improve the numerical stability of the analysis. Also, system scaling is generally used to improve the conditioning of the solving system. A discussion on the scaling strategies and their effectiveness can be found in [112].

The single-, two-, four- and eight-element meshes represented in Figure 3.4 are used to evaluate the convergence of the hybrid-Trefftz models under h-refinement. The leading dimensions of the finite elements are $10.0\,m$ for the first two meshes and $5.0\,m$ for the third and fourth.

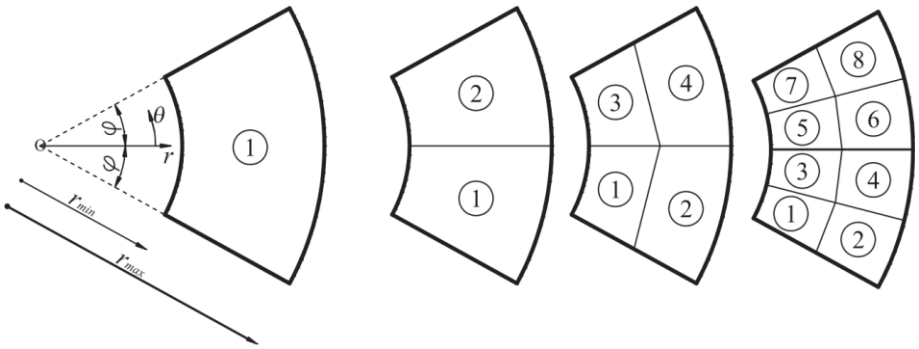

Figure 3.4: Testing mesh

For each testing mesh, p-refinement is performed by gradually increasing the degree of the harmonic and biharmonic bases $\boldsymbol{U}_b$ and $\boldsymbol{U}_h$. As the basis is built strictly hierarchically, increasing the p-refinement only requires computing the terms that correspond to the new additions to the basis, without the need of recalculating terms that were part of the previous, weaker, basis. Also, as the bases are not related in any way to the topology of the element, implementation of localized p-refinements is possible and indeed quite straightforward. For the present tests, however, the same p-refinement is used in all elements and on all essential boundaries of the elements.

The convergence patterns of the mechanical energy error measure defined as,

$$\varepsilon = \left|1 - \frac{E_{FE}}{E}\right| \tag{3.73}$$

are presented for both models in Figure 3.5. The values on the abscissa represent the total number of degrees of freedom (N), i.e., the dimension of the finite element solving system. Each plot contains four solid line graphs, representing the p-convergence patterns obtained using domain bases with degrees 3, 5 and 7 corresponding to boundary bases with degrees 1, 2 and 3

on each of the meshes represented in Figure 3.4, namely the meshes with one element (square symbol), two elements (diamond), four elements (circle) and eight elements (triangle). Also, each plot contains three dashed lines, representing the h-convergence patterns obtained maintaining the degree of p-refinement constant and varying the number of elements.

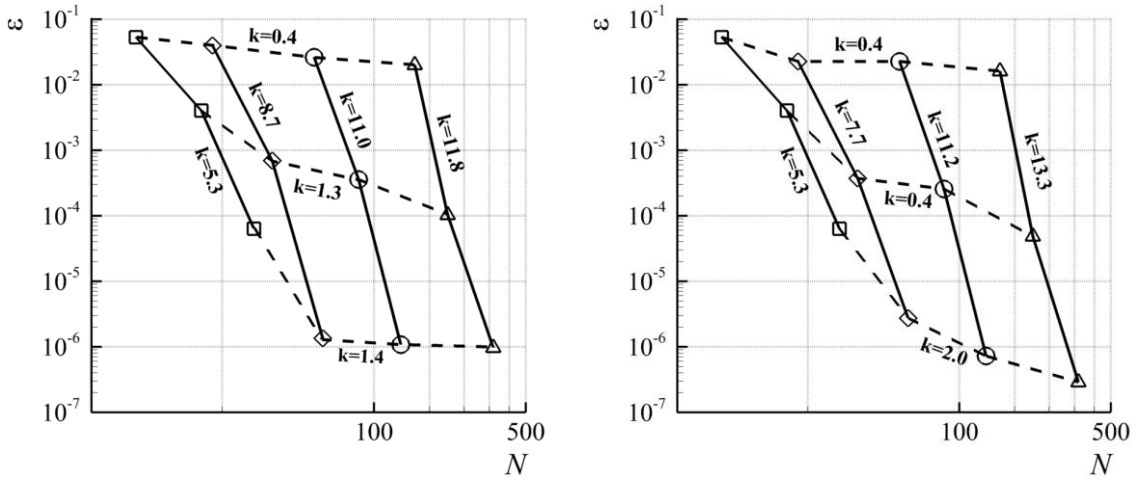

a) Displacement model b) Stress model

Figure 3.5: Convergence results in biphasic static problems

The results demonstrate that the convergence under p-refinement is high, even for small levels of h-refinement. On the other hand, the impact of h-refinement is weaker. The effectiveness of the alternative p- and h-refinements can be quantified by admitting that the logarithms of the error measures of freedom (N) are proportional through a convergence factor k. According to the convergence graphs, this assumption is reasonable for all but the most p-refined of the tested cases (the lowest dashed line in Figure 3.5). In this situation, the method yields a coarser estimate for the average convergence factor, computed over the whole h-refinement process.

Under this assumption, the convergence rate is of the order $O(R^k)$, where R represents the refinement level, defined as the ratio between the current and the previous number of degrees of freedom. For instance, doubling the total number of degrees of freedom corresponds to $R = 2$ and an error decrease of the order (2^k) should be expected. Therefore, higher values of k correspond to larger decreases of the error measure when the number of degrees of freedom is increased a given number of times. The p-refinement convergence factors, corresponding to the four solid lines in Figure 3.5 show that the p-convergence rate is similar for both displacement and stress element.

More importantly, Figure 3.5 shows that convergence factor k is larger when the p-refinement is performed on finer meshes. Substantial testing experience has proven that there exists a limited amount of accuracy a certain mesh can meet for a particular problem. Once this point is reached, further increasing the degree of p-refinement results in loss of precision because of the consequent ill-conditioning of the solving system. The convergence factors of the h-refinement tests (the three dashed lines in Figure 3.5) are significantly smaller than those obtained under p-refinement. However, they improve when the mesh refinement is performed on elements with higher orders of p-refinement. In relative terms, the convergence patterns under h-refinement are similar for both models.

3.2.2 Sensitivity to mesh distortion

Mesh distortion is an issue that may seriously hinder the performance of conventional finite elements. However, it may be unavoidable when meshing topologically complex domains, as it quite often occurs in geo- and biomechanical applications, especially when automatic procedures are used to generate the mesh.

The same testing problem is used to assess the sensitivity of the HTD and HTS models to mesh distortion. The distortion scheme shown in Figure 3.6 is applied to the four-element mesh, with $L = \frac{r}{2} = 0.5\,m$. The elements are successively distorted by decreasing the value of the distortion parameter η, from 10^{-1} to 10^{-6}. For each value of η, the energy error measure is,

$$\varepsilon = \left|1 - \frac{E_{dist}}{E_{undist}}\right| \tag{3.74}$$

where E_{dist} and E_{undist} are the deformation energies computed on the distorted and undistorted meshes. The maximum degree of the domain approximation functions is nine for all tests.

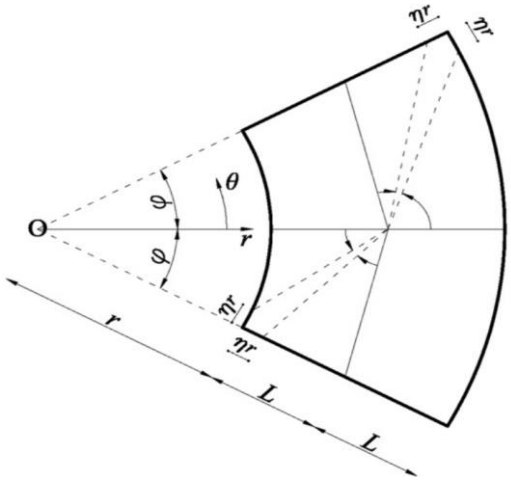

Figure 3.6: Distortion test model

Figure 3.7 presents plots of the variation of the error measure with the distortion parameter. For both displacement and stress models, the correct results are achieved with good precision for the whole range of distortion parameters. More importantly, the error does not increase with the level of distortion of the element, the (small) variations being due to the successive relocations of the origins of the local systems of reference, which follow the variations of the respective barycentre. In relative terms, the stress model seems to produce a lower error than the displacement model, although in absolute terms the errors are small in both cases.

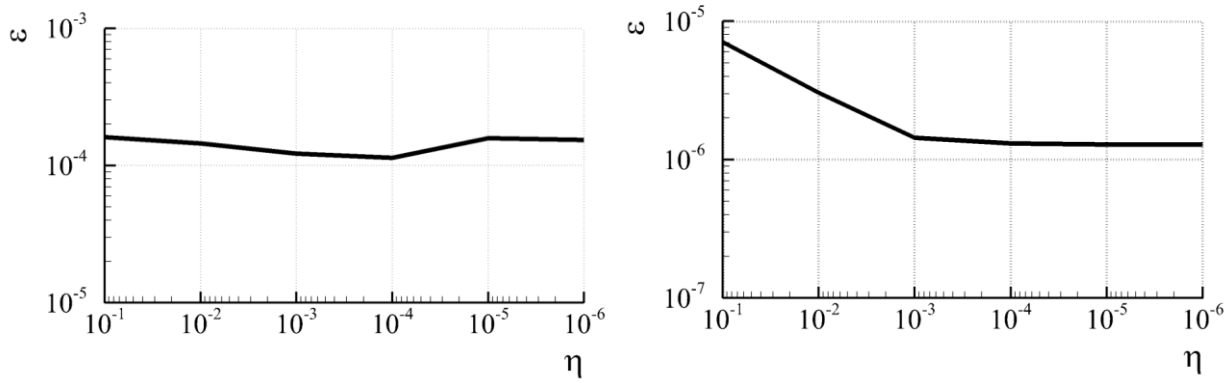

a) Displacement model b) Stress model

Figure 3.7: Sensitivity to mesh distortion in biphasic static problems

3.2.3 Sensitivity to near-incompressibility

In many bio- and geomechanical applications, the constituents of biphasic media are characterised by very high bulk moduli, posing the problem of adequately modelling nearly-incompressible media. In biomechanics, for instance, the mixture incompressibility may occur

when modelling soft tissues [120], while in geomechanics the ground water incompressibility may become an issue under low permeability conditions, when the fluid cannot easily drain out of the pores [121]. Either of these situations may result in severe mesh locking when conventional elements are used [1], with consequent losses in accuracy of the results.

Due to the practical importance of the situations involving nearly-incompressible media, this problem has received significant attention from the researchers. The incompressibility condition was enforced using the penalty method [122], or mixed formulations, with or without stabilization, e.g. [123]. In the Trefftz context, full soft tissue incompressibility was modelled using hybrid-Trefftz elements by constraining the shape functions to satisfy the incompressibility condition, e.g. [124]. However, these strategies generally require the incompressibility condition to be explicitly enforced at some level, and thus additional equations need to be solved (or additional constraints enacted on the approximation basis).

The sensitivity of the hybrid-Trefftz elements to near-incompressibility is assessed using the testing problem defined above. The Poisson ratio of the mixture is defined in form,

$$\nu = 0.5 - \eta \tag{3.75}$$

where η is the sensitivity parameter. The domain is meshed into four elements, as shown in Figure 3.4. The maximum degree of the domain approximation functions is nine and of the boundary approximation function is three. These functions are not adapted in any way to accommodate media with low compressibility.

For each value of η, ranging from 10^{-1} to 10^{-10}, the energy error ε is calculated using (the equivalent form of) definition (3.73). The results obtained are presented in Figure 3.8. They show that the elements are virtually insensitive to near-incompressibility (the limit taken for the Poisson ratio is $\nu = 0.5 - 10^{-10}$. The main reason for this robustness is the physical significance of the Trefftz-compliant approximation functions, which locally respect the domain elasticity equation, despite the high values of the bulk moduli. Significant degradation of the predicted results may, however, be caused by loss of numerical precision when parameter η is smaller than the numerical precision of the computer (the tests are run using double precision).

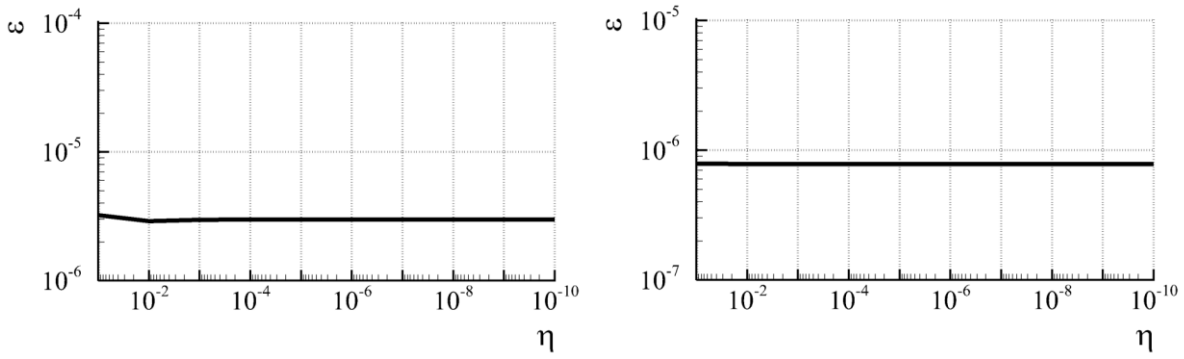

a) Displacement model b) Stress model

Figure 3.8: Sensitivity to near-incompressibility in biphasic static problems

3.2.4 Static response of biphasic media

The test problem defined in Figure 3.9 is solved to illustrate the ability of the hybrid-Trefftz elements to recover the inter-element continuity and the enforced boundary conditions. The two-layer medium is confined in a square tank ($L = 1.0m$) and subjected to a surface loading $f = 1Pa$. The upper layer is a water-saturated Molsand soil with a Young's modulus reduced to half the value given in the Appendix E. The lower layer is the same type of material, but with a Young's modulus eight times larger ($E_{lower}/E_{upper} = 8$).

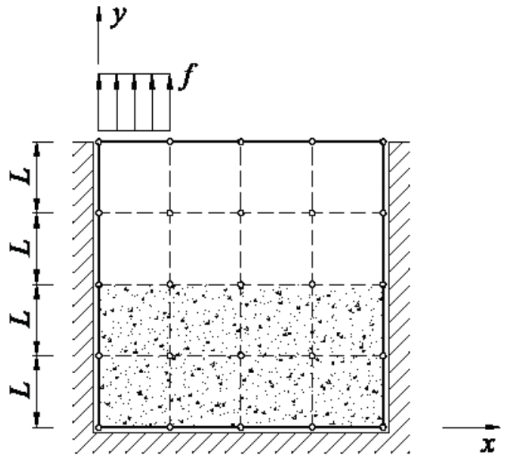

Figure 3.9: Surface traction test model

The boundary conditions are defined as follows: the surface force acts on the solid skeleton and the pore pressure is null on the free surface; the normal displacements in the solid phase and the fluid seepage are restricted along the walls of the rigid container; no constraints are imposed on the tangential components of the displacements on the frictionless tank walls; displacement and surface force continuity is assumed on the interface of the two layers.

The domain is meshed in 16 square elements. The domain approximation bases are constructed, for all elements, using polynomial functions of degree 15 and the boundary approximation bases are of maximum degree 5. The total number of degrees of freedom is 1,509 for the displacement model and 1,336 for the stress model.

The reference solution is obtained with ABAQUS^{TM}. The domain is discretized in 1,600 CPE4P elements [4]. CPE4P is a four-node (bilinear) displacement and pore pressure element, with three degrees of freedom per node, two nodal displacements and the nodal pore pressure. The total number of degrees of freedom is 5,043.

The stress fields obtained with conform elements (ABAQUS^{TM}) and hybrid-Trefftz elements (HTD and HTS) are presented in Figures 3.10 to 3.12. The variation of the solid phase displacements and total stresses along the vertical section $x = L/2$ (under the applied load, see Figure 3.9) is presented in Figure 3.13. It is noted that no smoothing is used in any of the graphs presented in Figures 3.10 to 3.12.

The plots show the stress and displacement fields are continuous within each layer (inter-element continuity) and satisfy both Neumann and Dirichlet boundary conditions. They also show that inter-layer continuity is adequately enforced. Moreover, they simulate correctly the expected behaviour on the interface of the layers: formally, the axial stress component σ_{xx} is not subject to a continuity condition and the discontinuity shown in Figure 3.10 is a direct consequence of the discontinuity of the stress fields in layers with distinct mechanical properties.

The effect of this physical discontinuity is also visible in the variation of the shear stress, σ_{xy}. Equilibrium on the interface is correctly modelled (continuity of σ_{xy} at $y = 2L$), as well as the effect of displacement continuity: the no-sliding condition is the main cause for the shear stress concentration on the interface.

Another source of high stress gradients is the discontinuity of the loading on the free surface $y = 4L$. The stress components σ_{yy} and σ_{xy} satisfy the boundary conditions and the high gradients present in all stress field components show that the Trefftz element solutions are converging to the (elastic) stress singularity developing at point $(x, y) = (L, 4L)$. It is recalled that this (weak) singular solution is not contained in the Trefftz approximation basis. Figure

3.12a) shows that the singularity causes some discontinuity in the shear stress field predicted by ABAQUS™, as element CPE4P assumes a linear variation for all stress components.

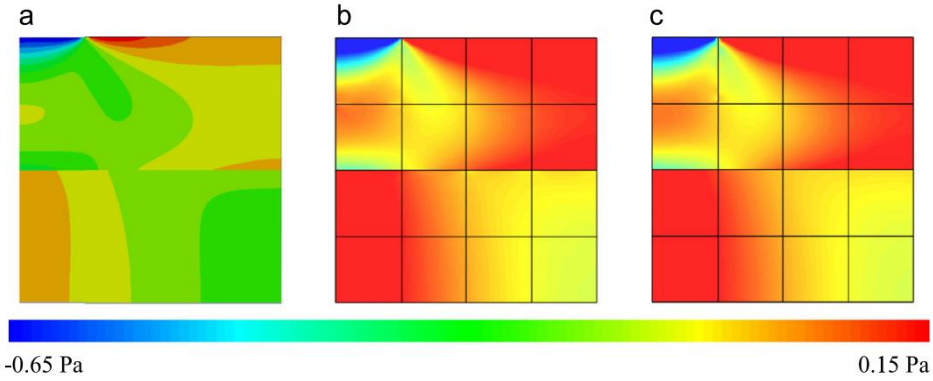

Figure 3.10: σ_{xx} diagrams. a) ABAQUS b) HTD c) HTS

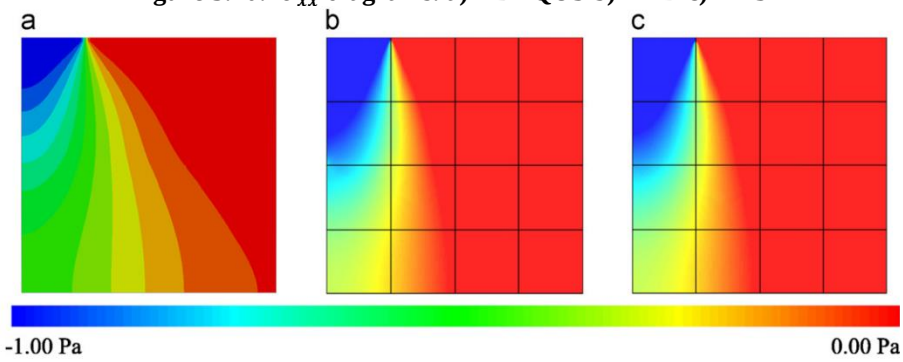

Figure 3.11: σ_{yy} diagrams. a) ABAQUS b) HTD c) HTS

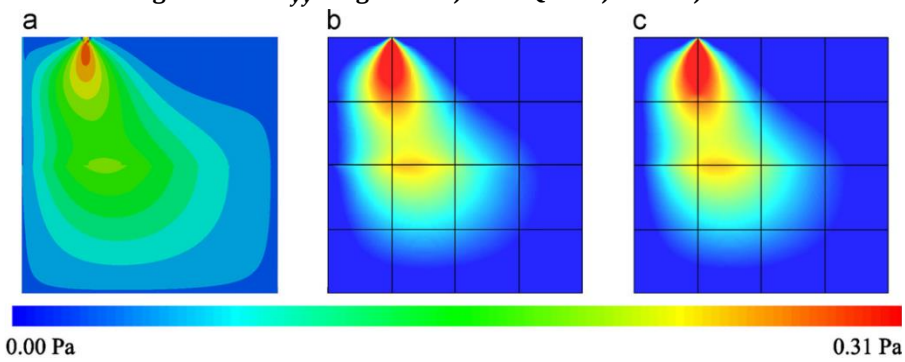

Figure 3.12: σ_{xy} diagrams. a) ABAQUS b) HTD c) HTS

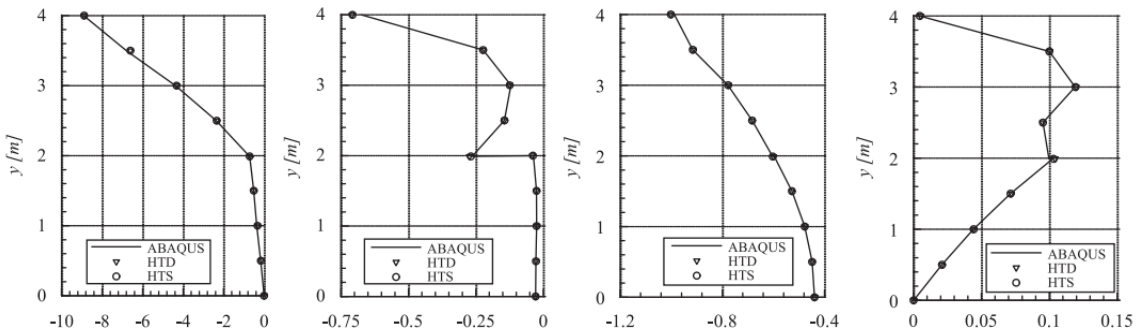

a) $\boldsymbol{u}_y$ profiles b) $\boldsymbol{\sigma}_{xx}$ profiles c) $\boldsymbol{\sigma}_{yy}$ profiles d) $\boldsymbol{\sigma}_{xy}$ profiles

Figure 3.13: Displacement and total stress profiles at $x = L/2$

The results presented in Figure 3.13 show that, as expected, the discrepancy in stiffness between the two layers causes sharp changes in all stress fields (except σ_{yy}) at interface $y = 2L$. The variation of the vertical displacement in the upper layer, see Figure 3.13a), is larger than in the (stiffer) lower layer. As shown in Figure 3.13b), normal stresses in the horizontal direction are discontinuous, as seen in Figure 3.10, and the increase in the shear stress at the interface is visible in Figure 3.13d)**.**

Overall, the results obtained with the hybrid-Trefftz models are in good agreement with those predicted by ABAQUS^{TM}, despite the significant difference in mesh refinement and the consequent discrepancy in terms of total number of degrees of freedom.

To illustrate the significance of the post-processing procedure described in Section 3.1.8, Figure 3.14 presents a comparison between the displacement fields obtained after the processing phase (discarding rigid-body displacements and free fluid flow) and after the post-processing procedure (including rigid-body displacements and free fluid flow). Red arrows represent the solid phase displacement field, while blue arrows denote the fluid seepage.

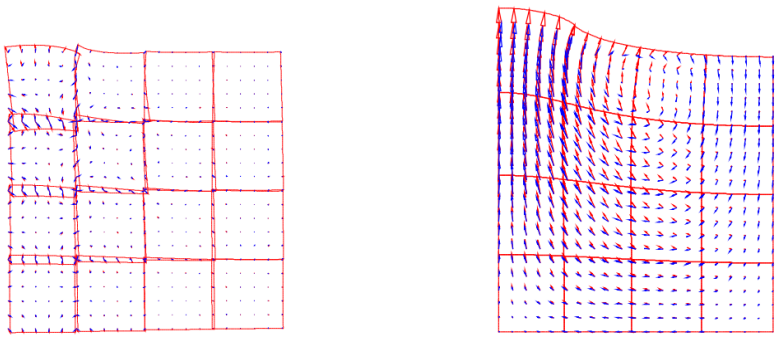

(a) No RBM. (b) RBM included.

Figure 3.14: Effect of the inclusion of rigid body and pure flow modes (RBM) in the solution.

It is clear that failure to include the rigid-body and free flow modes causes significant violations of the displacement continuity condition, both on the Dirichlet boundary of the medium and on the inter-element boundaries. However, when these modes are included, the displacement continuity conditions are respected throughout the domain.

3.3 Formulation of dynamic problems

The mathematical model presented in Section 2.1 is specialized here to simulate the dynamic response of biphasic media. The spectral problem is defined and solved to obtain the three sets of waves that propagate in biphasic media. They are used to set up the approximation bases of the displacement and stress models of the hybrid-Trefftz finite element formulation in forms (2.94) and (2.117) and establish the solving systems (2.116) and (2.138). The section closes with a brief summary of the procedures described in Section 2.3 to implement time integration.

3.3.1 Mathematical model

The homogeneous Navier equation (3.76) is rewritten from equation (2.54) as,

$$\boldsymbol{\mathcal{D}k\mathcal{D}}^{*}\boldsymbol{u}+\omega^{2}\boldsymbol{\rho u}=\mathbf{0} \quad \text{in } V \tag{3.76}$$

Using Figure 2.1 as reference (without a non-wetting fluid phase), and the boundary conditions defined in Section 2.1, the notation established in Section 3.1.1 and the definitions given in Appendix D, the Navier equation (3.76) takes the explicit form,

$$\begin{cases}\boldsymbol{\nabla}[(k_{12}+k_{33})\boldsymbol{\nabla}^{T}\boldsymbol{u}^{S}+k_{14}\boldsymbol{\nabla}^{T}\boldsymbol{w}]+k_{33}\boldsymbol{\nabla}^{2}\boldsymbol{u}^{S}+\omega^{2}(\rho\boldsymbol{u}^{S}+\rho_{W}\boldsymbol{w})=\mathbf{0}\\ \boldsymbol{\nabla}[k_{14}\boldsymbol{\nabla}^{T}\boldsymbol{u}^{S}+k_{44}\boldsymbol{\nabla}^{T}\boldsymbol{w}]+\omega^{2}(\rho_{w}\boldsymbol{u}^{S}+\rho_{W2}\boldsymbol{w})=\mathbf{0}\end{cases} \tag{3.77}$$

where vectors $\boldsymbol{u}^{S}$ and $\boldsymbol{w}$ define the solid phase displacements and the fluid seepage.

3.3.2 Trefftz approximation functions

The Navier system of equations (3.77) is reduced to the Helmholtz equation using dilatational and shear displacement potentials, leading to two sets of compressional waves and one set of shear waves.

❖ **Compressional waves**

The compressional wave solution is determined solving system (3.77) under the assumption that they derive from a gradient field. Two sets of wave numbers are obtained, $j=\{1,\ 2\}$,

$$\beta_{P_j}^2 = \omega^2 \frac{\rho+\gamma_{P_j}\rho_w}{\left(\chi+\alpha\gamma_{P_j}\right)} = \omega^2 \frac{\rho_w+\gamma_{P_j}\rho_{w2}}{\left(\alpha+\gamma_{P_j}\right)Q} \tag{3.78}$$

where the phase multipliers, γ_{P_j}, are the solutions of the following quadratic equation:

$$\left(1-\alpha\frac{\rho_{w2}}{\rho_w}\right)\gamma_P^2 + \left(\frac{\rho}{\rho_w}-\chi\frac{\rho_{w2}}{\rho_w}\right)\gamma_P + \left(\alpha\frac{\rho}{\rho_w}-\chi\right) = 0 \tag{3.79}$$

$$\chi = \alpha^2 + \frac{\lambda+2\mu}{Q} \tag{3.80}$$

The displacement and stress fields corresponding to each set of compressional waves are,

$$\boldsymbol{U}_{P_j} = \frac{1}{2}\beta_{P_j}^{-1}\begin{bmatrix} \left[J_{n-1}(z_j) - J_{n+1}(z_j)\right] \\ \hat{\imath}\left[J_{n-1}(z_j) + J_{n+1}(z_j)\right] \\ \gamma_{P_j}\left[J_{n-1}(z_j) - J_{n+1}(z_j)\right] \\ \hat{\imath}\gamma_{P_j}\left[J_{n-1}(z_j) + J_{n+1}(z_j)\right] \end{bmatrix} exp(\hat{\imath}n\theta) \tag{3.81}$$

$$\boldsymbol{S}_{P_j} = \frac{1}{2}\begin{bmatrix} S_{P_j}^r \\ S_{P_j}^\theta \\ \hat{\imath}\mu\left[J_{n-2}(z_j) - J_{n+2}(z_j)\right] \\ -2\left(\alpha+\gamma_{P_j}\right)QJ_n(z_j) \end{bmatrix} exp(\hat{\imath}n\theta) \tag{3.82}$$

$$\boldsymbol{S}_{P_j}^r = \mu\left(2J_n(z_j) + J_{n-2}(z_j) + J_{n+2}(z_j)\right) - 2\left(\chi+\alpha\gamma_{P_j}\right)QJ_n(z_j) \tag{3.83}$$

$$\boldsymbol{S}_{P_j}^\theta = \mu\left(2J_n(z_j) - J_{n-2}(z_j) - J_{n+2}(z_j)\right) - 2\left(\chi+\alpha\gamma_{P_j}\right)QJ_n(z_j) \tag{3.84}$$

Interior (exterior) problems are modelled with Bessel functions of the first (second) kind and order n, $J_n(z_j)$, with complex argument $z_j = \beta_{P_j} \cdot r$.

❖ **Shear wave**

A single shear wave satisfies the Navier problem (3.77). It is characterized by the following wave number and phase multiplier:

$$\beta_S^2 = \omega^2\left(1+\gamma_S\frac{\rho_w}{\rho}\right)\frac{\rho}{\mu} \tag{3.85}$$

$$\gamma_S = -\frac{\rho_w}{\rho_{w2}} \tag{3.86}$$

The shear wave displacement and stress fields are defined as follows, where $z_S = \beta_S \cdot r$:

$$\boldsymbol{U}_S = \frac{1}{2}\begin{bmatrix} \hat{\imath}\beta_S^{-1}[J_{n+1}(z_S) + J_{n-1}(z_S)] \\ \beta_S^{-1}[J_{n+1}(z_S) - J_{n-1}(z_S)] \\ \hat{\imath}\gamma_S\beta_S^{-1}[J_{n+1}(z_S) + J_{n-1}(z_S)] \\ \gamma_S\beta_S^{-1}[J_{n+1}(z_S) - J_{n-1}(z_S)] \end{bmatrix} exp(\hat{\imath}n\theta) \tag{3.87}$$

$$\boldsymbol{S}_S = \frac{1}{2}\mu\begin{bmatrix} \hat{\imath}[J_{n-2}(z_S) - J_{n+2}(z_S)] \\ -\hat{\imath}[J_{n-2}(z_S) - J_{n+2}(z_S)] \\ -[J_{n-2}(z_S) - J_{n+2}(z_S)] \\ 0 \end{bmatrix} exp(\hat{\imath}n\theta) \tag{3.88}$$

❖ **Illustration of compressional and shear wave modes**

The dynamic characteristics of the waves propagating through saturated soils are illustrated next in terms of the variation of the wavelength, $\lambda = 2\pi/\Re(\beta)$, where $\Re(\beta)$ is the real part of the wave number, and of the attenuation, defined as the imaginary part of the wave number. The wavelength and attenuation corresponding to the two compressional and the single shear wave are represented in Figures 3.15, 3.16 and 3.17 as functions of the (logarithm of the) hydraulic conductivity and excitation frequency, for the Molsand soil characterized in Appendix E.

The plots are presented for a range of frequencies of the propagating wave between $50Hz$ and $250Hz$. The hydraulic conductivity range is taken between $10^{-2}m/s$ and $10^{-6}m/s$. These limits correspond to pervious soils (e.g. well sorted sands, sand and gravel) and semi-pervious soils (e.g. fine sands, loess, and silt). Impervious soils, characterized by hydraulic conductivities lower than $10^{-6}m/s$, essentially block the propagation of compressional waves through the fluid phases, behaving like frozen-media.

The wavelength and the phase velocity $v = \lambda\frac{\omega}{2\pi}$ of the fast propagating P_1 wave (Figure 3.15) are insensitive to variations of the permeability of the medium. This is consistent with the physical nature of this compressional wave, which propagates essentially through direct contact between the solid particles and is thus insensitive to those properties of the medium that condition the movement of the flow constituents. Moreover, as the product $\lambda \cdot \omega$ is practically constant, the phase velocity of P_1 wave is also insensitive to the frequency of the travelling wave (i.e. the medium is not dispersive in respect to P_1 wave). The wave presents low attenuation, especially for the lower range of frequency.

The second compressional wave, Figure 3.16, is completely influenced by the frequency and permeability of the medium, which suggests that the propagation of this wave is determined by

the motion of the fluid phase. Both the wavelength and the phase velocity of the P_2 wave reach their maximum for the smallest permeability and the highest frequency tested. The phase velocity of the P_2 wave is proportional to its frequency; especially at higher permeability values. The attenuation of the P_2 wave doesn't significantly depend on the frequency. However, the increasing attenuation of P_2 wave is following the decreasing permeability. This happens because P_2 wave is transmitted through fluid motion, which is hindered by the low permeability of the medium.

As shear wave can only propagate through the solid phase, it does not induce pore pressures. Its vibration and attenuation characteristics, presented in Figure 3.17, are qualitatively similar to those of the P_1 wave. S wave propagates at a lower phase velocity than P_1 wave and is similarly attenuated.

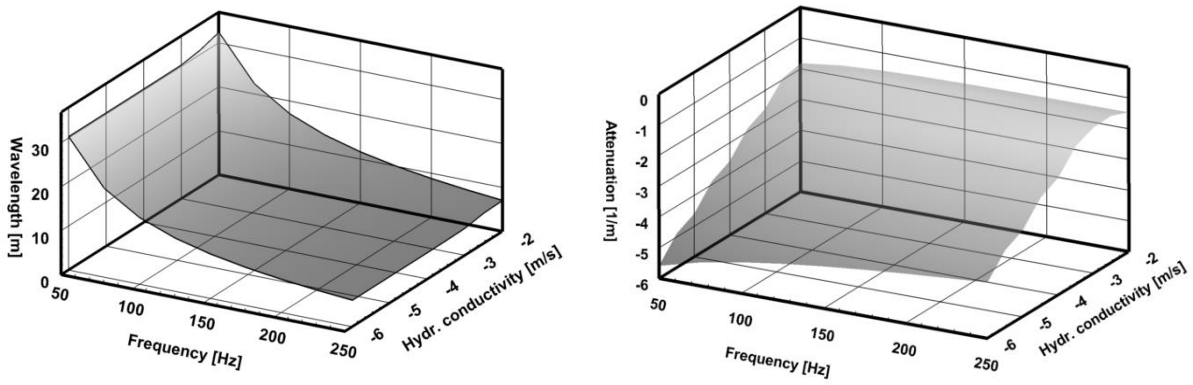

a) Wavelength variation b) Attenuation variation

Figure 3.15: Compressional wave P_1 in biphasic dynamic problems

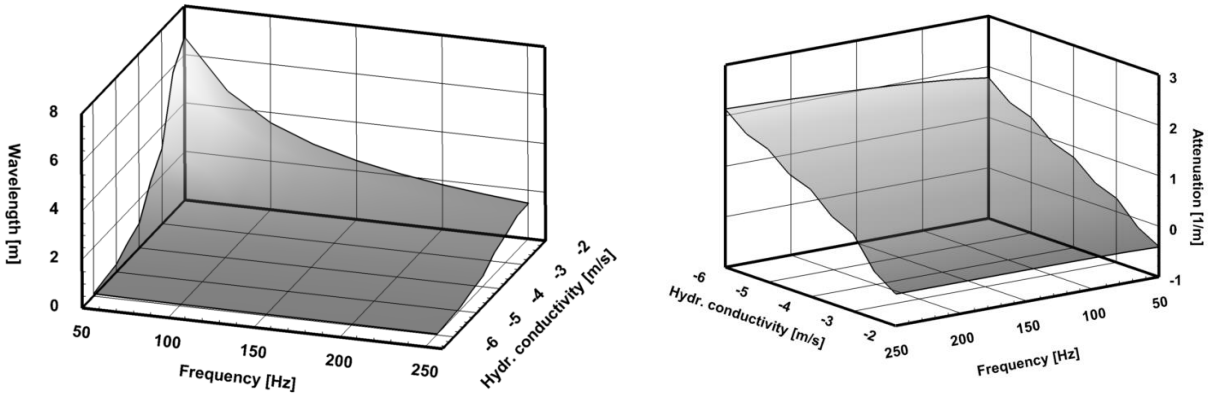

a) Wavelength variation b) Attenuation variation

Figure 3.16: Compressional wave P_2 in biphasic dynamic problems

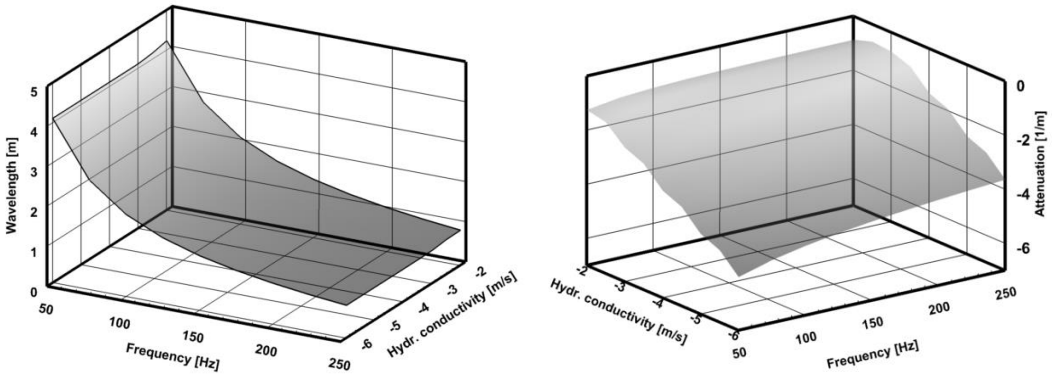

a) Wavelength variation b) Attenuation variation

Figure 3.17: Shear wave S in biphasic dynamic problems

3.3.3 Trefftz approximation bases

The Trefftz bases are constructed combining the solutions defined above, to yield the following expressions for the Trefftz approximations (2.94) and (2.117),

$$\boldsymbol{u} = \boldsymbol{U}_d \boldsymbol{X}_d + \boldsymbol{u}_0 \tag{3.89}$$

$$\boldsymbol{\sigma} = \boldsymbol{S}_d \boldsymbol{Y}_d + \boldsymbol{\sigma}_0 \tag{3.90}$$

$$\boldsymbol{U}_d = (\boldsymbol{U}_{P_1} \quad \boldsymbol{U}_{P_2} \quad \boldsymbol{U}_S) \tag{3.91}$$

$$\boldsymbol{S}_s = (\boldsymbol{S}_{P_1} \quad \boldsymbol{S}_{P_2} \quad \boldsymbol{S}_S) \tag{3.92}$$

The particular solutions terms $\boldsymbol{u}_0$ and $\boldsymbol{\sigma}_0$ are required if the dynamic problems are solved with analysis of initial conditions (e.g. non-periodic and transient problems). In this case, the particular solutions are approximated using the solutions of the static problems defined in Section 3.1.2, to yield following expressions.

$$\boldsymbol{u}_0 = \boldsymbol{U}_s \boldsymbol{X}_s + \boldsymbol{U}_r \boldsymbol{X}_r \tag{3.93}$$

$$\boldsymbol{\sigma}_0 = \boldsymbol{S}_s \boldsymbol{Y}_s \tag{3.94}$$

$$\boldsymbol{U}_s = (\boldsymbol{U}_{b_0} \quad \boldsymbol{U}_{b_n} \quad \boldsymbol{U}_h \quad \boldsymbol{U}_w) \tag{3.95}$$

$$\boldsymbol{U}_r = (\boldsymbol{U}_{rs} \quad \boldsymbol{U}_{rf} \quad \boldsymbol{U}_f) \tag{3.96}$$

$$\boldsymbol{S}_s = (\boldsymbol{S}_{b_0} \quad \boldsymbol{S}_{b_n} \quad \boldsymbol{S}_h \quad \boldsymbol{S}_w) \tag{3.97}$$

3.4 Solution of dynamic problems

The testing problem defined in Section 3.2 is used to assess the convergence and the robustness of the displacement and stress models of the hybrid-Trefftz finite element formulation for the elastodynamic analysis of biphasic media. These tests are presented in Sections 3.4.1 and 3.4.2, and are used in Section 3.4.3 to assess the sensitivity to frequency content. The section closes with the illustration of the solution of periodic and non-periodic problems. The modelling options described in Section 2.5 for time-stepping analyses are presented and assessed.

3.4.1 Convergence under *p*- and *h*-refinement

As for static tests, the option used here is to induce a reference wave to the medium represented in Figure 3.2 by means of imposed boundary tractions (displacement model) or boundary displacements (stress model) and to assess the convergence of the predicted mechanical energy.

The analytic wave is selected from the vibration modes defined in bases (3.81) and (3.82) for compressional waves and bases (3.87) and (3.88) for shear waves, under the condition that it is absent from the finite element approximation bases.

The geometry of the domain is defined by $r_{min} = 10.0m$, $r_{max} = 20.0m$ and $\theta = 0.5\,rad$. The material considered in the tests is the Molsand soil defined in Appendix E. The tests are conducted for all types of waves. The spectral frequencies range from $12.5Hz$ to $85.5Hz$ for all testing waves, P_1, P_2 and S.

❖ **Reference solution for compressional waves**

The Neumann problem for the displacement model is defined by boundary conditions,

$$t_\Gamma^n = 0.5\left[\mu(2H_5 + H_3 + H_7) - 2\left(\chi + \alpha\gamma_{P_j}\right)QH_5\right]exp(5\hat{\imath}\theta) \tag{3.98}$$

$$t_\Gamma^t = 0 \tag{3.99}$$

$$\pi = -\left(\alpha + \gamma_{P_j}\right)QH_5 exp(5\hat{\imath}\theta) \tag{3.100}$$

where $j = \{1,\ 2\}$ and $H_\alpha = H_\alpha\left(\beta_{P_j} r\right)$ represents the second kind Hankel functions of order α, referred to the (r, θ) referential represented in Figure 3.2. In the expression of the boundary-normal traction t_Γ^n, the positive sign corresponds to the circular boundary of the domain and the negative sign, to the radial boundary. No tangential tractions are applied to the boundary.

In the stress model test, compressional waves of type $j = \{1,\ 2\}$ are implemented applying normal displacements (3.101) and (3.102) to the circular boundaries and tangential displacement (3.103) to its radial boundaries, where n_r and n_θ are the direction cosines of the boundary:

$$u_{\Gamma_n}^S = -0.5n_r\beta_{P_j}^{-1}(H_4 - H_6)exp(5\hat{\imath}\theta) \tag{3.101}$$

$$u_{\Gamma_n}^W = -0.5n_r\beta_{P_j}^{-1}\gamma_{P_j}(H_4 - H_6)exp(5\hat{\imath}\theta) \tag{3.102}$$

$$u_{\Gamma_t}^S = 0.5n_\theta\beta_{P_j}^{-1}(H_4 - H_6)exp(5\hat{\imath}\theta) \tag{3.103}$$

The stress fields σ_{xx} produced by the P_1 and P_2 waves under the two selected frequencies are represented in Figure 3.18.

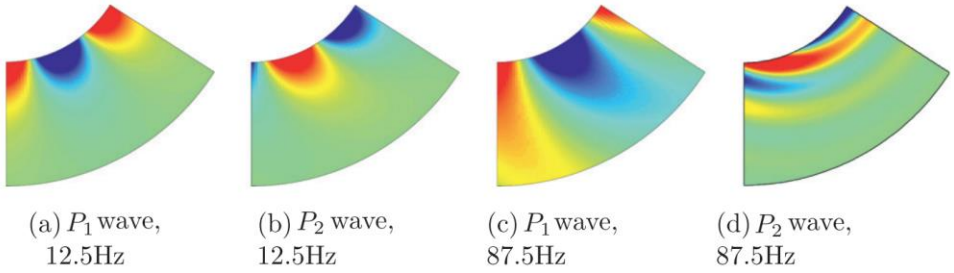

(a) P_1 wave, 12.5Hz (b) P_2 wave, 12.5Hz (c) P_1 wave, 87.5Hz (d) P_2 wave, 87.5Hz

Figure 3.18: σ_{xx} stress fields for the tested *P* waves in biphasic dynamic problems

❖ Reference solution for shear waves

In the displacement model test, analytic shear waves are induced to the medium applying the following tangential traction field on the circular and radial boundaries (the boundary-normal traction field and the pore pressures are null):

$$t_\Gamma^t = -0.5\mu(H_4 + H_6)exp(5\hat{\imath}\theta) \tag{3.104}$$

In the stress model test, the shear wave is induced applying the tangential displacements (3.105) on the circular boundaries and the normal displacements (3.106) and (3.107) on the linear boundaries:

$$u_{\Gamma_t}^S = 0.5n_r\beta_S^{-1}(H_4 - H_6)exp(5\hat{\imath}\theta) \tag{3.105}$$

$$u_{\Gamma_n}^S = -0.5n_\theta\beta_S^{-1}(H_4 - H_6)exp(5\hat{\imath}\theta) \tag{3.106}$$

$$u_{\Gamma_n}^W = -0.5n_\theta\beta_S^{-1}\gamma_S(H_4 - H_6)exp(5\hat{\imath}\theta) \tag{3.107}$$

The stress fields σ_{xx} produced by the S wave under the two selected frequencies are represented in Figure 3.19.

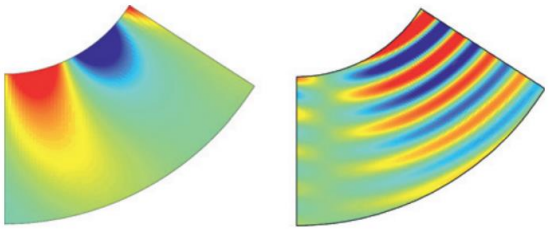

(a) 12.5Hz (b) 87.5Hz

Figure 3.19: σ_{xx} stress fields for the tested *S* wave in biphasic dynamic problems

❖ Mechanical energy of the induced wave

The mechanical energy dissipated by the medium per one vibration cycle is given by,

$$E = \frac{1}{2}\int \boldsymbol{\sigma}^* \boldsymbol{\varepsilon} dV - \frac{1}{2}\int \dot{\boldsymbol{u}}^* \boldsymbol{\rho} \dot{\boldsymbol{u}} dV \tag{3.108}$$

which simplifies to the following spectral form for the domain defined in Figure 3.2,

$$E = \varphi \int_{r_{min}}^{r_{max}} [(\boldsymbol{\mathcal{D}}\boldsymbol{U})^* \boldsymbol{S} - \omega^2 \boldsymbol{U}^* \boldsymbol{\rho} \boldsymbol{U}] r dr \tag{3.109}$$

where $\boldsymbol{U}$ and $\boldsymbol{S}$ represent the displacement and stress modes that define the reference wave.

Substituting approximations (2.94) and (2.96) into expression (3.108), the mechanical energy approximation predicted by the hybrid-Trefftz displacement element is obtained as,

$$E_{FE} = \frac{1}{2}\sum_{i=1}^{N_e} \boldsymbol{X}_i^* \boldsymbol{D}_i \boldsymbol{X}_i \tag{3.110}$$

where N_e is the total number of elements in the mesh and vector $\boldsymbol{X}_i$ collects the displacement unknowns in element i. Similarly, approximations (2.117) and (2.118) yield the following mechanical energy prediction for the hybrid-Trefftz stress element,

$$E_{FE} = \frac{1}{2}\sum_{i=1}^{N_e} \boldsymbol{Y}_i^* \boldsymbol{\mathcal{F}}_i \boldsymbol{Y}_i \tag{3.111}$$

where vector $\boldsymbol{Y}_i$ lists the stress unknowns in element i.

❖ **Convergence results**

The h-refinement is performed by meshing the domain into one, two and four elements, as presented in Figure 3.4. The p-refinement procedure is implemented increasing the orders of the domain and boundary approximation functions. Convergence of the finite element solutions is assessed using the mechanical energy error measure (3.73) under definitions (3.109), (3.110) and (3.111). Letting N represent the number of the degrees of freedom of the HTD and HTS finite element models, the convergence rate, k, is defined in form,

$$\log(\epsilon) = -k \cdot \log(N) \tag{3.112}$$

meaning that the convergence under a given refinement is of the order $O(R^k)$, where R is the ratio between the total number of degrees of freedom after and before the refinement. It is recalled that the convergence rate under h-refinement is $k = 2$ for conventional elements using linear approximations.

Figures 3.20 and 3.21 present the p- and h-refinement convergence graphs for the two compressional waves and for the shear wave. The mechanical energy error measure (3.73) is

plotted against the total number of degrees of freedom, that is, the total dimension of the assembled solving system (2.116) for displacement model and of the assembled solving system (2.138) for stress model. The p-refinement convergence patterns corresponding to the single-, two- and four-element meshes are represented with solid lines and with square, diamond and circle markers, respectively. The dashed lines in Figures 3.20 and 3.21 correspond to the convergence patterns obtained under h-refinement.

The variation of the convergence rate shown in Figures 3.20 and 3.21 leads to the following conclusions, similar to those stated for the static tests: similar convergence patterns are observed for the stress and displacement models of the hybrid-Trefftz finite element formulation; the convergence rate under h-refinement is of the same order of magnitude as the convergence rate of (linear) conventional elements; the (average) convergence under p-refinement is several times faster than the convergence under h-refinement. There is, however, only so much precision that can be reached by only increasing the order of p-refinement. Over-increasing the number of approximation functions eventually leads to loss of precision due to the consequent ill-conditioning of the finite element solving system.

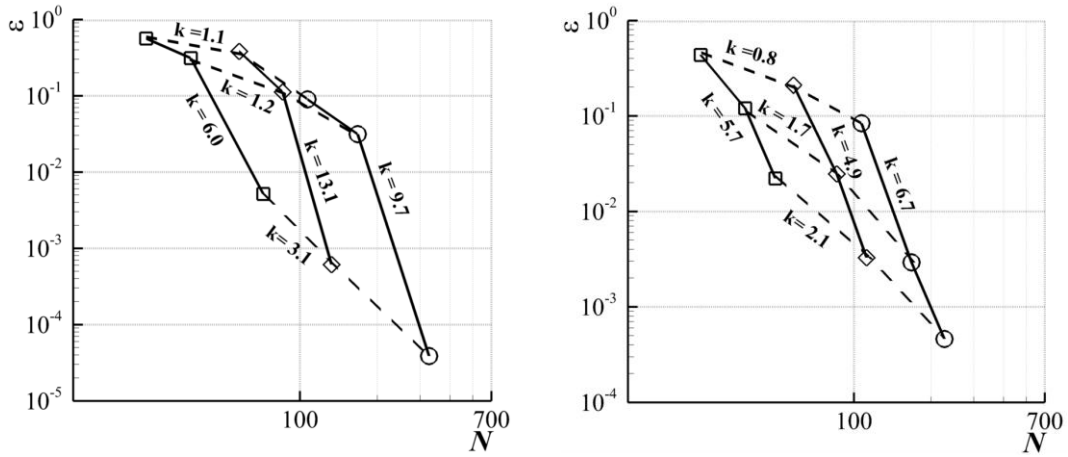

a) P_1 wave, 12.5 Hz b) P_1 wave, 87.5 Hz

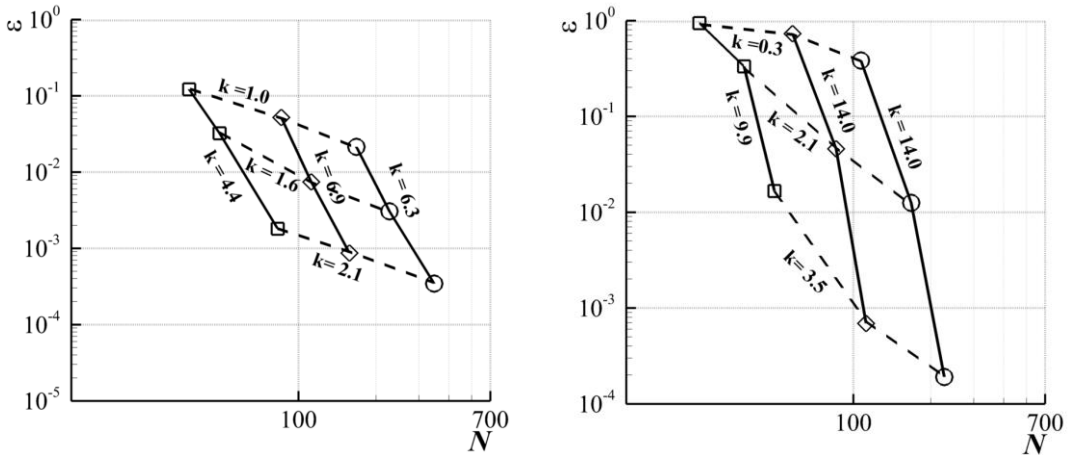

c) P_2 wave, 12.5 Hz d) P_2 wave, 87.5 Hz

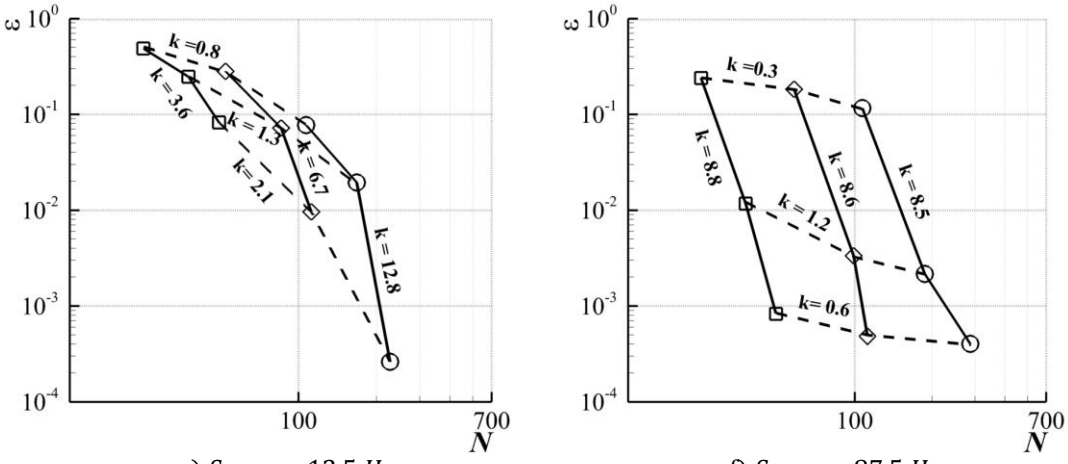

e) S wave, 12.5 Hz f) S wave, 87.5 Hz

Figure 3.20: Convergence results in biphasic dynamic problems (HTD)

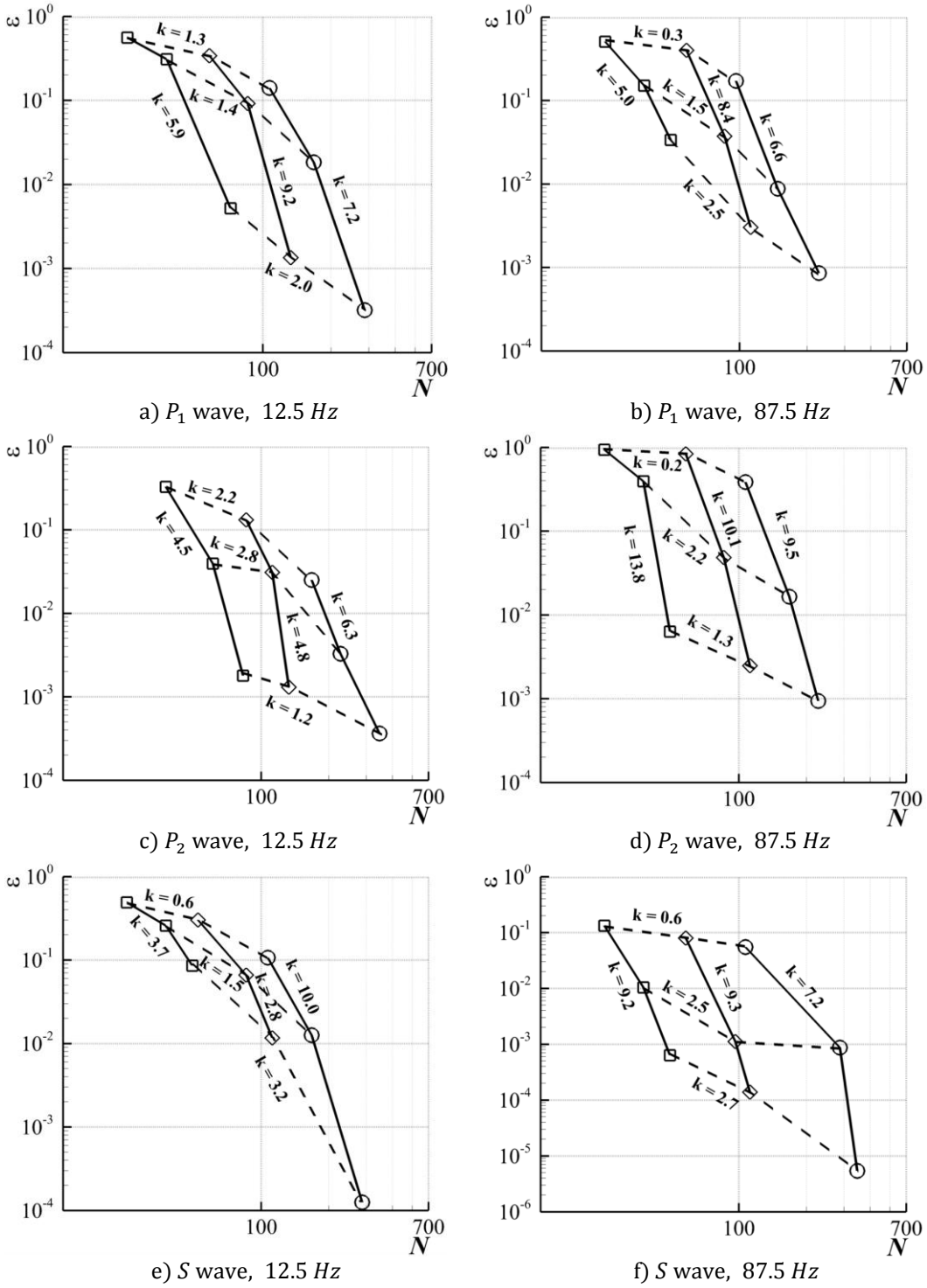

a) P_1 wave, 12.5 Hz b) P_1 wave, 87.5 Hz

c) P_2 wave, 12.5 Hz d) P_2 wave, 87.5 Hz

e) S wave, 12.5 Hz f) S wave, 87.5 Hz

Figure 3.21: Convergence results in biphasic dynamic problems (HTS)

3.4.2 Sensitivity to mesh distortion

To assess the mesh distortion sensitivity of the hybrid-Trefftz displacement and stress elements, the testing problem described above, which is only conducted for S wave and the spectral

frequency $12.5Hz$, is solved using the mesh represented in Figure 3.6, with $L = \frac{r}{2} = 5m$. The distortion scheme shown in that figure is used, with the distortion parameter, η, still ranging from 10^{-1} to 10^{-10}. The error measure is defined by equation (3.74) and the maximum order of the domain approximation functions is eleven for all tests.

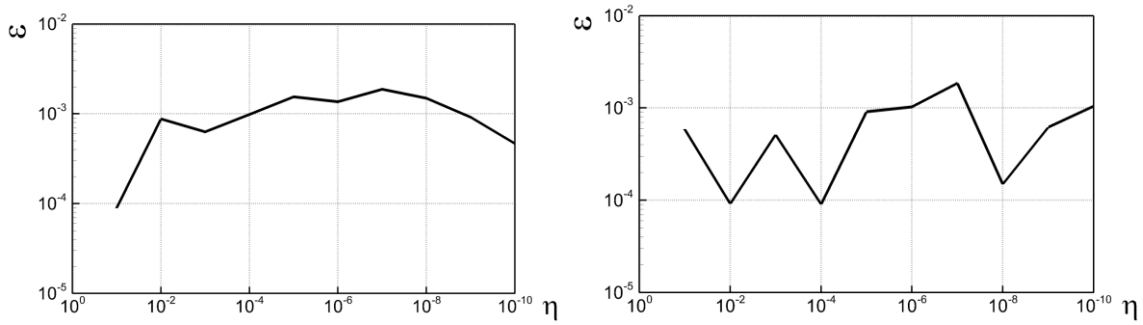

a) Displacement model b) Stress model

Figure 3.22: Sensitivity to mesh distortion in biphasic dynamic problems

Figure 3.22 presents the variation of the error measure ε with the distortion parameter η. The displacement and stress models remain basically insensitive to gross mesh distortion. In relative terms, the stress model seems to perform slightly better than the displacement model, although in absolute terms the errors are small in both cases.

3.4.3 Sensitivity to near-incompressibility

The procedure to assess sensitivity of the hybrid-Trefftz elements for static problems is repeated, under the same conditions and with definition (3.75) for the Poisson ratio of the mixture. As for the mesh distortion test, the analytic solution corresponds to an S wave with a spectral frequency of $12.5Hz$. The domain is meshed into four finite elements, as shown in Figure 3.4. The maximum order of the domain approximation functions is eleven. These functions are not adapted to accommodate media with low compressibility.

The sensitivity parameter, η, varies from 10^{-1} to 10^{-9}. For each value of parameter η, the energy error ε is calculated using the adapted form of definition (3.73). The results obtained are presented in Figure 3.23 and show that both models are virtually insensitive to the increases of the Poisson ratio up to limit used, $\nu = 0.5 - 10^{-9}$.

The justification for this level of robustness is the same as presented for static problems, namely the physical content of the Trefftz approximation functions, which locally respect the

domain elasticity equation, despite the high values of the bulk moduli. Significant degradation of the predicted results may, however, be caused by loss of numerical precision (the tests are ran using double precision).

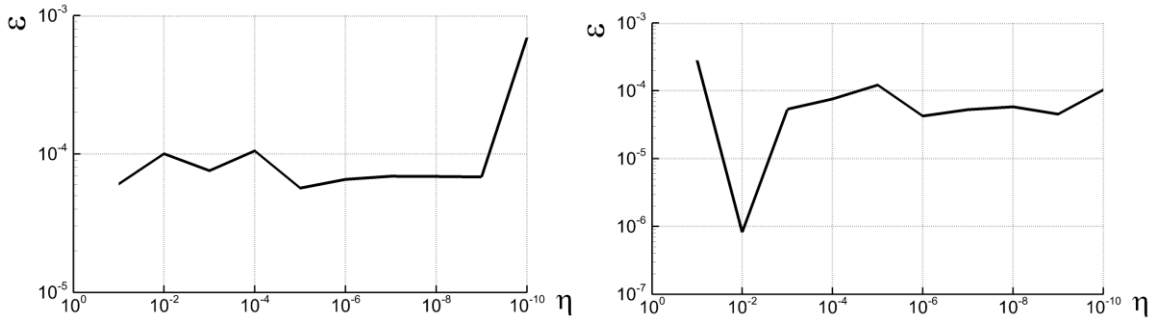

a) Displacement model b) Stress model

Figure 3.23: Sensitivity to near-incompressibility in biphasic dynamic problems

3.4.4 Sensitivity to frequency content

The same domain used for the convergence tests is modelled with a single finite element (Figure 3.4) and the robustness tests are implemented for S waves and frequencies varying between $5Hz$ and $1{,}500Hz$. The levels of p-refinement are varied according to the numerical difficulty of the analyzed problem.

Figure 3.24 represents the variation of the error measure defined by relation (3.73) and of the wavelength of the induced S wave as a function of the excitation frequency (the wavelength axis is logarithmic). The tested wavelengths cover a rather wide range, from $6.7m$ to $0.24m$. The solid and dashed lines represent the variation of the error measures and the wavelength, respectively.

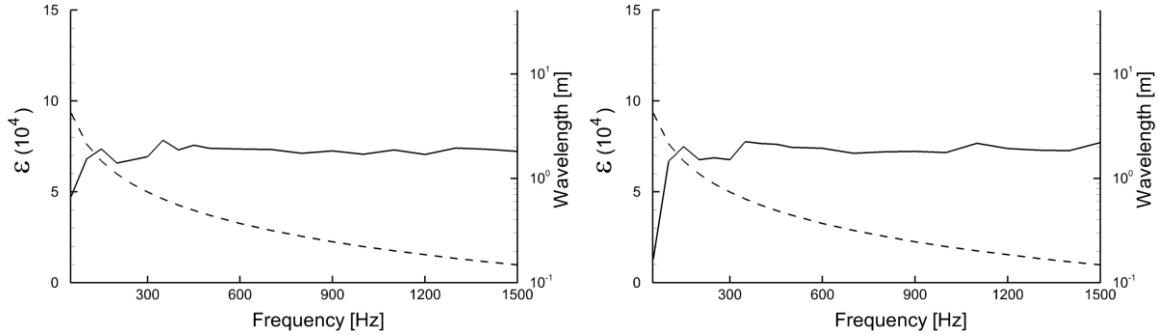

a) Displacement model b) Stress model

Figure 3.24: Sensitivity to high frequency excitations in biphasic dynamic problems

The accuracy of the results in Figure 3.24 shows that, in relative terms, both the stress model and displacement models of the hybrid-Trefftz elements perform well for all tested frequencies. It means that both models are basically insensitive to frequency variations in the saturated Molsand soil under testing.

3.4.5 Solution of periodic problems

The problem defined in Figure 3.25 is solved, under plane strain conditions, to illustrate the ability of the hybrid-Trefftz elements to recover the inter-element continuity and the prescribed boundary conditions under harmonic loading.

The biphasic medium is confined in a square tank ($L0 = 2.0m$, $L1 = 3.0m$) subjected to a surface loading $f = \bar{p} \cdot exp(\hat{\imath}\omega t)$, with amplitude $\bar{p} = 1\ (Pa)$, acting on the solid skeleton. The boundary conditions used in the steady-state test are adopted here: free surface flow of the fluid phase; constrained normal displacements in the solid phase and the fluid seepage along the walls of the container; unconstrained tangential displacements on the frictionless tank walls.

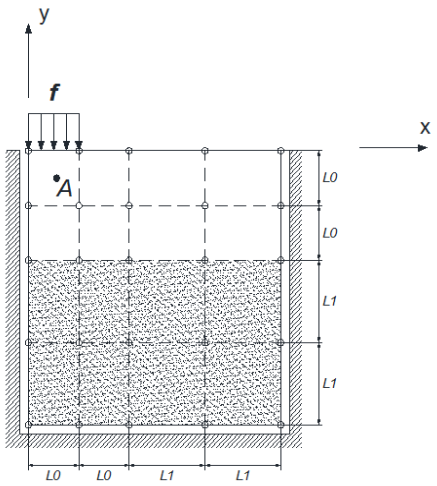

Figure 3.25: Finite element model for test

The two materials have the same hydraulic conductivity $k = 0.0001m/s$. The upper layer is a water-saturated Molsand soil with a Young's modulus reduced to half the value given in the appendix E. The material in the lower layer has the same properties, except for the Young's modulus, which is eight times larger ($E_{lower}/E_{upper} = 8$). The 16-element shown in Figure 3.25 is used.

Both stress and displacement models are tested with two excitation frequencies, $12.5Hz$ and $200Hz$, in order to illustrate their relative performance under rather distinct situations. The wavelengths in the upper layer are $\lambda = 0.78m$ for the high frequency test and $\lambda = 11.66m$ for the low frequency test. The corresponding numbers in the lower layer are $2.2m$ and $32.0m$, respectively.

For both testing frequencies, the domain approximation bases for the displacement and stress models are constructed using first kind Bessel functions of order $N_d = 13$. The boundary approximation is defined using Tchebychev polynomials with degree $M = 5$. The total number of degrees of freedom for displacement model is 1,824 (1,296 displacement modes and 528 boundary force modes). The stress model is implemented using 1,824 degrees of freedom (1,296 stress modes and 528 boundary displacement modes).

The amplitudes and contours of the stress fields are shown in Figures 3.26 and 3.27 for the displacement model and in Figures 3.28 and 3.29 for the stress model. The results clearly show that the inter-element continuity conditions are well respected and that the assumed boundary conditions are accurately recovered despite the significant physical differences of wave propagation phenomena for the two testing frequencies. The tests also indicate a good agreement between the responses predicted by the alternative models. As before, no smoothing is used in the graphs.

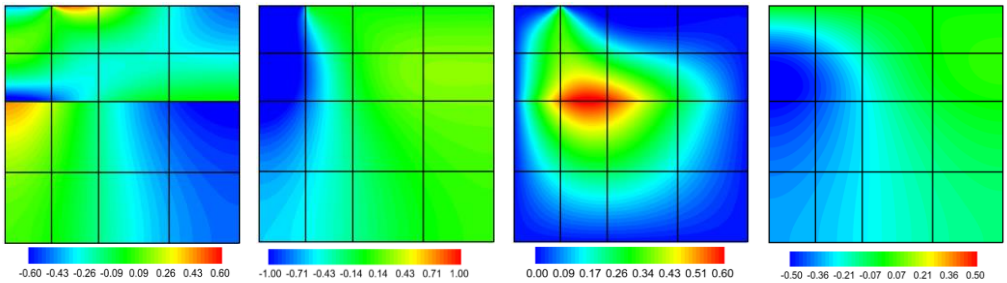

σ_{xx}(Pa) σ_{yy}(Pa) σ_{xy} (Pa) π(Pa)

Figure 3.26: Stress fields for displacement element ($\boldsymbol{\omega = 12.5\ Hz}$)

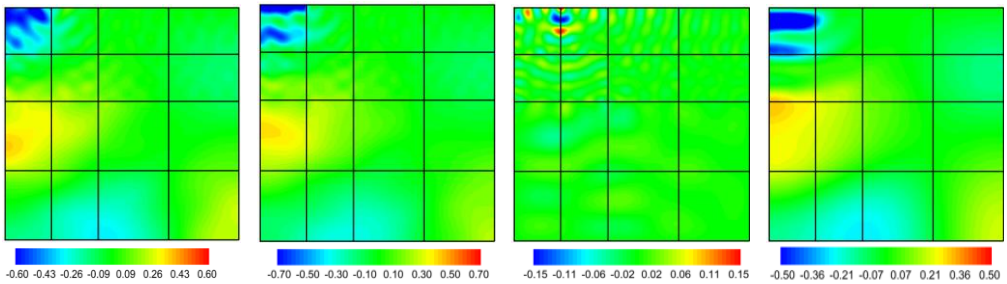

σ_{xx}(Pa) σ_{yy}(Pa) σ_{xy} (Pa) π(Pa)

Figure 3.27: Stress fields for displacement element ($\boldsymbol{\omega = 200\ Hz}$)

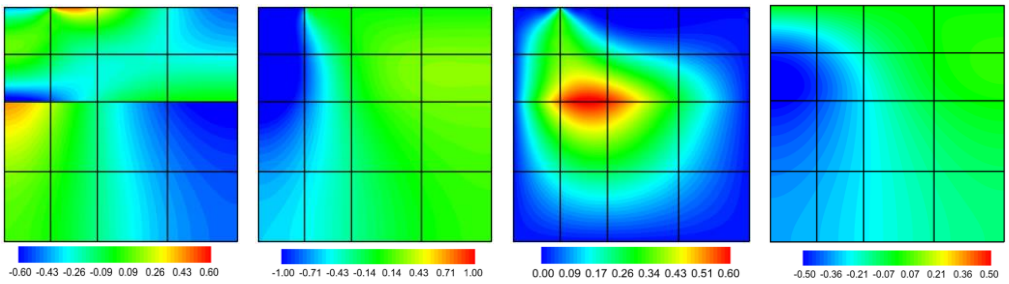

σ_{xx}(Pa) σ_{yy}(Pa) σ_{xy} (Pa) π(Pa)

Figure 3.28: Stress fields for stress element ($\boldsymbol{\omega = 12.5\ Hz}$)

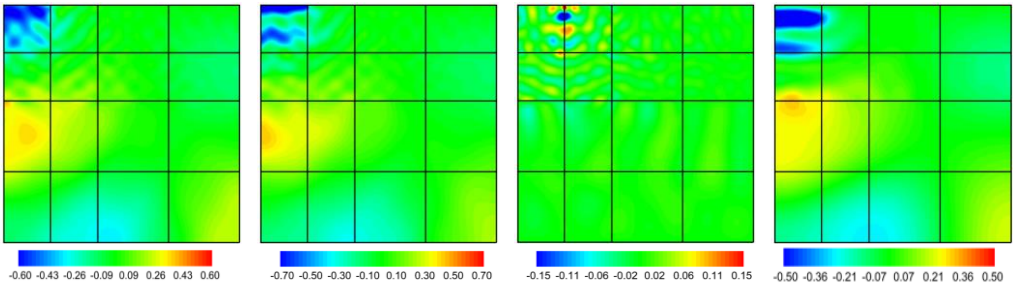

σ_{xx}(Pa) σ_{yy}(Pa) σ_{xy} (Pa) π(Pa)

Figure 3.29: Stress fields for stress element ($\boldsymbol{\omega = 200\ Hz}$)

It should be noted that the same (coarse) mesh is used to solve both problems, despite the difference between the excitation frequencies and consequently between the wavelengths of the propagating waves, thus reinforcing the lack of sensitivity of the models to the wavelength of the

propagating waves. It is recalled that, for conventional finite elements, the recommended element size should not exceed 1/8 of the excitation wavelength [125].

3.4.6 Solution of transient problems

The problem defined in Figure 3.25 is solved in the time domain to illustrate the ability of the hybrid-Trefftz displacement (HTD) and stress (HTS) elements to recover solutions of a saturated consolidation test. The same dimensions, material properties and boundary conditions and the same finite element mesh are used, the difference being that a step-load, $f = \bar{p} \cdot H(t)$ is applied, where $\bar{p}$ is the (unit) amplitude and $H(t)$ the Heaviside function.

The time basis is built with Legendre polynomials with degree 1, 3 and 5 (p-refinement in time) corresponding to 2, 4 and 6 pseudo-spectral problems in the time interval $t_0 = 0.0\,sec$ to $t_{max} = 1.0\,sec$. Both single- and multi-step analyses are performed, in the latter case with as many time steps as needed to attain convergence (h-refinement in time), as illustrated in Figure 3.30. Convergence and stability of the time integration procedure presented in Section 2.3.2 and of hybrid-Trefftz elements is assessed using strategy for implementing the particular solution defined in Section 2.5.

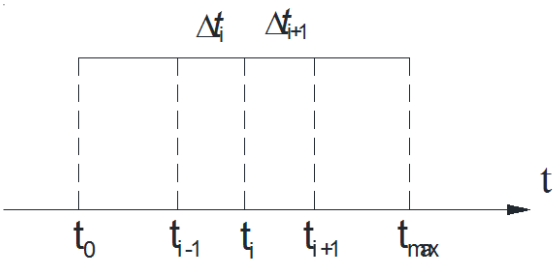

Figure 3.30: time steps for test model

In the upper layer, the Legendre time approximation bases generate a maximum complex frequency with absolute value $78.4Hz$. The P_1, P_2 and S wave velocities are $1{,}491.3m/s$, $18.5m/s$ and $145.3\,m/s$, for wavelengths of $119.5\,m$, $1.4\,m$ and $11.6\,m$. The corresponding values for the lower layer are wave velocities of $1{,}677.8m/s$, $46.5m/s$ and $410.9m/s$ and wavelengths of $134.4m$, $3.7m$ and $32.9m$.

The convergence under p- and h- refinement in time is illustrated comparing the variation of the pore pressure measured at point A, shown in Figure 3.25, with coordinates $(+1, -1)$. The reference ('exact') solution is obtained using ABAQUS™ with a mesh of 40,000 CPE4P finite

elements, with a total of 121,203 degrees of freedom. The ABAQUS^{TM} solution is obtained in 128 time steps and using Newton's backward difference method.

The domain approximation bases for both displacement and stress models are constructed using first kind Bessel functions of maximum order $N_d = 13$ and using polynomial functions of maximum degree $N_s = 9$. The boundary approximation is defined on Tchebychev polynomials, with the maximum degree $M = 5$. The total number of degrees of freedom for displacement model is 2,512 (1,936 displacement modes and 576 surface force modes). The stress model is implemented with 2,384 degrees of freedom (1,808 stress modes and 576 boundary displacement modes).

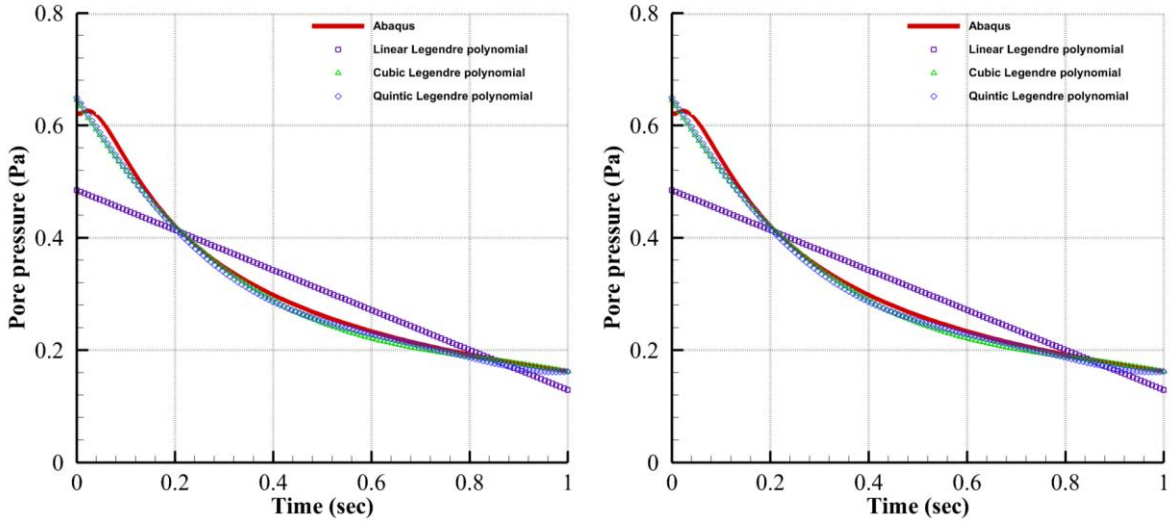

a)HTD b) HTS

Figure 3.31: Single step solutions of the pore pressure time-history at point A

Figure 3.31 shows the time-history of the pore pressure at testing point A obtained with the HTD and HTS models, as well as the predictions obtained with Newton's backward method as implemented in ABAQUS^{TM}. The time discretization is performed on a single time step and different p-refinement levels (linear, cubic and quintic Legendre polynomials).

The solutions obtained with a linear approximation in time and 4, 8, 16 and 32 time steps (h-refinement in time) are shown in Figure 3.32 for the displacement element and in Figure 3.33 for the stress element.

Figures 3.34 to 3.37 present the stress fields in the solid phase and the pore pressure in the liquid phase at five instants of the analysis. They are obtained with a linear approximation in

time and 16 time steps. Also shown are the ABAQUS^{TM} solutions obtained under the conditions defined above.

Those results clearly show that the boundary conditions and the inter-element continuity conditions are adequately modelled. Regarding the ABAQUS^{TM} solution (121,203 degrees of freedom and 128 time steps), the main difference in the hybrid-Trefftz solution (circa 2,500 degrees of freedom and 16 time steps) is on the estimate of the σ_{xx} stress field.

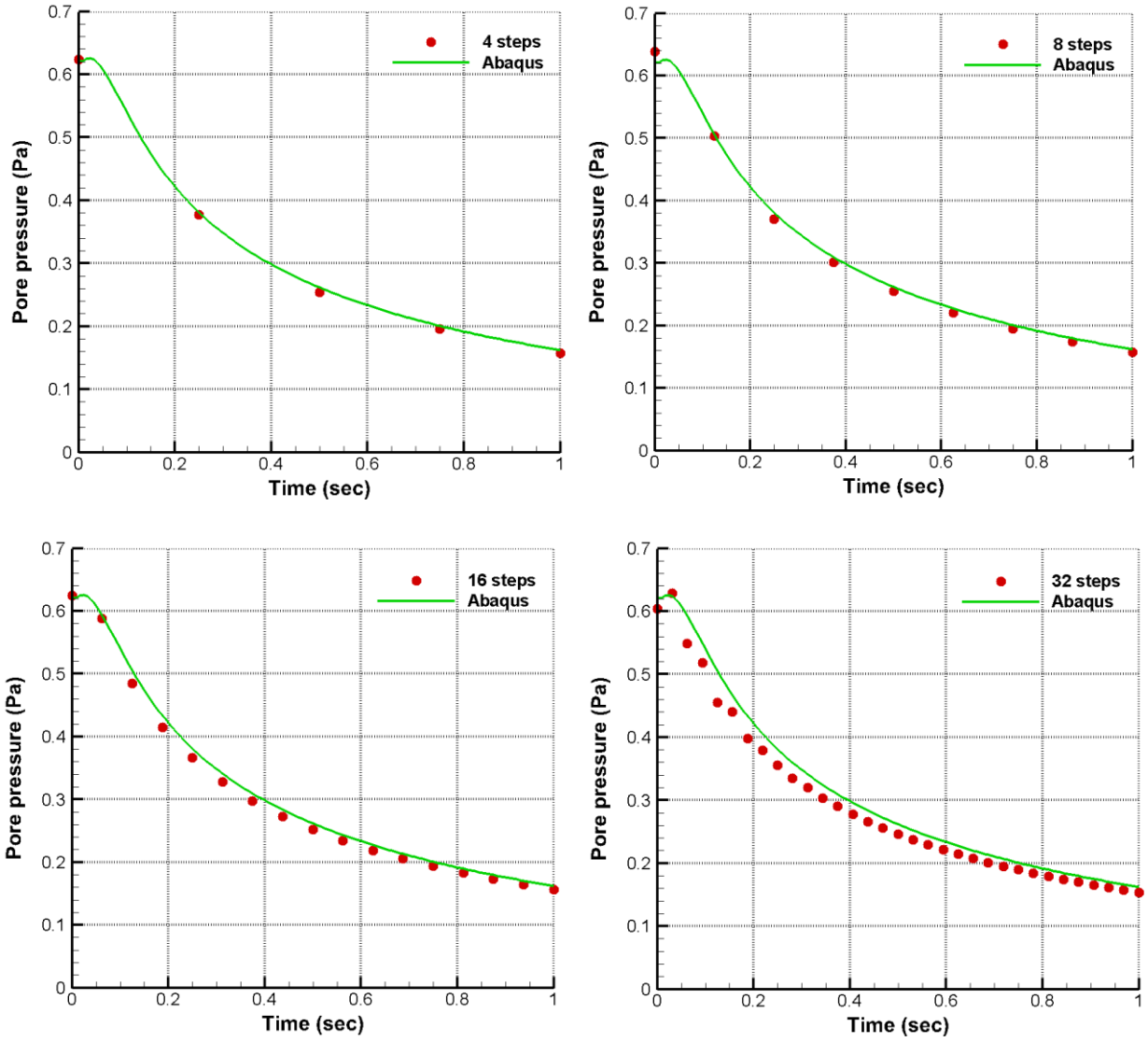

Figure 3.32: Linear, multi-step solutions of the pore pressure time-history at point A (HTD)

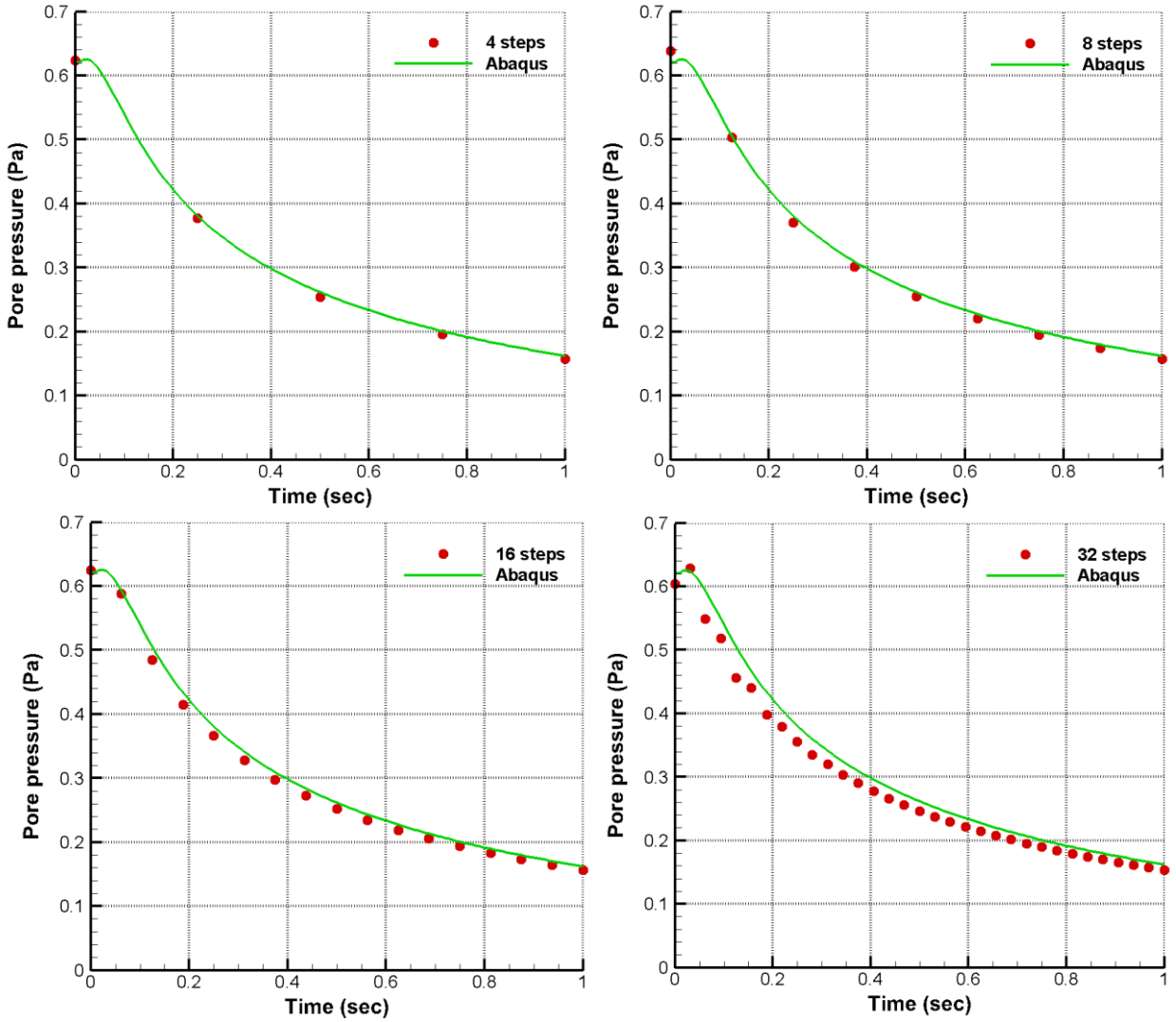

Figure 3.33: Linear, multi-step solutions of the pore pressure time-history at point A (HTS)

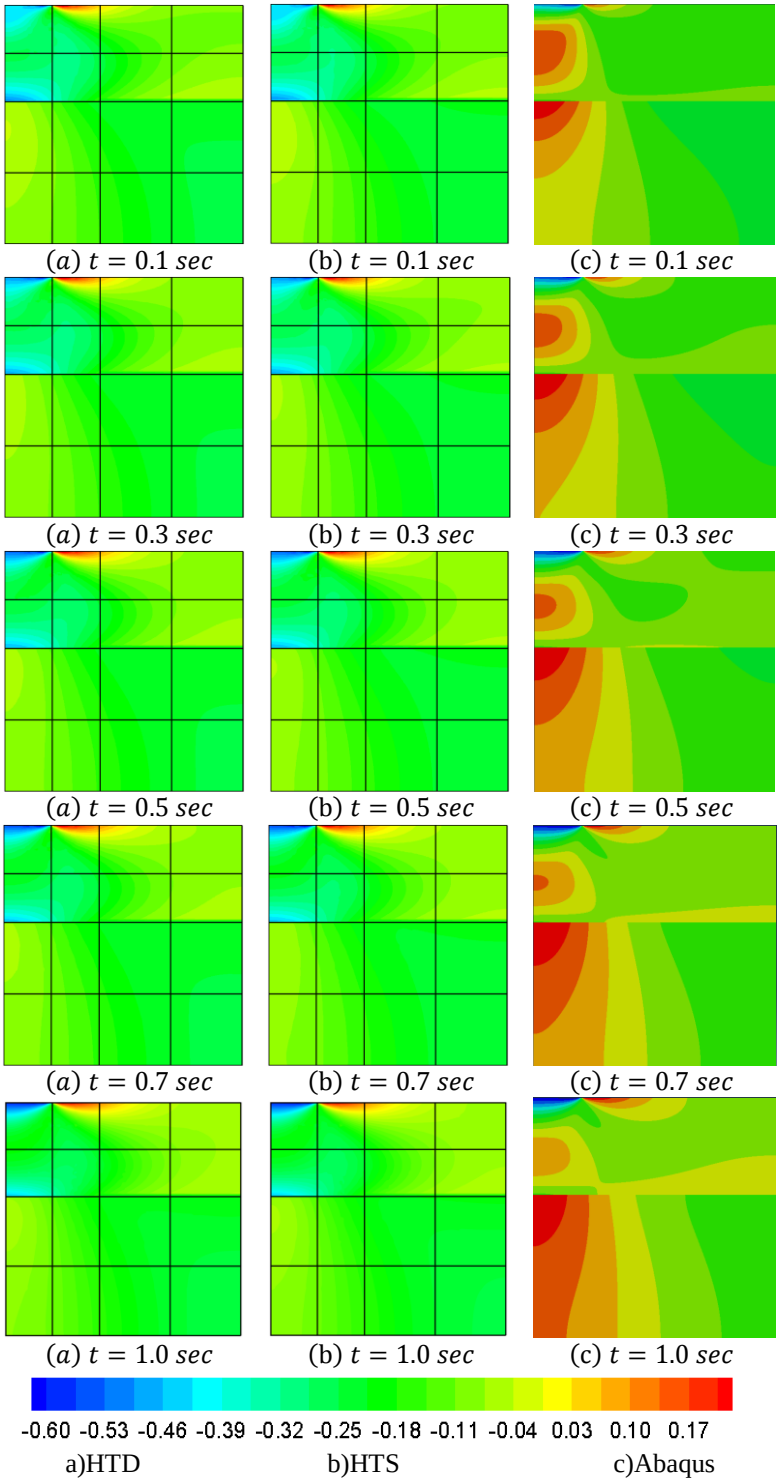

Figure 3.34: σ_{xx} (Pa) diagrams at selected time points

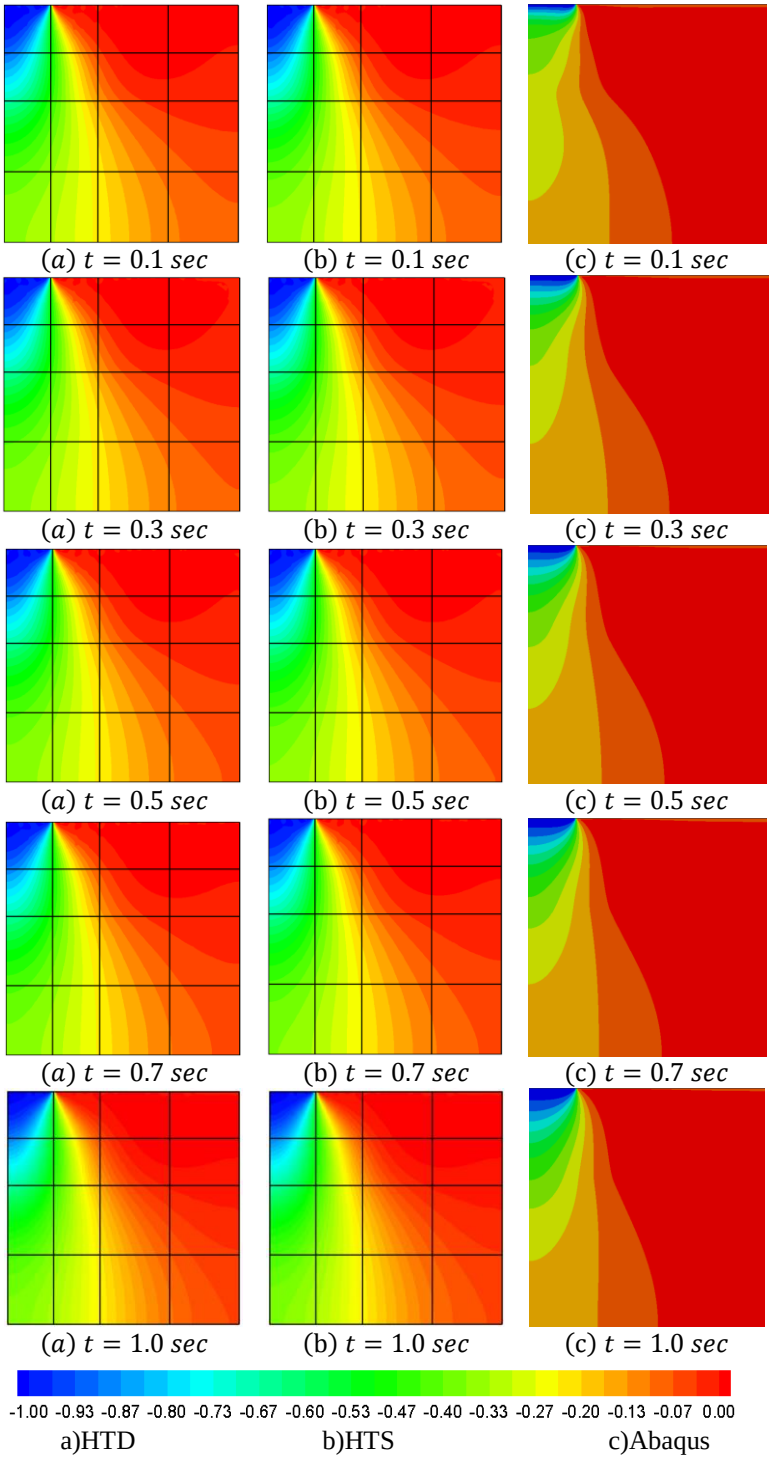

Figure 3.35: σ_{yy} (Pa) diagrams at selected time points

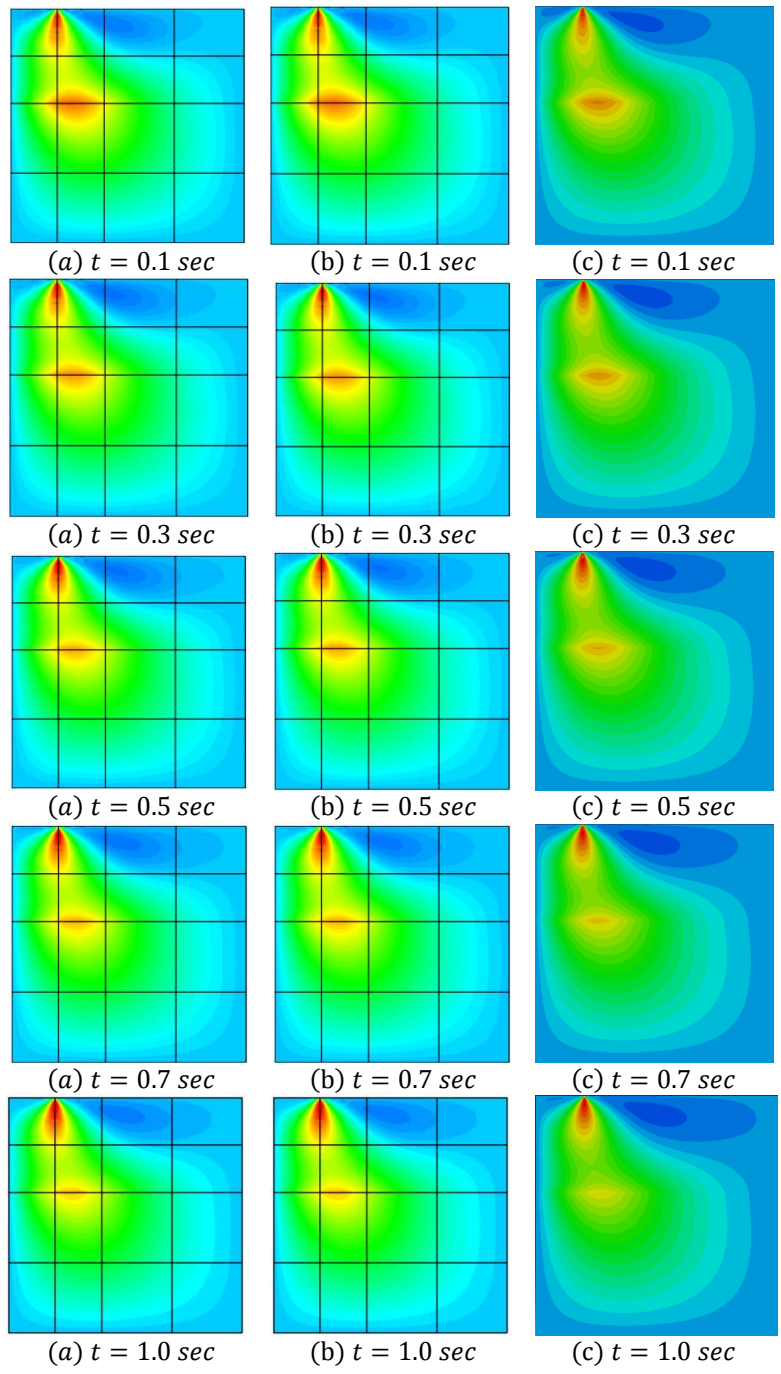

Figure 3.36: σ_{xy}(Pa) diagrams at selected time points

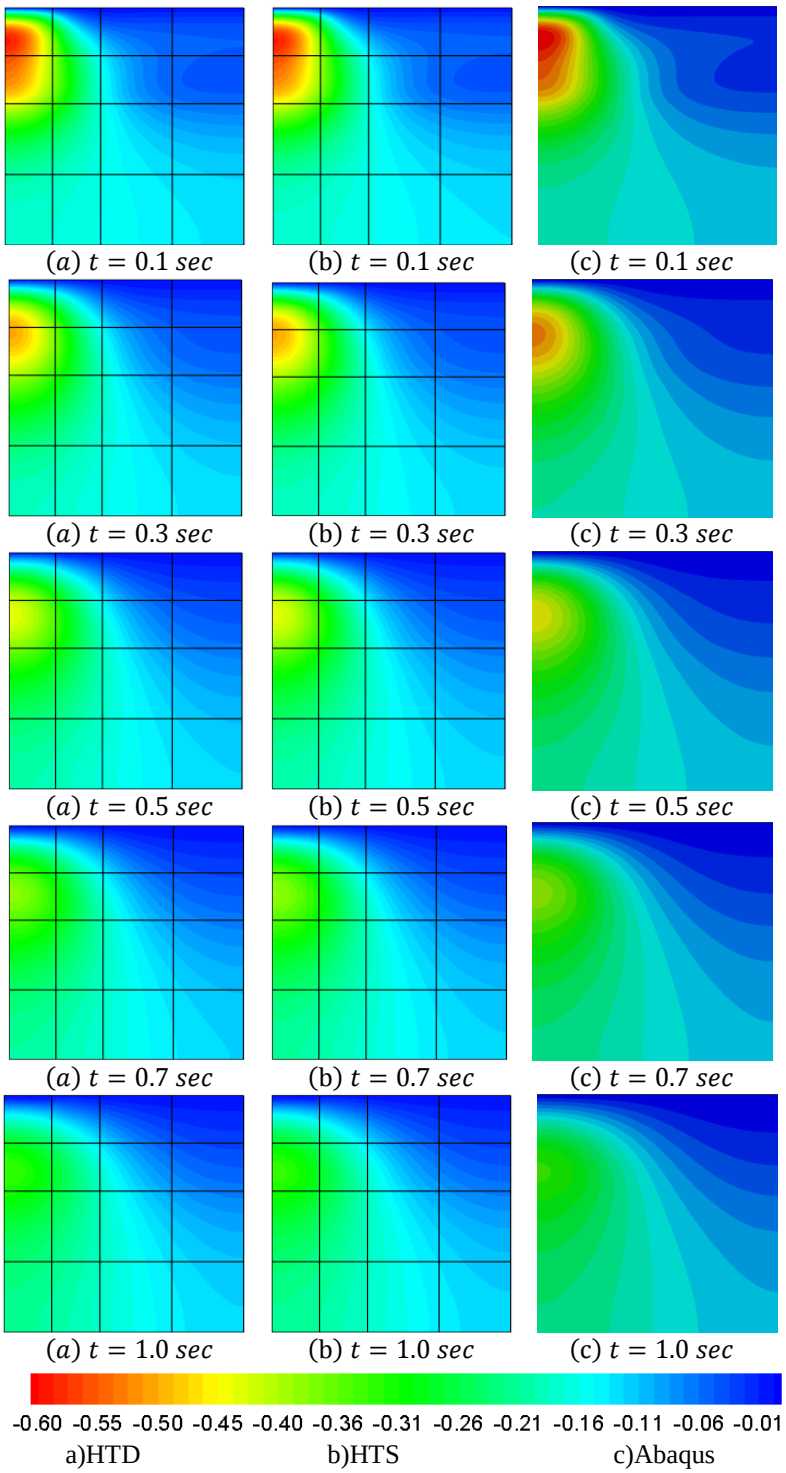

Figure 3.37: π (Pa) diagrams at selected time points

The results presented above show that the multi-stepping method suggested in Chapter 2 for elastodynamic analyses perform reasonably well, considering that the ABAQUS^{TM} solutions are close to full convergence. Further work is being done to simplify the programming of the algorithm and to extend the methods for the elastoplastic analysis of porous media.

The tests only show that p- and h-convergence in time is similar for both displacement and stress models.

Chapter 4

Hybrid-trefftz elements for triphasic media

The study presented in Chapter 3 is extended to the analysis of triphasic media (unsaturated soils) using the displacement and stress models of the hybrid-Trefftz variant of the finite element method, as reported in [55], [56] and [110].

The mathematical formulation is based on the linear elastic theory of mixtures with interfaces [97]. This thermodynamically consistent model is applied to problems defined on pervious and semi-pervious media, where the fluid seepage is driven by the action of external forces rather than by equilibrated capillary forces (swelling). Unlike most of the finite element models reported in the literature, the full coupling between the solid, fluid and gas phases is considered here.

The first two sections address basic issues in the solution of static and dynamic problems, namely the definition of the mathematical models and of the resulting expressions for the Trefftz approximation bases and the characterization of the structure and the indeterminacy numbers for the algebraic systems of equations that are obtained for the HTD and HTS elements. However, the presentation of the numerical testing results is restructured and scaled down in content to minimize duplication.

Convergence under p- and h-refinement is presented in Section 4.3 for both static and dynamic analyses because of their relevance in terms of numerical modelling. For the same reason, the sensitivity of both hybrid-Trefftz models to the frequency content of the excitation of triphasic media is presented in Section 4.4.

Sensitivity to gross mesh distortion, presented in Section 4.5, is only illustrated for static problems because the results under dynamic conditions are basically equivalent to those reported for biphasic media.

The illustration of the performance of hybrid-Trefftz elements in the analysis of steady-state and dynamic response of triphasic media is presented in the closing sections of this chapter, Sections 4.6, 4.7 and 4.8 respectively. Two dynamic applications are selected for tests on both periodic and transient problems. The response of a single-layer medium is used to illustrate the

propagation of the different types of waves in unsaturated soils. The effect material discontinuities have on wave propagation is illustrated using a two-layer medium.

4.1 Formulation of static problems

Closed-form solutions of the governing equations are derived, in cylindrical coordinates, for elastostatic triphasic problem. They are used to construct the domain approximation bases of the hybrid-Trefftz elements. As for the modelling of biphasic media, the hybrid-Trefftz displacement and stress model differ, essentially, on the type of boundary condition that is explicitly enforced, namely displacement continuity in the displacement model and traction continuity in the stress mode.

4.1.1 Mathematical model

Let V and Γ represent the domain and the boundary of the triphasic body under analysis, as represented in Figure 2.1. The decomposition of the boundary still follows the definitions given in Section 2.1.

The equilibrium, compatibility and elasticity equations (2.2), (2.3) and (2.11) governing the static response of the body still hold. However, in those expressions the independent components of the (total) stress tensor in the solid phase, σ^S, and the pore pressures in the wetting and non-wetting phases, π^W and π^N, are collected in vector $\boldsymbol{\sigma}(x,y) = \{\sigma^S \quad \pi^W \quad \pi^N\}^T$. Similarly, the independent components of the strain tensor in the solid phase, ε^S, and the fluid contents, ζ^W and ζ^N, are collected in vector $\boldsymbol{\varepsilon}(x,y) = \{\varepsilon^S \quad \zeta^W \quad \zeta^N\}^T$. Vector $\boldsymbol{u}(x,y) = \{u^S \quad u^W \quad u^N\}^T$ collects the displacement components in each phase.

The homogeneous Navier equation defined in equation (2.12) still holds,

$$\boldsymbol{\mathcal{D}k\mathcal{D}^*u} = \mathbf{0} \quad \text{in } V \tag{4.1}$$

under the following specialization, according to the definitions summarized in Appendix A:

$$\begin{cases} \boldsymbol{\nabla\nabla}^T[(M_{SS} + n^S\mu^S)\boldsymbol{u}^S + M_{SW}\boldsymbol{u}^W + M_{SN}\boldsymbol{u}^N] + n^S\mu^S\boldsymbol{\nabla}^2\boldsymbol{u}^S = \mathbf{0} \\ \boldsymbol{\nabla\nabla}^T[M_{SW}\boldsymbol{u}^S + M_{WW}\boldsymbol{u}^W + M_{WN}\boldsymbol{u}^N] = \mathbf{0} \\ \boldsymbol{\nabla\nabla}^T[M_{sN}\boldsymbol{u}^S + M_{WN}\boldsymbol{u}^W + M_{NN}\boldsymbol{u}^N] = \mathbf{0} \end{cases} \tag{4.2}$$

The solutions of system (4.2) are obtained using biharmonic and harmonic potentials, generating coupled ($\boldsymbol{U}_b$) and uncoupled ($\boldsymbol{U}_h$) pressure-free displacement modes, respectively.

These functions are included in the solution space $\boldsymbol{U}_s = \{\boldsymbol{U}_b \quad \boldsymbol{U}_h \quad \boldsymbol{U}_W \quad \boldsymbol{U}_N\}^T$, along with two constant pore pressure modes, one for each of the fluid phases. Stress-free modes satisfying system (4.2) are also found and collected in the solution space $\boldsymbol{U}_r = \{\boldsymbol{U}_{rs} \quad \boldsymbol{U}_{rW} \quad \boldsymbol{U}_{rN}\}^T$. They correspond to rigid-body displacements in the solid phase and to pure flow in each of the fluid phases. These solution sets are defined next.

❖ **Biharmonic solutions**

When biharmonic potentials are used to construct the solution set $\boldsymbol{U}_b$, they generate one single linear displacement mode and a series of complex conjugate displacement modes of higher degree. In the meantime, $\boldsymbol{U}_b$ and $\boldsymbol{S}_b$ collect the radial and tangential components of the respective fields.

The linear displacement mode and the associated constant stress field are,

$$\boldsymbol{U}_{b_0} = \begin{bmatrix} 1 \\ 0 \\ -\alpha_W \\ 0 \\ -\alpha_N \\ 0 \end{bmatrix} r \tag{4.3}$$

$$\boldsymbol{S}_{b_0} = 2\left(\bar{\lambda} + n^S \mu^S\right) \begin{bmatrix} 1 \\ 1 \\ 0 \\ 0 \\ 0 \\ 0 \end{bmatrix} \tag{4.4}$$

where, according to definitions of stiffness moduli in Appendix A:

$$\begin{bmatrix} \alpha_W \\ \alpha_N \end{bmatrix} = M^{-1} \begin{bmatrix} M_{NN} & -M_{WN} \\ -M_{WN} & M_{WW} \end{bmatrix} \begin{bmatrix} M_{SW} \\ M_{SN} \end{bmatrix} \tag{4.5}$$

$$M = M_{WW} M_{NN} - M_{WN}^2 \tag{4.6}$$

$$\bar{\lambda} = M_{SS} - M_{SW}\alpha^W - M_{SN}\alpha^N \tag{4.7}$$

The regular, higher-degree displacement and stress modes have the following expressions, with $n \geq 1$:

$$\boldsymbol{U}_{b_n} = \frac{1}{2(n+1)n^S\mu^S}\begin{bmatrix} \left[\left(\bar{\lambda}+3n^S\mu^S\right)-(n+1)\left(\bar{\lambda}+n^S\mu^S\right)\right] \\ \pm\hat{\imath}\left[\left(\bar{\lambda}+3n^S\mu^S\right)+(n+1)\left(\bar{\lambda}+n^S\mu^S\right)\right] \\ -2\alpha^W n^S\mu^S \\ \pm 2\hat{\imath}\alpha^W n^S\mu^S \\ -2\alpha^N n^S\mu^S \\ \pm 2\hat{\imath}\alpha^N n^S\mu^S \end{bmatrix} r^{n+1}\, exp[\pm\hat{\imath}\, n\theta] \qquad (4.8)$$

$$\boldsymbol{S}_{b_n} = \begin{bmatrix} -(n-2)\left(\bar{\lambda}+n^S\mu^S\right) \\ (n+2)\left(\bar{\lambda}+n^S\mu^S\right) \\ \pm\hat{\imath}\, n\left(\bar{\lambda}+n^S\mu^S\right) \\ 0 \\ 0 \end{bmatrix} r^n\, exp[\pm\hat{\imath}\, n\theta] \qquad (4.9)$$

❖ **Harmonic solutions**

When harmonic potentials are used to construct the solution set $\boldsymbol{U}_h$, they generate deviatory modes with static fluid behaviour. For degrees $n \geq 0$, pairs of complex conjugate solutions of the Navier equation (4.1) are obtained:

$$\boldsymbol{U}_h = \frac{1}{2(n+1)n^S\mu^S}\begin{bmatrix} 1 \\ \pm\hat{\imath} \\ 0 \\ 0 \\ 0 \\ 0 \end{bmatrix} r^{n+1}\, exp[\pm\hat{\imath}\,(n+2)\theta] \qquad (4.10)$$

$$\boldsymbol{S}_h = \begin{bmatrix} 1 \\ -1 \\ \pm\hat{\imath} \\ 0 \\ 0 \end{bmatrix} r^n\, exp[\pm\hat{\imath}\,(n+2)\theta] \qquad (4.11)$$

❖ **Constant fluid pressure modes**

If a constant pore pressure is applied to one of the fluid phases, it generates an hydrostatic state of stress $\boldsymbol{S}_f$ and a radial fluid displacement field $\boldsymbol{U}_f$, with $f = \{W, N\}$:

$$\boldsymbol{U}_W = \frac{1}{2M}\begin{bmatrix} 0 \\ 0 \\ M_{NN} \\ 0 \\ -M_{WN} \\ 0 \end{bmatrix} r \qquad (4.12)$$

$$\boldsymbol{S}_W = \begin{bmatrix} \alpha^W \\ \alpha^W \\ 0 \\ 1 \\ 0 \end{bmatrix} \tag{4.13}$$

$$\boldsymbol{U}_N = \frac{1}{2M} \begin{bmatrix} 0 \\ 0 \\ -M_{WN} \\ 0 \\ M_{WW} \\ 0 \end{bmatrix} r \tag{4.14}$$

$$\boldsymbol{S}_N = \begin{bmatrix} \alpha^N \\ \alpha^N \\ 0 \\ 0 \\ 1 \end{bmatrix} \tag{4.15}$$

❖ **Stress – free modes**

Besides the stress generating modes described above, the following rigid-body displacement modes defined on the solid phase also satisfy the Navier equation (4.1),

$$\boldsymbol{U}_{rs} = \begin{bmatrix} 0 & cos\,\theta & sin\,\theta \\ r & -sin\,\theta & cos\,\theta \end{bmatrix} \tag{4.16}$$

In the fluid phases, five linear free flow modes are identified,

$$\boldsymbol{U}_{rf} = \begin{bmatrix} cos\,\theta & sin\,\theta & 0 & r\,sin\,2\theta & r\,cos\,2\theta \\ -sin\,\theta & cos\,\theta & r & r\,cos\,2\theta & -r\,sin\,2\theta \end{bmatrix} \tag{4.17}$$

along with $n+2$ free flow modes of degree $n \geq 2$, with $0 \leq k \leq n-1$:

$$\boldsymbol{U}_{df} = \begin{bmatrix} sin^n\,\theta\,cos\,\theta & sin\,\theta\,cos^n\,\theta & (k + cos^2\,\theta - n\,sin^2\,\theta)\,sin^k\,\theta\,cos^{n-k-1}\,\theta \\ -sin^{n+1}\,\theta & cos^{n+1}\,\theta & -(1+n)\,sin^{k+1}\,\theta\,cos^{n-k}\,\theta \end{bmatrix} r^n \tag{4.18}$$

4.1.2 Trefftz approximation bases

The Trefftz bases are constructed combining the biharmonic, harmonic, two constant pore pressure, rigid body and pure flow modes defined above. In the domain of the element, the explicit forms of the hybrid-Trefftz approximations (2.13) and (2.34) for elastostatic problems are,

$$\boldsymbol{u} = \boldsymbol{U}_s\boldsymbol{X}_s + \boldsymbol{U}_W X_W + \boldsymbol{U}_N X_N + \boldsymbol{U}_{rs}\boldsymbol{X}_{rs} + \boldsymbol{U}_{rdW}\boldsymbol{X}_{rdW} + \boldsymbol{U}_{rdN}\boldsymbol{X}_{rdN} + \boldsymbol{u}_0 \tag{4.19}$$

$$\boldsymbol{\sigma} = \boldsymbol{S}_s\boldsymbol{Y}_s + \boldsymbol{S}_W Y_W + \boldsymbol{S}_N Y_N + \boldsymbol{\sigma}_0 \tag{4.20}$$

where the following notation is used:

$$\boldsymbol{U}_s = (\boldsymbol{U}_{b_0} \quad \boldsymbol{U}_{b_n} \quad \boldsymbol{U}_h) \tag{4.21}$$

$$\boldsymbol{S}_s = (\boldsymbol{S}_{b_0} \quad \boldsymbol{S}_{b_n} \quad \boldsymbol{S}_h) \tag{4.22}$$

$$\boldsymbol{U}_{rdW} = (\boldsymbol{U}_{rW} \quad \boldsymbol{U}_{dW}) \tag{4.23}$$

$$\boldsymbol{U}_{rdN} = (\boldsymbol{U}_{rN} \quad \boldsymbol{U}_{dN}) \tag{4.24}$$

The stress and displacement bases satisfy conditions (2.11), (2.2) and (2.3), consequently, the Trefftz conditions listed in Table 1. The generalized displacement and stress weights $\boldsymbol{X}_j$ and stresses $\boldsymbol{Y}_j$ should be equal upon full convergence of the alternative HTD and HTS models, for each phase $j = \{s, W, N\}$.

In general, the bases are implemented at element level and expressed in a local (polar) system of reference with origin at the barycenter of the element and axes parallel to the principal directions of the element. It is stressed that this form of implementation of Trefftz bases is used in all tests presented in this chapter.

The dimension of basis S_s with degree d_σ is, according to equations (4.3) to (4.11),

$$N_\sigma = 4d_\sigma + 3 \tag{4.25}$$

while equations (4.17) and (4.18) set the dimension of the basis $\boldsymbol{U}_{rdf}$ with degree d_f:

$$N_f = \tfrac{1}{2}\big(d_f + 1\big)\big(d_f + 4\big) \tag{4.26}$$

4.1.3 Solving system for the displacement element

Apart from the domain approximation (4.19), independent approximations of the generalized tractions are enacted on the extended Dirichlet boundary of the hybrid-Trefftz displacement element:

$$\boldsymbol{t} = \boldsymbol{Z}_s\boldsymbol{P}_s + \boldsymbol{Z}_W\boldsymbol{P}_W + \boldsymbol{Z}_N\boldsymbol{P}_N \tag{4.27}$$

The (hierarchical) bases $\boldsymbol{Z}_s$, $\boldsymbol{Z}_W$ and $\boldsymbol{Z}_N$ are chosen such to ensure independent approximations of the normal and tangential components of the traction in the solid phase, and of the pore pressure, respectively.

The explicit form of the solving system (2.33) of the hybrid-Trefftz displacement (HTD) element is,

$$\left[\begin{array}{ccc:ccc:ccc:c} \boldsymbol{K}_{ss} & \bullet & \bullet & \bullet & \bullet & \bullet & -\boldsymbol{B}_{ss} & \bullet & \bullet & \boldsymbol{X}_s \\ \bullet & K_{WW} & \bullet & \bullet & \bullet & \bullet & \bullet & -\boldsymbol{B}_{WW} & \bullet & X_W \\ \bullet & \bullet & K_{NN} & \bullet & \bullet & \bullet & \bullet & \bullet & -\boldsymbol{B}_{NN} & X_N \\ \hdashline \bullet & \bullet & \bullet & \bullet & \bullet & \bullet & -\boldsymbol{B}_{rs} & \bullet & \bullet & \boldsymbol{X}_{rs} \\ \bullet & \bullet & \bullet & \bullet & \bullet & \bullet & \bullet & -\boldsymbol{B}_{rdW} & \bullet & \boldsymbol{X}_{rdW} \\ \bullet & \bullet & \bullet & \bullet & \bullet & \bullet & \bullet & \bullet & -\boldsymbol{B}_{rdN} & \boldsymbol{X}_{rdW} \\ \hline -\boldsymbol{B}^*_{ss} & \bullet & \bullet & -\boldsymbol{B}^*_{rs} & \bullet & \bullet & \bullet & \bullet & \bullet & \boldsymbol{P}_s \\ \hdashline \bullet & -\boldsymbol{B}^*_{WW} & \bullet & \bullet & -\boldsymbol{B}^*_{rdW} & \bullet & \bullet & \bullet & \bullet & \boldsymbol{P}_W \\ \hdashline \bullet & \bullet & -\boldsymbol{B}^*_{NN} & \bullet & \bullet & -\boldsymbol{B}^*_{rdN} & \bullet & \bullet & \bullet & \boldsymbol{P}_N \end{array}\right] \cdot \left[\begin{array}{c} \boldsymbol{X}_s \\ X_W \\ X_N \\ \hdashline \boldsymbol{X}_{rs} \\ \boldsymbol{X}_{rdW} \\ \boldsymbol{X}_{rdW} \\ \hline \boldsymbol{P}_s \\ \hdashline \boldsymbol{P}_W \\ \hdashline \boldsymbol{P}_N \end{array}\right] = \left[\begin{array}{c} \boldsymbol{t}^u_{\Gamma_s} - \boldsymbol{t}^u_{0_s} \\ t^u_{\Gamma_W} - t^u_{0_W} \\ t^u_{\Gamma_N} - t^u_{0_N} \\ \hdashline \boldsymbol{t}^u_{\Gamma_{rs}} - \boldsymbol{t}^u_{0_{rs}} \\ \boldsymbol{t}^u_{\Gamma_{rdW}} - \boldsymbol{t}^u_{0_{rdW}} \\ \boldsymbol{t}^u_{\Gamma_{rdN}} - \boldsymbol{t}^u_{0_{rdN}} \\ \hline \boldsymbol{u}^u_{0_s} - \boldsymbol{u}^u_{\Gamma_s} \\ \hdashline \boldsymbol{u}^u_{0_W} - \boldsymbol{u}^u_{\Gamma_W} \\ \hdashline \boldsymbol{u}^u_{0_N} - \boldsymbol{u}^u_{\Gamma_N} \end{array}\right] \tag{4.28}$$

where the following definitions apply, with $j = \{s, W, N\}$ for each phase:

$$\boldsymbol{K}_{jj} = \int \boldsymbol{U}^*_j (\boldsymbol{N}\boldsymbol{S}_j) d\Gamma^e \tag{4.29}$$

$$\boldsymbol{B}_{jj} = \int \boldsymbol{U}^*_j \boldsymbol{Z}_j d\bar{\Gamma}^e_u \tag{4.30}$$

$$\boldsymbol{B}_{rs} = \int \boldsymbol{U}^*_{rs} \boldsymbol{Z}_s d\bar{\Gamma}^e_u \tag{4.31}$$

$$\boldsymbol{B}_{rdW} = \int \boldsymbol{U}^*_{rdW} \boldsymbol{Z}_W d\bar{\Gamma}^e_u \tag{4.32}$$

$$\boldsymbol{B}_{rdN} = \int \boldsymbol{U}^*_{rdN} \boldsymbol{Z}_N d\bar{\Gamma}^e_u \tag{4.33}$$

$$\boldsymbol{t}^u_{\Gamma_s} = \int \boldsymbol{U}^*_s \boldsymbol{t}_\Gamma d\Gamma^e_\sigma \tag{4.34}$$

$$\boldsymbol{t}^u_{\Gamma_{rs}} = \int \boldsymbol{U}^*_{rs} \boldsymbol{t}_\Gamma d\Gamma^e_\sigma \tag{4.35}$$

$$\boldsymbol{t}^u_{\Gamma_{rdW}} = \int \boldsymbol{U}^*_{rdW} \boldsymbol{t}_\Gamma d\Gamma^e_\sigma \tag{4.36}$$

$$\boldsymbol{t}^u_{\Gamma_{rdN}} = \int \boldsymbol{U}^*_{rdN} \boldsymbol{t}_\Gamma d\Gamma^e_\sigma \tag{4.37}$$

$$\boldsymbol{t}^u_{0_s} = \int \boldsymbol{U}^*_s (\boldsymbol{N}\boldsymbol{\sigma}_0) d\Gamma^e \tag{4.38}$$

$$\boldsymbol{t}^u_{0_{rdW}} = \int \boldsymbol{U}^*_{rdW} (\boldsymbol{N}\boldsymbol{\sigma}_0) d\Gamma^e \tag{4.39}$$

$$\boldsymbol{t}^u_{0_{rdN}} = \int \boldsymbol{U}^*_{rdN} (\boldsymbol{N}\boldsymbol{\sigma}_0) d\Gamma^e \tag{4.40}$$

$$\boldsymbol{u}^u_{\Gamma_j} = \int \boldsymbol{Z}^*_j \boldsymbol{u}_\Gamma d\Gamma^e_u \tag{4.41}$$

$$\boldsymbol{u}_{0_j}^{u} = \int \boldsymbol{Z}_j^{*} \boldsymbol{u}_0 d\Gamma_u^e \tag{4.42}$$

System (4.28) provides unique estimates for the displacement and seepage fields in the domain of the element, which are computed according to definition (4.19). The stress and pore pressure fields are determined using equation (4.20), where unknowns $\boldsymbol{Y}_j$ are substituted by their counterparts, $\boldsymbol{X}_j$.

On the (extended) Dirichlet boundary of the element, definition (4.27) provides estimates for the normal and tangential components of the tractions in the solid phase and of the pressures in the fluid phases. As for the biphasic model, these estimates are not unique, because estimates for the same fields can be alternatively computed from the domain stress field using equation (4.20). The two approximations should converge to the same results upon full convergence, and can be used for the assessment of the solution error.

4.1.4 Solving system for the stress element

Expression (4.43) is used to approximate the generalized displacements on the extended Neumann boundary of the hybrid-Trefftz stress element:

$$\boldsymbol{u} = \boldsymbol{Z}_s \boldsymbol{Q}_s + \boldsymbol{Z}_W Q_W + \boldsymbol{Z}_N Q_N \tag{4.43}$$

In the above definition, basis $\boldsymbol{Z}_s$ collects functions associated to the (independent) approximations of the solid phase displacements in the boundary normal and tangential directions, while bases $\boldsymbol{Z}_W = (0 \quad 0 \quad 1 \quad 0)^T$ and $\boldsymbol{Z}_N = (0 \quad 0 \quad 0 \quad 1)^T$ are used to approximate the fluid seepage fields normal to the boundary. They are constant to avoid dependencies in the solving system, as discussed in Section 4.1.6. Basis $\boldsymbol{Z}_s$ is hierarchical, independent from the domain displacement approximation (4.19), and only constrained to completeness and linear independence conditions.

The explicit form of the solving system (2.51) of the hybrid-Trefftz stress (HTS) element is,

$$\left[\begin{array}{ccc|ccc} \mathcal{F}_{ss} & \bullet & \bullet & -\boldsymbol{A}_{ss} & \circ & \circ \\ \bullet & \mathcal{F}_{WW} & \bullet & -\boldsymbol{A}_{Ws} & -A_{WW} & \circ \\ \bullet & \bullet & \mathcal{F}_{NN} & -\boldsymbol{A}_{Ns} & \circ & -A_{NN} \\ \hline -\boldsymbol{A}_{ss}^{*} & -\boldsymbol{A}_{Ws}^{*} & -\boldsymbol{A}_{Ns}^{*} & \bullet & \circ & \circ \\ \circ & -A_{WW}^{*} & \circ & \circ & \circ & \circ \\ \circ & \circ & -A_{NN}^{*} & \circ & \circ & \circ \end{array}\right] \cdot \left[\begin{array}{c} \boldsymbol{Y}_s \\ Y_W \\ Y_N \\ \hline \boldsymbol{Q}_s \\ Q_W \\ Q_N \end{array}\right] = \left[\begin{array}{c} \boldsymbol{u}_{\Gamma_s}^{\sigma} - \boldsymbol{u}_{0_s}^{\sigma} \\ u_{\Gamma_W}^{\sigma} - u_{0_W}^{\sigma} \\ u_{\Gamma_N}^{\sigma} - u_{0_N}^{\sigma} \\ \hline \boldsymbol{t}_{0_s}^{\sigma} - \boldsymbol{t}_{\Gamma_s}^{\sigma} \\ t_{0_W}^{\sigma} - t_{\Gamma_W}^{\sigma} \\ t_{0_N}^{\sigma} - t_{\Gamma_N}^{\sigma} \end{array}\right] \tag{4.44}$$

where the following definitions hold for phases $i, j = \{s, W, N\}$:

$$\boldsymbol{\mathcal{F}}_{jj} = \int \left(\boldsymbol{N}\boldsymbol{S}_j\right)^{*} \boldsymbol{U}_j d\Gamma^e \tag{4.45}$$

$$\boldsymbol{A}_{ij} = \int (\boldsymbol{N}\boldsymbol{S}_i)^{*} \boldsymbol{Z}_j d\bar{\Gamma}_{\sigma}^e \tag{4.46}$$

$$\boldsymbol{u}_{\Gamma_j}^{\sigma} = \int \left(\boldsymbol{N}\boldsymbol{S}_j\right)^{*} \boldsymbol{u}_{\Gamma} d\Gamma_u^e \tag{4.47}$$

$$\boldsymbol{u}_{0_j}^{\sigma} = \int \left(\boldsymbol{N}\boldsymbol{S}_j\right)^{*} \boldsymbol{u}_0 d\Gamma^e \tag{4.48}$$

$$\boldsymbol{t}_{\Gamma_j}^{\sigma} = \int \boldsymbol{Z}_j{}^{*} \boldsymbol{t}_{\Gamma}\, d\Gamma_{\sigma}^e \tag{4.49}$$

$$\boldsymbol{t}_{0_j}^{\sigma} = \int \boldsymbol{Z}_j{}^{*} (\boldsymbol{N}\boldsymbol{\sigma}_{0)}\, d\Gamma_{\sigma}^e \tag{4.50}$$

In the domain of the element, system (4.44) yields unique estimates for the stress and pore pressure fields, which are computed using definition (4.20). However, the displacement and seepage fields are not uniquely defined, as the rigid-body modes collected in basis (4.19) are stress-free. They can be recovered in the post-processing phase, as reported in Section 4.1.7.

On the extended Neumann boundary of the element, the normal and tangential components of the solid phase displacement and the normal component of the fluid displacement fields can be calculated using boundary approximation (4.43) or, alternatively, the domain displacement approximation (4.19). The two independent estimates should yield the same results upon full convergence.

4.1.5 Indeterminacy numbers of the HTD model

As for the biphasic model, assume that system (4.28) is written for a single-element mesh, meaning that the inter-element boundary variables and the associated inter-element compatibility conditions are absent, and let,

$$N_x = N_\sigma + N_W + N_N + 5 \tag{4.51}$$

be the dimension of the domain basis, defined by equation (3.14), where N_σ and N_f ($f = \{W, N\}$) are defined by equations (4.25) and (4.26). Equation (4.51) includes the harmonic and biharmonic modes, the two pore pressure modes, the three rigid-body solid displacement modes and the two fluid flow modes. The dimension of the boundary basis is,

$$N_p = N_{ps} + N_{pW} + N_{pN} \tag{4.52}$$

$$N_{ps} = 2s\left(1 + d_{ps}\right) \tag{4.53}$$

$$N_{pf} = s\left(1 + d_{pf}\right) \tag{4.54}$$

where N_{ps}, and N_{pf} are the dimensions of the traction and pore pressure bases $\boldsymbol{Z}_s$ and $\boldsymbol{Z}_f$ presented in equation (4.27); d_{ps}, and d_{pf} are the degrees of these bases, and s is the number of sides that form the extended Dirichlet boundary of the element. For the sake of simplicity, and without limiting the scope of the presentation, expressions (4.53) and (4.54) are obtained under the assumption that the same degree is used on all sides of the element.

The first three sets of equilibrium equations in system (4.28) show that the strain inducing modes are always statically indeterminate, with indeterminacies:

$$\alpha_s = N_{ps} > 0 \tag{4.55}$$

$$\alpha_f = N_{pf} > 0 \tag{4.56}$$

The interpretation of these conditions is based on the role played by the third, fourth and fifth equilibrium equations and follows the reasoning detailed in Chapter 3.

As the stress and pressure fields are self-equilibrated, the role of the equations mentioned above is to ensure that the approximations used for the boundary forces and the pore pressures are not arbitrary: their resultants must satisfy global equilibrium conditions.

The three equations forming the third set of equilibrium equations in system (4.28) are always linearly independent and have the following static indeterminacy number,

$$\alpha_{rs} = N_{ps} - 3 \tag{4.57}$$

which is non-negative regardless of the degree d_{ps} of the boundary basis $\boldsymbol{Z}_s$ if the number of Dirichlet sides (s) of the element is larger than one. If $s = 1, d_{ps}$ must be larger than zero for the set to be statically indeterminate. This restriction is easily met, as the dimension of basis $\boldsymbol{Z}_s$ is mainly conditioned by the necessity of adequately enforcing the compatibility equation on the Dirichlet boundary of the element.

On the other hand, to ensure a non-negative static indeterminacy number for the fourth and fifth set of equations in system (4.28), the following condition must be observed:

$$\alpha_{rdf} = N_{pf} - N_f \geq 0 \tag{4.58}$$

This enforces a strong restriction on the degrees d_{pf} of the boundary basis $\boldsymbol{Z}_f$, which must, in general, be larger than the degree d_f of the basis used for the free fluid flows:

$$d_{pf} \geq d_f \tag{4.59}$$

This reasoning can be dualized to state the kinematic admissibility conditions of the last three sets of equations in system (4.28).

The kinematic indeterminacy of the first set of compatibility equations, that is, the sixth set in system (4.28), implies that,

$$\beta_{ps} = N_\sigma + 3 - N_{ps} \geq 0 \tag{4.60}$$

which essentially ensures that the degree of the boundary approximation does not exceed the degree of the strain inducing domain modes:

$$d_\sigma \geq d_{ps} \tag{4.61}$$

For the second and third set of compatibility equations, the kinematic indeterminacy is conditioned by:

$$N_f + 1 - N_{pf} \geq 0 \tag{4.62}$$

Combined with equation (4.58), condition (4.62) eventually yields,

$$N_f \leq N_{pf} \leq N_f + 1 \tag{4.63}$$

Equation (4.63) sets a strong restriction on the choice of the degree d_{pf} of the boundary basis $\boldsymbol{Z}_f$. Depending on the number of Dirichlet sides and the degrees d_f of the free flow bases $\boldsymbol{U}_{rdf}$, it may indeed be impossible to satisfy this condition (e.g. when $d_f = 1$ and $s = 4$).

As in the modelling of biphasic media, this restriction can be accepted and special purpose solvers used to consistently deal with it (e.g. least-squares solvers). However, if more than one element is used to construct the mesh, the restriction can be removed by redefining the support of the free fluid flow approximation $\boldsymbol{U}_{rdf}$ as the whole domain in analysis rather than the domain of each element.

The governing system preserves the form (4.28) and its algebraic properties, with the difference that the fourth and fifth equilibrium equations are now written on the exterior boundary of the domain, to yield,

$$-\sum_{j=1}^{N_{\Gamma_u}} \left(\boldsymbol{B}_{rdf}\, \boldsymbol{P}_f \right)_j = \sum_{k=1}^{N_{\Gamma_\sigma}} \left(\boldsymbol{t}^u_{\Gamma_{rdf}} \right)_k - \boldsymbol{t}^u_{0_{rdf}} \tag{4.64}$$

where N_{Γ_u} and N_{Γ_σ} represent the numbers of exterior Dirichlet and Neumann sides of the domain, respectively. Also, term $t^u_{0_{rdf}}$ is now defined as a boundary integral taken over the exterior boundary of the domain. The boundary seepage compatibility equations written on the interior boundaries also lose the boundary terms $\boldsymbol{B}^*_{rdf}$. They only remain present on the exterior Dirichlet boundaries of the domain.

4.1.6 Indeterminacy numbers of the HTS model

The total number of static degrees of freedom is equal to the dimension of the domain basis,

$$N_y = N_\sigma + 2 \tag{4.65}$$

assuming that system (4.44) is written for a single-element mesh. Equation (4.65) includes the N_σ harmonic and biharmonic modes and the two pore pressure modes. The total number of kinematic degrees of freedom is,

$$N_q = N_{qs} + N_{qW} + N_{qN} \tag{4.66}$$

$$N_{qs} = 2s\left(1+d_{qs}\right) \tag{4.67}$$

$$N_{qf} = s\left(1+d_{qf}\right) \tag{4.68}$$

where N_{qs} and N_{qf} ($f = \{W, N\}$) are the dimensions of the boundary bases $\boldsymbol{Z}_s$ and $\boldsymbol{Z}_f$ presented in definition (4.43), where and d_{qs} and d_{qf} define the degrees of these approximation bases. As for the displacement element, expressions (4.67) and (4.68) are obtained considering that the same degree is used on all sides of the element.

The compatibility (i.e. first three) equations of system (4.44) are always kinematically indeterminate, with indeterminacy numbers equal to, respectively,

$$\beta_s = N_{qs} \tag{4.69}$$

$$\beta_f = N_{qs} + N_{qf} \tag{4.70}$$

The static indeterminacy condition of the first set of boundary equilibrium equations,

$$\alpha_{qs} = N_\sigma + 2 - N_{qs} \geq 0 \tag{4.71}$$

is observed, in general, if the degree of the boundary approximation does not exceed the degree of the strain inducing domain modes:

$$d_\sigma \geq d_{qs} \tag{4.72}$$

The static indeterminacy condition of the second and third (pressure) boundary condition,

$$\alpha_{qf} = 1 - N_{qf} = 1 - s\left(1+d_{qf}\right) \geq 0 \tag{4.73}$$

deserves special attention, as it clearly cannot be met unless $d_{qf} = 0$ and the element has one single Neumann (or interior) side. To clarify the source of the problem, it is recalled that the second boundary equation is used to enforce the pressure equilibrium on each Neumann and interior boundary of the element. As the pore pressure can only be constant, it is allocated one single degree of freedom, $Y_f = 0$, in the domain approximation (4.20), whose value only requires one equation to be determined. This is the reason why basis $\boldsymbol{Z}_f$ is defined with a single mode. However, as shown in Figure 3.1, even when the pressure equilibrium is enforced in the weakest possible way (constant approximation for the boundary seepage), all but one of the equations written for an element are redundant.

This source of linear dependency can be solved in the different ways described in Section 3.1.7. Instead of developing a logic that ensures that only one pressure continuity condition is transmitted to each element of the mesh, the option followed here is to redefine the support of pressure approximation presented in definition (4.20) as the domain in analysis.

The governing system still preserves form (4.44), with the only difference that its second (domain compatibility) equation is now defined at the structural level. This means that this equation now only collects boundary terms defined on the exterior (structural) Neumann boundary, the inter-element boundaries no longer being part of it,

$$\mathcal{F}_{ff} Y_f - \sum_{j=1}^{N_{\Gamma_\sigma}} \left(\boldsymbol{A}_{fs} \boldsymbol{Q}_s + A_{ff} Q_f \right)_j = \sum_{k=1}^{N_{\Gamma_u}} \left(u^{\sigma}_{\Gamma_f} \right)_k - u^{\sigma}_{0_f} \tag{4.74}$$

where N_{Γ_σ} and N_{Γ_u} are the numbers of exterior Neumann and Dirichlet sides, respectively. In equation (3.61), terms $\mathcal{F}_{ff}$ and $u^{\sigma}_{0_f}$ are now defined as boundary integrals taken on the whole domain. Terms $\boldsymbol{A}^*_{fs}$ and A^*_{ff} also vanish from the inter-element equilibrium equations, remaining present only on the exterior Neumann sides of the domain.

4.1.7 Recovery of the stress-free modes

The procedure described in Section 3.1.8 to recover the rigid-body and free flow modes in the post-processing phase of analyses performed using the HTS element is extended to triphasic media.

After solving system (4.44), approximation (3.14) can be written in the following form,

$$\boldsymbol{u} = \boldsymbol{U}_r \boldsymbol{X}_r + \bar{\boldsymbol{u}} \tag{4.75}$$

where $\boldsymbol{U}_r = (\boldsymbol{U}_{rs} \quad \boldsymbol{U}_{rdW} \quad \boldsymbol{U}_{rdN})$, $\boldsymbol{X}_r^T = (\boldsymbol{X}_{rs} \quad \boldsymbol{X}_{rdW} \quad \boldsymbol{X}_{rdN})$ and vector

$$\bar{\boldsymbol{u}} = \boldsymbol{U}_s \boldsymbol{Y}_s + \boldsymbol{U}_W Y_W + \boldsymbol{U}_N Y_N + \boldsymbol{u}_0 \tag{4.76}$$

is known from the processing phase.

Under this notation, equations (4.75) and (4.76) still hold. They are used now to recover (in a non-unique way) the stress free modes in the analysis of triphasic media with hybrid-Trefftz stress elements.

4.2 Formulation of dynamic problems

The mathematical model presented in Section 4.1 is extended to simulate the dynamic response of triphasic media. The supporting information is structured in the same way: definition of the spectral problem and derivation of its formal solutions; derivation and characterization of the discretization in time and in space using both the displacement and stress models of the hybrid-Trefftz finite element formulation.

4.2.1 Mathematical model

The thermodynamically consistent mathematical model adopted in this section was suggested by Wei and Muraleetharan [97] in 2002. It explicitly includes the dynamic compatibility conditions on the interfaces between the three phases and endorses the distinction between the microscopic fluid flow, caused by the capillary relaxation process (particularly relevant in swelling soils) and the macroscopic fluid flow, driven by the pore pressure gradients caused by the application of exterior loads to the medium.

The capillary relaxation process is associated to changes in the volume fractions of the fluids. When this process is omitted from the analysis (i.e. the capillary equilibrium is reached immediately), the model becomes linear elastic. Also, the model recovers the Biot's theory when the saturation of the medium is increased to 1.0.

The linear-elastic model obtained by neglecting the effect of the capillary relaxation is used here. Its equations are fully derived and commented in [97]. They are restated here for the sake of convenience, but their interpretation is limited to aspects considered relevant for their finite element solution.

The homogeneous Navier equation still holds as,

$$\boldsymbol{\mathcal{D}k\mathcal{D}}^{*}\boldsymbol{u}+\omega^{2}\boldsymbol{\rho u}=\mathbf{0} \quad \text{in } V \tag{4.77}$$

Under the notation defined in Section 4.1, and using the definitions given in Appendix A, the following expression is found for the spectral Navier equation (4.77) as,

$$\begin{cases} \boldsymbol{\nabla\nabla}^{T}[(M_{SS}+n^{S}\mu^{S})\boldsymbol{u}^{S}+M_{SW}\boldsymbol{u}^{W}+M_{SN}\boldsymbol{u}^{N}]+n^{S}\mu^{S}\boldsymbol{\nabla}^{2}\boldsymbol{u}^{S} \\ +\omega^{2}(\rho_{SS}\boldsymbol{u}^{S}+\rho_{SW}\boldsymbol{u}^{W}+\rho_{SN}\boldsymbol{u}^{N})=\mathbf{0} \\ \boldsymbol{\nabla\nabla}^{T}[M_{SW}\boldsymbol{u}^{S}+M_{WW}\boldsymbol{u}^{W}+M_{WN}\boldsymbol{u}^{N}]+\omega^{2}(\rho_{SW}\boldsymbol{u}^{S}+\rho_{WW}\boldsymbol{u}^{W})=\mathbf{0} \\ \boldsymbol{\nabla\nabla}^{T}[M_{sN}\boldsymbol{u}^{S}+M_{WN}\boldsymbol{u}^{W}+M_{NN}\boldsymbol{u}^{N}]+\omega^{2}(\rho_{SN}\boldsymbol{u}^{S}+\rho_{NN}\boldsymbol{u}^{N})=\mathbf{0} \end{cases} \tag{4.78}$$

where:

$$\rho_{SS} = n^S \rho^S - \frac{\hat{\imath}}{\omega}(\mu^W + \mu^N) \tag{4.79}$$

$$\rho_{WW} = n^W \rho^W - \frac{\hat{\imath}}{\omega}\mu^W \tag{4.80}$$

$$\rho_{NN} = n^N \rho^N - \frac{\hat{\imath}}{\omega}\mu^N \tag{4.81}$$

$$\rho_{SW} = \frac{\hat{\imath}}{\omega}\mu^W \tag{4.82}$$

$$\rho_{SN} = \frac{\hat{\imath}}{\omega}\mu^N \tag{4.83}$$

The solutions of the spectral problem (4.78) involve three compressional waves and one shear wave.

❖ **Compressional waves**

The displacements corresponding to the compressional waves are determined by solving the following eigen problem, for the wave numbers β_{P_j}, with $j = \{1,\ 2,\ 3\}$, and the corresponding phase multipliers $\gamma_{P_j}^{\alpha}$, with $\alpha = \{S,\ W,\ N\}$:

$$\left[-\frac{\beta_{P_j}^2}{\omega^2}\begin{pmatrix} M_{SS}+n^S\mu^S & M_{SW} & M_{SN} \\ M_{SW} & M_{WW} & M_{WN} \\ M_{SN} & M_{WN} & M_{NN} \end{pmatrix} + \begin{pmatrix} \rho_{SS} & \rho_{SW} & \rho_{SN} \\ \rho_{SW} & \rho_{WW} & 0 \\ \rho_{SN} & 0 & \rho_{NN} \end{pmatrix}\right]\begin{bmatrix} \gamma_{P_j}^S \\ \gamma_{P_j}^W \\ \gamma_{P_j}^N \end{bmatrix} = \begin{bmatrix} 0 \\ 0 \\ 0 \end{bmatrix} \tag{4.84}$$

The displacement and stress fields corresponding to each compressional wave are,

$$\boldsymbol{U}_{P_j} = \frac{1}{2}\beta_{P_j}^{-1}\begin{bmatrix} [J_{n-1}(z_j) - J_{n+1}(z_j)] \\ \hat{\imath}[J_{n-1}(z_j) + J_{n+1}(z_j)] \\ \gamma_{P_j}^W[J_{n-1}(z_j) - J_{n+1}(z_j)] \\ \hat{\imath}\gamma_{P_j}^W[J_{n-1}(z_j) + J_{n+1}(z_j)] \\ \gamma_{P_j}^N[J_{n-1}(z_j) - J_{n+1}(z_j)] \\ \hat{\imath}\gamma_{P_j}^N[J_{n-1}(z_j) + J_{n+1}(z_j)] \end{bmatrix} exp(\hat{\imath}n\theta) \tag{4.85}$$

$$\boldsymbol{S}_{P_j} = \begin{bmatrix} S^r_{P_j} \\ S^\theta_{P_j} \\ \hat{\imath}n^S\mu^S\left[J_{n-2}(z_j) - J_{n+2}(z_j)\right] \\ -2\left(M_{SW} + \gamma^W_{P_j}M_{WW} + \gamma^N_{P_j}M_{WN}\right)J_n(z_j) \\ -2\left(M_{SN} + \gamma^W_{P_j}M_{WW} + \gamma^N_{P_j}M_{WN}\right)J_n(z_j) \end{bmatrix} exp(\hat{\imath}n\theta) \tag{4.86}$$

where:

$$\boldsymbol{S}^r_{P_j} = n^S\mu^S\left[2J_n(z_j) + J_{n-2}(z_j) + J_{n+2}(z_j)\right] - 2\left[(M_{SS} + 2n^S\mu^S) + \gamma^W_{P_j}M_{SW} + \gamma^N_{P_j}M_{SN}\right]J_n(z_j) \tag{4.87}$$

$$\boldsymbol{S}^\theta_{P_j} = n^S\mu^S\left[2J_n(z_j) - J_{n-2}(z_j) - J_{n+2}(z_j)\right] - 2\left[(M_{SS} + 2n^S\mu^S) + \gamma^W_{P_j}M_{SW} + \gamma^N_{P_j}M_{SN}\right]J_n(z_j) \tag{4.88}$$

Bessel functions of the first (second) kind and order n, $J_n(z_j)$ with $z_j = \beta_{P_j}.r$, are used to implement interior (exterior) problems. Hankel functions of the first (second) kind can also be used to model outgoing (incoming) waves satisfying locally the Sommerfeld radiation condition [35].

It is important to understand the dynamic characteristics of the compressional waves propagating through unsaturated soils, as reflected by the solutions derived above. To discuss this, the variations of the wavelength, λ, and of the (logarithm of the) attenuation of the three compressional waves are presented in Figures 4.1 and 4.2 as functions of the (logarithm of the) hydraulic conductivity and saturation of the medium. The problem is defined on the Massilon sandstone characterized in Appendix B.

The plots are presented for two frequencies of the propagating wave, namely $100Hz$ and $500Hz$. The saturation range used in the plots ($10\% \leq S \leq 95\%$) corresponds to the limits of the adopted mathematical model, which is valid between the residual and the air-entry degrees of saturation. Indeed, for saturations smaller than 10%, the water is mainly adsorptive, while for ($S \geq 95\%$), the air is present in bubble form and the medium can be analyzed using biphasic models, e.g. Smeulders [92].

The hydraulic conductivity range is taken between $10^{-2}m/s$ (pervious soils, such as well sorted sands, sand and gravel) and $10^{-6}m/s$ (semi-pervious soils such as very fine sands, loess and silt). As noted in Chapter 3, impervious soils, characterized by hydraulic conductivities lower than $10^{-6}m/s$, essentially block the propagation of compressional waves through the fluid phases, behaving like frozen-media. They are not treated here, as triphasic models are not necessary for the correct representation of this situation.

As expected, the wavelengths are significantly larger for the lower frequency case (left hand side of Figure 4.1) than for the higher frequency case (right hand side of the same figure). While the wavelength variation of a given type of wave is quite similar for both tested frequencies, significant differences exist between the three compressional waves.

The wavelength and the phase velocity $v = \lambda \frac{\omega}{2\pi}$ of the fast propagating P_1 wave exhibit limited sensitivity to variations of the permeability and saturation of the medium. This is consistent with the physical nature of this compressional wave, which propagates essentially through direct contact between the solid particles and is thus insensitive to those properties of the medium that condition the movement of the fluid constituents. Moreover, as the product $\lambda.\omega$ is practically constant, the phase velocity of P_1 waves is also insensitive to the frequency of the travelling wave (i.e. the medium is not dispersive in respect to P_1 waves). The wave presents low attenuation, especially for the lower frequency case.

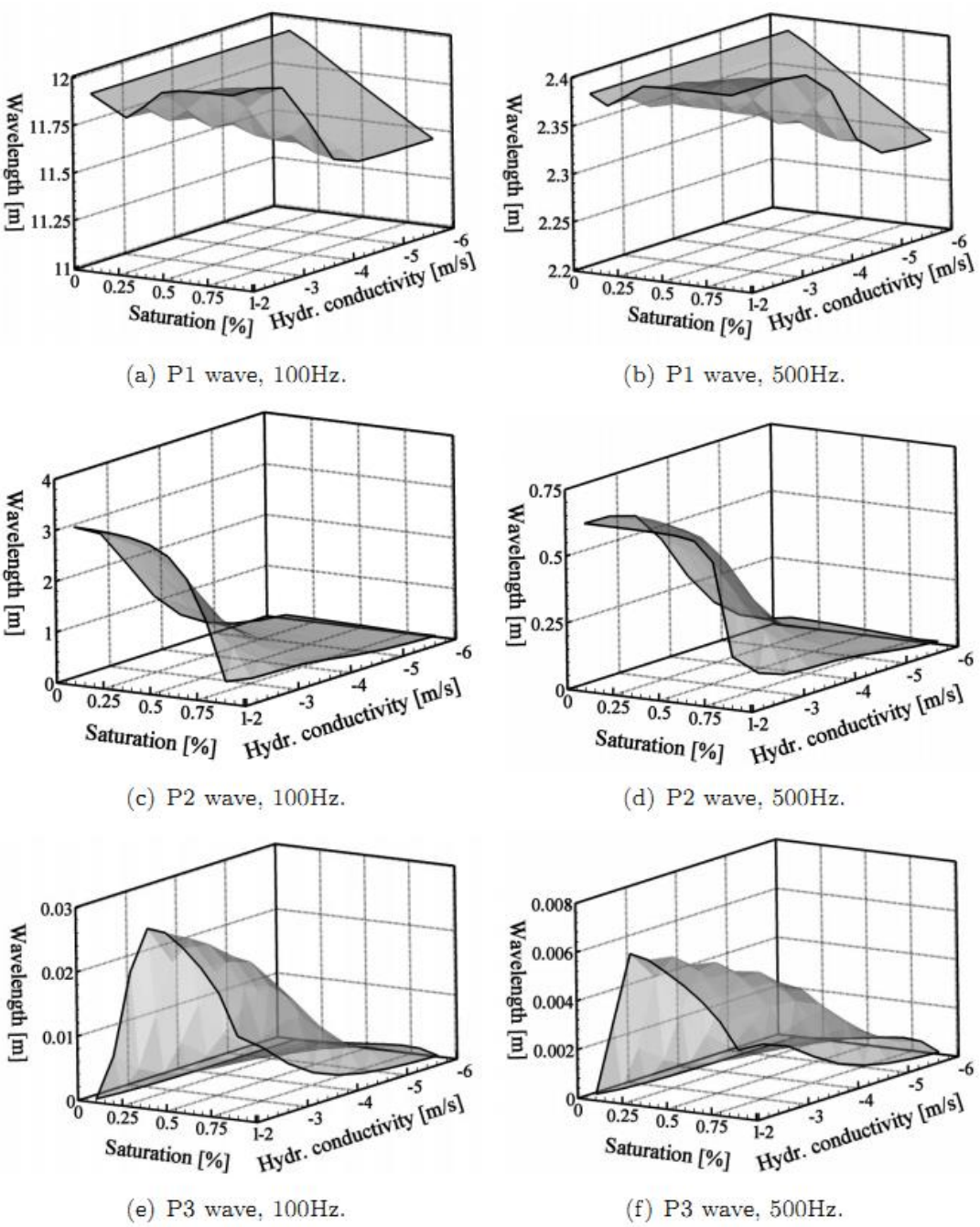

Figure 4.1: Wavelength variation for compressional waves in triphasic dynamic problems

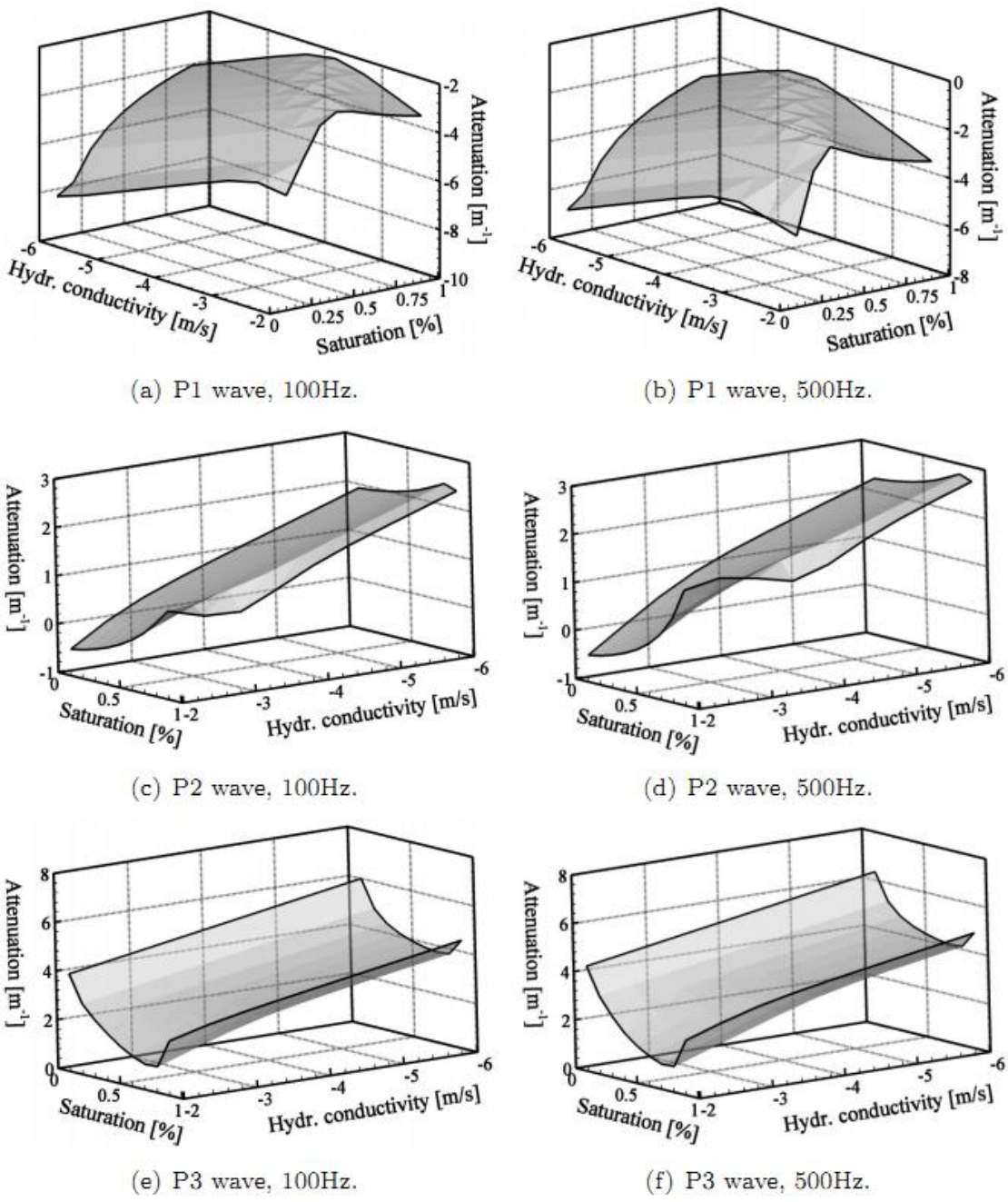

Figure 4.2: Attenuation variation for compressional waves in triphasic dynamic problems

Conversely, the second compressional wave is strongly influenced by the saturation and permeability of the medium, which suggests that the propagation of this wave is determined by the motion of the fluid phases. Both the wavelength and the phase velocity of the P_2 wave reach their maximum for the smallest saturation and permeability tested. Compared to the P_1 wave, the second compressional wave propagates slower and its wavelength is significantly smaller. The

phase velocity of the P_2 wave is proportional to its frequency, especially at lower saturation values (i.e. the medium is dispersive in respect to P_2 waves). The P_2 wave is more attenuated than the P_1 wave, especially for low permeability media. This happens because P_2 waves are transmitted through fluid motion, which is hindered by the low permeability of the medium. However, unlike P_1 waves, the attenuation of the P_2 wave does not significantly depend on the frequency.

Finally, the third compressional wave is only significant for mid-range saturation values. When saturation is below 10% or above 90%, the phase velocity of the P_3 wave is very small and the attenuation large. This indicates that the P_3 wave is conditioned by the existence of capillary pressures, which constitute its mean of propagation. When the fluid phases tend to disconnect (the liquid phase disconnects when the medium is close to dry, while the opposite is true for the gas phase), the capillary pressures vanish and the P_3 wave disappears. The third compressional wave propagates slower and is more attenuated than any of the other waves, which means that its contribution to the dynamic response of the medium is only relevant at close field. The phase velocity of the P_3 wave increases with the frequency (i.e. the medium is P_3-dispersive), but the attenuation is essentially frequency-independent.

The features of the three compressional waves have important consequences on their computational modeling using conventional finite elements, mainly because of the necessity to calibrate the leading dimension of the finite element to the wavelength of the propagating wave Pluymers [125]. Due to the extremely small wavelength of the P_3 wave, the correct modeling of this wave is practically impossible when conventional elements are used. This is especially problematic for high permeability media, where the attenuation is smaller, and has a lesser impact on the results at far-field and for low permeability soils. The same problem may also hinder the modeling of the P_2 wave, especially at higher frequencies. Indeed, high frequencies significantly reduce the wavelength of the second compressional wave, but (unlike the case of P_1 waves) do not increase significantly its attenuation. This means that the wave may still propagate deep into the medium, but it becomes much harder to model due to its reduced wavelength.

The hybrid-Trefftz elements for elastodynamic problems presented below are aimed to give a consistent response to these modeling issues. Due to their physically-meaningful approximations,

hybrid-Trefftz elements are less sensitive to wavelength variations than conventional elements and are not bounded to observe the condition given in Pluymers [125].

❖ **Shear wave**

A single shear wave satisfies the Navier equation (4.77). It is characterized by the following wave numbers and phase multipliers,

$$\beta_S^2 = \omega^2 \frac{\rho_{SS}+\gamma_S^W \rho_{SW}+\gamma_S^N \rho_{SN}}{n^S \mu^S} \tag{4.89}$$

$$\gamma_S^W = -\frac{\rho_{SW}}{\rho_{WW}} \tag{4.90}$$

$$\gamma_S^N = -\frac{\rho_{SN}}{\rho_{NN}} \tag{4.91}$$

The displacement and stress fields corresponding to the shear wave are defined below, where $z_S = \beta_S.r$:

$$\boldsymbol{U}_S = \frac{1}{2}\beta_S^{-1}\begin{bmatrix} \hat{\imath}[J_{n+1}(z_S)+J_{n-1}(z_S)] \\ [J_{n+1}(z_S)-J_{n-1}(z_S)] \\ \hat{\imath}\gamma_S^W[J_{n+1}(z_S)+J_{n-1}(z_S)] \\ \gamma_S^W[J_{n+1}(z_S)-J_{n-1}(z_S)] \\ \hat{\imath}\gamma_S^N[J_{n+1}(z_S)+J_{n-1}(z_S)] \\ \gamma_S^N[J_{n+1}(z_S)-J_{n-1}(z_S)] \end{bmatrix} exp(\hat{\imath}n\theta) \tag{4.92}$$

$$\boldsymbol{S}_S = \frac{1}{2}n^S\mu^S\begin{bmatrix} \hat{\imath}[J_{n-2}(z_S)-J_{n+2}(z_S)] \\ -\hat{\imath}[J_{n-2}(z_S)-J_{n+2}(z_S)] \\ -[J_{n-2}(z_S)-J_{n+2}(z_S)] \\ 0 \\ 0 \end{bmatrix} exp(\hat{\imath}n\theta) \tag{4.93}$$

As shear waves can only propagate through the solid phase, they do not induce pore pressures. Their vibration and attenuation characteristics, presented in Figures 4.3 and 4.4, are qualitatively similar to those of the P_1 waves. Dispersion of these waves is low, and the attenuation (represented logarithmically in Figure 4.4) is proportional to the frequency. *S* waves propagate at a lower phase velocity than P_1 waves and are similarly attenuated.

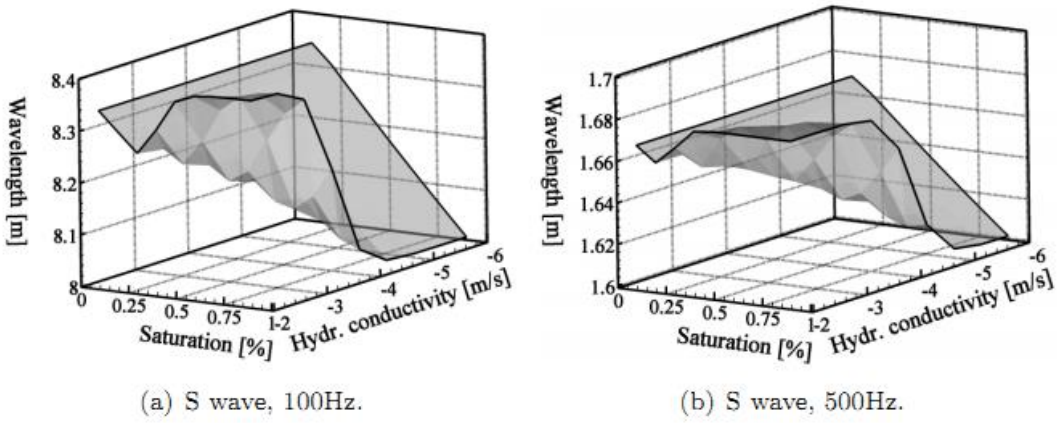

(a) S wave, 100Hz. (b) S wave, 500Hz.

Figure 4.3: Wavelength variation for shear waves in triphasic dynamic problems

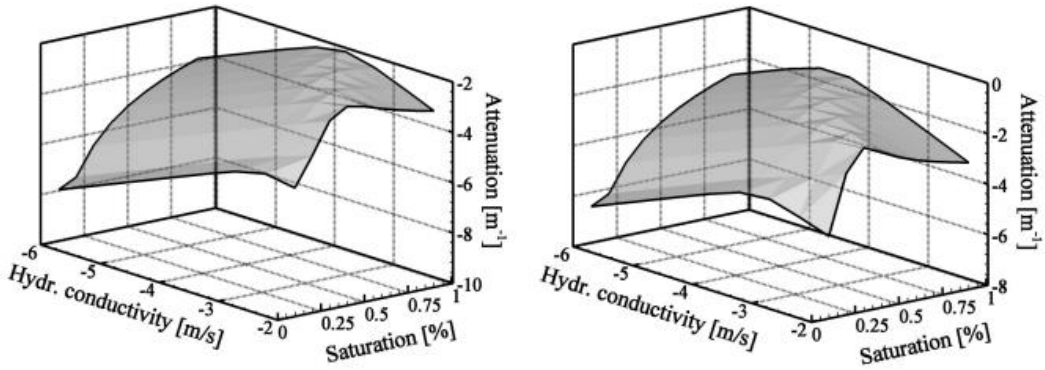

(a) S wave, 100Hz. (b) S wave, 500Hz.

Figure 4.4: Attenuation variation for shear waves in triphasic dynamic problems

4.2.2 Trefftz approximation bases

The Trefftz bases are constructed combining the solutions defined above, to yield the following expressions for the Trefftz approximations (2.94) and (2.117) for elastodynamic problems:

$$\boldsymbol{u} = \boldsymbol{U}_d \boldsymbol{X}_d + \boldsymbol{u}_0 \tag{4.94}$$

$$\boldsymbol{\sigma} = \boldsymbol{S}_d \boldsymbol{Y}_d + \boldsymbol{\sigma}_0 \tag{4.95}$$

$$\boldsymbol{U}_d = \begin{pmatrix} \boldsymbol{U}_{P_1} & \boldsymbol{U}_{P_2} & \boldsymbol{U}_{P_3} & \boldsymbol{U}_S \end{pmatrix} \tag{4.96}$$

$$\boldsymbol{S}_d = \begin{pmatrix} \boldsymbol{S}_{P_1} & \boldsymbol{S}_{P_2} & \boldsymbol{S}_{P_3} & \boldsymbol{S}_S \end{pmatrix} \tag{4.97}$$

The particular solutions, $\boldsymbol{u}_0$, and $\boldsymbol{\sigma}_0$, are determined in Section 2.5. If the dynamic problems are solved with analysis of initial conditions (e.g. non-periodic and transient problems), the

Trefftz approximations of particular solutions are combining the solutions of static problems defined in Section 4.1.1, to yield following expressions:

$$\boldsymbol{u}_0 = \boldsymbol{U}_s\boldsymbol{X}_s + \boldsymbol{U}_r\boldsymbol{X}_r \tag{4.98}$$

$$\boldsymbol{\sigma}_0 = \boldsymbol{S}_s\boldsymbol{Y}_s \tag{4.99}$$

$$\boldsymbol{U}_s = (\boldsymbol{U}_{b_0} \quad \boldsymbol{U}_{b_n} \quad \boldsymbol{U}_h \quad \boldsymbol{U}_W \quad \boldsymbol{U}_N) \tag{4.100}$$

$$\boldsymbol{U}_r = (\boldsymbol{U}_{rs} \quad \boldsymbol{U}_{rW} \quad \boldsymbol{U}_{dW} \quad \boldsymbol{U}_{rN} \quad \boldsymbol{U}_{dN}) \tag{4.101}$$

$$\boldsymbol{S}_s = (\boldsymbol{S}_{b_0} \quad \boldsymbol{S}_{b_n} \quad \boldsymbol{S}_h \quad \boldsymbol{S}_W \quad \boldsymbol{S}_N) \tag{4.102}$$

4.3 Convergence under *p*- and *h*-refinement

All numerical applications presented in this section are performed on the body represented in Figure 3.2, with dimensions of $r_{min} = 10.0m$, $r_{max} = 20.0m$ and $\theta = 0.5\,rad$. The material considered in the tests is the Massilon sandstone characterized in Appendix B.

The testing procedure is described in Sections 4.3.1 and 4.3.2: a reference solution is taken from the solution set of systems (4.2) and (4.78) in the convergence tests on static and dynamic problems, respectively; the corresponding surface tractions (displacements) are used to define the boundary conditions in the assessment of the performance of the HTD (HTS) finite element model. It is ensured, in both instances, that the reference solution is not included in the finite element approximation bases.

4.3.1 Static problems

The reference solution used in the assessment of convergence under static conditions is derived from the biharmonic displacement potential $\phi(r,\theta) = r^2\,log(r)$. The normal and shear (total) stress fields corresponding to the test described above are presented in Figure 4.5.

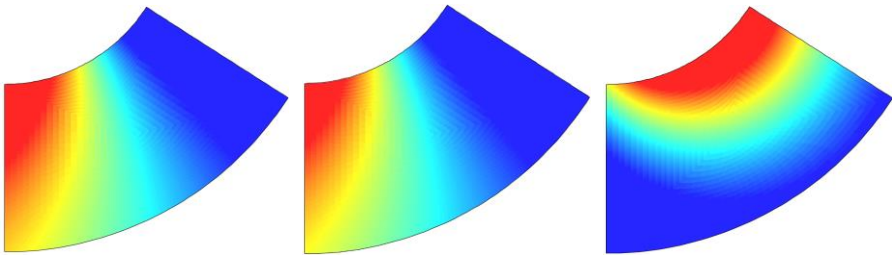

a) $\boldsymbol{\sigma}_{rr}$ field b) $\boldsymbol{\sigma}_{\theta\theta}$ field c) $\boldsymbol{\sigma}_{r\theta}$ field

Figure 4.5: Reference stress fields for triphasic static problems

The normal and tangential components of the solid phase tractions on the radial boundaries are given by expression (4.103), while equation (4.104) defines the same quantities on the circular sides of the medium (the wetting and non-wetting pressures are null):

$$\boldsymbol{t}_{\Gamma_r} = -\frac{n^S\mu^S}{r}\begin{bmatrix} cos\,\theta + sin\,\theta \\ cos\,\theta - sin\,\theta \end{bmatrix} \tag{4.103}$$

$$\boldsymbol{t}_{\Gamma_c} = \frac{n^S\mu^S}{r}\begin{bmatrix} \frac{2\bar{\lambda}+3n^S\mu^S}{\mu}(cos\,\theta + sin\,\theta) \\ cos\,\theta - sin\,\theta \end{bmatrix} \tag{4.104}$$

The normal and tangential components of the solid phase displacement field and the normal component of the wetting and non-wetting displacements on the radial boundaries of the domain are given by expression (4.105), while their counterparts on the circular boundaries are defined by relation (4.106):

$$\boldsymbol{u}_{\Gamma_r} = \frac{\pm 1}{4n^S\mu^S}\begin{bmatrix} \left[3\bar{\lambda} + 7n^S\mu^S + 2\left(\bar{\lambda} + 3n^S\mu^S\right) log\, r\right](cos\,\theta - sin\,\theta) \\ -\left[\bar{\lambda} + 5n^S\mu^S + 2\left(\bar{\lambda} + 3n^S\mu^S\right) log\, r\right](cos\,\theta + sin\,\theta) \\ -4n^S\mu^S\alpha_W(log\, r + 1)(cos\,\theta - sin\,\theta) \\ -4n^S\mu^S\alpha_N(log\, r + 1)(cos\,\theta - sin\,\theta) \end{bmatrix} \tag{4.105}$$

$$\boldsymbol{u}_{\Gamma_c} = \frac{\pm 1}{4n^S\mu^S}\begin{bmatrix} \left[\bar{\lambda} + 5n^S\mu^S + 2\left(\bar{\lambda} + 3n^S\mu^S\right) log\, r\right](cos\,\theta + sin\,\theta) \\ \left[3\bar{\lambda} + 7n^S\mu^S + 2\left(\bar{\lambda} + 3n^S\mu^S\right) log\, r\right](cos\,\theta - sin\,\theta) \\ -4n^S\mu^S\alpha_W(log\, r + 1)(cos\,\theta - sin\,\theta) \\ -4n^S\mu^S\alpha_N(log\, r + 1)(cos\,\theta - sin\,\theta) \end{bmatrix} \tag{4.106}$$

The analytic expression of the deformation energy is expressed in form (3.70) and its finite element approximation is defined as follows for the displacement and stress models, where N_e is the total number of elements in the mesh:

$$E_{FE} = \frac{1}{2}\sum_{j=1}^{N_e}\left(\boldsymbol{X}_s^*\boldsymbol{K}_{ss}\boldsymbol{X}_s + X_W^*K_{WW}X_W + X_N^*K_{NN}X_N\right)_j \tag{4.107}$$

$$E_{FE} = \frac{1}{2}\sum_{j=1}^{N_e}\left(\boldsymbol{Y}_s^*\boldsymbol{\mathcal{F}}_{ss}\boldsymbol{Y}_s + Y_W^*\mathcal{F}_{WW}Y_W + Y_W^*\mathcal{F}_{WW}Y_W\right)_j \tag{4.108}$$

The single-, two- and four-element meshes represented in Figure 3.4 are used to evaluate the convergence of the hybrid-Trefftz models under h-refinement. The leading dimensions of the finite elements are $10.0\ m$ for the first two meshes and $5.0\ m$ for the third mesh. For each of the testing meshes, the p-refinement is performed by increasing the degree of the harmonic and biharmonic bases $\boldsymbol{U}_b$ and $\boldsymbol{U}_h$ defined in Section 4.1.1.

The convergence patterns of the mechanical energy error measure defined in form (3.73) are presented in Figure 4.6 for both models. The values on the abscissa represent (logarithmically) the total number of degrees of freedom, N. Solid lines in Figure 4.6 represent the p- convergence patterns obtained using domain bases with degrees 7, 9 and 11 and boundary bases with maximum degree 5 on the three meshes represented in Figure 3.4, with one element (square symbol), two elements (diamond) and four elements (circle). As before, the dashed lines represent the h-convergence patterns obtained maintaining the degree of p-refinement constant and varying the number of elements.

According to the convergence rate measure defined in equation (4.109), k, the results confirm that the convergence under p-refinement is high, even for small levels of h-refinement, and similar for both finite element models. The results shown in Figure 4.6 also show that the convergence factor k is larger when the p-refinement is performed on finer meshes (typically in the two-element mesh).

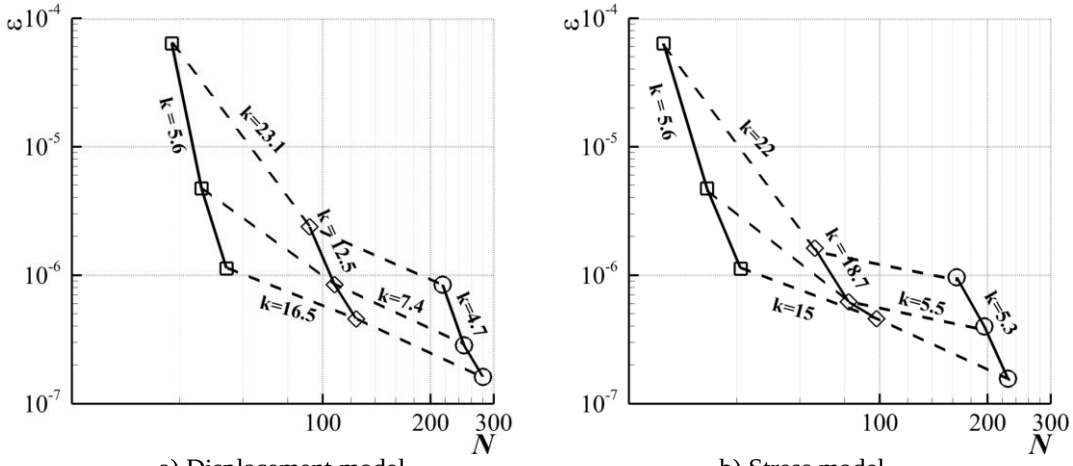

a) Displacement model b) Stress model

Figure 4.6: Convergence results in triphasic static problems

The convergence rates obtained for the h-refinement tests (the three dashed lines in Figure 4.6) are significantly lower than those obtained under p-refinement, but still similar for both finite element models.

4.3.2 Dynamic problems

The same testing scheme is used in the assessment of the rates of convergence in the solution of dynamic problems with the alternative HTD and HTS finite elements. The geometry of the

domain (Figure 3.2) is defined by $r_{min} = 1.0m$, $r_{max} = 2.0m$ and $\theta = 0.5\,rad$, and the testing spectral frequencies are $500Hz$ for the P_1, P_2 and S waves and $50Hz$ for the P_3 wave. The hydraulic conductivity of the Massilon sandstone is $10^{-2}m/s$, corresponding to an intrinsic permeability of $1.55 \cdot 10^{-8}m/s$. The high permeability value is designed to minimize the attenuation of the P_2 and P_3 waves, thus avoiding their localization at close-range.

❖ **Compressional waves**

The Neumann problem used to test the displacement model is defined by the following set of prescribed boundary tractions and pressures:

$$t_\Gamma^n = n^S \mu^S (H_0 \pm H_2) - \left[(M_{SS} + 2n^S \mu^S) + \gamma_{P_j}^W M_{SW} + \gamma_{P_j}^N M_{SN} \right] H_0 \tag{4.110}$$

$$t_\Gamma^t = 0 \tag{4.111}$$

$$\pi_\Gamma^W = -\left[M_{SW} + \gamma_{P_j}^W M_{WW} + \gamma_{P_j}^N M_{WN} \right] H_0 \tag{4.112}$$

$$\pi_\Gamma^N = -\left[M_{SN} + \gamma_{P_j}^W M_{WN} + \gamma_{P_j}^N M_{NN} \right] H_0 \tag{4.113}$$

where $j = \{1,\ 2,\ 3\}$ and $H_\alpha\left(\beta_{P_j} r\right)$ is the second kind Hankel functions of order α, which is not contained in the finite element approximation bases. In the expression of the boundary-normal traction t_Γ^n, the positive sign corresponds to the circular boundary of the domain and the negative sign, to its radial boundary. No tractions are applied in the boundary-tangential direction.

The stress element is tested under the following set of Dirichlet boundary conditions, where n_r and n_θ are the direction cosines of the boundary:

$$u_{\Gamma_n}^S = -n_r \beta_{P_j}^{-1} H_1\left(z_{P_j}\right) \tag{4.114}$$

$$u_{\Gamma_n}^W = -n_r \beta_{P_j}^{-1} \gamma_{P_j}^W H_1\left(z_{P_j}\right) \tag{4.115}$$

$$u_{\Gamma_n}^N = -n_r \beta_{P_j}^{-1} \gamma_{P_j}^N H_1\left(z_{P_j}\right) \tag{4.116}$$

$$u_{\Gamma_t}^S = n_\theta \beta_{P_j}^{-1} H_1\left(z_{P_j}\right) \tag{4.117}$$

In this reference solution for compressional waves of type $j = \{1,\ 2,\ 3\}$, equations (4.114) to (4.116) define displacements normal to the circular boundary and equation (4.117) defines tangential component on the radial boundaries of the domain defined in Figure 3.2.

❖ **Shear waves**

In the displacement model test, analytic shear waves yield null boundary-normal traction and pore pressure fields. The tangential traction on the circular and radial boundaries of the medium has the following definitions:

$$t_\Gamma^t = -n^S \mu^S \, H_2(z_S) \tag{4.118}$$

For the stress model test, the same shear wave is induced to the medium through the application of the tangential displacements on circular boundaries,

$$u_{\Gamma_t}^S = n_r \beta_S^{-1} H_1(z_S) \tag{4.119}$$

and normal displacements on the radial boundaries:

$$u_{\Gamma_n}^S = -n_\theta \beta_S^{-1} H_1(z_S) \tag{4.120}$$

$$u_{\Gamma_n}^W = -n_\theta \beta_S^{-1} \gamma_S^W H_1(z_S) \tag{4.121}$$

$$u_{\Gamma_n}^N = -n_\theta \beta_S^{-1} \gamma_S^N H_1(z_S) \tag{4.122}$$

❖ **Convergence results**

To illustrate the reference solutions defined above, the normal stress fields σ_{rr} produced by the P_1, P_2 and P_3 waves and the tangential stress field $\sigma_{r\theta}$ generated by the S wave are represented in Figure 4.7. The frequency of the P_1, P_2 and S is $500Hz$, and the frequency of the P_3 wave is $50Hz$. The wavelengths of the induced waves vary between $2.40m$ for the P_1 wave to less than $4cm$ for the P_3 wave. Consequently, in order to obtain acceptable solutions for the tested problems, the leading dimension of a conventional element should range from $40cm$ for the P_1 problem to less than $7mm$ for the P_3 wave. The latter restriction would be, of course, unacceptable in most geotechnical applications.

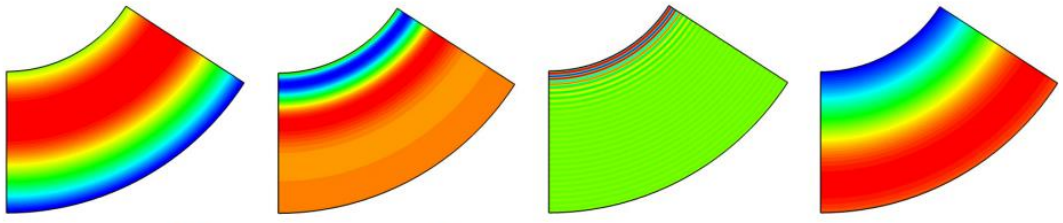

(a) P_1 wave solution, 500 Hz. (b) P_2 wave solution, 500 Hz. (c) P_3 wave solution, 50 Hz. (d) S wave solution, 500 Hz.

Figure 4.7: Reference stress fields in triphasic dynamic problems

The h-refinement is performed by meshing the domain into one, two and four elements, as presented in Figure 3.4. The p-refinement procedure is implemented increasing the orders of the domain with maximum degree 11 for P_1, P_2 ,S waves and maximum degree 60 for P_3 wave and boundary approximation functions of maximum degree 5. The mechanical energy error measure (3.73) is used, under definition (3.109) for the exact solution, and approximations (3.110) and (3.111) for the displacement and stress models, respectively.

Figures 4.8 and 4.9 present the p- and h-refinement convergence graphs for the three compressional waves and for the shear wave. The average convergence rates, k, associated to each refinement process (i.e. three refinement points) are shown next to the respective plot. The p-refinement convergence patterns corresponding to the single-, two- and four-element meshes are represented with solid lines and with square, diamond and circle markers, respectively. The dashed lines correspond to the convergence patterns obtained under h-refinement.

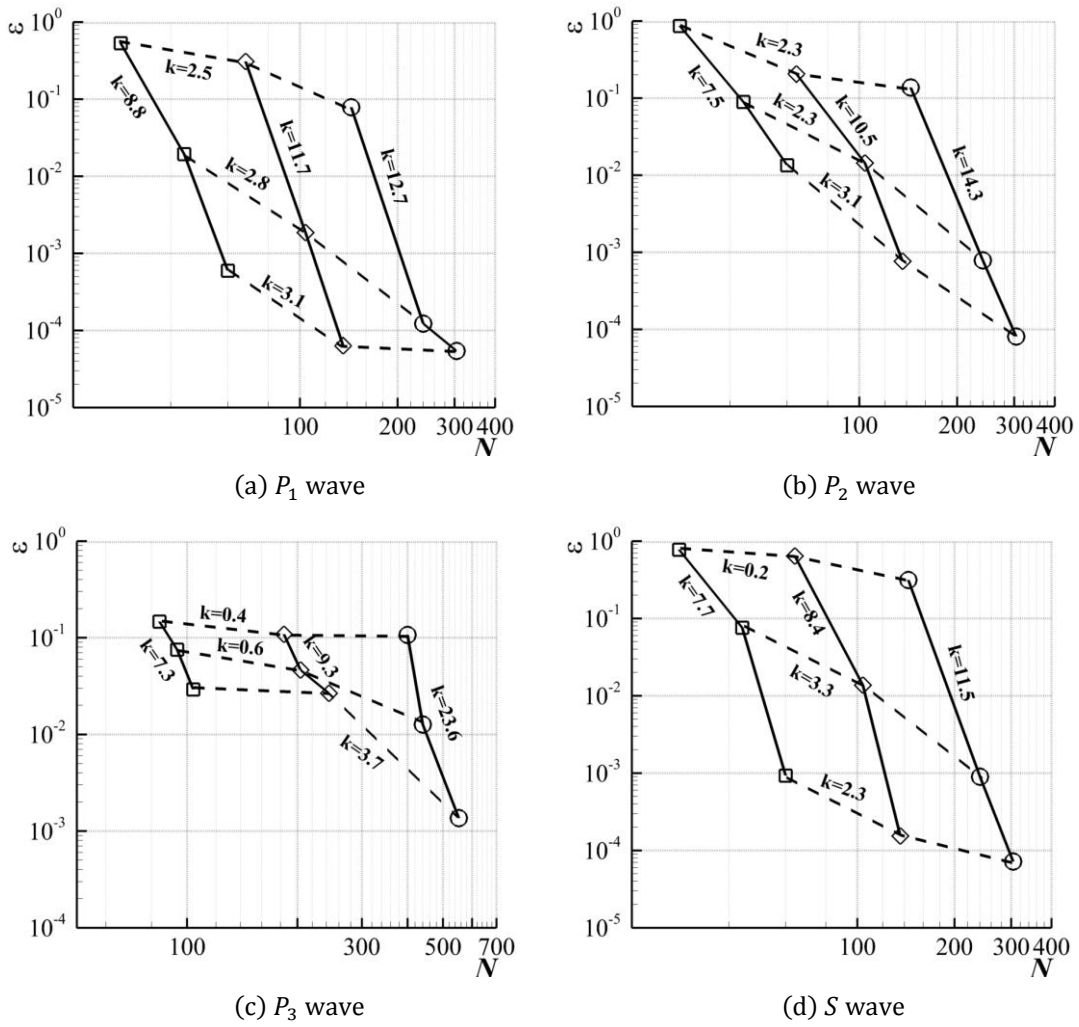

(a) P_1 wave (b) P_2 wave

(c) P_3 wave (d) S wave

Figure 4.8: Convergence results in triphasic dynamic problems (HTD)

As the hybrid-Trefftz elements are neither locally equilibrated, nor locally compatible, the convergence of the mechanical energy is not always monotonic [126]. This means that the exact mechanical energy is generally neither a minimum nor a maximum of its finite element approximation, as is the case in displacement-based and force-based conventional elements. For this reason, the convergence rate concept should be treated with caution when applied to hybrid-Trefftz elements, as the convergence rate may vary significantly during the refinement process.

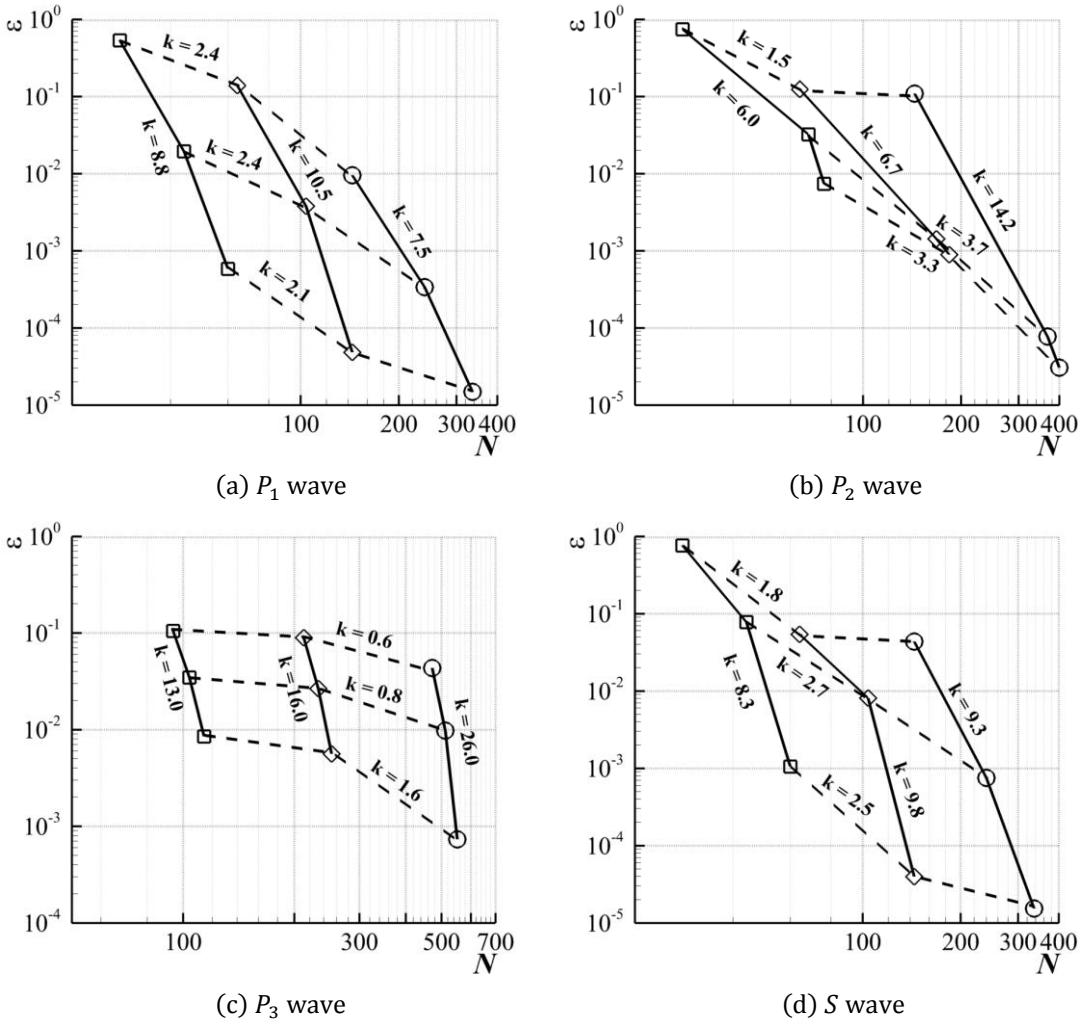

(a) P_1 wave (b) P_2 wave

(c) P_3 wave (d) S wave

Figure 4.9: Convergence results in triphasic dynamic problems (HTS)

Typically, the convergence rate is low in the initial phase of the process (especially when the solution is highly oscillatory), increasing significantly when Trefftz functions with oscillation patterns similar to the correct solution are inserted into the domain basis. Close to the correct solution, the convergence rate decreases and may even become negative as the predicted solution is oscillating around the exact solution (conversely, conventional elements present monotonic convergence patterns).

Despite the variability of the convergence rate, the analysis of Figures 4.8 and 4.9 shows that the convergence rates are similar for the HTD and HTS elements and the convergence rate under h-refinement is of the same order of magnitude as the convergence rate of (linear) conventional elements. It also shows that the (average) convergence under p-refinement is several times faster than the convergence under h-refinement. There is, however, only so much precision that can be

reached by only increasing the order of p-refinement. Over-increasing the number of approximation functions eventually leads to loss of precision due to the consequent ill-conditioning of the finite element solving system.

4.4 Sensitivity to frequency content

The domain used for the convergence tests, represented in Figure 3.4, is modeled with a single finite element, using the geometric and material data defined in Section 4.3.2. The robustness test consists in assessing the quality of the HTD and HTS solutions obtained for each type of wave and frequencies varying from $10^{-1}Hz$ to $10^{3}Hz$ for P_1, P_2 and S waves, and from $10^{-1}Hz$ to $300Hz$ for wave P_3. As for the tests on biphasic media, the levels of p-refinement are varied according to the numerical difficulty of the analyzed problem. The p-refinement procedure is implemented increasing the orders of the domain with maximum degree 11 for P_1, P_2, S waves and maximum degree 60 for P_3 wave.

Figures 4.10 and 4.11 represent the variation of the error measure defined by equation (3.73) and of the wavelength of the induced wave as functions of the excitation frequency (the wavelength axis is logarithmical). The tested wavelengths cover a rather wide range, from $236m$ (corresponding to the lowest frequency P_1 test) to only $6.4mm$ (for the P_3 test with $300Hz$ frequency).

Consequently, different levels of p-refinement are used to adequately capture the solution using hybrid-Trefftz elements. Problems involving the propagation of low frequency P_1 and S waves are implemented with a low number of displacement modes: 60 for displacement model and 57 for the stress model. The highly oscillatory P_3 waves require the use of 114 and 124 modes for displacement and stress models, respectively.

It is clear that the accuracy of the results in Figures 4.10 and 4.11 depends on the wavelength of the propagating wave, even when hybrid-Trefftz elements are used to construct the model. P_1 and S waves, characterized by low wavelengths, are modelled with good precision for all tested frequencies. Conversely, the error associated with the P_2 wave, with a wavelength roughly two orders of magnitude smaller than that of the P_1 wave, exceeds 1% for the highest tested frequency ($10^{3}Hz$).

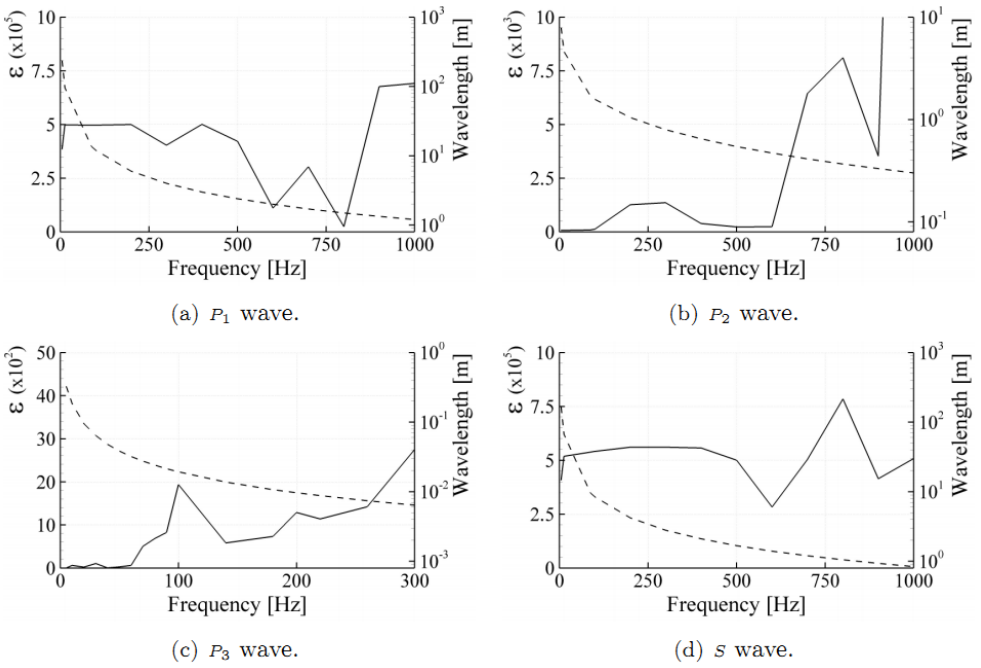

Figure 4.10: Robustness to high frequency excitations in triphasic dynamic problems (HTD)

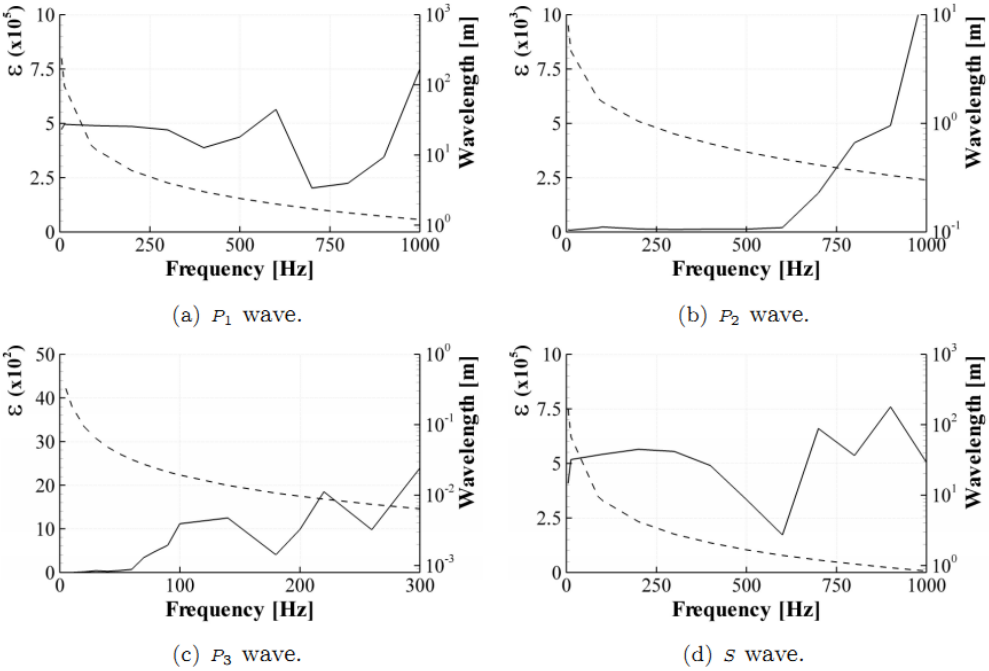

Figure 4.11: Robustness to high frequency excitations in triphasic dynamic problems (HTS)

As expected, the most challenging situation occurs for the P_3 wave, where the errors are significant for frequencies over $70Hz$. Still, the element with a leading dimension of $1.0m$ is capable of modelling the $6.4mm$ wavelength P_3 wave (that is, more than 150 wavelengths per element) within a 30% error. Based on substantial testing experience, it seems that correct

results can be reached within 99% accuracy using (sufficiently p-refined) hybrid-Trefftz elements, if their leading dimension is inferior to roughly 15 wavelengths. It is stressed that this restriction is more than 100 times more permissive than its conventional element counterpart Pluymers [125].

This advantage, due to the physical significance of the approximation functions, is especially relevant for the modeling of multi-phase soils, as it endorses the consistent representation of all compressional waves propagating through the fluid phases. It is noted, also, that the hybrid-Trefftz stress and displacement elements present basically the same robustness patterns.

4.5 Sensitivity to mesh distortion

The testing setup represented in Figure 3.6, with $L = \frac{r}{2} = 0.5m$, is used to assess the mesh distortion sensitivity of the hybrid-Trefftz displacement and stress elements in the analysis of static problems. The domain is divided in four elements. The range of the distortion parameter is $10^{-8} \leq \eta \leq 10^{-1}$ and the energy error is measured in form (3.74).

Figure 4.12 illustrates the variation of the error measure with the distortion parameter. It is seen that both displacement and stress models remain insensitive to gross mesh distortion. The (small) variations are due to the successive relocations of the origins of the local systems of reference, which follow the variations of the respective barycentre. In relative terms, the stress model seems to produce a lesser error than the displacement model, although in absolute terms the errors are small in both cases.

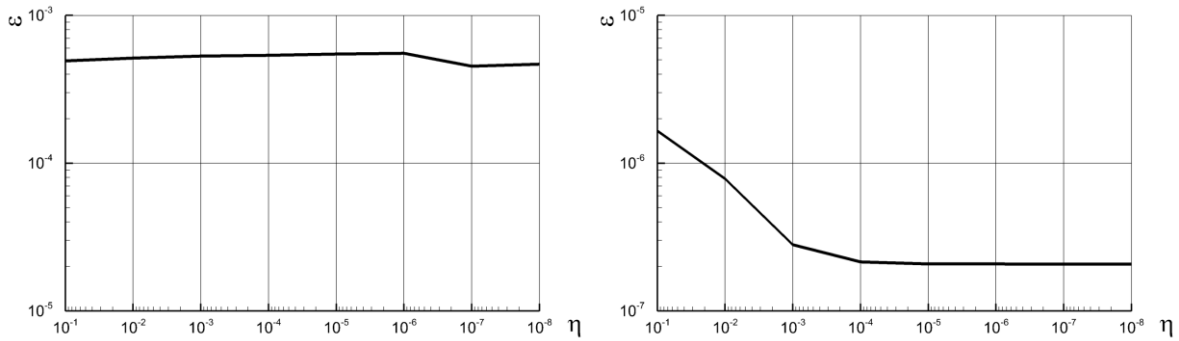

a) Displacement model b) Stress model

Figure 4.12: Sensitivity to mesh distortion in triphasic static problems

4.6 Static response of triphasic media

The single-layer problem defined the same geometry and finite mesh as in Figure 3.9 is solved to illustrate the ability of the hybrid-Trefftz elements to recover the boundary conditions and the inter-element continuity conditions under a more complex loading situation.

The loading $f = 1Pa$ is applied to the solid skeleton. Free surface flows are permitted for the wetting (liquid) and non-wetting (gas) phases. The normal displacements in the solid, Liquid and gas phases are restricted along the walls of the container. No constraints are imposed on the tangential components of the displacements on the frictionless tank walls.

The geomechanical characteristics are given in Appendix C. A saturation degree of 0.5 is used. The domain is meshed in 16 square elements with side length $L = 1.0m$. The domain approximation bases are constructed, for all elements, using polynomial functions of degree 15. The total number of degrees of freedom is 1,648 for the displacement model and 1,492 for the stress model.

The total stress fields predicted by the hybrid-Trefftz displacement and stress elements are presented in Figures 4.13 and 4.15. The results show that the hybrid-Trefftz finite element solutions are continuous on the inter-element boundaries and model adequately the enforced boundary conditions, for both HTD and HTS models.

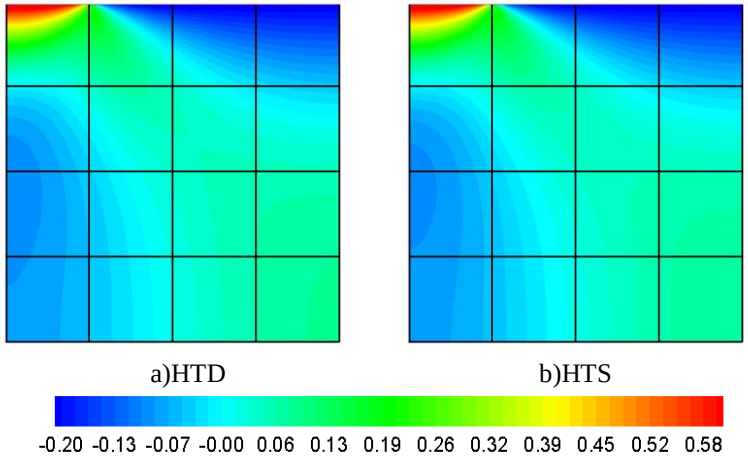

Figure 4.13: σ_{xx} (Pa) diagrams

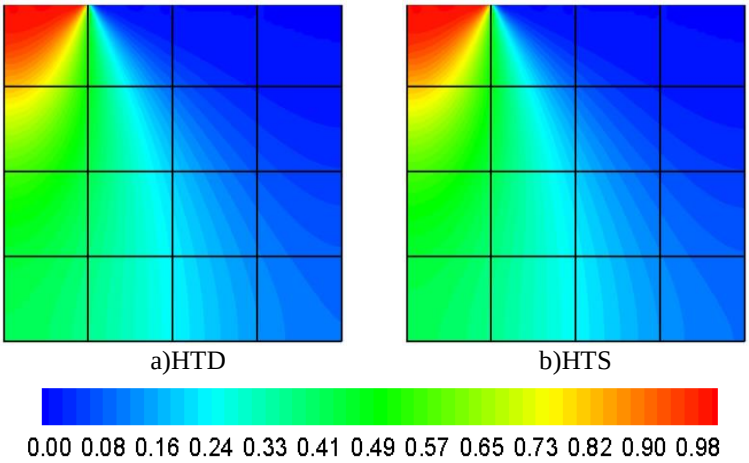

Figure 4.14: σ_{yy} (Pa) diagrams

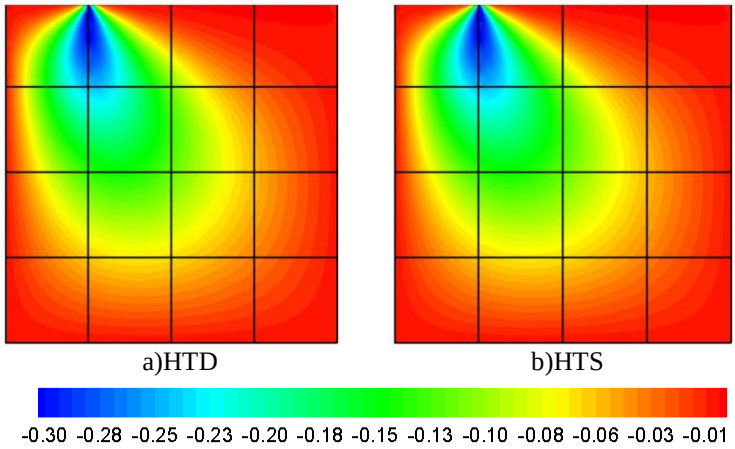

Figure 4.15: σ_{xy} (Pa) diagrams

4.7 Periodic response of triphasic media

The problem solved here, under plane strain conditions, is used to illustrate the ability of the hybrid-Trefftz elements to recover the inter-element continuity and the prescribed boundary conditions under harmonic loading. Two situations are considered. A single-layer medium is used to illustrate the propagation of the different types of waves. The effect material discontinuities have on the wave propagation patterns is illustrated using a two-layer medium. The geomechanical characteristics of the medium are given in Appendix C with a bulk modulus of the air phase ten times larger to in order to obtain non-zero gas pressure and be able to meaningfully assess their quality. Both stress and displacement models are tested with two excitation frequencies, $12.5Hz$ and $100Hz$, in order to illustrate their relative performance under rather distinct situations.

4.7.1 Wave propagation in a single-layer medium

The triphasic medium defined in Figure 4.16 ($L = 0.25m$) is subjected to a surface loading $p(x) = \bar{p} \cdot exp(\hat{\imath}\omega t)$, with amplitude $\bar{p} = 1\ (Pa)$, acting on the solid skeleton. Null pore pressures are assumed at the free surface for both fluid phases. The containing tank is rigid and has frictionless walls. Consequently, the normal displacements of all phases are restricted on boundaries $x = \pm 2L$ and $y = -L$.

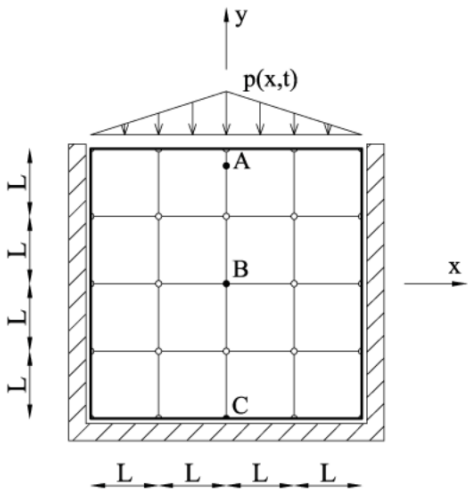

Figure 4.16: Description for the harmonic tests model for single-layered problem

The wavelengths in the medium are 7.5cm (P_1 wave), 4.6cm (P_2 wave), 1.6cm (P_3 wave) and 2.5cm (S wave) for the high frequency test, and are 59.6cm (P_1 wave), 13.5cm (P_2 wave), 13.2cm (P_3 wave) and 20.6cm (S wave) for the low frequency test.

For both testing frequencies, the domain approximation bases for the displacement and stress models are constructed using first kind Bessel functions of order $N_d = 11$. The boundary approximation is defined using Tchebychev polynomials with degree $M = 5$. The total number of degrees of freedom for displacement model is 2,264 (1,472 displacement modes and 792 boundary force modes). The stress model is implemented using 2,216 degrees of freedom (1,472 stress modes and 744 boundary displacement modes).

The amplitudes and contours of the stress fields are shown in Figures 4.17 and 4.18 for the displacement model and in Figures 4.19 and 4.20 for the stress model. The results clearly show that the inter-element continuity conditions are well respected and that the assumed boundary conditions are accurately recovered despite the significant physical differences of wave propagation phenomena for the two testing frequencies. The tests also indicate a good agreement between the responses predicted by the alternative models. As before, no smoothing is used in the graphs.

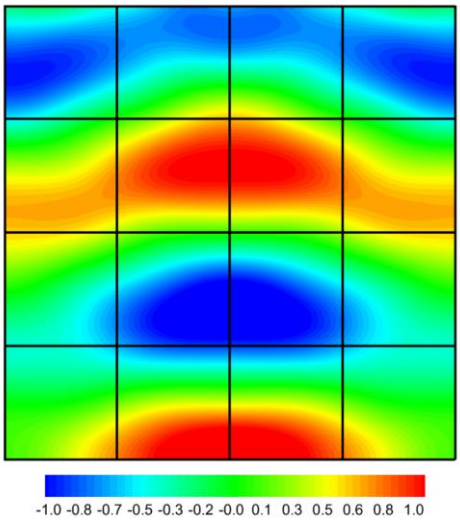

a) σ_{xx}(Pa)

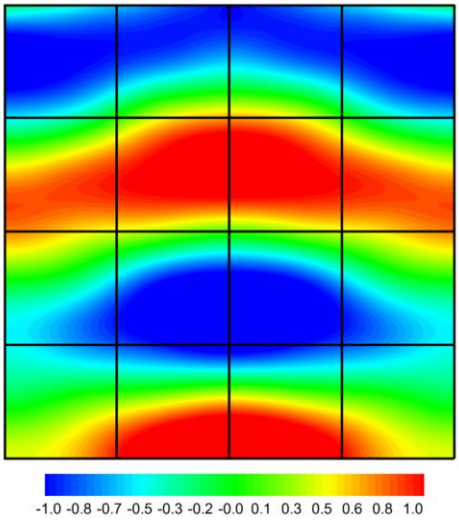

b) σ_{yy}(Pa)

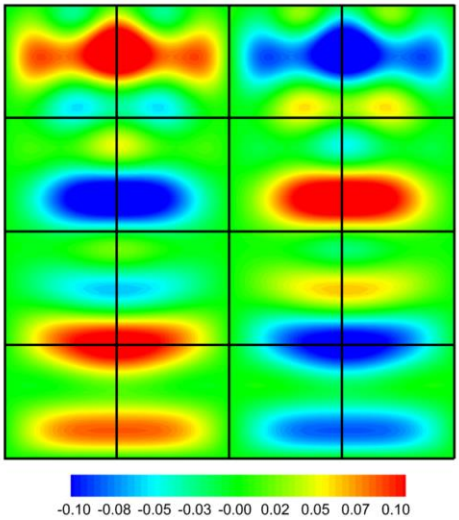

c) σ_{xy}(Pa)

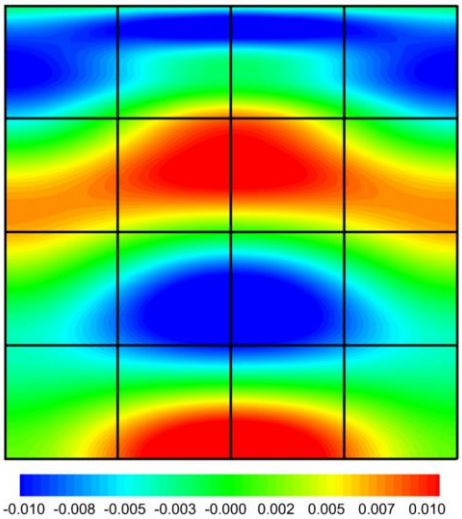

d) π^W(Pa)

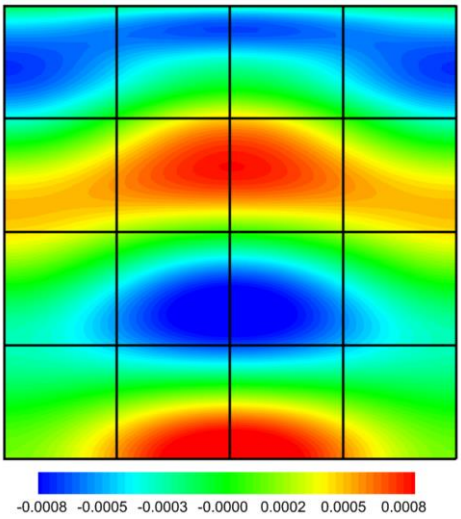

e) π^N(Pa)

Figure 4.17: Stress fields for displacement element ($\boldsymbol{\omega = 12.5\ Hz}$)

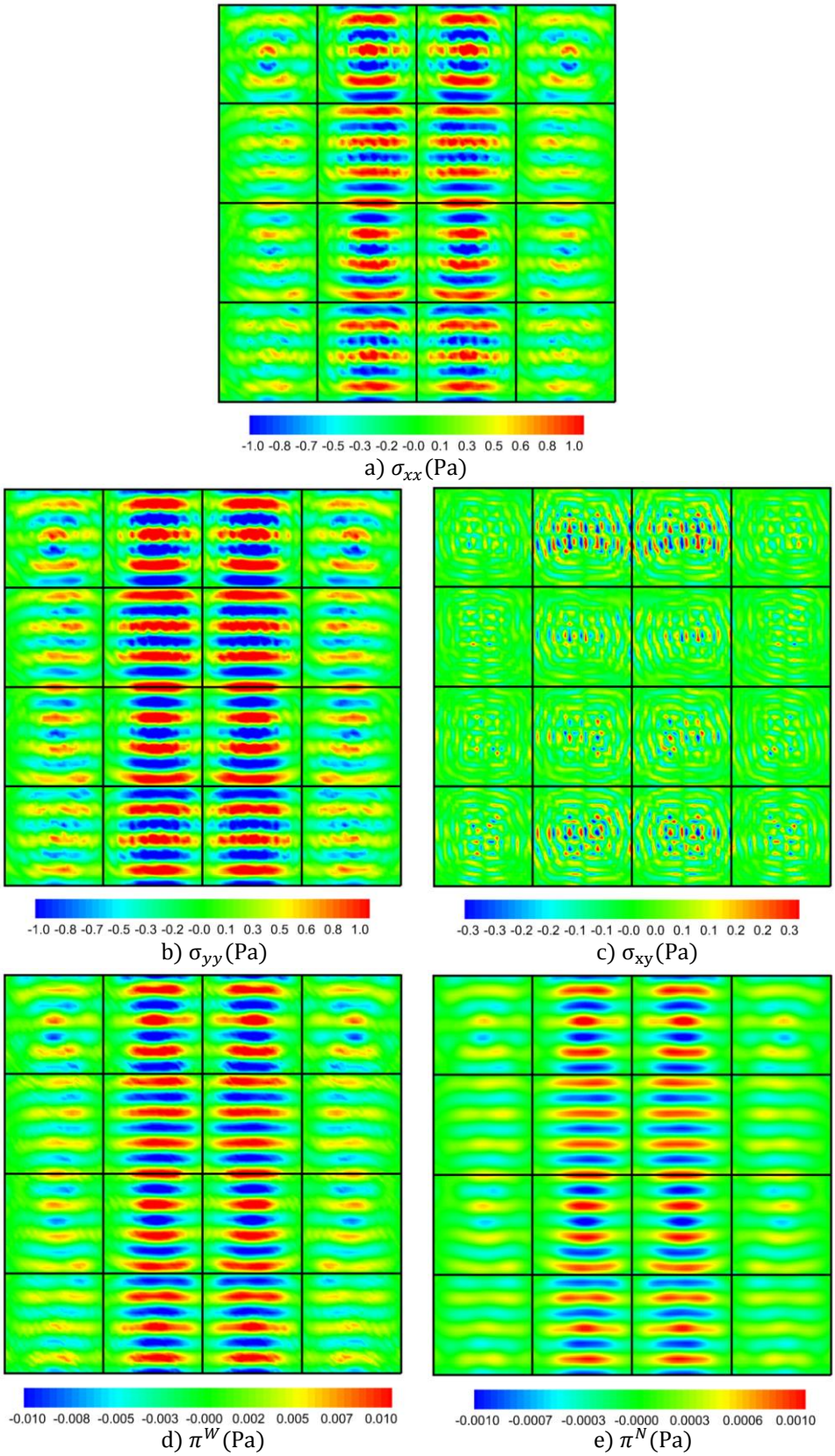

a) σ_{xx}(Pa)

b) σ_{yy}(Pa)

c) σ_{xy}(Pa)

d) π^W(Pa)

e) π^N(Pa)

Figure 4.18: Stress fields for displacement element ($\boldsymbol{\omega = 100\ Hz}$)

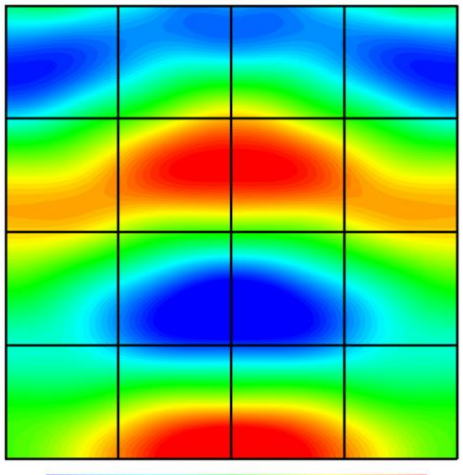

a) σ_{xx}(Pa)

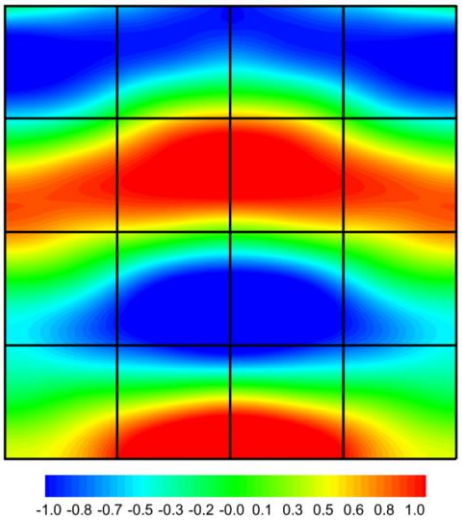

b) σ_{yy}(Pa)

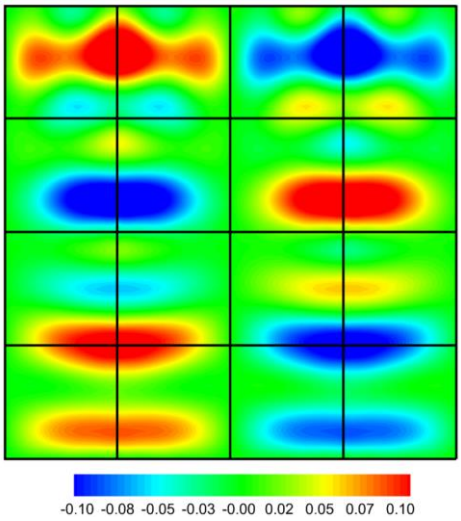

c) σ_{xy}(Pa)

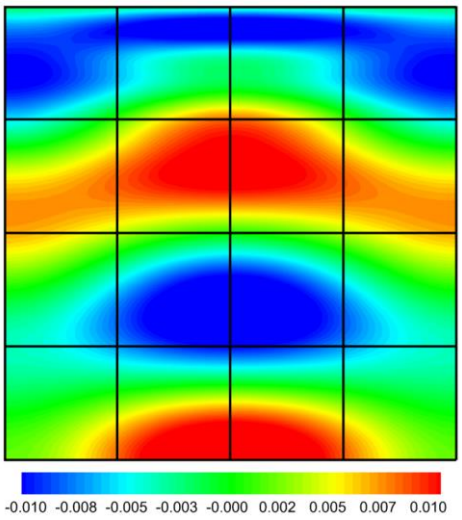

d) π^{W}(Pa)

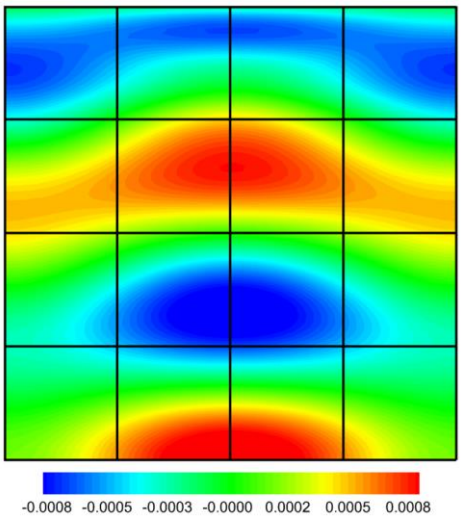

e) π^{N}(Pa)

Figure 4.19: Stress fields for stress element ($\boldsymbol{\omega = 12.5\ Hz}$)

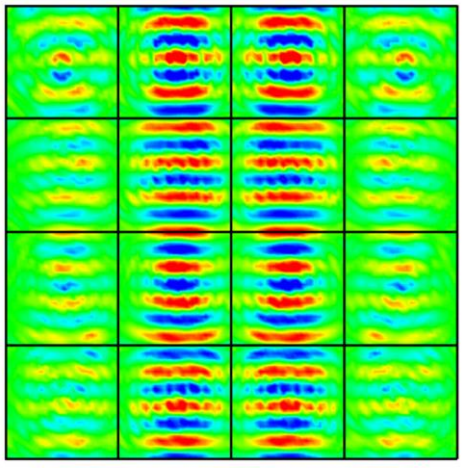

a) σ_{xx}(Pa)

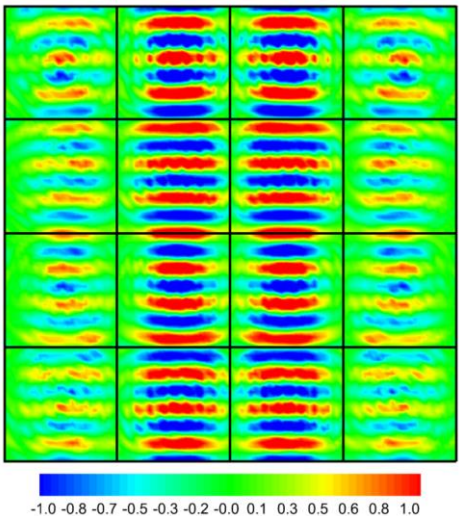

b) σ_{yy}(Pa)

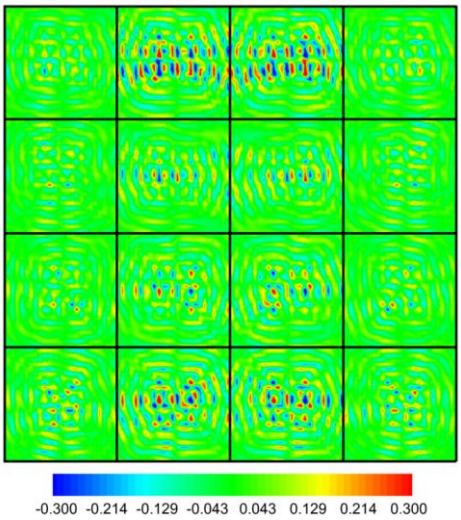

c) σ_{xy}(Pa)

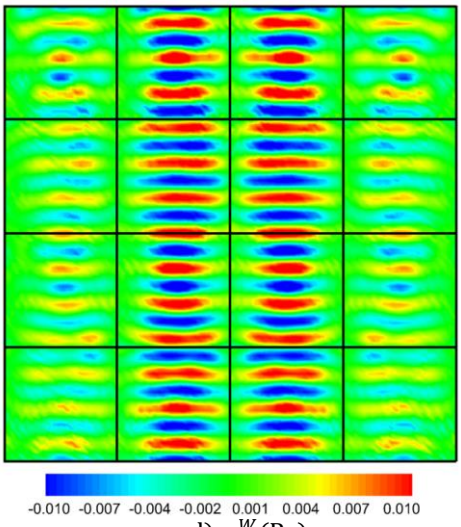

d) π^W(Pa)

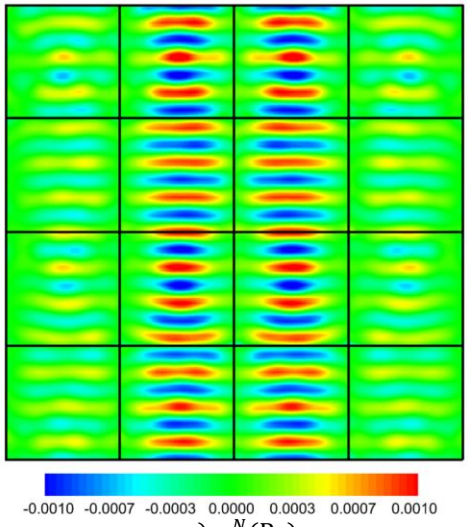

e) π^N(Pa)

Figure 4.20: Stress fields for stress element ($\boldsymbol{\omega = 100\ Hz}$)

4.7.2 Wave propagation in a two-layer medium

The two-layer triphasic medium defined in Figure 4.21 ($L = 0.125m$) is modelled with both displacement and stress elements. The problem setup is similar to that used in the single-layer test with two exceptions: the spatial distribution of the loading $p = \bar{p} \cdot exp(\hat{\imath}\omega t)$, with amplitude $\bar{p} = 1$ (Pa), and the presence of two layers of different materials, each with $4L = 0.5m$ thickness. The upper layer consists of the unsaturated medium defined in Appendix C, while the lower layer is formed of the same material with a Young's modulus eight times larger.

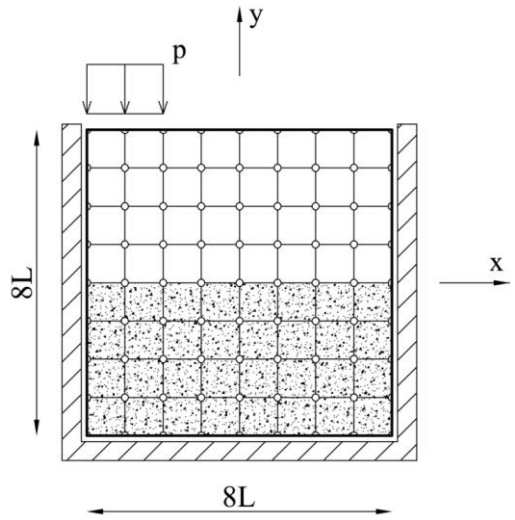

Figure 4.21: Description of the harmonic tests model for two-layer problem

The wavelengths in the upper layer are defined in the previous section. In the lower layer, the wavelengths are 9.1cm (P_1 wave), 4.6cm (P_2 wave), 1.6cm (P_3 wave) and 5.1cm (S wave) for the high frequency test, and are 693.1cm (P_1 wave), 88.9cm (P_2 wave), 43.2cm (P_3 wave) and 387.1cm (S wave) for the low frequency test.

For both testing frequencies, the domain approximation bases for the displacement and stress models are constructed using first kind Bessel functions of order $N_d = 11$. The boundary approximation is defined using Tchebychev polynomials with degree $M = 5$. The total number of degrees of freedom for displacement model is 9,008 (5,888 displacement modes and 3,120 boundary force modes). The stress model is implemented using 8,912 degrees of freedom (5,888 stress modes and 3,024 boundary displacement modes).

The amplitudes and contours of the stress fields are shown in Figures 4.22 and 4.23 for the displacement model and in Figures 4.24 and 4.25 for the stress model. The results clearly show that the inter-element continuity conditions are well respected and also indicate a good

agreement between the responses predicted by the alternative models. The same (coarse) mesh is used to solve both problems, despite the difference between the excitation frequencies and consequently between the wavelengths of the propagating waves, thus reinforcing the lack of sensitivity of the models to the wavelength of the propagating waves.

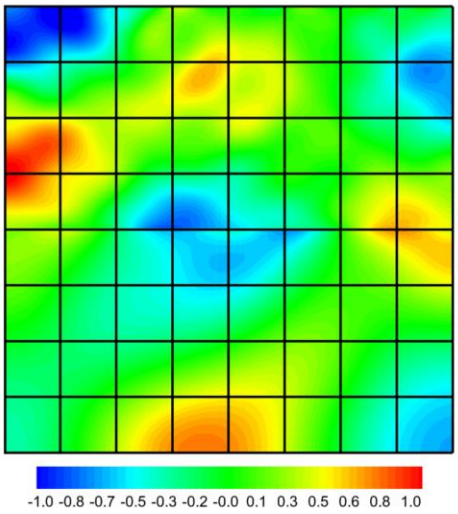

a) σ_{xx}(Pa)

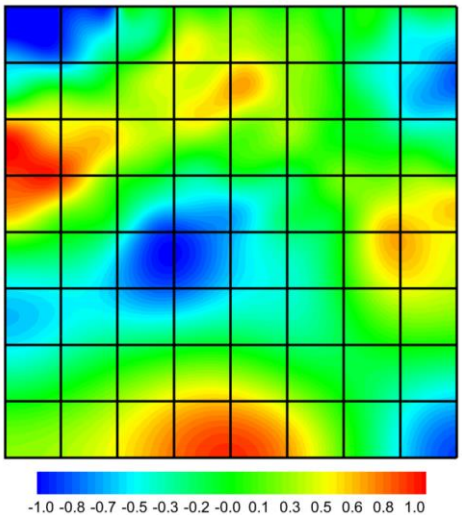

b) σ_{yy}(Pa)

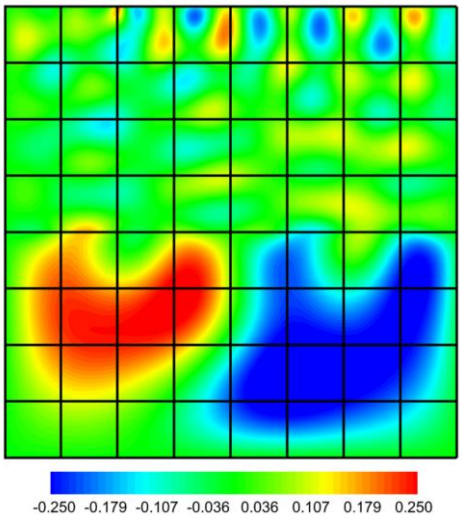

c) σ_{xy}(Pa)

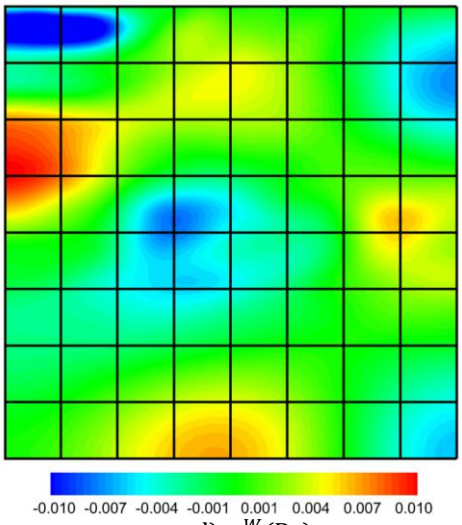

d) π^W(Pa)

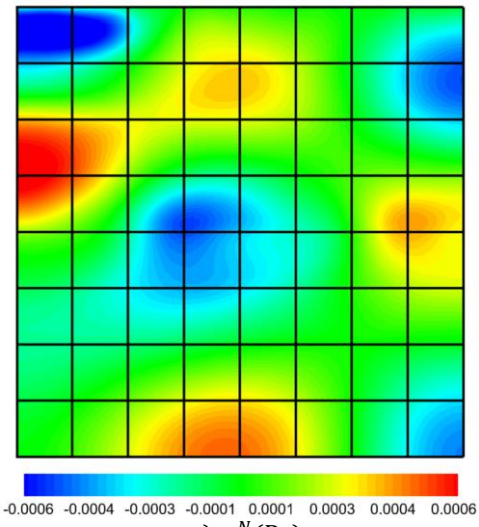

e) π^N(Pa)

Figure 4.22: Stress fields for displacement element ($\boldsymbol{\omega = 12.5\ Hz}$)

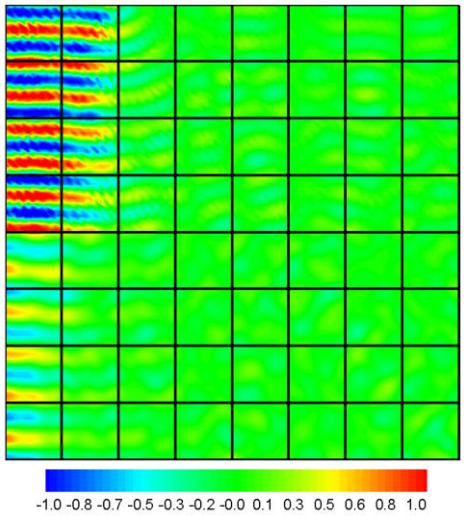

a) σ_{xx}(Pa)

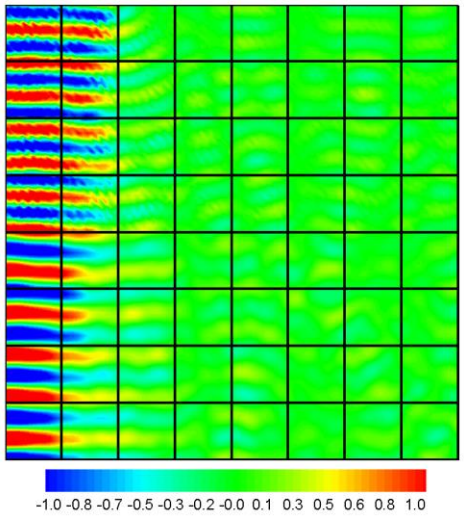

b) σ_{yy}(Pa)

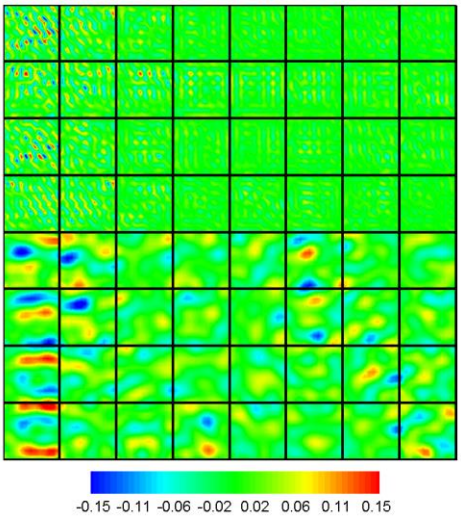

c) σ_{xy}(Pa)

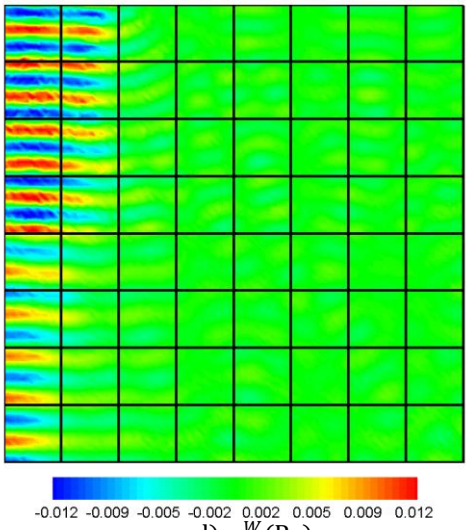

d) π^{W}(Pa)

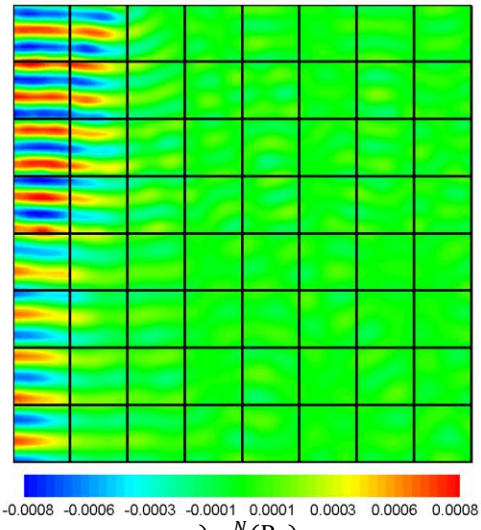

e) π^{N}(Pa)

Figure 4.23: Stress fields for displacement element ($\boldsymbol{\omega = 100\ Hz}$)

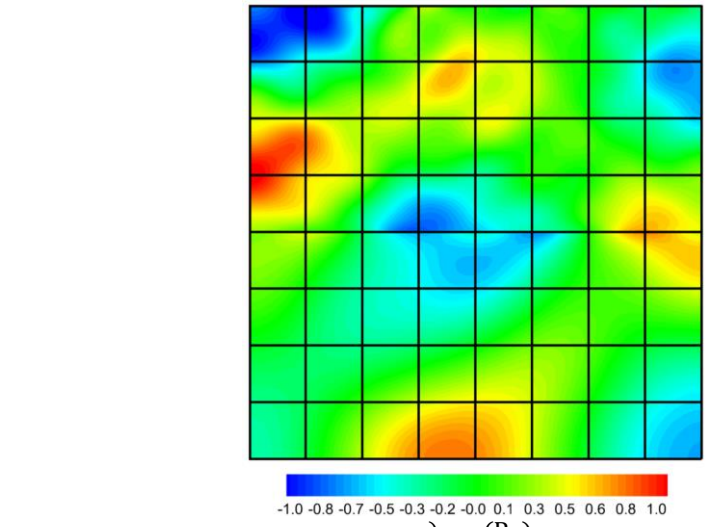

a) σ_{xx}(Pa)

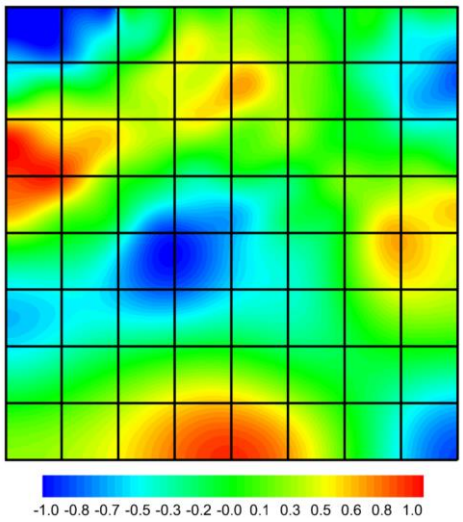

b) σ_{yy}(Pa)

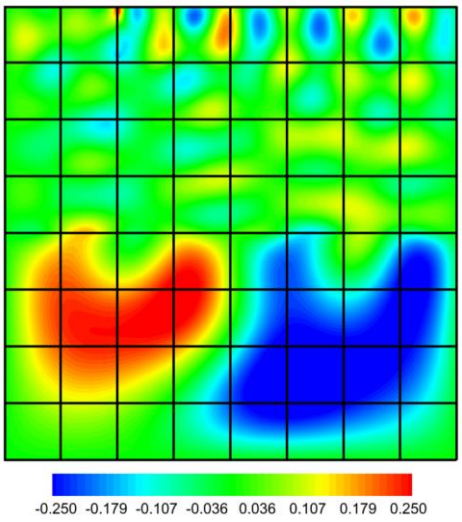

c) σ_{xy}(Pa)

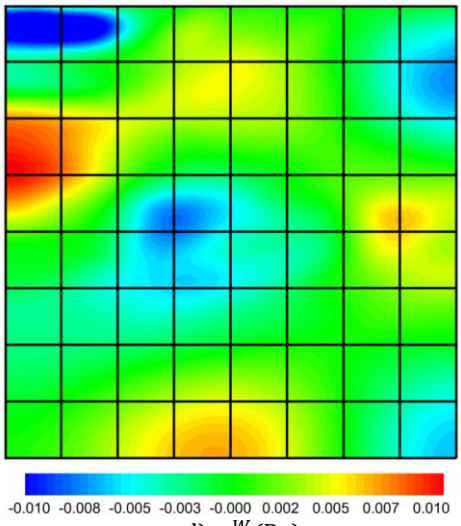

d) π^{W}(Pa)

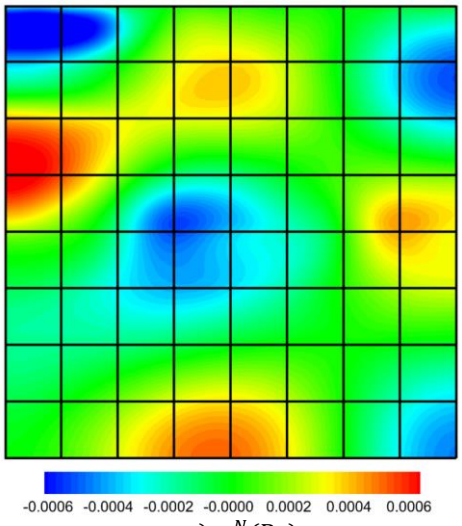

e) π^{N}(Pa)

Figure 4.24: Stress fields for stress element ($\boldsymbol{\omega = 12.5\ Hz}$)

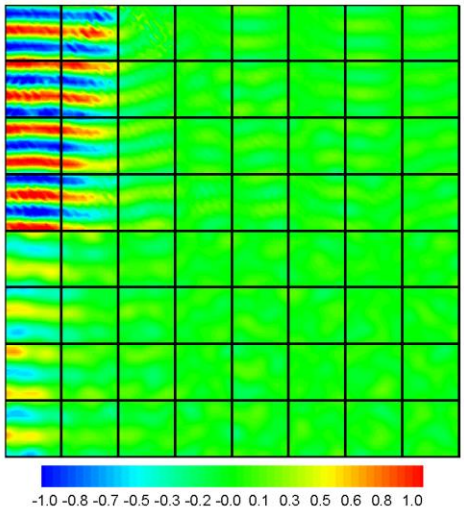

a) σ_{xx}(Pa)

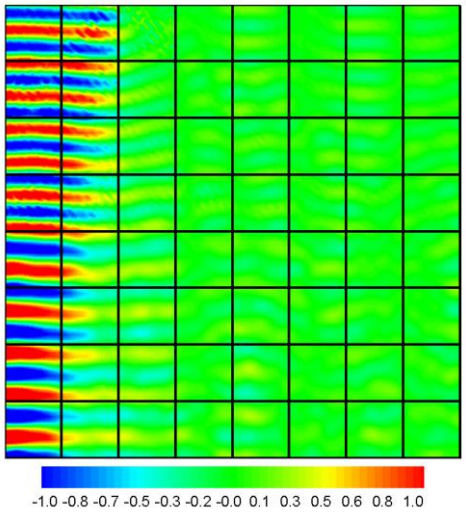

b) σ_{yy}(Pa)

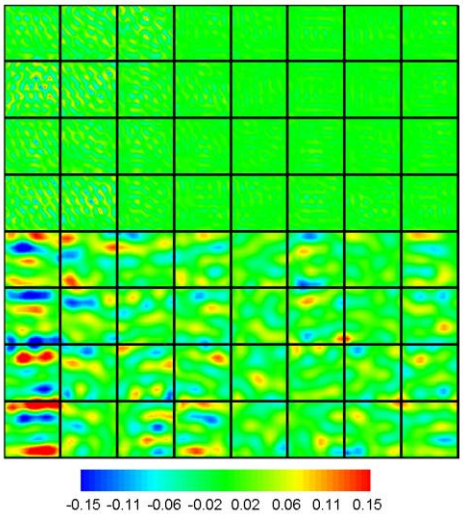

c) σ_{xy}(Pa)

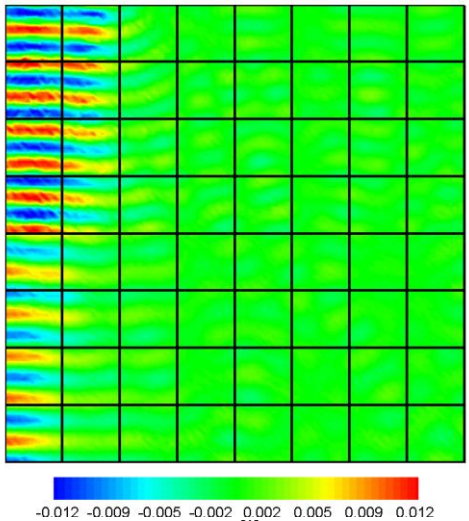

d) π^{W}(Pa)

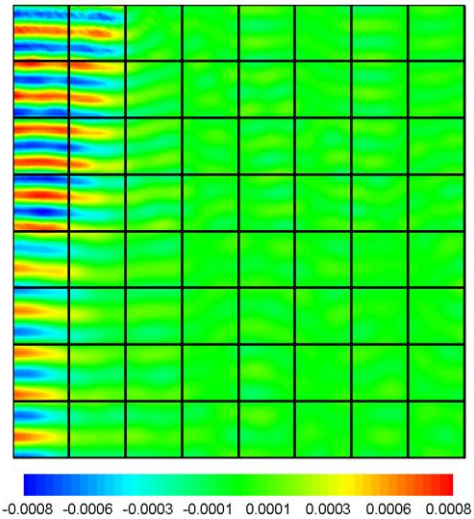

e) π^{N}(Pa)

Figure 4.25: Stress fields for stress element ($\omega = 100$ Hz)

4.8 Transient response of triphasic media

To illustrate the results obtained with the hybrid-Trefftz displacement and stress elements under transient loading conditions, the propagation of a shock wave through a triphasic medium is modelled next. Two situations are considered. A single-layer medium is used to illustrate the propagation of the different types of waves. The effect material discontinuities have on the wave propagation patterns is illustrated using a two-layer medium.

The triphasic material is designed to obtain a phase velocity of the first compressional wave low enough for its propagation to be easily observed during the total analysis time of $1.0sec$. The geomechanical characteristics of the medium are given in Appendix C.

As both applications are linear, the total duration of the analyses is modelled in a single time step ($1.0sec$). The same time basis is used in both tests, as they share the same variation in time of the applied (impulse) load. This basis is constructed using Daubechies wavelets and scale functions of the fourth family.

4.8.1 Shock wave propagation in a single-layer medium

In this test, the shock wave is caused by a pulse load $p(x) \cdot f(t)$, with amplitude $p_{max} = 1Pa$, applied on the free surface of the medium represented in Figure 4.26 ($L = 0.25m$) and acting on the solid skeleton. Null pore pressures are assumed at the free surface for both fluid phases. The containing tank is rigid and has frictionless walls. Consequently, the normal displacements of all phases are restricted on boundaries $x = \pm 2L$ and $y = -L$. Plane strain conditions are assumed.

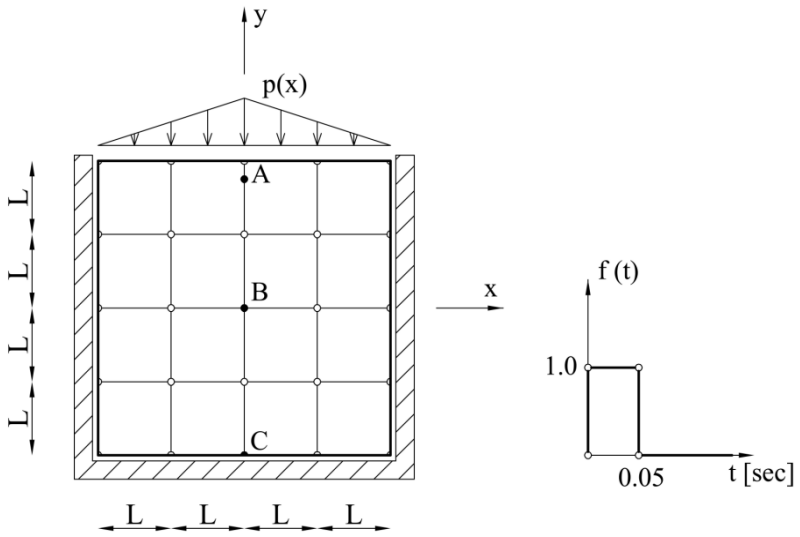

Figure 4.26: Description of the pulse test model

The wavelet time basis generates 32 spectral problems with algorithmic frequencies with moduli ranging from $1.93Hz$ to $17.39Hz$. The phase velocities of the (non-dispersive) P_1 and S waves are $7.35m/s$ and $2.5m/s$. The wave velocities of the compressional waves travelling through the fluid phases range between $1.38m/s$ and $1.66m/s$ (P_2 wave) and $0.32m/s$ and $0.67m/s$ (P_3 wave). The minimum wavelengths are $42.87cm$ (P_1 wave), $9.35cm$ (P_2 wave), $3.85cm$ (P_3 wave) and $14.6cm$ (S wave).

The domain is discretized in 16 finite elements, as shown in Figure 4.26. The domain basis is constructed using first kind Bessel functions, according to definitions (4.94) and (4.95) for the displacement and stress models, respectively. For the displacement model, the total number of displacement degrees of freedom per element is 92. Tchebychev polynomials are used for the traction approximation on the essential boundaries of the element, generating a total of 44 degrees of freedom per boundary. The total dimension of the assembled solving system is 2,264. The same h- and p-refinements are used for all spectral problems. For the stress model, the total number of stress degrees of freedom is 1,472. The boundary displacement field is approximated with Tchebychev polynomials, generating a total of 744 degrees of freedom. The total dimension of the assembled finite element solving system is 2,216.

Figures 4.27 to 4.30 present the displacement element estimates of the stress and water pore pressure fields at selected instants during the first 0.5sec of the time interval. The pore pressure in the gas phase remains very low at all times. The stress element estimates are presented in

Figures 4.31 to 4.34. In these illustrations, the stress fields are superimposed to the deformed shapes of the medium.

The results show that the shock wave propagates downwards and reaches the bottom of the tank after roughly $0.14sec$. This is consistent with the propagation velocity of the P_1 wave, which is the fastest of all types of waves. The stress intensity at the wavefront doubles upon impact with the bottom of the tank and the wave reflects back towards the surface. The wavefront causes a positive vertical movement of the free surface at $0.22sec$, which causes a dilatational wavefront which re-initiates the downward propagation pattern. The damping effect is clearly visible as the intensity of all stress fields diminishes with time. The enforced boundary conditions are well respected both in terms of stresses and displacements.

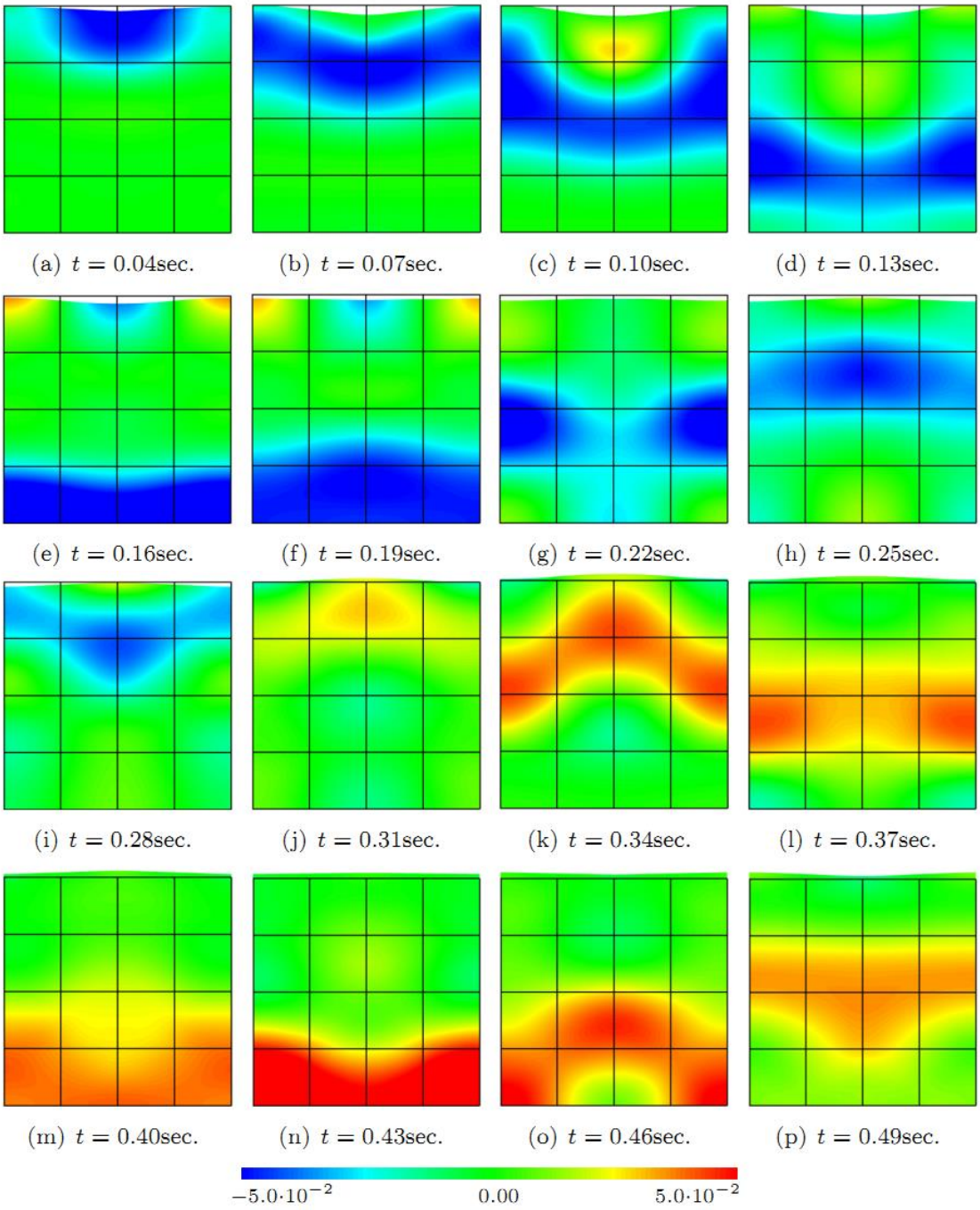

Figure 4.27: σ_{xx} (Pa) diagrams (HTD)

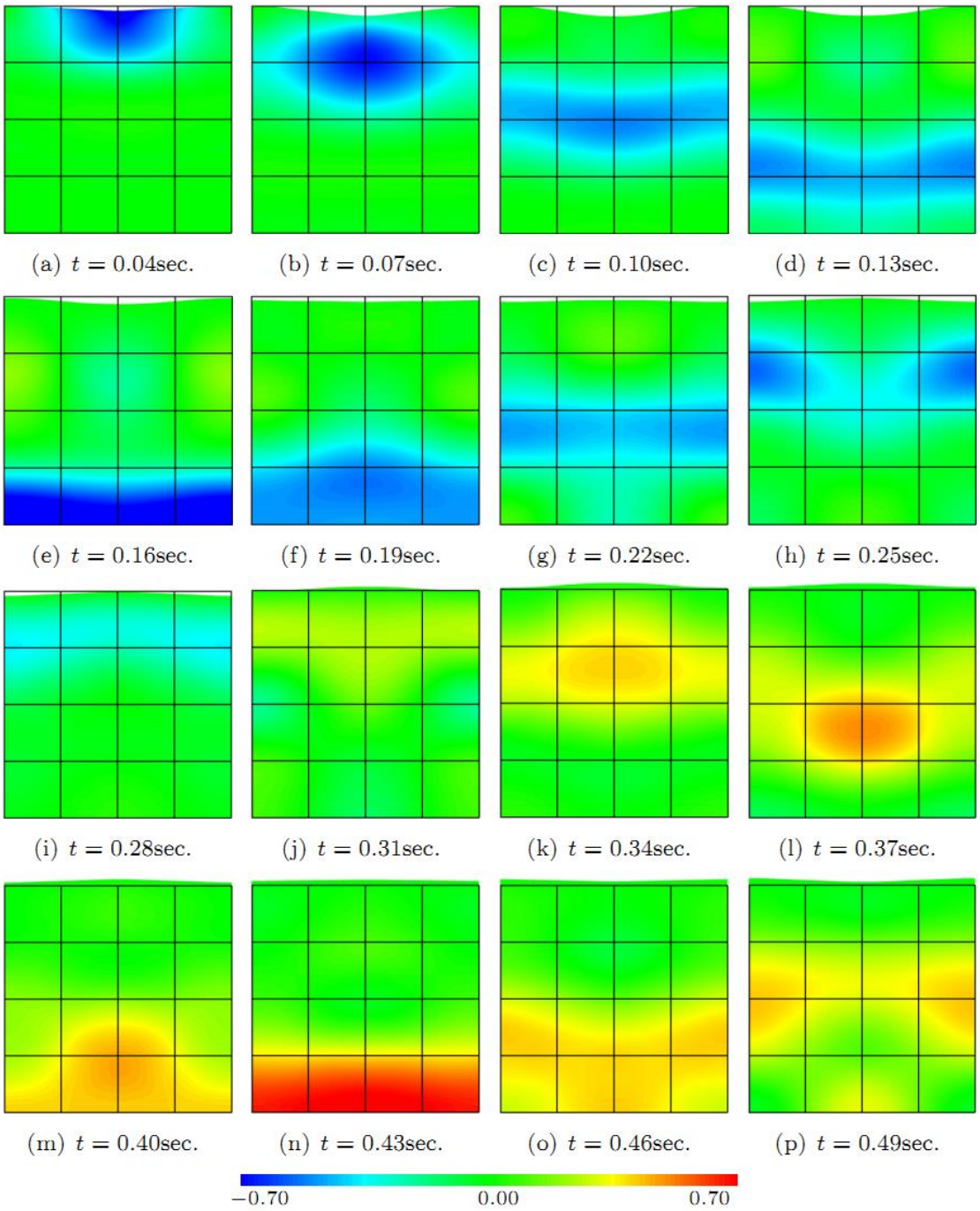

Figure 4.28: σ_{yy} (Pa) diagrams (HTD)

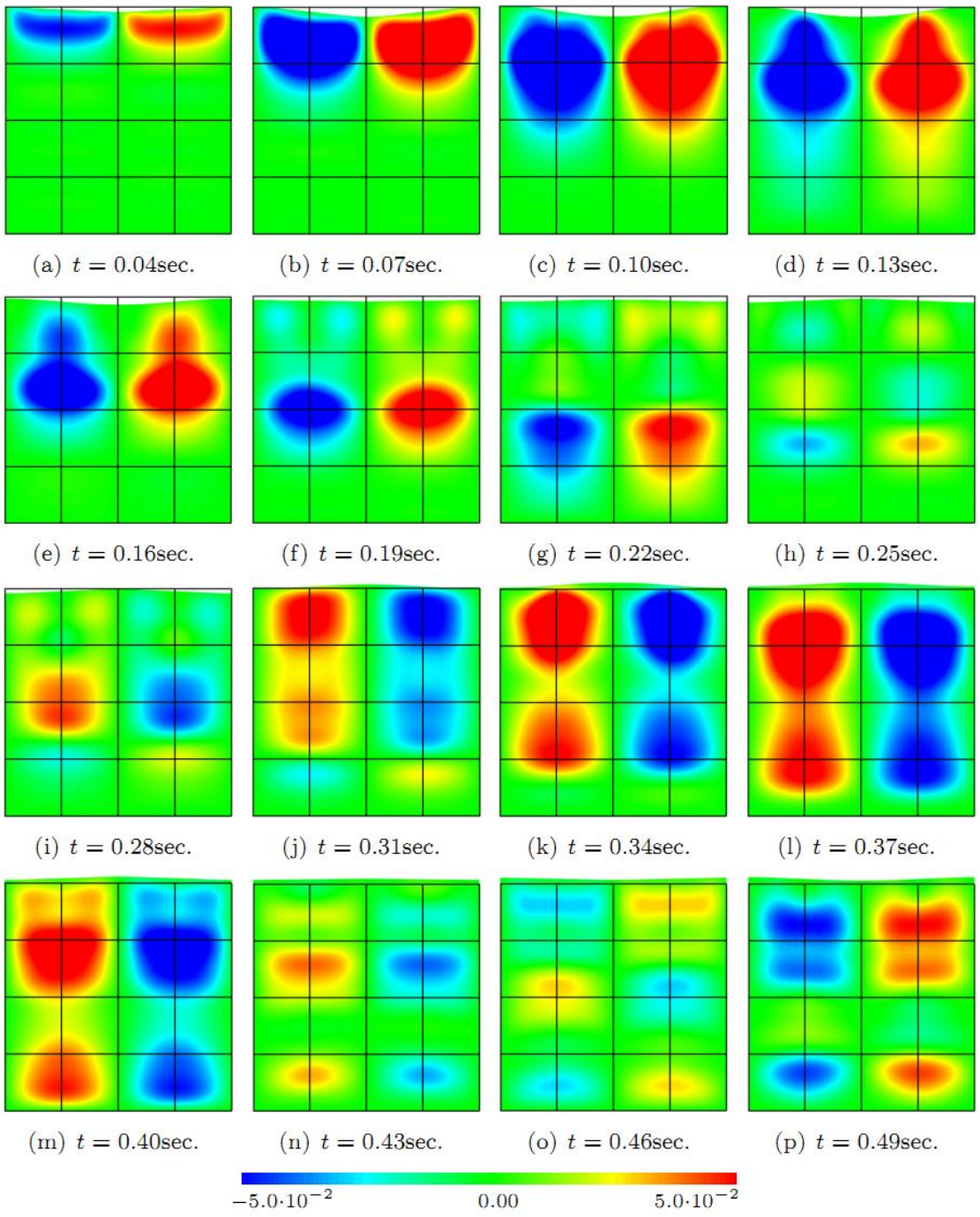

Figure 4.29: σ_{xy} (Pa) diagrams (HTD)

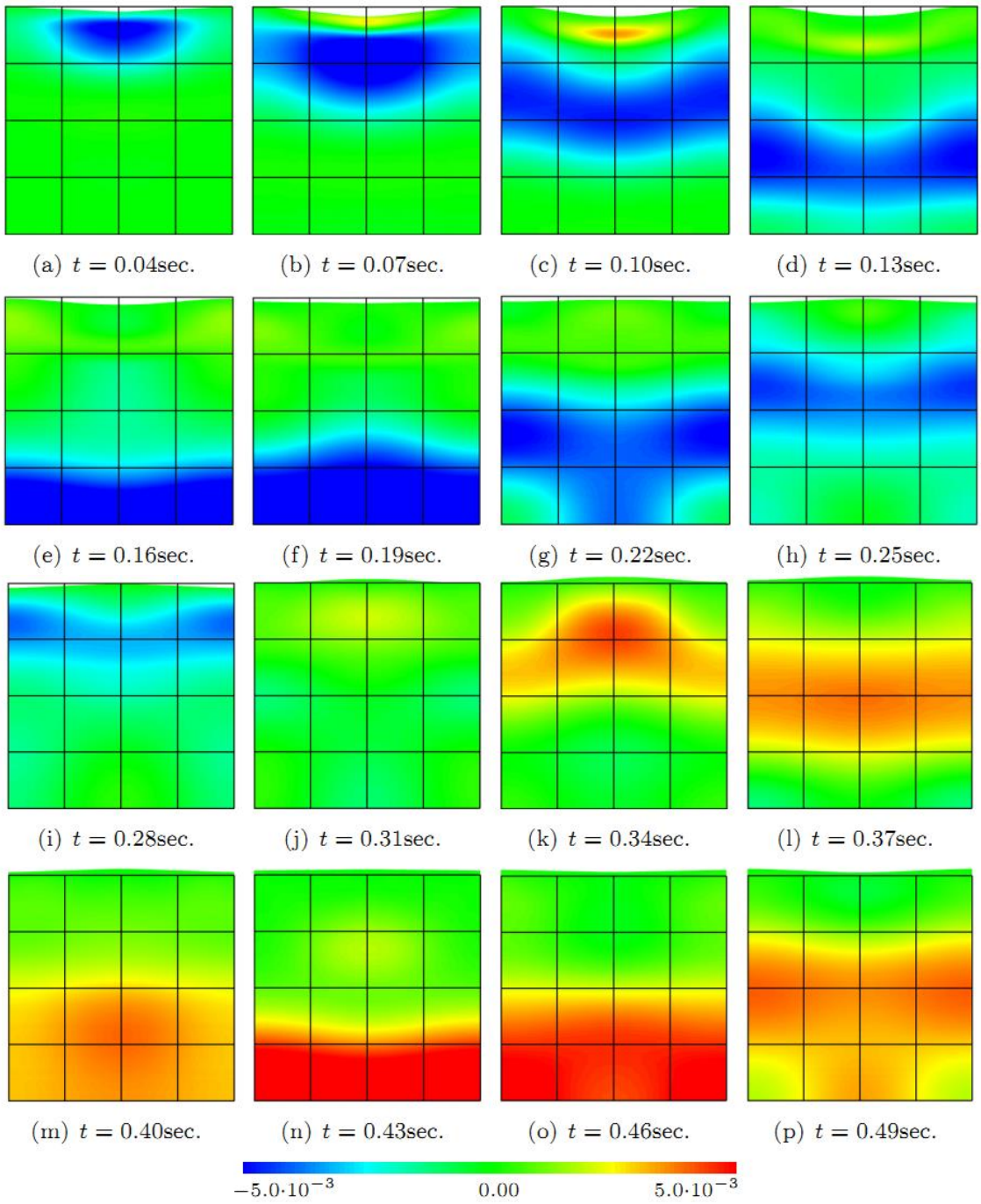

Figure 4.30: π^W (Pa) diagrams (HTD)

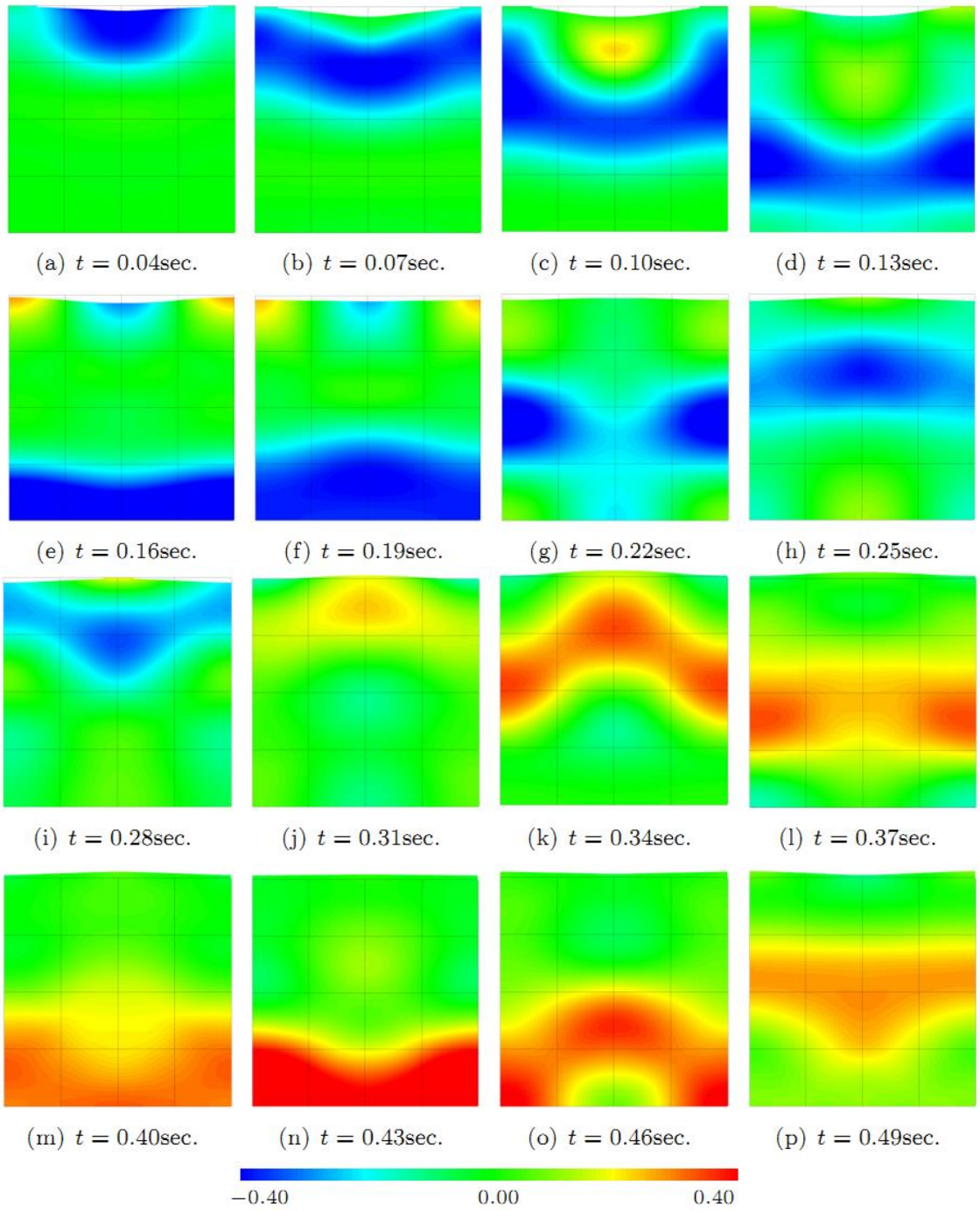

Figure 4.31: σ_{xx} (Pa) diagrams (HTS)

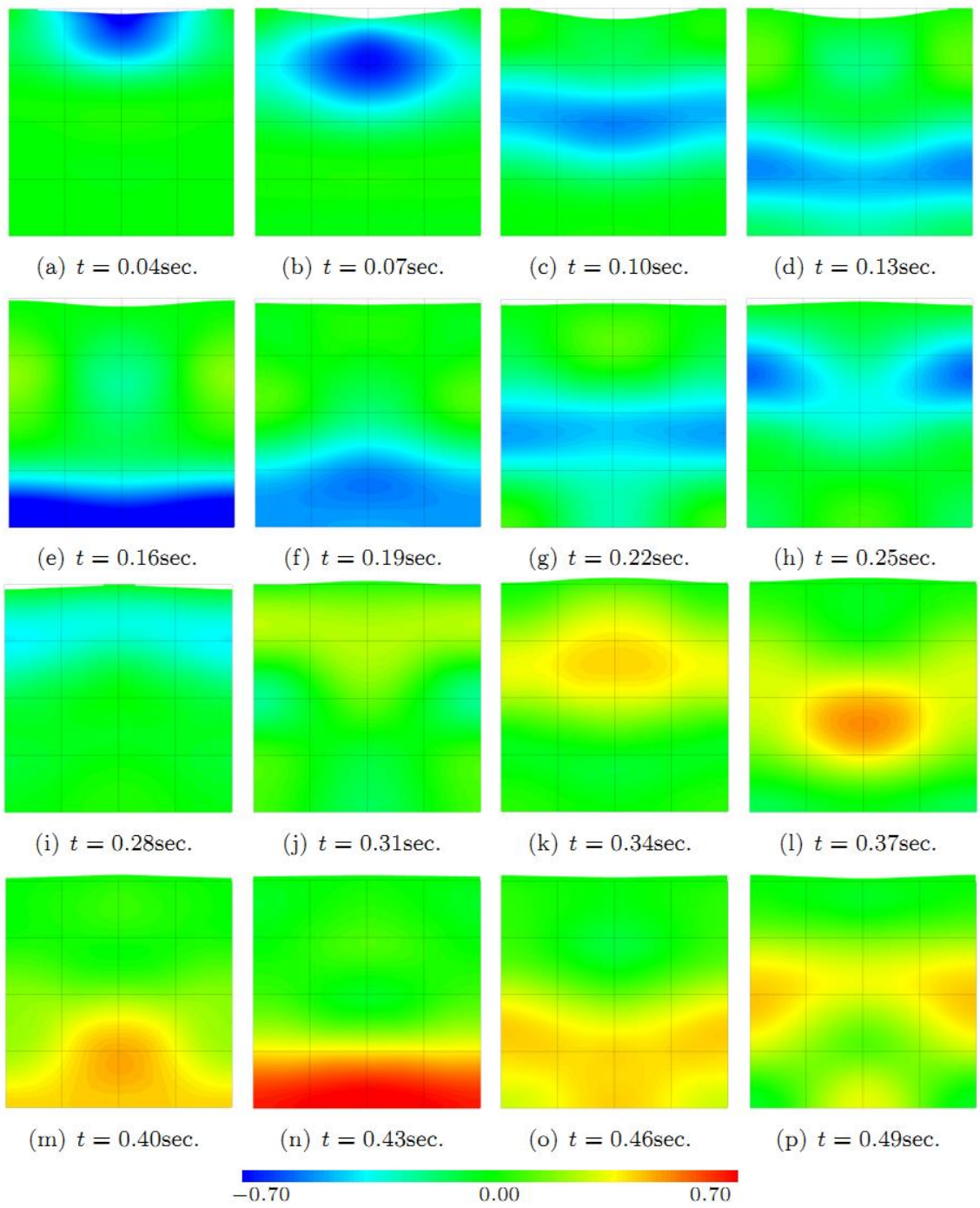

Figure 4.32: σ_{yy} (Pa) diagrams (HTS)

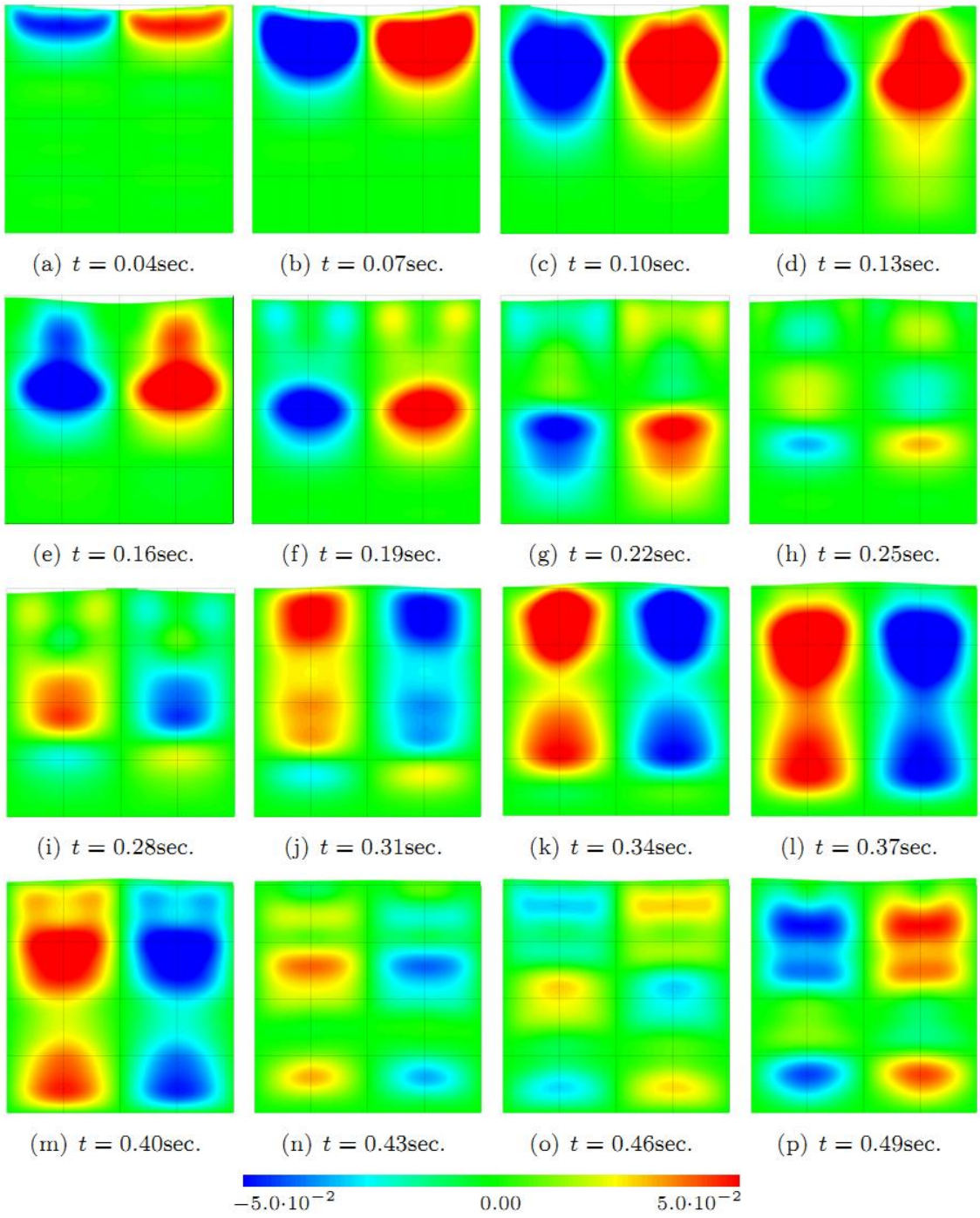

Figure 4.33: σ_{xy} (Pa) diagrams (HTS)

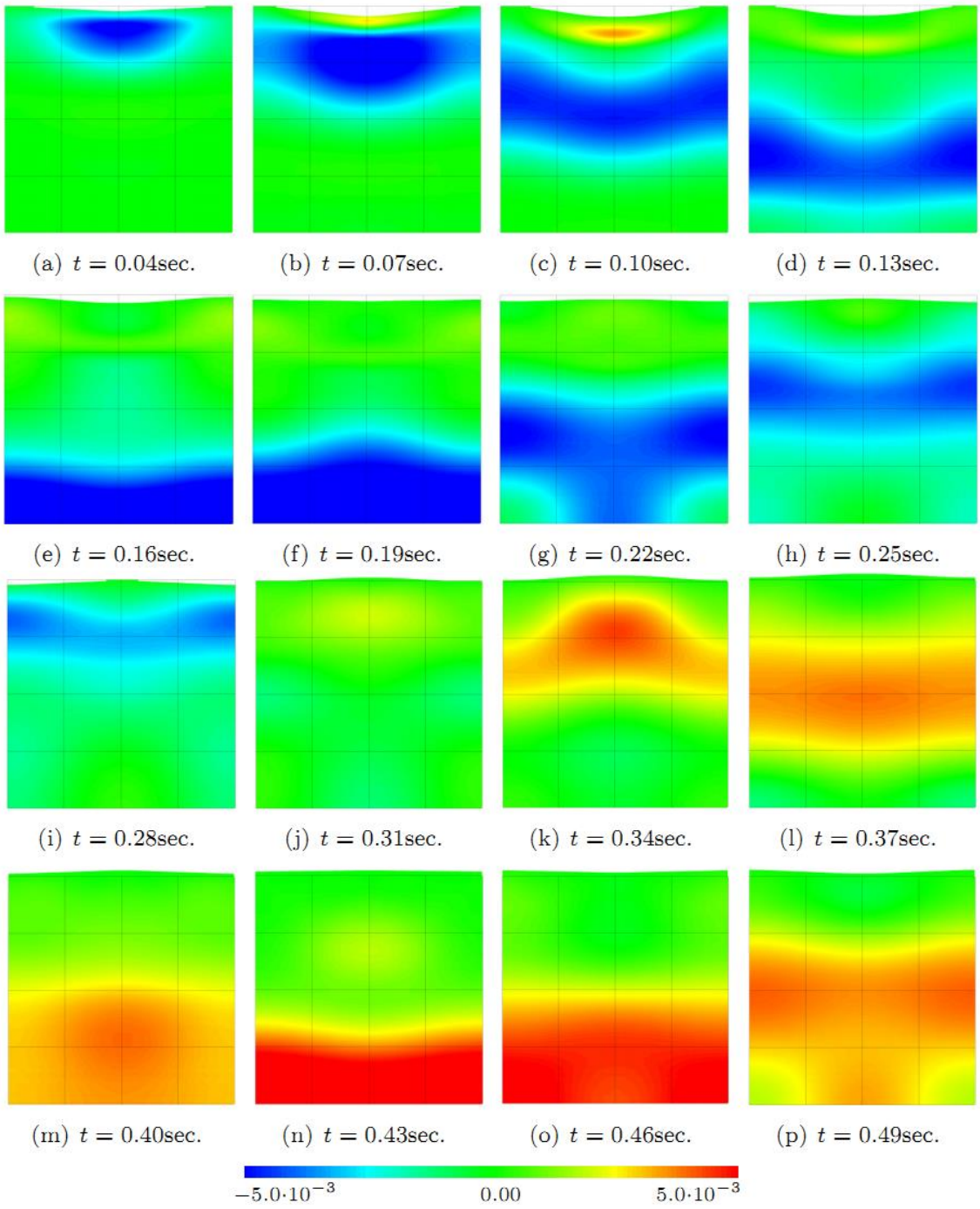

Figure 4.34: π^W (Pa) diagrams (HTS)

The three testing points shown in Figure 4.26, $A\ (0.0, 1.8L)$, $B\ (0.0, 0.0)$ and $A\ (0.0, -2L)$, are used to illustrate the variation in time of the vertical displacement in solid and fluid phases, u_y^S and u_y^W, and stress and pore pressure fields, σ_{yy} and π^W, throughout the duration of the analysis.

The displacement element solutions are presented in Figures 4.35 and 4.36. Similar solutions are obtained with stress model, as shown in Figures 4.37 and 4.38. To support this relative assessment, the results obtained with the hybrid-Trefftz displacement element are represented with circular markers in Figures 4.37 and 4.38. The correspondence is very good in all graphs.

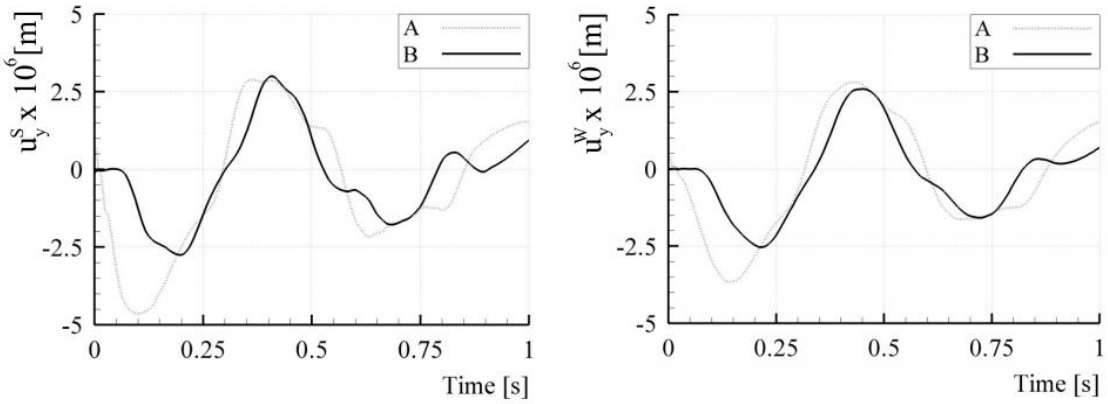

Figure 4.35: Vertical displacement time-histories (HTD)

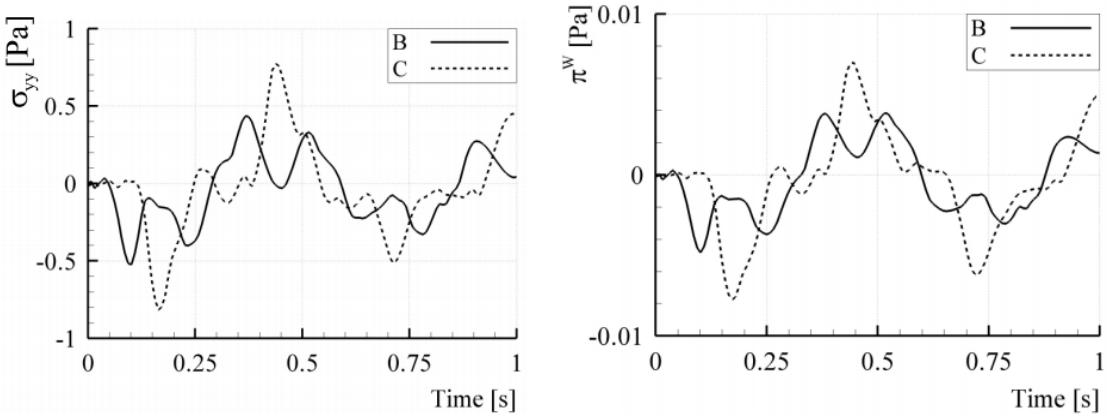

Figure 4.36: Normal stress and pore pressure time-histories (HTD)

The results presented in Figure 4.37 and 4.38 confirm that the initial conditions are correctly recovered, despite not being explicitly enforced in the time-integration procedure presented in Section 2.3.2, and preserved until the wavefront reaches the respective depth. At point C, the stress/pore pressure intensity is doubled, as expected, due to the reflection effect. The damping of the wave causes the reduction of the amplitudes of successive wave fronts passing through a given point. The propagation velocity of the wavefront is consistent with the P_1 wave. It is noted,

also, that the initial values of the stress fields are relatively well recovered, despite not being explicitly enforced by the time discretization procedure.

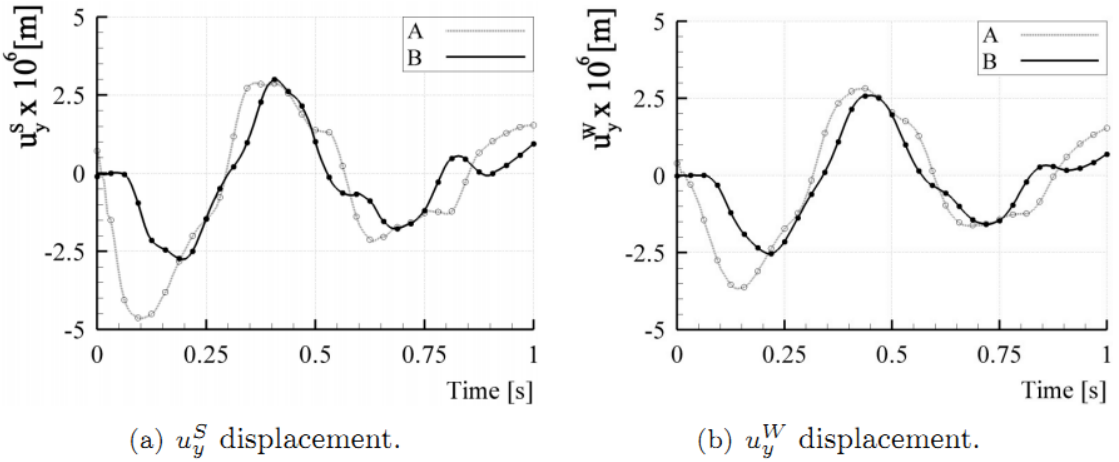

(a) u_y^S displacement. (b) u_y^W displacement.

Figure 4.37: Vertical displacement time-histories (HTS)

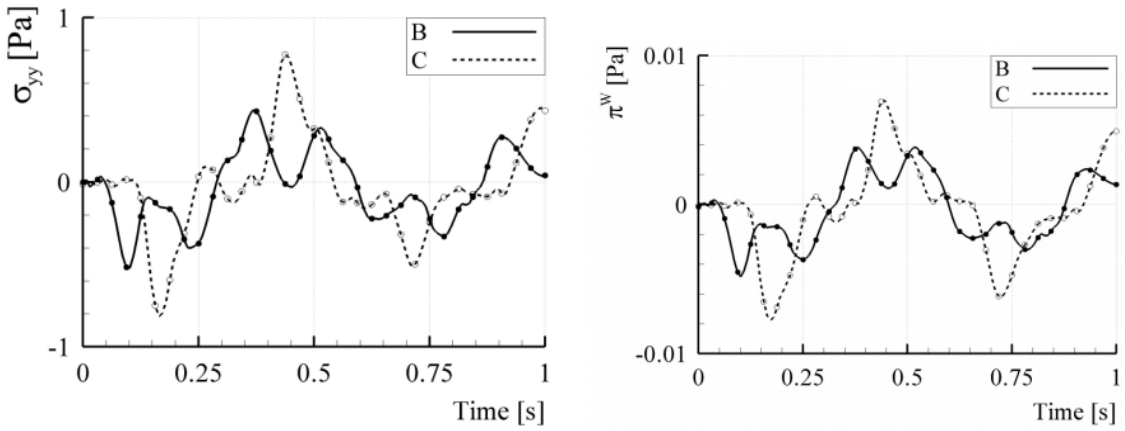

(a) σ_{yy} stress. (b) π^W pressure.

Figure 4.38: Normal stress and pore pressure time-histories (HTS)

It is seen, also, that the incoming wavefront causes a steep variation of the displacement fields at point A in the initial stage of the analysis, due to the larger intensity of the applied force at $x = 0.0$. After the initial stress concentration dissipates through the width of the tank, the displacement amplitudes near the surface remain only slightly larger than at mid-height.

Although the P_1 compressional wave propagates mainly through the direct contact of the solid particles which form the solid skeleton, it does trigger fluid motion through consolidation and swelling effects. However, the motion of the liquid is slightly delayed and less steep when compared to the solid phase, as these effects take time to develop.

4.8.2 Shock wave propagation in a two-layer medium

The propagation of a shock wave through a two-layer triphasic medium is modelled with the stress element. The problem setup is similar to that used in the single-layer test with two exceptions: the spatial distribution of the loading, see Figure 4.39, and the presence of two layers of different materials, each with $4L = 0.5m$ thickness. The upper layer consists of the unsaturated medium defined in Appendix C, while the lower layer is formed of the same material with a Young's modulus eight times larger.

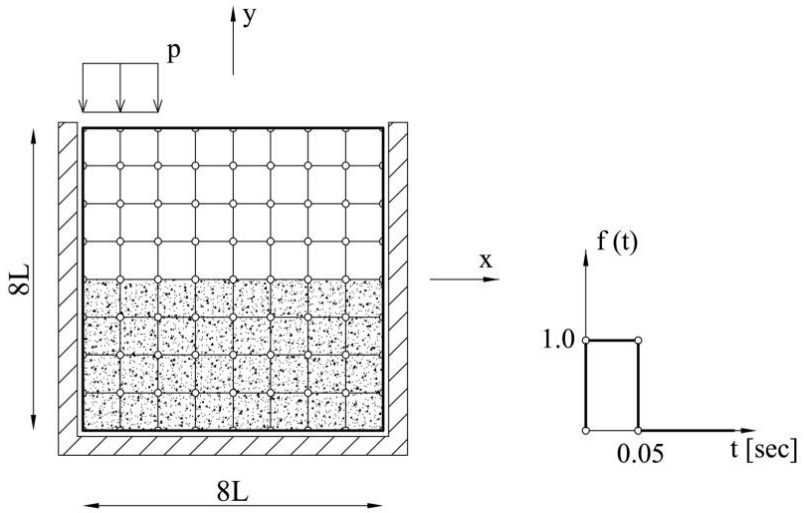

Figure 4.39: Description of the tests model for two-layer problem

The phase velocities and wavelengths in the upper layer procedure by the wavelet time basis are those defined in the previous section. In the lower layer, the phase velocities of the P_1 and S waves are $9.0m/s$ and $5.0m/s$, while the velocities range between $1.24m/s$ and $1.63m/s$ for the P_2 wave, and from $0.23m/s$ to $0.67m/s$ for the P_3 wave. The minimum wavelengths are $51.9cm$ for P_1 waves, $9.4cm$ for P_2 waves, $3.8cm$ for the P_3 waves and $29.2cm$ for the S waves.

The medium is meshed into 64 square elements with side length $L = 12.5cm$ and the stress approximation basis defined in the single-layer test is also used here, under the same implementation conditions. A total of 5,888 stress modes and 3,024 boundary displacement modes yield a solving system with 8,912 degrees of freedom.

The time histories of the stresses in the solid phase and of the liquid pore pressures during the first 0.5sec of the analysis are presented (on the deformed shape of the medium) in Figures 4.40 to 4.43.

The results shown that all fields are continuous between elements, except for the axial stress field, σ_{xx}, which is not subjected to a continuity condition on the interface between the two layers, $y = 0$. This behaviour and the associated shear stress concentration have been explained in detail in Section 3.2.4 for biphasic media. The justification given there for the stress singularity at the discontinuity of the applied load, point $(x, y) = (-2L, 4L)$ in Figure 4.39, still applies to triphasic media.

All fields recover well both static and kinematic boundary conditions, despite the latter not being explicitly enforced in the formulation (i.e. they are only continuous upon full convergence). It is noted, also, that the Rayleigh wave is clearly visible on the free surface of the domain.

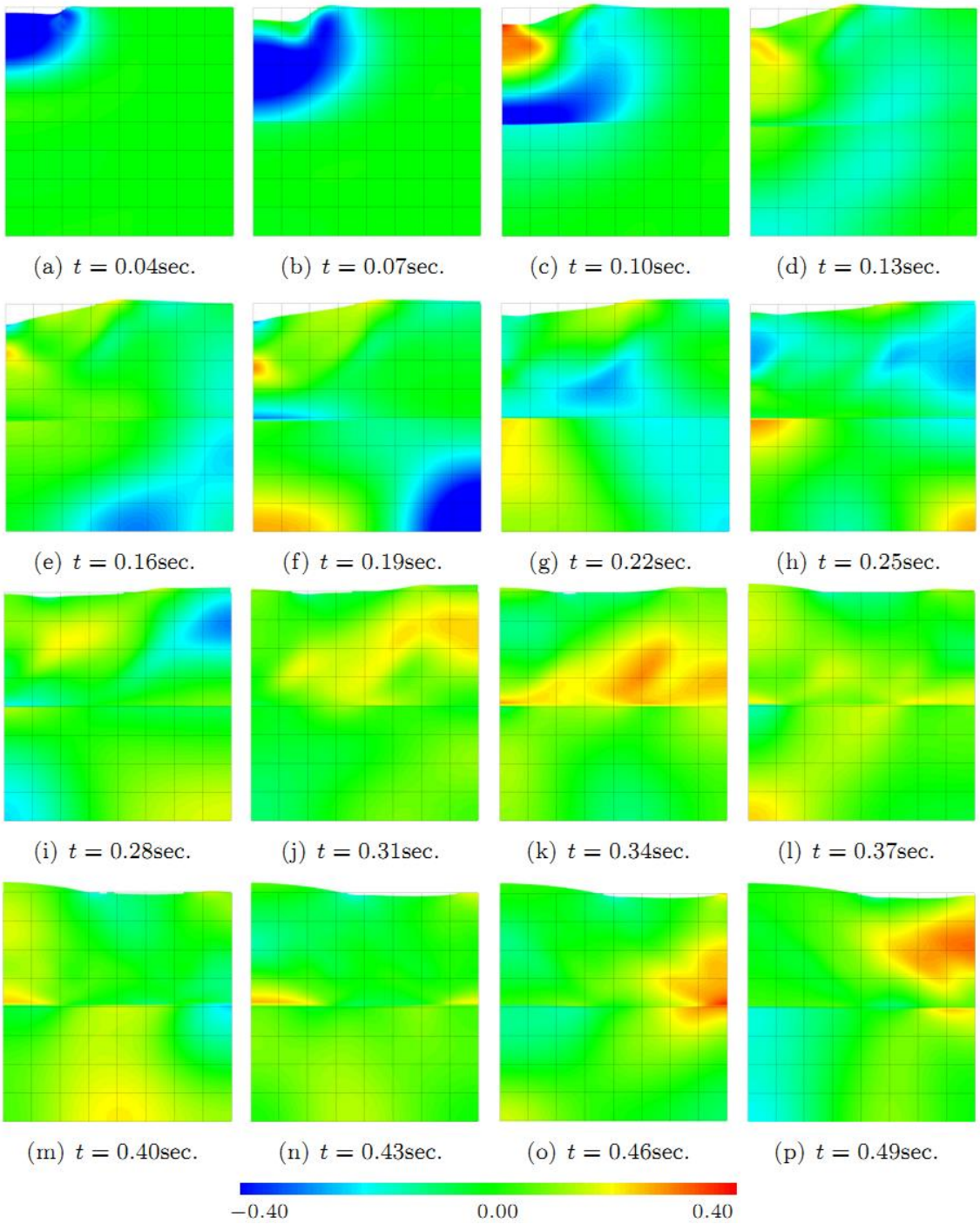

Figure 4.40: σ_{xx} (Pa) diagrams (HTS)

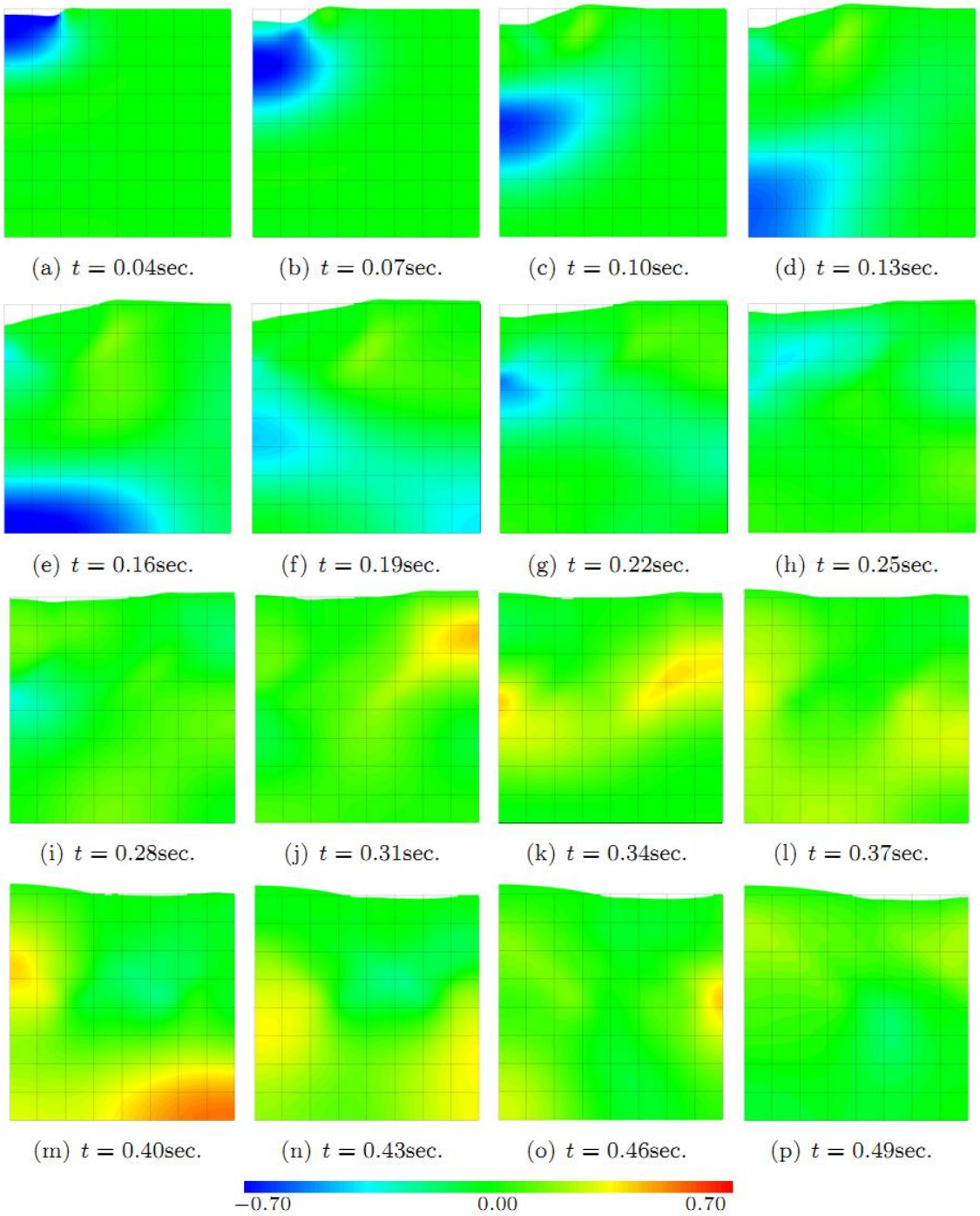

Figure 4.41: σ_{yy} (Pa) diagrams (HTS)

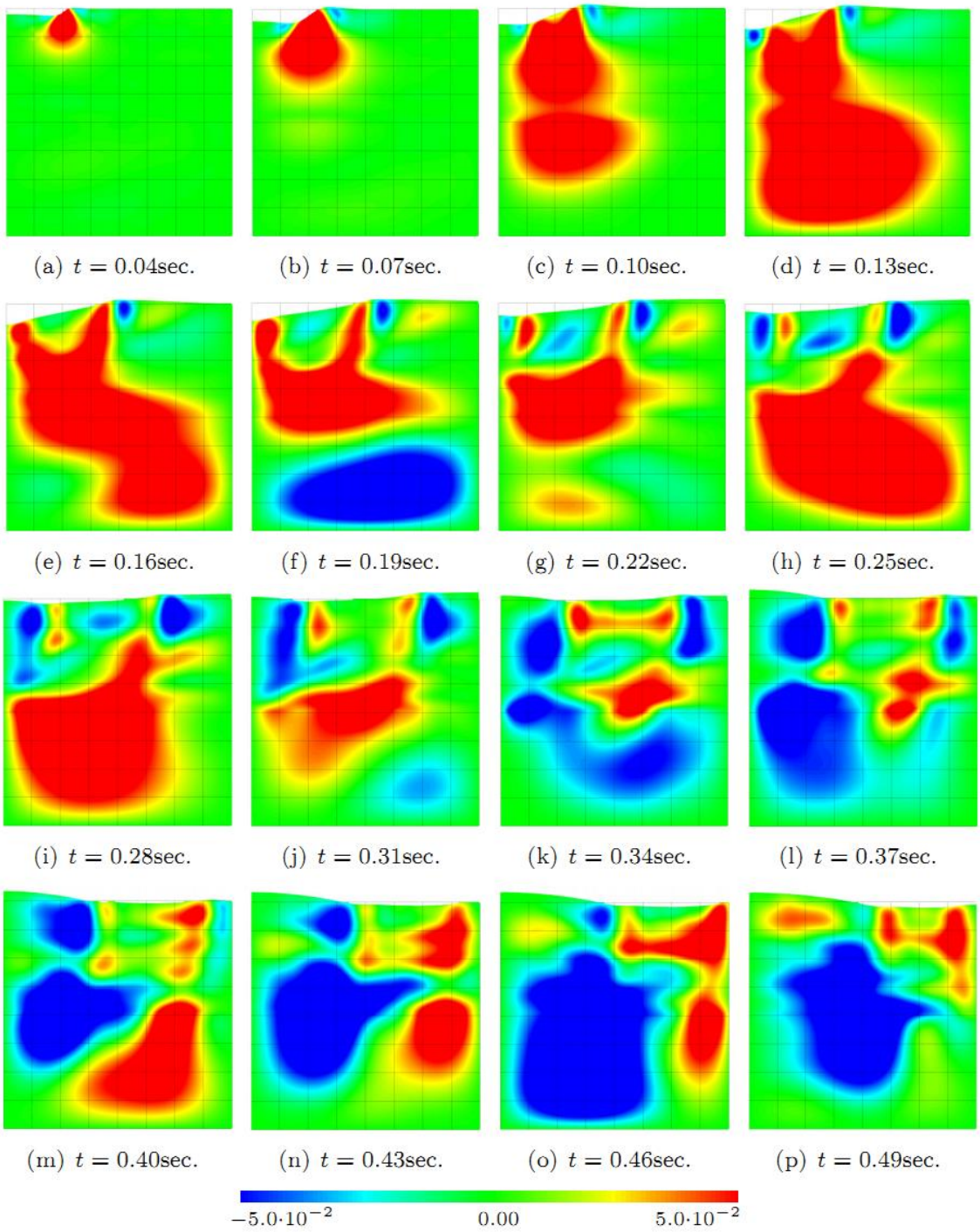

Figure 4.42: σ_{xy} (Pa) diagrams (HTS)

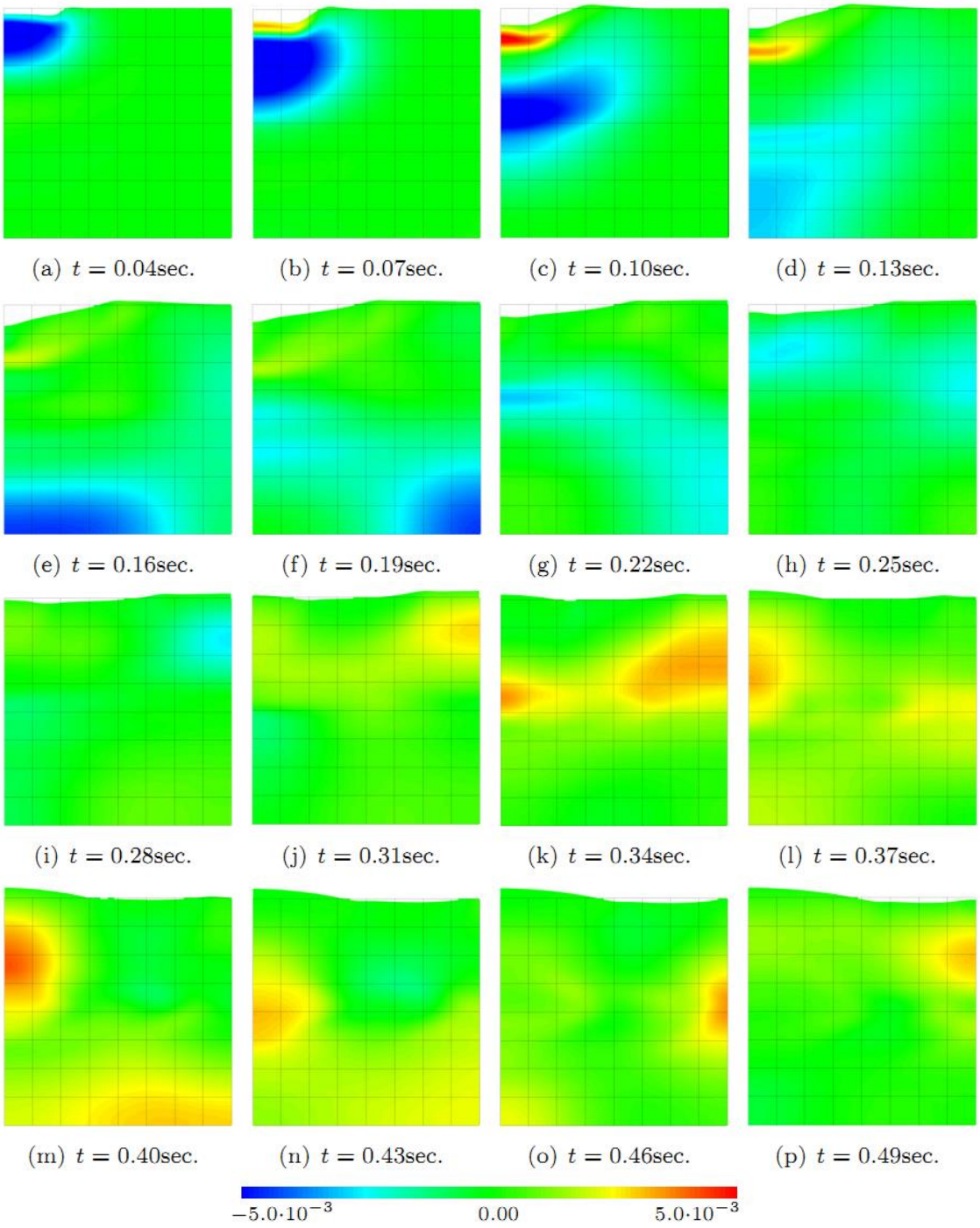

Figure 4.43: π^W (Pa) diagrams (HTS)

Chapter 5

Conclusions and future research

5.1 Conclusion

Single phase mathematical models are sufficient to describe accurately the dynamic response of multiphase media with frozen-medium behaviour (e.g. impervious soils). When significant relative motion occurs between the solid and fluid phases, however, more rigorous models, taking into account the interface interaction between the phases, are needed. These models predict the existence of as many compressional waves as the medium's constituents and a single shear wave. The propagation of one of the compressional waves and the shear wave is supported by direct interaction of the solid particles and is essentially insensitive to saturation and permeability variations of the medium. The opposite is true for the other compressional waves, which propagate through the fluid phases. Their highly oscillatory nature poses serious difficulties when conventional finite elements are used to model the response of the medium, mainly due to the well-known wavelength dependency of the leading dimension of the finite element. These difficulties are typically circumvented by adopting simplifying assumptions that are, in most cases, inadequate for semi-pervious and pervious media.

Mathematical models governing the behaviour of multiphase media have reached a high level of refinement in the recent years. For saturated porous media, most models are based on the Biot's Theory. Despite such models having been extended to unsaturated media, they fail to make physical sense when the medium is far from saturated. Alternative fully triphasic models have been developed for such situations, based either on the theory of mixtures or the averaging theory. Both theories rigorously take into account the microscopic interaction between phases.

Hybrid-Trefftz displacement and stress elements are formulated here for the elastostatic and elastodynamic analysis of biphasic and triphasic media. The elements are derived using the hybrid element framework, in the sense that dual fields are independently approximated in the domain of the element and on its essential boundary. However, unlike other hybrid elements, the domain approximation functions are constrained to satisfy locally the homogeneous form of the domain equations (the Trefftz condition). As typical of hybrid displacement (stress) elements, these functions are used to enforce weakly the domain equilibrium (compatibility) and elasticity

equations, while the domain compatibility (equilibrium) equation is enforced locally. The boundary traction (displacement) field is approximated on the Dirichlet (Neumann) and inter-element boundaries and the basis used to enforce weakly the boundary compatibility (equilibrium) equations. Boundary equilibrium (compatibility) is not enforced explicitly on the inter-element boundaries and is only observed upon full convergence. All bases are constructed hierarchically and their weights have no particular physical significance. This property enhances the suitability of the elements to adaptive refinement and parallel processing, especially when the solving system is not condensed on the boundary displacement variables. On the other hand, system condensation allows for hybrid-Trefftz stress elements to be coupled to conventional elements using the direct stiffness method, provided that the same boundary displacement approximation is used for the neighbouring elements.

A direct consequence of the use of Trefftz-compliant domain approximation functions is that all terms present in the finite element solving system are defined by boundary integral expressions if the problem is naturally homogeneous. If this is not the case, additional 'particular solution' functions must be added to the domain basis to recover the effect of the source terms. The issue of defining approximate particular solutions for problems where exact particular solutions cannot be derived (which is typically the case of dynamic problems with non-null initial conditions) is also addressed here. The particular solution basis is constructed using functions that satisfy the homogeneous form of the static problem obtained by setting to zero the time-derivative terms in the governing equation. The Trefftz-compliant and the particular solution functions are mixed in the same basis and used to enforce weakly the domain equations. The approximation functions are thus free to combine such as to recover the enforced equations in the best possible way. In particular, this approach allows the particular solution functions to contribute to the modelling of the general solution, should the Trefftz-compliant functions be insufficient for its correct recovery.

As the domain approximation functions embody physically relevant information on the modelled problem, hybrid-Trefftz elements present high levels of convergence under p-refinement, while the convergence under h-refinement is comparable to that of conventional finite elements. For the same reason, hybrid-Trefftz elements present high robustness to gross mesh distortions and near-incompressibility of the constituents. The wavelength dependency of the leading size of the element is reduced by a factor of 100 as compared to conventional finite

elements. These features distinguish the hybrid-Trefftz elements from other finite elements previously formulated for poroelastic problems, ultimately allowing for high quality results to be obtained on coarser meshes and with significantly less degrees of freedom. The price to be paid for securing these advantages is that the Trefftz-compliant functions may be numerically difficult to handle and may not support analytic integration.

5.2 Future research

The hybrid-Trefftz finite elements reported here prove to have the potential of avoiding critical limitations of the conventional finite elements, while offering, at the same time, superior convergence rates and considerable flexibility in choosing, for each element and essential boundary, the orders of approximation which best correspond to each specific problem. On the other hand, the present work is restricted to the development of the finite element formulations, as well as their implementation, performance assessment and validation against other finite element software. In order for these elements to be usable by analysts with no background in non-conventional formulations, considerable research effort must still be conducted in four complementary directions:

- the validation of the models through the laboratory testing of saturated and unsaturated media;
- the extension of the models to account for media with elastic non-linear and elastoplastic behaviour;
- the integration of hybrid-Trefftz elements into a widely used (preferably open-source) finite element platform;
- the inclusion of automatic *p*-adaptive refinement capabilities.

Due to the virtual lack of relevant and well documented laboratory experiments, the validation of the hybrid-Trefftz finite elements reported here was done using alternative finite element packages, rather than laboratory results. This is especially true for unsaturated media, where a considerable number of mechanical properties are specific to the adopted mathematical model and cannot be directly measured by experiments. It is clear, however, that for the models to be practically usable, they must be calibrated against experimentally acquired data, to highlight their limits and limitations. To that effect, a collaboration effort is currently being delineated with a Geotechnical research team at the University of Minho. It includes

experimental testing of the dynamic response of saturated and unsaturated sands using piezoelectric bender elements, under harmonic and transient (pulse) loading conditions.

Despite the recognized advantages of the hybrid-Trefftz elements, their direct application to non-linear problems is not feasible, as it would require the reconstruction of the domain basis at every iteration. The alternative strategy to be adopted involves the linearization of the governing equations, treating the non-linear residuum as a non-homogeneous term. The influence of this term can be efficiently modelled using the new particular solution strategy described in Section 2.5. This technique avoids most of the drawbacks of other methods for constructing approximate particular solutions, while preserving the symmetry and sparseness of the solving system. Two lines of research may be pursued, namely the modelling of porous media with elastic non-linear behaviour and with elastoplastic constitutive laws. Under the first line, the model should be able to account for changes in the fluid densities and volume fraction with variations of the pore pressure and volume of the solid skeleton, respectively. Various non-linear constitutive laws are available to characterize the postelastic behaviour of the solid skeleton (fluids are typically considered elastic). The Mohr-Coulomb model is probably the simplest and the most widely used. However, multi-surface plasticity models (e.g. Dafalias-Manzari), capable to account for such phenomena as dilatancy and liquefaction, have become increasingly popular and should be considered in future developments.

The implementation and testing of the hybrid-Trefftz elements has produced a significant amount of software. However, the computational implementation served mostly to assess the applicability of theoretical ideas, meaning that, in their current stage of development, the use of hybrid-Trefftz elements by an external analyst is hindered by the lack of a unified and fully automatic analysis tool. In fact, this is in general the case for hybrid elements, which are still a very rare presence in commercially available finite element software and almost non-existent in general purpose open-source platforms. In order to bring their capabilities to the fingertips of the international scientific community, the hybrid-Trefftz elements should be integrated into a mainstream open-source finite element platform. The OpenSees framework (http://opensees.berkeley.edu/) seems to be an adequate choice to this respect. OpenSees is an object-oriented platform for finite element analysis. It focuses on the dynamic analysis of structural and geotechnical models, therefore fitting well into the scope of this research. It offers an extensive database of conventional elements for single-phase and biphasic media, which

justifies its worldwide popularity, but currently no hybrid elements are included into its main distribution.

The success of this integration strongly depends on two factors. First, hybrid-Trefftz elements must be designed to work in a standalone manner, but also to connect with conventional elements present in the OpenSees main distribution. The standalone mode offers the analyst a larger breadth of elements and full flexibility in choosing the approximation bases. Conversely, the connectivity to conventional elements is endorsed by the fact that hybrid-Trefftz stress elements can be condensed on the boundary displacement variables and integrated into the standard Direct Stiffness Method framework that is currently used in most finite element software. It should be noted, however, that this approach excludes the displacement model and links the boundary approximation to the nodes of the element.

Second, the burden of optimizing the domain and boundary approximations of the hybrid-Trefftz elements must be lifted from the user. To achieve this, a deformation energy-based adaptive p-refinement procedure, previously developed for the analysis of single-phase media, is being extended to multi-phase materials. Also, an improved p-refinement strategy, using local, stress-based measures of error, is currently under development.

Besides the main directions of future research mentioned here, secondary lines of research may include, for instance, the extension of the formulations to tri-dimensional problems and the formulation and implementation of hybrid-Trefftz elements with absorbing boundaries to model semi-infinite domains.

Publications by the author contained in the thesis

1. Moldovan, I.D., **Cao, D.T.**, and Freitas, J.A.T., Elastic wave propagation in unsaturated porous media using hybrid-Trefftz stress element. International Journal for Numerical Methods in Engineering, 2013, (Accepted).
2. Moldovan, I.D., **Cao, D.T.**, and Freitas, J.A.T., Hybrid-Trefftz displacement finite elements for elastic unsaturated soils. Int. J. Comput. Methods, Special Issue on"Computational Geomechanics", 11(2)2013.
3. Moldovan, I. D., **Cao, D.T.**, Freitas, J. A. Hybrid-Trefftz finite elements for biphasic elastostatics. Finite Elements in Analysis and Design, 66: 68-82 (2012).
4. Moldovan, I. D., **Cao, D.T.**, and Freitas, J.A.T. Dynamic analysis of unsaturated porous media using hybrid-Trefftz finite elements. The 11^{th} International Conference on Vibration Problems (ICOVP-2013), September 9 - 12, (2013). Lisbon, Portugal.
5. Moldovan, I. D., **Cao, D.T.**, and Freitas, J.A.T. Hybrid-Trefftz Stress Elements for Biphasic Elastostatics. Congresso de Métodos Numéricos em Engenharia, June 14-17 (2011). Coimbra, Portugal.
6. Moldovan, I. D., **Cao, D.T.**, and Freitas, J.A.T. Hybrid-Trefftz Displacement and Stress Elements for Biphasis ElastoStatics. The 19th International Conference on Computer Methods in Mechanics, May 9-12 (2011). Warszawa, Poland.
7. Moldovan, I. D., Freitas, J.A.T, **Cao, D.T**. Sensitivity Assessment of Hybrid-Trefftz Stress and Displacement Elements for Poroelasticity. Proceedings of the IV European Conference on Computational Mechanics; May 16-21, 2010, Paris.
8. Moldovan, I. D., **Cao, D.T.**, and Freitas, J.A.T. Hybrid-Trefftz Elements for Elastic Unsaturated Porous Media, Internal Report, Catholic University of Portugal, Lisbon, 2012.
9. Freitas, J.A.T, Moldovan, I. D., **Cao, D.T.** Dependencies in the implementation of hybrid-Trefftz elements for poroelastostatics. Internal Report, ICIST, 2010.

Appendix A

Explicit expressions of matrices and coefficients for triphasic problems

The definitions of the matrices and coefficients given below were established in accordance with Wei and Muraleetharan [97]. The notations used in the original article were maintained, whenever possible.

The generalized divergence and gradient operators are defined in Cartesian and cylindrical coordinates by expressions (A.1), (A.2), and (A.3), respectively,

$$\boldsymbol{\mathcal{D}} = \begin{bmatrix} \frac{\partial}{\partial x} & 0 & \frac{\partial}{\partial y} & 0 & 0 \\ 0 & \frac{\partial}{\partial y} & \frac{\partial}{\partial x} & 0 & 0 \\ 0 & 0 & 0 & \frac{\partial}{\partial x} & 0 \\ 0 & 0 & 0 & \frac{\partial}{\partial y} & 0 \\ 0 & 0 & 0 & 0 & \frac{\partial}{\partial x} \\ 0 & 0 & 0 & 0 & \frac{\partial}{\partial y} \end{bmatrix} = \boldsymbol{\mathcal{D}}^T \tag{A.1}$$

$$\boldsymbol{\mathcal{D}}^T = \begin{bmatrix} \frac{\partial}{\partial r}+\frac{1}{r} & -\frac{1}{r} & \frac{1}{r}\frac{\partial}{\partial \theta} & 0 & 0 \\ 0 & \frac{1}{r}\frac{\partial}{\partial \theta} & \frac{\partial}{\partial r}+\frac{2}{r} & 0 & 0 \\ 0 & 0 & 0 & \frac{\partial}{\partial r} & 0 \\ 0 & 0 & 0 & \frac{1}{r}\frac{\partial}{\partial \theta} & 0 \\ 0 & 0 & 0 & 0 & \frac{\partial}{\partial r} \\ 0 & 0 & 0 & 0 & \frac{1}{r}\frac{\partial}{\partial \theta} \end{bmatrix} \tag{A.2}$$

$$\boldsymbol{\mathcal{D}} = \begin{bmatrix} \frac{\partial}{\partial r} & 0 & 0 & 0 & 0 & 0 \\ \frac{1}{r} & \frac{1}{r}\frac{\partial}{\partial \theta} & 0 & 0 & 0 & 0 \\ \frac{1}{r}\frac{\partial}{\partial \theta} & \frac{\partial}{\partial \theta} - \frac{1}{r} & 0 & 0 & 0 & 0 \\ 0 & 0 & \frac{\partial}{\partial r} + \frac{1}{r} & \frac{1}{r}\frac{\partial}{\partial \theta} & 0 & 0 \\ 0 & 0 & 0 & 0 & \frac{\partial}{\partial r} + \frac{1}{r} & \frac{1}{r}\frac{\partial}{\partial \theta} \end{bmatrix} \tag{A.3}$$

The expression of the damping $\boldsymbol{d}_0$ and mass $\boldsymbol{\rho}_0$ matrices present in equilibrium equation (2.53) are,

$$\boldsymbol{d}_0 = \begin{bmatrix} \mu^W + \mu^N & 0 & -\mu^W & 0 & -\mu^N & 0 \\ 0 & \mu^W + \mu^N & 0 & -\mu^W & 0 & -\mu^N \\ -\mu^W & 0 & \mu^W & 0 & 0 & 0 \\ 0 & -\mu^W & 0 & \mu^W & 0 & 0 \\ -\mu^N & 0 & 0 & 0 & \mu^N & 0 \\ 0 & -\mu^N & 0 & 0 & 0 & \mu^N \end{bmatrix} \tag{A.4}$$

$$\boldsymbol{\rho}_0 = \begin{bmatrix} n^S \rho^S & 0 & 0 & 0 & 0 & 0 \\ 0 & n^S \rho^S & 0 & 0 & 0 & 0 \\ 0 & 0 & n^W \rho^W & 0 & 0 & 0 \\ 0 & 0 & 0 & n^W \rho^W & 0 & 0 \\ 0 & 0 & 0 & 0 & n^N \rho^N & 0 \\ 0 & 0 & 0 & 0 & 0 & n^N \rho^N \end{bmatrix} \tag{A.5}$$

The expression of the damping $\boldsymbol{\rho}$ matrices is as,

$$\boldsymbol{\rho} = \begin{bmatrix} \rho_{SS} & 0 & \rho_{SW} & 0 & \rho_{SN} & 0 \\ 0 & \rho_{SS} & 0 & \rho_{SW} & 0 & \rho_{SN} \\ \rho_{SW} & 0 & \rho_{WW} & 0 & 0 & 0 \\ 0 & \rho_{SW} & 0 & \rho_{WW} & 0 & 0 \\ \rho_{SN} & 0 & 0 & 0 & \rho_{NN} & 0 \\ 0 & \rho_{SN} & 0 & 0 & 0 & \rho_{NN} \end{bmatrix} \tag{A.6}$$

The expressions of the material flexibility and stiffness matrices $\boldsymbol{f}$ and $\boldsymbol{k}$ present in elasticity equations are,

$$\boldsymbol{k} = \begin{bmatrix} M_{SS}+2n^S\mu^S & M_{SS} & 0 & M_{SW} & M_{SN} \\ M_{SS} & M_{SS}+2n^S\mu^S & 0 & M_{SW} & M_{SN} \\ 0 & 0 & n^S\mu^S & 0 & 0 \\ M_{SW} & M_{SW} & 0 & M_{WW} & M_{WN} \\ M_{SW} & M_{SN} & 0 & M_{WN} & M_{NN} \end{bmatrix} = \boldsymbol{f^{-1}} \tag{A.7}$$

$$\boldsymbol{Z} = \boldsymbol{I}_n \cos(m\cos^{-1}\eta_s) \quad \text{with } 0 \le m \le M \tag{A.8}$$

where $\boldsymbol{I}_n$ represents the identity matrix of rank n ($n = 3$ for biphasic medium and $n = 4$ for triphasic medium) and M is degree of p-refinement selected on the boundary.

In expressions (A.4) to (A.7), $n^\alpha, \alpha = \{S,\ W,\ N\}$, represent the volume fractions of each phase and,

$$\mu^f = \frac{\left(n^f\right)^2 \upsilon^f}{k k_r^f} \qquad \text{where } f = W, N \tag{A.9}$$

In expression(A.9), υ^f is the dynamic viscosity of the fluid, k is the intrinsic permeability and k_r^f is the relative permeability of the $f-$fluid.

The stiffness moduli present in definition (A.7) are given by the following expressions:

$$M_{SS} = n^S\left(K_S + \lambda^S - 2\lambda_{\rho e}^S\right) - \frac{n^S\left(-2D_N D_W + D_N + D_W\right)\left(K_S - 2\lambda_{\rho e}^S\right)^2}{K_S\left(1 - D_N D_W\right)} \tag{A.10}$$

$$M_{SW} = -\frac{\left(1 - D_N\right) D_W K_W n^S\left(\lambda_{\rho e}^S - K_S\right)}{K_S\left(1 - D_N D_W\right)} \tag{A.11}$$

$$M_{SN} = -\frac{D_N\left(1 - D_W\right) K_N n^S\left(\lambda_{\rho e}^S - K_S\right)}{K_S\left(1 - D_N D_W\right)} \tag{A.12}$$

$$M_{WW} = K_W n^W - \frac{D_W K_W^2 n^S}{K_S\left(1 - D_N D_W\right)} \tag{A.13}$$

$$M_{WN} = \frac{D_N D_W K_N K_W n^S}{K_S\left(1 - D_N D_W\right)} \tag{A.14}$$

$$M_{NN} = K_N n^N - \frac{D_N K_N^2 n^S}{K_S\left(1 - D_N D_W\right)} \tag{A.15}$$

$$D_W = \frac{K_S n^W}{K_S n^W + K_W n^S + n^S\left(n^W\right)^2 \Theta^W} \tag{A.16}$$

$$D_N = \frac{K_S n^N}{K_S n^N + K_N n^S + n^S\left(n^N\right)^2 \Theta^N} \tag{A.17}$$

In the above expressions, μ^S and λ^S are the Lamé's coefficients. Elastic constants λ_{pe}^S, Θ^W and Θ^N can be determined experimentally, following the procedures described in [97]. The bulk moduli of the phases are denoted by $K^\alpha,\ \alpha = \{S,\ W,\ N\}$.

The matrix $\boldsymbol{N}$ (2.5) is expression as (A.18):

$$\boldsymbol{N} = \begin{bmatrix} n_x & 0 & n_y & 0 & 0 \\ 0 & n_y & n_x & 0 & 0 \\ 0 & 0 & 0 & 1 & 0 \\ 0 & 0 & 0 & 0 & 1 \end{bmatrix} \tag{A.18}$$

Appendix B

Geomechanical characteristics of the Massilon sandstone for triphasic problem

- Bulk modulus of the solid particle: $K_S = 3.5 \cdot 10^{10}\ Pa$;
- Bulk modulus of the water: $K_W = 2.25 \cdot 10^{9}\ Pa$;
- Bulk modulus of the air $K_N = 1.1 \cdot 10^{5}\ Pa$: ;
- Lamé's coefficients: $\mu^S = 1.87 \cdot 10^{9}\ Pa$ and $\lambda^S = 2.94 \cdot 10^{9}\ Pa$;
- Elastic constants: $\lambda_{\rho e}^S = 1.0 \cdot 10^{10}\ Pa$, $\Theta^W = 6.85 \cdot 10^{4}\ Pa$, $\Theta^N = 1.67 \cdot 10^{5}\ Pa$;
- Saturation (reference value): 0.8;
- Intrinsic permeability: varies between $10^{-8}\ m^2$ and $10^{-12}\ m^2$;
- Density of the solid particle: $\rho_S = 2650\ kg/m^3$;
- Density of the water: $\rho_W = 1000\ kg/m^3$;
- Density of the air: $\rho_N = 1.1\, kg/m^3$;
- Dynamic viscosity of the water: $v^W = 1.0 \cdot 10^{-3}\ Pa \cdot s$;
- Dynamic viscosity of the air: $v^N = 1.8 \cdot 10^{-5}\ Pa \cdot s$;
- Relative permeability of the water: $k_r^W = 0.431$;
- Relative permeability of the air: $k_r^N = 0.011$;
- Porosity: $n_0 = 0.23$.

Appendix C

Geomechanical characteristics of the pulse load test material for triphasic problem

- Bulk modulus of the solid particle: $K_S = 1.0 \cdot 10^5\ Pa$;
- Bulk modulus of the water: $K_W = 1.0 \cdot 10^4\ Pa$;
- Bulk modulus of the air: $K_N = 10.0\ Pa$;
- Lamé's coefficients: $\mu^S = 1.3 \cdot 10^4\ Pa$ and $\lambda^S = 9.13 \cdot 10^4\ Pa$;
- Elastic constants: $\lambda_{\rho e}^S = 2.86 \cdot 10^4\ Pa$, $\Theta^W = 6.85 \cdot 10^4\ Pa$, $\Theta^N = 1.67 \cdot 10^5\ Pa$;
- Saturation (reference value): 0.8;
- Intrinsic permeability: $1.55 \cdot 10^{-8}\ m^2$;
- Density of the solid particle: $\rho_S = 2000\ kg/m^3$;
- Density of the water: $\rho_W = 1000\ kg/m^3$;
- Density of the air: $\rho_N = 1.1\ kg/m^3$;
- Dynamic viscosity of the water: $v^W = 1.0 \cdot 10^{-3}\ Pa \cdot s$;
- Dynamic viscosity of the air: $v^N = 1.8 \cdot 10^{-5}\ Pa \cdot s$;
- Relative permeability of the water: $k_r^W = 0.431$;
- Relative permeability of the air: $k_r^N = 0.011$;
- Porosity: $n_0 = 0.23$.

Appendix D

Elasticity relations and Poroelasticity for Biphasic problems

$$K_d = \frac{3\lambda + 2\mu}{3} = \frac{E}{3(1-2\nu)} = \mu\frac{2(1+\nu)}{(1-2\nu)} = \lambda\frac{1+\nu}{3\nu} \tag{D.1}$$

$$E = 2\mu(1+\nu) = \frac{\mu(3\lambda+2\mu)}{\lambda+\mu} \tag{D.2}$$

$$\mu = \frac{E}{2(1+\mu)} = \frac{3}{2}(K_d - \lambda) = \lambda\frac{1-2\nu}{2\nu} = 3K_d\frac{1-2\nu}{2(1+\nu)} \tag{D.3}$$

$$\nu = \frac{E}{2\mu} - 1 = \frac{\lambda}{2(\lambda+\mu)} = \frac{\lambda}{2K_d - \lambda} = \frac{3K_d - 2\mu}{2(3K_d+\mu)} \tag{D.4}$$

$$\lambda = \frac{\nu E}{(1+\nu)(1-2\nu)} = K_d - \frac{2}{3}\mu = \frac{2\nu\mu}{1-2\nu} = 3K_d\frac{\nu}{1+\nu} \tag{D.5}$$

$$\rho = \rho_S(1-n^W) + \rho_W n^W \tag{D.6}$$

$$\rho_d = \rho_S(1-n^W) \tag{D.7}$$

$$\alpha = 1 - \frac{K_d}{K_s} \tag{D.8}$$

$$K = K_d + \alpha^2 Q \tag{D.9}$$

$$\frac{1}{M} = \frac{\alpha - n^W}{K_S} + \frac{n^W}{K_W} \tag{D.10}$$

$$k = \hbar_I\frac{\rho_W g}{\eta} = \hbar_I\frac{g}{\nu_k} = \hbar\rho_W g \tag{D.11}$$

$$\hbar = \frac{\hbar_I}{\eta} \tag{D.12}$$

$$\eta = \rho_W \nu_k \tag{D.13}$$

$$e = \frac{n^W}{1-n^W} \tag{D.14}$$

$$\xi = \frac{\rho_W g}{k}(n^W)^2 \tag{D.15}$$

$$\omega_0 = g\frac{\rho n^W}{k(\rho a - \rho_W n^W)} \tag{D.16}$$

The generalized divergence and gradient operators are defined in Cartesian and cylindrical coordinates by expressions (D.17), (D.18), and (D.19), respectively,

$$\boldsymbol{\mathcal{D}} = \begin{bmatrix} \frac{\partial}{\partial x} & 0 & \frac{\partial}{\partial y} & 0 \\ 0 & \frac{\partial}{\partial y} & \frac{\partial}{\partial x} & 0 \\ 0 & 0 & 0 & \frac{\partial}{\partial x} \\ 0 & 0 & 0 & \frac{\partial}{\partial y} \end{bmatrix} = \boldsymbol{\mathcal{D}}^T \tag{D.17}$$

$$\boldsymbol{\mathcal{D}}^T = \begin{bmatrix} \frac{\partial}{\partial r}+\frac{1}{r} & -\frac{1}{r} & \frac{1}{r}\frac{\partial}{\partial \theta} & 0 \\ 0 & \frac{1}{r}\frac{\partial}{\partial \theta} & \frac{\partial}{\partial r}+\frac{2}{r} & 0 \\ 0 & 0 & 0 & \frac{\partial}{\partial r} \\ 0 & 0 & 0 & \frac{1}{r}\frac{\partial}{\partial \theta} \end{bmatrix} \tag{D.18}$$

$$\boldsymbol{\mathcal{D}} = \begin{bmatrix} \frac{\partial}{\partial \theta} & 0 & 0 & 0 \\ \frac{1}{r} & \frac{1}{r}\frac{\partial}{\partial \theta} & 0 & 0 \\ \frac{1}{r}\frac{\partial}{\partial \theta} & \frac{\partial}{\partial r}-\frac{1}{r} & 0 & 0 \\ 0 & 0 & \frac{\partial}{\partial r}+\frac{1}{r} & \frac{1}{r}\frac{\partial}{\partial \theta} \end{bmatrix} \tag{D.19}$$

The expression of the mass $\boldsymbol{\rho}$ matrices is as,

$$\boldsymbol{\rho} = \begin{bmatrix} \rho & 0 & \rho_W & 0 \\ 0 & \rho & 0 & \rho_W \\ \rho_W & 0 & \rho_{W2} & 0 \\ 0 & \rho_W & 0 & \rho_{W2} \end{bmatrix} \tag{D.20}$$

$$\rho_{W2} = \frac{\rho_W a}{n^W} - \frac{\hat{i}\zeta}{\omega\left(n^W\right)^2} \tag{D.21}$$

The matrix $\boldsymbol{N}$ (2.5) is expression as (D.22):

$$\boldsymbol{N} = \begin{bmatrix} n_x & 0 & n_y & 0 \\ 0 & n_y & n_x & 0 \\ 0 & 0 & 0 & 1 \end{bmatrix} \tag{D.22}$$

The expressions of the elasticity matrices present in elasticity equations (2.3) are as,

$$\boldsymbol{k} = \begin{bmatrix} k_{11} & k_{12} & 0 & k_{14} \\ k_{12} & k_{22} & 0 & k_{14} \\ 0 & 0 & k_{33} & 0 \\ k_{14} & k_{14} & 0 & k_{44} \end{bmatrix} = \boldsymbol{f}^{-1} \tag{D.23}$$

$$k_{11} = k_{22} = k_{12} + 2k_{33} \tag{D.24}$$

$$k_{12} = \lambda + \alpha^2 Q \tag{D.25}$$

$$k_{33} = \mu \tag{D.26}$$

$$k_{14} = \alpha Q \tag{D.27}$$

$$k_{44} = Q \tag{D.28}$$

Appendix E

Geomechanical characteristics of water-saturated Molsand soil for biphasic problem

- Fluid Density: $\rho_W = 1000\ kg/m^3$;
- Mixture density: $\rho = 2650\, kg/m^3$;
- The Biot's first coefficient: $\alpha = 1$;
- The Biot's second coefficient: $Q = 5.67 \cdot 10^9\ N/m^2$;
- Young's modulus of the drained rock: $E = 2.98 \cdot 10^8\ N/m^2$;
- Lamé's first coefficient of drained rock : $\lambda = 2.229 \cdot 10^8\ N/m^2$;
- Lamé's second coefficient: $\mu = 1.118 \cdot 10^8\ N/m^2$;
- Bulk modulus of the mixture: $K = 5.97 \cdot 10^9\ N/m^2$;
- Liquid volume fraction: $n^W = 0.388$;
- Poission's coefficient of the drained rock: $\upsilon = 0.333$.
- Tortuosity factor : $a = 1.0$;
- Hydraulic conductivity: $k = 0.01\, m/s$

Bibliography

1. Zienkiewicz, O.C., Taylor, R.L., and Zhu, J.Z., *The Finite Element Method: Its Basis and Fundamentals* 2006: Elsevier.

2. Freitas, J.A.T., *Hybrid finite element formulations for elastodynamic analysis in the frequency domain.* International Journal of Solids and Structures, 1999. **36**(13): p. 1883-1923.

3. Castro, L.M.S., and Freitas, J.A.T., *Wavelets in hybrid-mixed stress elements.* Computer Methods in Applied Mechanics and Engineering, 2001. **190**(31): p. 3977-3998.

4. Hibbit., K., and Sorensen. , *ABAQUS/Standard, in: User Manual. Version 6.12-1*. 2012.

5. Trefftz, E., and Ein Gegenstuck zum Ritzschen Verfahren., in *Second International Congress of Applied Mechanics*1926: Zurich.

6. Jirousek, J., *Basis for development of large finite elements locally satisfying all field equations.* Computer Methods in Applied Mechanics and Engineering, 1978. **14**: p. 65-92.

7. Herrera, I., *Boundary methods; a criterion for completness.* Proceedings of the National Academy of Sciences, 1980. **77**: p. 4395– 4398.

8. Jirousek, J., and Venkatesh, A., *A simple stress error estimator for hybrid-Trefftz p-version elements.* International Journal for Numerical Methods in Engineering, 1989. **28**(1): p. 211-236.

9. Jirousek, J., and Teodorescu, P., *Large finite elements method for the solution of problems in the theory of elasticity.* Computers & Structures, 1982. **15**: p. 575-587.

10. Jirousek, J., and Guex, L., *The hybrid-Trefftz finite element model and its application to plate bending.* International Journal for Numerical Methods in Engineering, 1986. **23**(4): p. 651-693.

11. Zielinski, A.P., and Zienkiewicz, O.C., *Generalized finite element analysis with T-complete boundary solution functions.* International Journal for Numerical Methods in Engineering, 1985. **21**: p. 509-528.

12. Piltner, R., *Special finite elements with holes and internal cracks.* International Journal for Numerical Methods in Engineering, 1985. **21**: p. 1471-1485.

13. Herrera, I., and Gourgeon, H., *Boundary methods C-complete systems for Stokes problems.* Computer Methods in Applied Mechanics and Engineering, 1982. **30**: p. 225-241.

14. Herrera, I., *Boundary Methods - an Algebraic Theory.* Pitman Advanced Publishing Program, Boston, London, Melbourne, 1984.

15. Herrera, I., Ewing, R.E., Celia, M.E., and Russel , T.F., *Eulerian-Lagrangian localized adjoint method: the theoretical framework.* Numerical Methods for Partial Differential Equations, 1993. **9**: p. 431-457.

16. Cheung, Y.K., Jin, W.G., and Zienkiewicz, O.C., *Solution of Helmholtz equation by Trefftz method.* International Journal for Numerical Methods in Engineering, 1991. **32(1)**: p. 63-78.

17. Cheung, Y.K., Jin, W.G., and Zienkiewicz, O.C., *Direct solution procedure for solution of harmonic problems using complete, non-singular, Trefftz functions.* Communications in Numerical Methods in Engineering, 1989. **5**(3): p. 159-169.

18. Mikhlin, S.G., *Variational Methods in Mathematical Physics*. Pergamon Press, Oxford. 1964.

19. Shaw, R., Huang, S.-C., and Zhao, C.-X., *The embedding integral and the Trefftz method for potential problems with partitioning.* Engineering Analysis with Boundary Elements, 1992. **9**(1): p. 83-90.

20. Leitão, V.M.A., *On the implementation of a multi-region Trefftz-collocation formulation for 2-D potential problems.* Engineering Analysis with Boundary Elements, 1997. **20**(1): p. 51-61.

21. Balakrishnan, K., and Ramachandran, P.A., *A particular solution Trefftz method for non-linear Poisson problems in heat and mass transfer.* Journal of Computational Physics, 1999. **150**(1): p. 239-267.

22. Jirousek, J., and Qin, Q.H., *Application of hybrid-Trefftz element approach to transient heat conduction anallysis.* Computers & Structures, 1996. **58**(1): p. 195-201.

23. Qin, Q.H., and Wang, H., *MATLAB and C Programming for Trefftz Finite Element Methods*. 2009, Boca Raton, London, New York: CRC Press.

24. Freitas, J.A.T., and Cismasiu, C., *Formulation of hybrid-Trefftz displacement elements*, in *In Proceedings of The Third International Conference in Computational Structures Technology*1996, B. Topping, Ed., vol. Advances in Finite Element Technology, Civil-Comp Press, Edinburgh, Scotland: Budapest, 21-23 August (1996). p. 195-202.

25. Freitas, J.A., *Formulation of elastostatic hybrid-Trefftz stress elements.* Comp. Meth. Appl. Mech. Engng., 1998. **153**: p. 127-151.

26. Freitas, J.A.T., Cismasiu, C., and Wang, Z.M., *Comparative analysis of hybrid-Trefftz stress and displacement elements.* Archives of Computational Methods in Engineering, 1999. **6**(1): p. 35-59.

27. Freitas, J.A.T., Cismasiu, C., and Wang, Z.M., *Numerical applications with hybrid-Trefftz stress and displacement elements.* STROJNÍCKY CASOPIS 50, c., 1999. **2**: p. 73-95.

28. Jin, F., Cheung, Y.K., and Zienkiewicz, O.C., *Application of the Trefftz method in plane elasticity problems.* International Journal for Numerical Methods in Engineering, 1990. **30**(6): p. 1147-1161.

29. Freitas, J.A.T., and Bussamra, F.L.S., *Three-dimensional hybrid-Trefftz stress elements.* International Journal for Numerical Methods in Engineering, 2000. **47**: p. 927-950.

30. Piltner, R., *The use of complex valued functions for the solution of three-dimensional elasticity problems.* Journal of Elasticity, 1987. **18**: p. 191-225.

31. Piltner, R., *The representation of three-dimensional elastic displacement fields with the aid of complex valued functions for several curvilinear coordinates.* Mechanics Research Communications, 1988. **15**(2): p. 79-85.

32. Piltner, R., *On the representation of three-dimensional elasticity solutions with the aid of complex valued functions.* Journal of Elasticity, 1989. **22**: p. 45-55.

33. Cismasiu, C., and Freitas, J.A.T., *Hybrid-Trefftz finite element formulation for spectral elastodynamic analysis.* In 2nd Int. PhD Symposium in Civil Engineering (Budapest), 1998.

34. Freitas, J.A.T., *Hybrid-Trefftz displacement and stress elements for elastodynamic analysis in the frequency domain.* Computer Assisted Mechanics and Engineering Sciences, 1997. **4**: p. 345-368.

35. Cismasiu, C., *The hybrid-Trefftz displacement element for static and dynamic structural analysis problems*, 2000, Universidade Técnica de Lisboa.

36. Stojek, M., and Mahrenholtz, O., *Diffraction loads on multiple vertical cylinders with rectangular cross section by Trefftz-type finnite elements.* Computers & Structures, 2000. **75**: p. 335-345.

37. Wu, Y.-C., and Yu, D.-J., *Trefftz method for hydrodynamic pressure on rigid dams with non-vertical upstream face.* International Journal for Numerical Methods in Fluids, 1989. **9**(1): p. 1-7.

38. Sze, K.Y., Wang, H.T., and Fan, H., *A finite element approach for computing edge singularities in piezoelectric materials.* International Journal of Solids and Structures, 2001. **38**: p. 9233-9252.

39. Qin, Q.H., *Variational formulations for TFEM of piezoelectricity.* International Journal of Solids and Structures, 2003. **40**: p. 6335-6346.

40. Jirousek, J., *Hybrid-Trefftz plate bending elements with p-method capabilities.* International Journal for Numerical Methods in Engineering, 1987. **24**: p. 1367-1393.

41. Jirousek, J., and Leon, N., *A powerful finite element for plate bending.* Computer Methods in Applied Mechanics and Engineering, 1977. **12**: p. 77-96.

42. Jirousek, J., Wróblewski, A., and He, X.-Q., *A family of quadrilateral hybrid-Trefftz p-elements for thick plate analysis.* Computer Methods in Applied Mechanics and Engineering, 1995. **127**(1/4): p. 315-344.

43. Jirousek, J., Wróblewski, A., and Szybinski, B., *A new 12 DOF quadrilateral element for analysis of thick and thin plates.* International Journal for Numerical Methods in Engineering, 1995. **38**(15): p. 2619-2638.

44. Piltner, R., *The application of a complex 3-dimensional elasticity solution representation for the analysis of a thick rectangular plate.* Acta Mechanica, 1988. **75**: p. 77-91.

45. Piltner, R., *Three-dimensional stress and displacement representations for plate problems.* Mechanics Research Communications, 1991. **18**(1): p. 41-49.

46. Qin, Q.H., *Postbuckling analysis of thin plates by a hybrid Trefftz finite element method.* Computer Methods in Applied Mechanics and Engineering, 1995. **128**(1/2): p. 123-136.

47. Qin, Q.H., *Hybrid Trefftz finite-element approach for plate bending on an elastic foundation.* Applied Mathematical Modelling, 1994. **18**(6): p. 334-339.

48. Qin, Q.H., *Hybrid-Trefftz finite element method for Reissner plates on an elastic foundation.* Computer Methods in Applied Mechanics and Engineering, 1995. **122**(3/4): p. 379-392.

49. Moldovan, I.D., Cao, D.T, and Freitas, J.A.T., *Hybrid-Treffiz finite elements for biphasic elastostatics.* Finite Elements in Analysis and Design, 2012. **66**: p. 68-82.

50. Moldovan, I.D., and Freitas, J.A.T., *Hybrid-Treffiz displacement and stress elements for bounded poroelasticity problems.* Computers and Geotechnics, 2012. **42**: p. 129–144.

51. Moldovan, I.D., and Freitas, J.A.T. , *Hybrid-Treffiz stress and displacement elements for dynamic analysis of bounded and unbounded saturated porous media.* Computer Assisted Methods in Engineering and Science, 2008. **15**: p. 289–303.

52. Freitas, J.A.T., Moldovan, I.D., and Cismasiu, C., *Hybrid-Trefftz displacement element for bounded and unbounded poroelastic media.* Computational Mechanics, 2011. **48**: p. 659-673.

53. Freitas, J.A.T., and Moldovan, I.D., *Hybrid-Trefftz stress element for bounded and unbounded poroelastic media.* International Journal of Numerical Methods in Engineering, 2011. **85(10)**: p. 1280-1305.

54. Freitas, J.A.T., *Mixed finite element solutions of time-dependent problems.* Computer Methods in Applied Mechanics and Engineering, 2008. **197**: p. 3657-3678.

55. Moldovan, I.D., Cao, D.T., and Freitas, J.A.T. , *Hybrid-Treffiz displacement finite elements for elastic unsaturated soils.* International Journal of Computational Methods, Special Issue on "Computational Geomechanics", 2013. **11**(2).

56. Moldovan, I.D., Cao, D.T., and Freitas, J.A.T., , *Elastic wave propagation in unsaturated porous media using hybrid-Trefftz stress element.* International Journal for Numerical Methods in Engineering, 2013. **(Accepted)**.

57. Yan, F., Feng, X. T., and Zhou, H., *Dual reciprocity hybrid radial boundary node method for the analysis of Kirchhoff plates.* Applied Mathematical Modelling, 2011. **35**: p. 5691–5706.

58. Freitas, J.A.T., and Wang, Z.M., *Hybrid-Trefftz stress elements for elastoplasticity.* International Journal for Numerical Methods in Engineering, 1998. **43**(4): p. 655-683.

59. Tong, P., Pian, P.H., and Lasry, S.L., *A hybrid-element approach to crack problems in plane elasticity.* International Journal for Numerical Methods in Engineering, 1973. **7**: p. 297-308.

60. Lin, K., and Tong, P., *Singular finite elements for the fracture analysis of V-notched plates.* International Journal for Numerical Methods in Engineering, 1980. **15**: p. 1343-1354.

61. Degrande, G., *A spectral and finite element method for wave propagation in dry and saturated poroelastic media*, 1992, Katholieke Universiteit te Leuven.

62. Venkatesh, A., and Jirousek, J., *Contact Loading and Local Effects in Thin Walled Plated and Shell Structures*, in *Springer-Verlag, Berlin, ch. Finite Element Formulation for the Analysis of Local Effects.*1991.

63. Venkatesh, A., and Jirousek, J., *Accurate representation of local effects due to concentrated and discontinuous loads in hybrid-Trefftz plate bending elements.* Computers & Structures, 1995. **57**(5): p. 863-870.

64. Jesus, A.H., Cismasiu, I., and Freitas, J.A.T., *Fully automatic p-adaptive hybrid-Trefftz displacement element*, in *The 19th International Conference on Computer Methods in Mechanics*2011: Warszawa, Poland.

65. Cismasiu, I., Almeida, J.P.B.M., Castro, L.M.S., and Harbis, D., *Parallel solution techniques for hybrid-mixed finite element models*, in *In Innovative Computational Methods for Structural Mechanics, M. Papadrakakis, Ed. Saxe-Coburg Publisher, Edinburgh*1998.

66. Kita, E., and Kamiya, N., *Trefftz method: an overview.* Advances in Engineering Software, 1995. **24**: p. 3-12.

67. Jin, W.G., and Cheung, Y.K., *Trefftz direct method.* Advances in Engineering Software, 1995. **24**: p. 65-69.

68. Piltner, R., *Recent developments in the Trefftz method for finite element and boundary element applications.* Advances in Engineering Software, 1992. **24**: p. 107-115.

69. Jirousek, J., and Wróblewski, A., *T-elements: state of the art and future trends.* Archives of Computational Methods in Engineering, 1996(3/4): p. 323-434.

70. Fillunger, P., *Der Auftrieb von Talsperren.* Wochenschrift fur den offentlichen Baudienst, 1913. **I - III**(7): p. 532-510

71. Terzaghi, K., *Die Berechnung der Durchlassigkeit des Tones aus dem Verlauf der hydromechanischen Spannungserscheinungen.* Sitzungsber. Akad. Wissensch., Math.-Naturwiss. Klasse, 1923. **123**: p. 125-138

72. Truesdell, C., and Toupin, R.A., *The classical field theory.* Handbuch der Physik Encyclopedia of Physics, 1960. **III**(226-793).

73. Bowen, R.M., *Theory of Mixtures.* Continuum Physics, 1976. **3**(Academic Press, New York, ch.): p. 1-127.

74. Bowen, R.M., *Compressible porous media models by use of the theory of mixtures.* . International Journal of Engineering Science, 1982. **20**: p. 697-735.

75. Bowen, R.M., *Incompressible porous media models by use of the theory of mixtures.* International Journal of Engineering Science, 1980. **18**: p. 1129-1148.

76. Ehlers, W., *An Elastoplasticity Model in Porous Media Theories.* Transport in Porous Media 1992. **9**: p. 49-59.

77. Ehlers, W., *Continuum mechanics in environmental sciences and geophysics.* Constitutive Equations for Granular Materials in Geomechanical Context, 1993. **337**(CISM Courses and Lecture Notes): p. 313-402.

78. Biot, M.A., *General theory of the three-dimensional consolidation.* Journal of Applied Physics, 1941. **12**: p. 155-164.

79. Biot, M.A., *Theory of elasticity and consolidation for a porous anisotropic solid.* Journal of Applied Physics, 1955. **26**: p. 182-185.

80. Biot, M.A., *Theory of propagation of elastic waves in a fluid saturated porous solid. I. Low frequency range.* Journal of the Acoustic Society of America, 1956. **28**: p. 168-178.

81. Biot, M.A., *Theory of propagation of elastic waves in a fluid saturated porous solid. II. High frequency range.* Journal of the Acoustic Society of America, 1956. **28**: p. 179-191.

82. Plona, T.J., *Observation of a secon bulk compressional wave in a porous medium at ultrasonic frequencies.* Applied Physics Letters, 1980. **36**(4): p. 259-261.

83. Jones, J., *Rayleigh waves in a porous, elastic, saturated solid.* Journal of the Acoustical Society of America, 1961. **33**(7): p. 959-962.

84. Deresiewicz, H., and Rice, J.T., *The effect of boundaries on wave propagation in a liquid-filled porous solid: III. Reflection of plane waves at a free plane boundary (general case).* Bulletin of the Seismological Society of America, 1962. **52**(3): p. 595-625.

85. Schanz, M., and Diebels, S., *A comparative study of Biot's theory and the linear Theory of Porous Media for wave propagation problems.* Acta Mechanica, 2003. **161**: p. 213-235.

86. Simon, B.R., Wu, J.S-S., Zienkiewicz, O.C., and Paul, D.K., *Evaluation of u-w and u-π finite element methods for the dynamic response of saturated porous media using one-dimensional models.* International Journal for Numerical and Analytical Methods in Geomechanics, 1986. **10**: p. 461-482.

87. Kim, S.H., Kim, K.J., and Blouin, S.E., *Analysis of wave propagation in saturated porous media. I. Theoretical solution.* Computer Methods in Applied Mechanics and Engineering, 2002. **191**: p. 4061-4073.

88. Halpern, L., and Christiano, P., *Response of poroelastic halfspace to steady-state harmonic surface tractions.* International Journal for Numerical and Analytical Methods in Geomechanics, 1986. **10**: p. 609-632.

89. Akiyoshi, T., Fuchida, K., and Fang, H.L., *Absorbing boundary conditions for dynamic analysis of fluid-saturated porous media.* Soil Dynamics and Earthquake Engineering, 1994. **13**: p. 387-397.

90. Khalili, N., Yazdchi, M., and Valliappan, S., *Wave propagation analysis of two-phase saturated porous media using coupled finite-infinite element method.* Soil Dynamics and Earthquake Engineering, 1999. **18**: p. 533-553.

91. Zienkiewicz, O.C., and Shiomi, T., *Dynamic behaviour of saturated porous media; the generalized Biot formulation and its numerical solution.* International Journal for Numerical and Analytical Methods in Geomechanics, 1984. **8**: p. 71-96.

92. Smeulders, D.M.J., *On wave propagation in saturated and partially saturated porous media*, 1992, Technische Universiteit Eindhoven.

93. Berryman, J.G., Thigpen, L. and Chin, R.C.Y., *Bulk elastic wave propagation in partially saturated porous solids.* Journal of the Acoustical Society of America, 1988. **84**(1): p. 360–373.

94. Brutsaert, W., *The propagation of elastic waves in unconsolidated unsaturated granular mediums.* Journal of Geophysical Research, 1964. **69**(2): p. 243–257.

95. Loret, B.a.K., N., *A three-phase model for unsaturated soils.* International Journal for Numerical and Analytical Methods in Geomechanics, 2000. **24**: p. 893–927.

96. Muraleetharan, K.K., and Wei, C., *Dynamic behavior of unsaturated porous media: governing equations using the theory of mixtures with interfaces (TMI).* International Journal for Numerical and Analytical Methods in Geomechanics, 1999. **23**: p. 1579–1608.

97. Wei, C., Kanthasamy, K., and Muraleetharan., *Acontinuum Theory of Porous Media Saturated by Multiple Immiscible Fluids: I. Linear Poroelasticity.* International Journal of Engineering Science, 2002. **40**: p. 1087-1833.

98. Hassanizadeh, S.M., and Gray, W.G., *General conservation equations for multi-phase systems: 1. Averaging procedure.* Advances in Water Resources, 1979. **2**: p. 131–144.

99. Hassanizadeh, S.M., and Gray, W.G., *General conservation equations for multi-phase systems: 2. Mass, momenta, energy and entropy equations.* Advances in Water Resources, 1979. **2**: p. 191–203.

100. Hassanizadeh, S.M., and Gray, W.G., *General conservation equations for multi-phase systems: 3. Constitutive theory for porous media flow.* Advances in Water Resources, 1980. **3**: p. 25–40.

101. Oettl, G., Stark, R.F., and Hofstetter, G., *Numerical simulation of geotechnical problems based on a multi-phase finite element approach.* Computers and Geotechnics, 2004. **31**: p. 643–664.

102. de Boer, R., Ehlers, W., Kowalski, S., and Plischka, J., *Porous media, a survey of different approaches. Forschungsberichte aus dem Fachbereich Bauwesen*, 1991: Universitat Gesamthochschule Essen. Essen, Germany.

103. de Boer, R., *Highlights in the historical development of the porous media theory: toward a consistent macroscopic theory.* Applied Mechanics Reviews, 1996. **49**(4): p. 201–261.

104. Sheng, D., Gens, A., Fredlund, D.G., and Sloan, S.W., *Unsaturated soils: From constitutive modelling to numerical algorithms.* Computers and Geotechnics, 2008. **35**: p. 810–824.

105. Sheng, D., *Review of fundamental principles in modelling unsaturated soil behaviour.* Computers and Geotechnics, 2011. **38**: p. 757–776.

106. Wu, Y.S., and Forsyth, P.A. , *On the selection of primary variables in numerical formulation for modeling multiphase flow in porous media.* Journal of Contaminant Hydrology, 2001. **48**: p. 277–304.

107. Callari, C., and Abati, A., *Finite element methods for unsaturated porous solids and their application to dam engineering problems.* Computers & Structures, 2009. **87**: p. 485–501.

108. Khoei, A.R., and Mohammadnejad, T. , *Numerical modeling of multiphase fluid flow in deforming porous media: A comparison between two- and three-phase models for seismic analysis of earth and rockfill dams.* Computers and Geotechnics, 2011. **38**: p. 142–166.

109. Moldovan, I.D., Cao, D.T., and Freitas, J.A.T., *Hybrid-Trefftz Displacement and Stress Elements for Biphasis ElastoStatics.*, in *The 19th International Conference on Computer Methods in Mechanics*2011: Warszawa, Poland.

110. Moldovan, I.D., Cao, D.T., and Freitas, J.A.T., *Dynamic analysis of unsaturated porous media using hybrid-Trefftz finite elements*, in *The 11th International Conference on Vibration Problems (ICOVP-2013)*2013: Lisbon, Portugal.

111. Moldovan, I.D., Freitas, J.A.T., and Cao, D.T., *Sensitivity Assessment of Hybrid-Trefftz Stress and Displacement Elements for Poroelasticity*, in *Proceedings of the IV European Conference on Computational Mechanics*2010: Paris, France

112. Moldovan, I.D., and Freitas, J.A.T., *Hybrid-Trefftz displacement and stress elements for bounded poroelasticity problems.* Computers and Geotechnics, 2011.

113. Tamma, K.K., Zhoux, X., and Sha, D.A., *The time dimension: A theory towards the evolution, classication, characterisation and design of computational algorithms for transient/dynamic applications.* Archives of Computational Methods in Engineering, 2000. **7**(2): p. 67-290.

114. Tamma, K.K., Zhoux, X., and Sha, D., *A theory of development and design of generalized integration operators for computational structural dynamics.* International Journal for Numerical Methods in Engineering, 2001. **50**: p. 1619-1664.

115. Sneddon, I.N., *Fourier transforms*. 1995, New York: Dover.

116. Moldovan, I.D., *Hybrid-Trefftz finite elements for elastodynamic analysis of saturated porous media*, 2008, Universidade Técnica de Lisboa.

117. Moldovan, I.D., Cao, D.T., and Freitas, J.A.T., *Hybrid-Trefftz stress element for biphasic elastostatics*, in *CMNE 2011: Congresso de Métodos Numéricos em Engenharia*2011: Coimbra, Portugal.

118. Freitas, J.A.T., and Ji, Z.Y., *Hybrid-Trefftz finite element formulation for simulation of singular stress fields.* International Journal for Numerical Methods in Engineering, 1996. **39(2)**: p. 281-308.

119. Freitas, J.A.T., Moldovan, I.D., and Toan, C.D., *Dependencies in the Implementation of Hybrid-Trefftz Elements for Poroelastostatics*, 2010, Internal Report, ICIST, Technical Unversity of Lisbon.

120. Mow, V.C., Kuei, S.C., Lai, W.M., and Armstrong, C.G., *Biphasic creep and stress relaxation of articular cartilage in compression: theory and experiments.* Journal of Biomechanical Engineering, 1980. **102**: p. 73-83.

121. Detournay, E., and Cheng, A.H.-D., *Comprehensive Rock Engineering: Principles, Practice and Projects*. 1993: Pergamon Press.

122. Spilker, R.L., and Suh, J.-K., *Formulation and evaluation of a finite element model of soft hydrated tissue.* Computers & Structures, 1990. **35**: p. 425–439.

123. Pastor, M., Tongchun, L., and Merodo, J.A, *Stabilized finite elements for harmonic soil dynamics problems near the undrained-incompressible limit.* Soil Dynamics and Earthquake Engineering, 1997. **16**: p. 161-171.

124. Freitas, J.A.T., and Toma, M., *Hybrid-Trefftz stress elements for incompressible biphasic media.* International Journal for Numerical Methods in Engineering, 2009. **79**: p. 205-238.

125. Pluymers, B., van Hal, B., Vandepitte, D., and Desmet, W., *Trefftz-based methods for time-harmonic acoustics.* Archives of Computational Methods in Engineering, 2007. **14**: p. 343–381.

126. Pian, T.H.H., and Wu, C.C., *Hybrid and Incompatible Finite Element Methods*. 2006: Chapman & Hall/CRC, Boca Raton.